

University of Windsor

Scholarship at UWindor

Electronic Theses and Dissertations

Theses, Dissertations, and Major Papers

2005

Adhesion and material transfer between aluminum and surfaces coated with diamond-like carbon and other coatings.

Erkan Konca
University of Windsor

Follow this and additional works at: <https://scholar.uwindsor.ca/etd>

Recommended Citation

Konca, Erkan, "Adhesion and material transfer between aluminum and surfaces coated with diamond-like carbon and other coatings." (2005). *Electronic Theses and Dissertations*. 895.
<https://scholar.uwindsor.ca/etd/895>

This online database contains the full-text of PhD dissertations and Masters' theses of University of Windsor students from 1954 forward. These documents are made available for personal study and research purposes only, in accordance with the Canadian Copyright Act and the Creative Commons license—CC BY-NC-ND (Attribution, Non-Commercial, No Derivative Works). Under this license, works must always be attributed to the copyright holder (original author), cannot be used for any commercial purposes, and may not be altered. Any other use would require the permission of the copyright holder. Students may inquire about withdrawing their dissertation and/or thesis from this database. For additional inquiries, please contact the repository administrator via email (scholarship@uwindsor.ca) or by telephone at 519-253-3000ext. 3208.

INFORMATION TO USERS

This manuscript has been reproduced from the microfilm master. UMI films the text directly from the original or copy submitted. Thus, some thesis and dissertation copies are in typewriter face, while others may be from any type of computer printer.

The quality of this reproduction is dependent upon the quality of the copy submitted. Broken or indistinct print, colored or poor quality illustrations and photographs, print bleedthrough, substandard margins, and improper alignment can adversely affect reproduction.

In the unlikely event that the author did not send UMI a complete manuscript and there are missing pages, these will be noted. Also, if unauthorized copyright material had to be removed, a note will indicate the deletion.

Oversize materials (e.g., maps, drawings, charts) are reproduced by sectioning the original, beginning at the upper left-hand corner and continuing from left to right in equal sections with small overlaps.

ProQuest Information and Learning
300 North Zeeb Road, Ann Arbor, MI 48106-1346 USA
800-521-0600

UMI[®]

**ADHESION AND MATERIAL TRANSFER BETWEEN ALUMINUM AND
SURFACES COATED WITH DIAMOND-LIKE CARBON AND OTHER
COATINGS**

By

ERKAN KONCA

**A Dissertation
Submitted to the Faculty of Graduate Studies and Research
through Engineering Materials
in Partial Fulfillment of the Requirements for
the Degree of Doctor of Philosophy at the
University of Windsor**

Windsor, Ontario, Canada

2005

© 2005 Erkan Konca



Library and
Archives Canada

Bibliothèque et
Archives Canada

0-494-09703-5

Published Heritage
Branch

Direction du
Patrimoine de l'édition

395 Wellington Street
Ottawa ON K1A 0N4
Canada

395, rue Wellington
Ottawa ON K1A 0N4
Canada

Your file *Votre référence*

ISBN:

Our file *Notre référence*

ISBN:

NOTICE:

The author has granted a non-exclusive license allowing Library and Archives Canada to reproduce, publish, archive, preserve, conserve, communicate to the public by telecommunication or on the Internet, loan, distribute and sell theses worldwide, for commercial or non-commercial purposes, in microform, paper, electronic and/or any other formats.

The author retains copyright ownership and moral rights in this thesis. Neither the thesis nor substantial extracts from it may be printed or otherwise reproduced without the author's permission.

AVIS:

L'auteur a accordé une licence non exclusive permettant à la Bibliothèque et Archives Canada de reproduire, publier, archiver, sauvegarder, conserver, transmettre au public par télécommunication ou par l'Internet, prêter, distribuer et vendre des thèses partout dans le monde, à des fins commerciales ou autres, sur support microforme, papier, électronique et/ou autres formats.

L'auteur conserve la propriété du droit d'auteur et des droits moraux qui protègent cette thèse. Ni la thèse ni des extraits substantiels de celle-ci ne doivent être imprimés ou autrement reproduits sans son autorisation.

In compliance with the Canadian Privacy Act some supporting forms may have been removed from this thesis.

Conformément à la loi canadienne sur la protection de la vie privée, quelques formulaires secondaires ont été enlevés de cette thèse.

While these forms may be included in the document page count, their removal does not represent any loss of content from the thesis.

Bien que ces formulaires aient inclus dans la pagination, il n'y aura aucun contenu manquant.


Canada

ABSTRACT

Adhesion and transfer of aluminum to the surfaces of tool coatings that are potential candidates for dry machining of Al-Si alloys were investigated. First, 319 Al alloy pins were tested against various industrial coatings (CrN, TiB₂, TiAlN, TiN, and TiCN) using a pin-on-disc tribometer. The analyzed Scanning Electron Microscope (SEM) images of the wear tracks were used to rank the coatings according to the amount of Al transferred on their surfaces. In general, the TiB₂ and TiCN coatings exhibited the least amount of Al transfer on their surfaces compared to the other coatings.

Second, the tribological behaviour of the diamond-like carbon (DLC) coatings against Al was investigated since aluminum has much lower tendency to adhere to DLC in ambient air compared to other hard coatings tested. Magnetron sputtered non-hydrogenated DLC coatings were tested against 319 Al, tungsten carbide (WC) and sapphire (Al₂O₃) at 120, 300 and 400°C and under various test atmospheres including air (0-85 % RH), vacuum, inert gases (Ar, He and N₂) and 40% H₂-60% He.

Although much softer than WC and Al₂O₃, 319 Al alloy inflicted the most severe wear of non-hydrogenated DLC especially at elevated temperatures. Non-hydrogenated DLC coatings showed high coefficient of friction, (COF), (0.45-0.75) and high wear rates in inert gases and vacuum compared to ambient air (COF= 0.09-0.16). Very low COF values (0.01-0.02) were observed in 40% H₂-60% He mixture. The low COF values in ambient air and in 40% H₂-60% He mixture were associated with formation of carbonaceous transfer layers on counterfaces. Formation of easy-to-shear transfer layer together with adsorption and dissociation of the atmospheric water on the sliding surfaces were suggested as the possible mechanisms that minimize COF in ambient air.

To elucidate the effect of material properties on adhesion, 1100 Al, Cu, and Ti were tested against CrN, non-hydrogenated DLC, and TiB₂ coatings in ambient air and argon. Cu exhibited the least amount of transfer to all three coatings. Chemical affinity towards the counterface, yield strength, and thermal conductivity were found as the most critical properties that determine adhesion and transfer between a given material pair during dry sliding contact.

To
my parents Gulsum and Enver,
my sisters Gul Esin and Sibel,
and to
my brother Hakan

ACKNOWLEDGEMENTS

There are two individuals whom I would like to especially acknowledge: First, thank you Dr. Alpas for accepting me as a graduate student. Thank you so much for your diligent supervision and continuous support throughout my study at the University of Windsor. Second, thank you YT for your supervision and endless inspiration that always motivated me; even at times I was pessimistic.

I would like to acknowledge all the faculty and staff of the University of Windsor for their support and assistance throughout my studies. I especially thank Ms. Qin Tu, Ms. Barbara Denomey, Mr. John Robinson and the staff at the Technical Support Centre. Also, I would like to thank all members of my dissertation committee for their careful revisions and suggestions.

I am grateful to Dr. J. Dasch, A. Weiner, M. Lukitsch and T. Perry of the GM R&D Center for their help and friendship especially during the summers I spent there as a summer intern. I also would like to thank M. Militello, B. Powell, R. Waldo, B. Paluch, C. Hayden, and C.C. Ang of GM R&D Center for their assistance. Thanks to all my current and past roommates and members of the Industrial Research Chair, especially to Levent, Mustafa and Subutay, for their help and friendship. Finally, I am so grateful to my family who always gave me energy and morale in every opportunity they had.

TABLE OF CONTENTS

	Page
ABSTRACT	iii
DEDICATION	iv
ACKNOWLEDGEMENTS	v
LIST OF TABLES	xi
LIST OF FIGURES	xii
LIST OF APPENDICES	xxiv
LIST OF ABBREVIATIONS	xxv
CHAPTER 1	
INTRODUCTION	1
1.1. Driving Force for Dry Machining and Manufacturing: Social and Economic Aspects.....	1
1.2. Dry Machining of Aluminum and Associated Challenges.....	1
1.3. Metalworking Fluids and Alternative Ways of Cooling.....	2
1.4. Optimization of Machining Parameters and Tool Geometry.....	3
1.5. Use of Coatings to Reduce Material Adhesion to Tool Surfaces.....	3
1.6. The Need for the Current Study.....	4
1.7. Scope and Objectives.....	4
1.7.1. Transfer of 319 Al to Various Coating Surfaces.....	4
1.7.2. Transfer of Al, Cu and Ti to CrN, DLC and TiB ₂ Coatings.....	5
1.7.3. Tribological Behaviour of Non-Hydrogenated DLC Coatings.....	5
1.8. Organisation of the Dissertation.....	5
CHAPTER 2	
LITERATURE REVIEW	8
2.1. Terminology.....	8
2.2. Previous Studies on Adhesion and Material Transfer	8
2.2.1. Effect of Environment on Adhesion and Material Transfer in Normal and Sliding Contact.....	14
2.3. Previous Studies on the Machining Performance and Tribological Behaviour of Some Coatings against Aluminum	17
2.3.1. Carbon Based Coatings.....	17
2.3.2. Titanium Diboride (TiB ₂) Coatings.....	20
2.3.3. Solid Lubricant Coatings.....	22
2.4. Review of the Tribological Behaviour of the Diamond-like Carbon Coatings.....	22
2.4.1. Effect of Hydrogen Content of the DLC Films.....	24
2.4.2. Transfer Layer Formation and Friction-induced Structural Changes....	26

2.4.3. Effect of Test Environment on the Tribological Behaviour of DLC Coatings.....	28
2.4.4. Modeling the Dependency of the Tribological Behaviour of DLC and Graphite on the Sorption of Gaseous Species on Their Surfaces.....	30
2.4.5. Effect of Test Temperature on the Tribological Behaviour of DLC Coatings	31
2.5. Remarks.....	32

CHAPTER 3

EXPERIMENTAL METHODS AND MATERIALS.....	54
3.1. Characterization of Test Materials.....	54
3.1.1. Thickness Measurement of Coatings Using Radial Sectioning Method	54
3.1.2. Mechanical Property Measurement Tools.....	55
3.1.2.1. Rockwell Hardness Measurement.....	55
3.1.2.2. Vickers Micro Hardness Measurement.....	55
3.1.2.3. Nanoindentation of Coatings.....	55
3.1.3. Structural Characterization Methods.....	56
3.1.3.1. X-ray Diffraction.....	56
3.1.3.2. Raman Spectroscopy.....	57
3.1.4. Surface Profilometry.....	58
3.2. Description of the Substrate Material and the Coatings.....	58
3.2.1. M2 Tool Steel Substrates.....	58
3.2.2. Diamond-like Carbon Coatings.....	58
3.2.2.1. 60 and 80-V DLC coatings.....	58
3.2.2.2. Teer Graphitic™ DLC Coatings.....	61
3.2.3. TiB ₂ Coatings.....	61
3.2.4. CrN Coatings.....	61
3.2.5. TiN Coatings.....	62
3.2.6. TiAlN Coatings.....	62
3.2.7. TiCN Coatings.....	62
3.3. Description of 319 Al Alloy Counterfaces and other Counterface Materials.	63
3.3.1. 319 Al Alloy Pins.....	63
3.3.2. Other Counterface Materials: Al, Cu, Mg, Ti, Al ₂ O ₃ and WC.....	63
3.4. Pin-on-disc Tribometers.....	66
3.4.1. High Temperature Tribometer.....	66
3.4.2. High Temperature Vacuum Tribometer.....	66
3.4.3. ISC 450 Tribometer.....	67
3.5. Conditions.....	67
3.5.1. Loading Conditions.....	67
3.5.2. Control of Test Atmosphere.....	67
3.6. Evaluation Tools and Procedures.....	68
3.6.1. Optical and Scanning Electron Microscopy, Energy Dispersive Spectroscopy	68
3.6.2. Quantification of the Amount of Adhesion	68
3.6.3. Measurement of the Wear Rates.....	69

CHAPTER 4	
ADHESION AND TRANSFER BEHAVIOUR OF 319 Al ALLOY TO INDUSTRIAL COATINGS.....	91
4.1. Pin-on-disc Tests in Ambient air.....	91
4.2. Effect of Speed.....	92
4.3. Pin-on-disc Tests in Argon.....	93
4.4. Pin-on-disc Tests at 160°C.....	93
4.5. Discussion.....	93
4.5.1. Aluminum Transfer and Debris Generation under Ambient Atmosphere.....	93
4.5.2. Effect of Sliding Speed on Aluminum Transfer and Debris Generation.....	95
4.5.3. Effect of Atmosphere on Aluminum Transfer and Debris Generation.....	95
4.5.4. Effect of Temperature on Aluminum Transfer and Debris Generation.....	96
4.5.5. Effect of Surface Roughness Aluminum Transfer and Debris Generation.....	97
4.6. Summary and Remarks.....	98
4.7. Outlook.....	99

CHAPTER 5	
TRIBOLOGICAL BEHAVIOUR OF THE NON-HYDROGENATED DLC COATINGS AGAINST 319 Al ALLOY.....	121
5.1. Tribological Behaviour of the 80-V DLC Coatings against 319 Al under Various Test Environments.....	121
5.1.1. Tests in Vacuum.....	121
5.1.2. Tests in Nitrogen.....	122
5.1.3. Tests in Dry air.....	122
5.1.4. Tests in Air with 20 - 85% Relative Humidity.....	122
5.2. Tribological Behaviour of the 80-V DLC Coatings against WC.....	123
5.2.1. Tests in Vacuum and Nitrogen Atmospheres.....	123
5.2.2. Tests in Dry Air (0% RH).....	123
5.2.3. Tests in Air with 20 - 85 % Relative Humidity.....	124
5.3. Tribological Behaviour of the Graphit-iC DLC Coatings against 319 Al under Various Test Environments.....	125
5.3.1. Tests in Vacuum, Argon, Helium, and Nitrogen.....	125
5.3.2. Tests in Dry Air (0% RH).....	125
5.3.3. Tests in Ambient Air.....	125
5.3.4. Tests in H ₂ -He mixture against 319 Al	126
5.3.5. Tests in H ₂ -He mixture against WC.....	126
5.4. Elevated Temperature Testing of DLC Coatings against 319 Al, WC and Al ₂ O ₃	127
5.4.1. Effect of Counterface Material.....	128
5.4.2. Effect of Deposition Conditions.....	129
5.5. Discussion.....	130

5.5.1. Tribological Behavior of the Non-hydrogenated DLC Coatings against 319 Al in Vacuum and Inert Gas Environments.....	130
5.5.2. Tribological Behavior of the Non-hydrogenated DLC Coatings in Dry Air against 319 Al - Interaction of DLC Coating Surface with O ₂	131
5.5.3. The Effect of Water Vapour on the Tribological Behavior of Non-hydrogenated DLC against 319 Al.....	132
5.5.3.1. The Role of Material Transfer to the Counterface on Very Low COF.....	133
5.5.4. Tribological Behaviour of the Non-hydrogenated DLC Coatings in an H ₂ -He Environment.....	134
5.5.4.1. Material Transfer to the Contact Surface of the 319 Al Pin.....	134
5.5.4.2. The Role of Hydrogen Pressure on the Very Low COF Behaviour.....	135
5.5.4.3. Interaction Mechanisms of Hydrogen with the Sliding Surfaces.....	136
5.5.5. Elevated Temperature Tribological Behaviour of Non-hydrogenated DLC Coatings.....	138
5.5.5.1. Stability of the Coatings at High Temperature.....	139
5.5.5.2. Comparison of the Wear Mechanisms of DLC Coating against 319 Al with WC and Al ₂ O ₃	140
5.6. Summary and Remarks.....	142
5.6.1. Effect of Test Atmosphere.....	142
5.6.2. Effect of Temperature.....	144
5.7. Outlook.....	144

CHAPTER 6

ADHESION AND TRANSFER BEHAVIOUR OF PURE METALS

(Al, Cu AND Ti) TO Graphit-iC DLC, CrN, AND TiB₂ COATINGS.....	195
6.1. Adhesion and Transfer to Graphit-iC DLC.....	195
6.1.1. 1100 Al against Graphit-iC DLC in Argon.....	195
6.1.2. 1100 Al against Graphit-iC DLC in Ambient Air.....	196
6.1.3. Cu against Graphit-iC DLC in Argon.....	196
6.1.4. Cu against Graphit-iC DLC in Ambient Air.....	197
6.1.5. Ti against Graphit-iC DLC in Argon.....	197
6.1.6. Ti against Graphit-iC DLC in Ambient Air.....	198
6.2. Adhesion and Transfer to TiB ₂	198
6.2.1. 1100 Al against TiB ₂ in Argon.....	198
6.2.2. 1100 Al against TiB ₂ in Ambient Air.....	199
6.2.3. Cu against TiB ₂ in Argon.....	199
6.2.4. Cu against TiB ₂ in Ambient Air.....	199
6.2.5. Ti against TiB ₂ in Argon.....	200
6.2.6. Ti against TiB ₂ in Ambient Air.....	200
6.3. Adhesion and transfer to CrN.....	201
6.3.1. 1100 Al against CrN in Argon.....	201
6.3.2. 1100 Al against CrN in Ambient Air.....	201
6.3.3. Cu against CrN in Argon.....	201

6.3.4. Cu against CrN in Ambient Air.....	202
6.3.5. Ti against CrN in Argon.....	202
6.3.6. Ti against CrN in Ambient Air.....	202
6.4. Remarks.....	202
6.5. General Discussion of the Adhesion and Material Transfer Phenomena during Sliding Wear.....	204
6.5.1. Adhesion and Material Transfer in an Argon Atmosphere.....	204
6.5.1.1. Why Does Cu Not Adhere to the CrN, DLC or TiB ₂ Coatings in Argon?.....	204
6.5.1.2. Why Does Ti Have High Tendency to Adhere to CrN, DLC and TiB ₂ Coatings in Argon?.....	205
6.5.1.3. Effect of Sliding Speed on Adhesion and Material Transfer in Argon.....	206
6.5.2. Frictional Heating of the Sliding Surfaces.....	206
6.5.3. Adhesion and Material Transfer in Ambient Air.....	209
6.5.3.1. Mechanism Debris Generation during Sliding.....	209
6.5.3.2. Tribochemistry at Sliding Interfaces in Ambient Air.....	211
6.5.3.3. Effect of Sliding Speed on Adhesion and Material Transfer in Ambient Air.....	212
CHAPTER 7	
CONCLUSIONS.....	270
7.1. Transfer of 319 Al to Various Coating Surfaces.....	270
7.2. Study of the Transfer of Al, Cu and Ti to CrN, DLC and TiB ₂ Coatings.....	271
7.3. Investigation of the Tribological Behaviour of Non-Hydrogenated DLC Coatings	272
7.4. Practical Conclusions.....	274
7.5. Suggestions for Future Work.....	274
APPENDICES	
A.1. Frictional Heating of Sliding Surfaces.....	277
A.2. Impingement Rate (Flux) of Gaseous Species [134].....	282
REFERENCES.....	283
VITA AUCTORIS	295

LIST OF TABLES

Table No	Caption	Page
Table 2.1.	Metal pairs studied by Hwang [23]	12
Table 3.1.	Deposition parameters of the DLC coatings	60
Table 3.2.	Properties of the coatings	64
Table 3.3.	Chemical composition (wt. %) of the 319 Al pins	65
Table 3.4.	Hardness values of the counterface materials	65
Table 6.1.	The calculated flash temperature values.	208
Table A.1.1.	a) Nomenclature, and b) expressions for the equivalent heat diffusion distances	280
Table A.1.2.	The material properties, values of the other parameters and assumptions used to calculate the bulk and flash temperatures that were discussed in section 6.5.2.	281
Table A.1.3.	The measured average COF and radius of nominal contact area values in ambient air.	281

LIST OF FIGURES

Figure No	Caption	Page
Figure 1.1.	The image of an uncoated HSS drill subjected to dry drilling of 319 Al alloy. The severity of aluminum adhesion to drill flutes is clearly seen (courtesy of the GM R&D Center). The drill was 6.35 mm diameter, 2-flute, high helix, 118° point angle, HSS drills from Precision Twist Drill Co., (Crystal Lake, IL). Drilling was done at 61 m/min speed and 0.13 mm/rev. feed.	7
Figure 2.1.	The plot of the COA values of the self-mated metal pairs with respect to their hardness [13].	34
Figure 2.2.	The plot of the static (initial) COF values of various metals pairs with respect to their hardness ratios [23].	35
Figure 2.3.	Adhesive transfer of the slip tongue [18].	36
Figure 2.4.	Adhesive transfer of the wedge [18].	37
Figure 2.5.	The variation of the static COF values of Cu, Fe and steel with respect to inverse of adsorbate concentration (from ref 19 in [17]).	38
Figure 2.6.	The plot of the pull-off forces vs. elastic modulus values of various metals when they were tested against polycrystalline manganese zinc ferrite in ultrahigh vacuum before and after being cleaned [22].	39
Figure 2.7.	The plot of the COF vs. shear modulus values of various metals when they were tested against polycrystalline manganese zinc ferrite in ultrahigh vacuum before and after being cleaned [22].	40
Figure 2.8.	The vacuum COF values between various metals and SiC surface as a function of the total surface energy of the respective metal in real area of contact [22].	41
Figure 2.9.	The variation of the COA as a function of the exposure to (A) water vapour, and (B) water vapour and oxygen [31]. 1 L = 1×10^{-6} Torr · sec.	42
Figure 2.10.	Illustration of a possible mechanism of the role of the low friction coating during a machining operation [5].	43
Figure 2.11.	Proposed wear mechanism for the counter body against DLC film [56].	44
Figure 2.12.	Diamond coatings deposited at a) 1183 K b) 779 K [57].	45
Figure 2.13.	Chips produced when cutting with uncoated and DLC coated cemented carbide tools. Small and curled chips are easier to evacuate [58].	46
Figure 2.14.	Experimental setup [64].	47
Figure 2.15.	Test configuration [65].	48
Figure 2.16.	Test configuration [66].	49
Figure 2.17.	Tribometer used by Murakawa and Takeuchi [69].	50
Figure 2.18.	Various forms of carbon-hydrogen alloys [70].	51

Figure 2.19. Raman spectra of the as-deposited DLC coating (DLN2) and its transfer films after running in humid air for 2×10^3 cycles and in dry air for 3×10^2 cycles [110].	52
Figure 2.20. The effect of RH in air on wear rate of the DLC coating at sliding speeds of 0.05 and 0.25 m/s. Data for sliding in water is plotted at a RH of 100% [84].	53
Figure 3.1. a) Side view of the radial sectioning configuration. A hard rotating sphere is pressed against the coated sample and abrasive suspension is fed to the contact region to remove material by three-body abrasive wear. b) Top view of the resulting worn area of the diamond-like carbon coating deposited at 80 V bias (80-V DLC). The diameters of the inner and outer circles (ID and OD) are measured to calculate the coating thickness (t) using Eqn. 3.1.	70
Figure 3.2. The indentation load-displacement curve for the diamond-like carbon coating deposited at 60 V bias (60-VDLC).	71
Figure 3.3. Optical image of a typical M2 tool steel disc on which the coatings used in this study were deposited. The diameter and the thickness of the M2 tool steel discs were 25.4 mm and 10 mm respectively.	72
Figure 3.4. Optical images of the microstructure of the M2 tool steel substrate. The small brighter/whiter particles are various carbides of Cr, V, W and Mo.	73
Figure 3.5. A schematic drawing of the configuration of the Teer UDP 550 unbalanced magnetron sputtering system used to deposit DLC coatings. The letters N and S denote the magnets of the sputtering units.	74
Figure 3.6. The Raman spectra of the as-deposited Teer Graphit-iC™, 60-V and 80-V DLC coatings.	75
Figure 3.7. X-Ray diffraction patterns of the studied coatings; a) TiB ₂ , b) CrN.	76
Figure 3.7. X-Ray diffraction patterns of the studied coatings; c) TiN, d) TiAlN.	77
Figure 3.7. X-Ray diffraction patterns of the studied coatings; e) TiCN. Some peaks that belong to M2 steel substrate are also indicated.	78
Figure 3.8. Optical images of the microstructure of the 319 Al pins.	79
Figure 3.9. Cu, Al and Ti pins used in this study.	80
Figure 3.10. Optical images of the microstructures of the a) Al, b) Cu pins.	81
Figure 3.10. c) The optical image of the microstructure of the Ti pins.	82
Figure 3.11. a) and b) The high temperature tribometer (CSM, Switzerland) at the University of Windsor.	83
Figure 3.12. Setup screen of the computer program for pin-on-disc tests.	84
Figure 3.13. The high temperature vacuum tribometer (CSM, Switzerland) at the GM R&D Center.	85
Figure 3.14. Schematic of the pin-on-disc configuration.	86
Figure 3.15. SEM images were taken at the locations shown on the sliding track.	87
Figure 3.16. a) SEI and b) BEI mode SEM images of a section of the sliding track of the M2 steel when tested in ambient air at 0.12 m/s sliding speed for 18 m. Dark particles are the transferred aluminum and the	88

light particles are the debris.

- Figure 3.17.** Measurement of the wear rates. 89
- Figure 3.18.** **a)** The surface, and **b)** the cross-sectional profiles of a region of the wear track on 60-V DLC coating tested against 319 Al at 120°C. 90
- Figure 4.1.** Percentages of the surface areas of the coating sliding tracks covered by aluminum and loose debris when tested in ambient air (33-51% RH) at a sliding speed of 0.12 m/s for 18 m of sliding distance. The applied load was 5 N. 100
- Figure 4.2.** SEM images of sections of the sliding tracks of **a)** smooth ($R_a = 16$ nm) and **b)** rough ($R_a = 83$ nm) TiB₂ coatings tested against 319 Al for 300 revolutions (18 m) in ambient air (43% RH) at 0.12 m/s sliding speed. The applied load was 5 N. The white particles are the loose debris generated during sliding. 101
- Figure 4.3.** EDS analyses of **a)** the smooth TiB₂ coating, **b)** a typical loose debris particle indicated in Figure 4.2.a, and **c)** an adhered Al piece on the TiB₂ shown in Figure 4.2.a. 102
- Figure 4.4.** **a)** SEI and **b)** BEI SEM images of a section of the sliding track of the CrN coating when tested in ambient air (41% RH) at 0.12 m/s sliding speed for 18 m. The applied load was 5 N. Significant amount of Al transfer to the CrN coating surface occurred. 103
- Figure 4.4.** **c)** The EDS analysis of the location shown in Figure 4.4.b). The adhered Al pieces were significantly oxidized. 104
- Figure 4.5.** Effect of test speed on the percentage of the coating surface area covered by aluminum. Tests were done at sliding speeds of 0.12 and 0.60 m/s for 18 m of sliding distance under 5 N of load in ambient air. 105
- Figure 4.6.** Effect of test speed on the percentage coating surface area covered by debris. Tests were done at sliding speeds of 0.12 and 0.60 m/s for 18 m of sliding distance under 5 N load in ambient air. 106
- Figure 4.7.** Effect of test atmosphere on the percentage of the coating surface area covered by aluminum. Tests were done under ambient air and argon gas at a sliding speed of 0.12 m/s for a sliding distance 18 m under 5 N load. 107
- Figure 4.8.** Effect of test atmosphere on the percentage of the coating surface area covered by debris. Tests were done under ambient air and argon at a sliding speed of 0.12 m/s for a sliding distance 18 m under 5 N load. 108
- Figure 4.9.** The COF curves of the samples tested against 319 Al under argon and ambient air; **a)** TiB₂ (16 nm R_a), **b)** TiB₂ (83 nm R_a). 109
- Figure 4.9.** The COF curves of the samples tested against 319 Al under argon and ambient air; **c)** M2 steel, **d)** CrN. 110
- Figure 4.9.** The COF curves of the samples tested against 319 Al under argon and ambient air; **e)** TiN, **f)** TiAlN. 111
- Figure 4.9.** The COF curves of the samples tested against 319 Al under argon and ambient air; **g)** TiCN. Tests were done at a sliding speed of 0.12 112

m/s under an applied load of 5 N. The COF curves recorded in argon generally had less fluctuation than those recorded in ambient air.

- Figure 4.10.** Effect of test temperature on the percentage of the coating surface 113 area covered by aluminum. Tests were done at 25 and 160°C at a sliding speed of 0.12 m/s for 18 m of sliding distance under 5 N load.
- Figure 4.11.** BEI SEM images of the contact surfaces of the 319 Al pins tested 114 against TiCN coatings under a) ambient air and b) argon gas. The tests were performed at 0.12 m/s sliding speed under an applied load of 5 N for a sliding distance of 18 m.
- Figure 4.12.** EDS analyses of selected locations indicated in Figures 4.11.a&b: a) 115 Location 1 in Figure 4.11.a. b) Location 2 in Figure 4.11.a.
- Figure 4.12.** EDS analyses of selected locations indicated in Figures 4.11.a&b: c) 116 Location 3 in Figure 4.11.b., d) Location 4 in Figure 4.11.b.
- Figure 4.13.** Percentage of the area covered by aluminum versus sliding distance 117 for smooth ($R_a = 16$ nm) and rough ($R_a = 83$ nm) TiB₂. Tests were done in ambient air at 0.12 m/s sliding speed under 5 N load.
- Figure 4.14.** SEM images for a) smooth ($R_a = 16$ nm) and b) rough ($R_a = 83$ nm) 118 TiB₂ at 50 revolutions (3 m) when tested against 319 Al in ambient air at 0.12 m/s sliding speed under 5 N of applied load.
- Figure 4.14.** c) Enlarged view of a region in Figure 4.14.b). 60 % of the surface 119 area of the rough TiB₂ was covered with mostly thin layers of aluminum.
- Figure 4.15.** COF curves for a) rough ($R_a = 83$ nm) and b) smooth ($R_a = 16$ nm) 120 TiB₂ coatings when tested in ambient air at 0.12 m/s sliding speed for 18 m of sliding distance under an applied load of 5 N.
-
- Figure 5.1.** a) The COF curve between the 80-V DLC coating and 319 Al 146 during sliding in vacuum (6.65×10^{-3} Pa) for 8.5×10^3 revolutions, b) The SEI SEM image of a section of the wear track of the 80-V DLC coating. The DLC coating was heavily worn. Adhered Al pieces were observed on the wear track. The applied load and sliding speed were 5 N and 0.12 m/s.
- Figure 5.2.** SEI SEM images of a) a section of the wear track of the 80-V DLC 147 coating tested against 319 Al in nitrogen (101.3 kPa), and b) enlarged view of the location indicated in a) showing the aluminum transfer. The applied load and sliding speed were 5 N and 0.12 m/s.
- Figure 5.3.** a) The COF between the 80-V DLC coating and 319 Al during 148 sliding in dry air for 3.5×10^3 revolutions, b) the SEM image of a section of the wear track of the 80-V DLC coating.
- Figure 5.3.** c) A closer look at the debris generated during sliding between 319 149 Al and 80-V DLC coating in dry air, d) EDS analysis of the 80-V DLC coating surface.
- Figure 5.3.** e) A typical EDS curve of a debris particle while it is analyzed on 150 the coating surface. The applied load and sliding speed were 5 N and 0.12 m/s, respectively.

- Figure 5.3.** f) SEM image of the contact surface of the corresponding 319 Al 151 pin, and g) the EDS analysis of the location indicated in f).
- Figure 5.4.** a) The COF curve, b) SEM image of a section of the wear track of 152 the 80-V DLC coatings tested against the 319 Al pin in air with 22% RH for 3.5×10^3 revolutions.
- Figure 5.4.** c) SEM image of the contact surface of the corresponding 319 Al 153 pin, d) EDS analysis of the location indicated in c).
- Figure 5.5.** SEM images of a) a region of the wear track of the 80-V DLC 154 coating tested against the WC ball in vacuum for 1.2×10^3 revolutions and b) the contact surface of the corresponding WC ball (1) with coating material around (2).
- Figure 5.5.** c) SEM image of a section of the wear track of the DLC coating 155 tested against the WC ball in vacuum for 3.5×10^3 revolutions, and d) the EDS analysis of the location indicated in c). A significant amount of WC transfer to the 80-V DLC coating surface was observed as verified by EDS. The applied load and the sliding speed were 4.9 N and 0.12 m/s.
- Figure 5.6.** SEM images of a) a region of the wear track of the 80-V DLC 156 coating tested against the WC ball in dry air (0% RH) for 1.2×10^3 revolutions and b) the contact surface of the corresponding WC ball.
- Figure 5.6.** c) EDS analysis of the location indicated in b). The applied load and 157 the sliding speed were 5 N and 0.12 m/s.
- Figure 5.7.** SEM images of a) a region of the wear track of the 80-V DLC 158 coatings tested against the WC ball in air with 50% RH for 1.2×10^3 revolutions and b) the contact surface of the corresponding WC ball.
- Figure 5.7.** c) The EDS analysis of the location indicated on the transfer layer 159 formed on the contact surface of the WC ball. The applied load and the sliding speed were 5 N and 0.12 m/s.
- Figure 5.8.** a) The wear rates, and b) the steady state COF values of the 80-V 160 DLC coating against 319 Al and WC under various test environments. The applied load and sliding speed were 5 N and 0.12 m/s.
- Figure 5.9.** The COF curves for the Graphit-iC DLC coating tested against the 161 319 Al alloy in a) vacuum (6.65×10^{-4} Pa), b) argon.
- Figure 5.9.** The COF curves for the Graphit-iC DLC coating tested against the 162 319 Al alloy in c) helium, and d) nitrogen. The applied load was 5 N and the sliding speed was 0.12 m/s.
- Figure 5.10.** a) SEI SEM image of a region of the wear track of the Graphit-iC 163 DLC coating tested against 319 Al alloy in vacuum for 1×10^4 revolutions, b) an enlarged view of the location indicated by a rectangle in b).
- Figure 5.10.** c) BEI SEM image of the contact surface of the corresponding 319 164 Al pin, and d) the EDS analysis of the location indicated in c). The applied load and the sliding velocity were 5 N and 0.12 m/s.
- Figure 5.11.** The variation of the COF between the 319 Al and Graphit-ic DLC 165 during sliding in dry air. The applied load and sliding speed were 5 N

and 0.12 m/s.

- Figure 5.12.** The COF curve for the Graphit-iC DLC coating tested against the 166 319 Al alloy at 0.12 m/s sliding speed and 5 N applied load in ambient air (47 % RH).
- Figure 5.13.** a) The COF curve for the Graphit-iC DLC coating tested against the 167 319 Al alloy at 0.12 m/s sliding speed and 5 N applied load in the 40% H₂-60% He atmosphere, b) expanded view of the first 300 revolutions.
- Figure 5.14.** a) The COF curve for the non-hydrogenated DLC coating tested 168 against WC at 0.12 m/s sliding speed and 5 N applied load in He-H₂ mixture, and b) semi-log scale plot of a).
- Figure 5.15.** a) The measured wear rates, and b) the steady state COF values of 169 the Graphit-iC DLC coating against 319 Al under various environments. The applied load and sliding speed were 5 N and 0.12 m/s.
- Figure 5.16.** The COF curves between the 80-V DLC coated disc and the 319 Al 170 pin at 25, 120 and 300°C. Tests were run for 60 m of sliding distance (1x10³ revolutions) under an applied load of 5 N at 0.12 m/s sliding speed.
- Figure 5.17.** BEI SEM images of the regions of the wear tracks of the 80-V DLC 171 coating tested against the 319 Al pin at 300°C for a) 1x10³ revolutions and b) 1x10⁴ revolutions. The applied load was 5 N.
- Figure 5.18.** The variation of the wear rate of the 80-V DLC coating with 172 temperature when tested against 319 Al, WC and sapphire at 25, 120 and 300°C. Tests were run for 1,500 m of sliding distance (2.5x10⁴ revolutions) at 25°C and for 60 m of sliding distance (1x10³ rev.) at 120 and 300°C using 5 N applied load.
- Figure 5.19.** Comparison of the changes in the wear rates of the 60-V DLC, 80-V 173 DLC and the Graphit-iC DLC coatings with temperature. Tests were run against 319 Al for 1,500 m of sliding distance (2.5x10⁴ revolutions) at 25°C and for 60 m of sliding distance (1x10³ revolutions) at 120 and 300°C under an applied load of 5 N.
- Figure 5.20.** The BEI SEM image of a section of the wear track of the 60-V DLC 174 coating tested against 319 Al pin at 120°C. Test was run for 60 m of sliding distance (1x10³ revolutions) using 4.9 N applied load. In backscattered electron imaging mode, the image is created according to atomic mass difference where heavier elements appear brighter. Therefore the dark colored area is the DLC coating and the lighter color areas are the M2 steel substrate.
- Figure 5.21.** SEI SEM image of a section of the wear track of the Graphit-iC 175 DLC coating tested against 319 Al alloy at 400°C showing a large amount of aluminum transfer. The test was run for 250 revolutions under applied load of 5 N at 0.12 m/s.
- Figure 5.22.** The adhesive wear mechanism that operates in vacuum and inert gas 176 environments: a) The interaction of the surface atoms with unsatisfied bonds that results in, b) transfer of aluminum to the DLC

- surface, and/or c) transfer of carbon to the Al pin surface.
- Figure 5.23.** The oxidational and abrasive wear mechanisms of the non- 177
hydrogenated DLC coating in dry air.
- Figure 5.24.** a) and b) The oxidational and abrasive wear mechanisms of the non- 178
hydrogenated DLC coating in ambient air, c) easy-to-shear
carbonaceous material at the sliding interface.
- Figure 5.25.** a) The COF curve for the ambient air to vacuum test when 319 Al 179
sliding against the 80-V DLC coating. The test started in ambient air
(52% RH). After some sliding in ambient air (8.5×10^2 revolutions),
the test chamber was pumped down to vacuum. The COF decreased
with the pressure inside the chamber and reached its minimum value
of 0.006 when the pressure was around 0.173 Pa. Further decrease in
pressure did not change the COF value. Finally, the very low COF
period ended and the COF abruptly jumped to high values (0.55).
The applied load and the sliding speed were 5 N and 0.04 m/s, and
b) expanded view of the initial portion of the COF curve.
- Figure 5.26.** a) The COF curve for the ambient air to vacuum test when WC was 180
tested against the 80-V DLC coating. The test started in ambient air
(22% RH). After some sliding in ambient air (3.0×10^3 revolutions),
the test chamber was pumped down to vacuum. The COF decreased
as the pressure inside the chamber was lowered. The low COF
period lasted for 2.2×10^3 revolutions and then the COF increased to
high values (0.52). The applied load and the sliding speed were 5 N
and 0.05 m/s, and b) a semi-log scale plot of the same curve.
- Figure 5.27.** a) SEI, and b) BEI SEM images of the contact surface of the 319 Al 181
pin that was run against the non-hydrogenated DLC in H₂-He
environment.
- Figure 5.27.** c) The EDS analysis of the location indicated in b). 182
- Figure 5.28.** The COF between the 319 Al alloy pin and the Graphit-iC DLC 183
coating in H₂-He environment at 0.12 m/s sliding speed and 5 N
applied load. The test was paused for 30 seconds and then re-started
at 1000, 1500, 2000, 2500 and 3000 revolutions (as indicated by the
arrows). The high COF period was observed only at the beginning of
the tests indicating that it was related with the formation the
carbonaceous transfer layer.
- Figure 5.29.** The COF between the Graphit-iC DLC coating and the 319 Al alloy 184
pin at 0.12 m/s sliding speed under 5 N applied load. First, the
tribopair was run in ambient air of 32% RH for 1×10^3 revolutions.
Then, the test was stopped and the chamber was evacuated to
 5.45×10^{-3} Pa. After flushing with nitrogen, the chamber was
evacuated to 5.45×10^{-3} Pa again. Finally, the hydrogen (40% H₂-
60% He mixture) was introduced and the test was resumed. Together
with the test depicted in **Figure 5.25**, this test shows that the
observed high COF at the beginning of the sliding in hydrogen was
due to the transfer layer formation on the contact surface of the 319
Al alloy pin.

- Figure 5.30.** The effect of the pressure of the 40% H_2 -60%He mixture on the COF between the Graphit-iC DLC coating and the 319 Al alloy pin as a function of the number of revolutions. The sliding speed and the applied load were 0.12 m/s and 5 N. 185
- Figure 5.31.** The COF between the Graphit-iC DLC coating and the 319 Al alloy pin as a function of the pressure of 40% H_2 -60%He. The sliding speed and the applied load were 0.12 m/s and 5 N. 186
- Figure 5.32.** Micro-Raman spectra of the worn and unworn regions of the Graphit-iC DLC that was run against the 319 Al alloy pin in H_2 -He mixture at 0.12 m/s and under an applied load of 5 N. 187
- Figure 5.33.** The friction mechanism of non-hydrogenated DLC coating in H_2 -He environment. 188
- Figure 5.34.** The wear rates of the 60-V DLC and 80-V DLC coatings before and after annealing at 300°C for 7.7 minutes. The tests that were done at 300°C are also included for comparison. All tests were run for 1×10^3 revolutions of sliding distance under an applied load of 5 N. 189
- Figure 5.35.** The EDS analyses of the a) 60-V DLC and b) 80-V DLC coatings before and after annealing at 300°C in air for 77 minutes. 190
- Figure 5.36.** SEM images of the contact surfaces of the counterface materials tested against the 60-V DLC coating for 1×10^3 revolutions under 5 N applied load at 0.12 m/s, a) WC ball at 25°C, and b) 319 Al pin at 25°C. 191
- Figure 5.36.** SEM images of the contact surfaces of the counterface materials tested against the 60-V DLC coating for 1×10^3 revolutions under 4.9 N applied load at 0.12 m/s, c) 319 Al pin at 120°C, d) the EDS analysis of the location indicated in c). 192
- Figure 5.37.** The surface profiles of the sections of the wear tracks of the 80-V DLC coating tested against a) 319 Al, b) WC and at 120°C for 1×10^3 revolutions of sliding distance under 5 N applied load. 193
- Figure 5.38.** a) Schematic of the pin-on-disc test. Suggested mechanism of debris generation: First, the aluminum gets oxidized and the oxide thickness reaches a certain value (b & c). Then the oxide layer cracks, delaminates and fragments into loose debris (d & e). Some debris stay free at the sliding interface and some become embedded back on the 319 Al pin surface (f) causing abrasion of the DLC. 194
- Figure 6.1.** a) SEI and b) BEI SEM images of a section of the wear track of the Graphit-iC DLC coating tested against 1100 Al in argon for 300 revolutions (18 m). 214
- Figure 6.1.** c) SEI and d) BEI SEM images of the corresponding 1100 Al pin. The applied load and the sliding speed were 5 N and 0.65 m/s. 215
- Figure 6.2.** The variation of the COF between Al and the Graphit-iC DLC coatings in argon at 0.02, 0.12 and 0.65 m/s. The constant applied load was 5 N. 216
- Figure 6.3.** The variation of the COF between 1100 Al and the Graphit-iC DLC coatings in ambient air (51% RH) at the sliding speeds of 0.02, 0.12 217

and 0.65 m/s. The constant applied load was 5 N.

- Figure 6.4.** SEI SEM images of **a)** a section of the wear track of the Graphit-ic 218
DLC coating tested against Al in ambient air (51% RH) for 300
revolutions (18 m). **b)** the contact surface of the corresponding Al
pin.
- Figure 6.4.** BEI SEM images of **c)** the contact surface of the corresponding Al 219
pin, **d)** an enlarged view of the location indicated in **b)** showing the
layer delamination.
- Figure 6.4.** **e)** EDS analysis of the location indicated in **d)**. The applied load and 220
the sliding speed were 5 N and 0.12 m/s.
- Figure 6.5.** **a)** Optical image of the contact surface of the Cu pin tested against 221
the Graphit-iC DLC coating in argon at a sliding speed of 0.12 m/s
for 1×10^4 revolutions, **b)** SEI SEM image of the contact surface of
the Cu pin tested against the Graphit-iC DLC coating in argon at a
sliding speed of 0.12 m/s for 3×10^3 revolutions.
- Figure 6.6.** The variation of the COF between Cu and the Graphit-iC DLC 222
coatings in argon at 0.02, 0.12 and 0.65 m/s.
- Figure 6.7.** **a)** SEI SEM image of a section of the wear track of the Graphit-iC 223
DLC tested against Cu in ambient air (58% RH) for 3×10^2
revolutions (18 m), **b)** the contact surface of the corresponding Cu
pin.
- Figure 6.7.** **c)** An enlarged view of the location indicated in **b)** showing the layer 224
formation, and **d)** EDS analysis of the location indicated in **c)**. The
applied load and the sliding speed were 5 N and 0.12 m/s.
- Figure 6.8.** The variation of the COF between Cu and the Graphit-iC DLC 225
coatings in ambient air at 0.02, 0.12 and 0.65 m/s. The applied load
was 5 N.
- Figure 6.9.** SEM images of **a)** a section of the wear track of the Graphit-iC DLC 226
coating tested against Ti in argon at 0.12 m/s for 3×10^2 rev., **b)** the
corresponding Ti pin.
- Figure 6.9.** SEM images of **c)** a section of the wear track of the Graphit-iC DLC 227
coating tested against Ti in argon at 0.65 m/s for 3×10^2 rev., and **d)**
the corresponding Ti pin. The applied load was 5 N in all tests.
- Figure 6.10.** SEM images of **a)** a section of the wear track of the Graphit-iC DLC 228
coating tested against Ti in argon at 0.02 m/s for 3×10^2 rev., **b)** the
corresponding Ti pin showing material transfer to its surface. The
applied load was 5 N.
- Figure 6.11.** The variation of the COF between Ti and the Graphit-iC DLC 229
coatings in argon at 0.02, 0.12 and 0.65 m/s. The applied load was 5
N.
- Figure 6.12.** SEM images of **a)** a section of the wear track of the Graphit-iC DLC 230
tested against Ti in ambient air (59% RH) at 0.12 m/s for 3×10^3 rev.,
b) the corresponding Ti pin. The applied load was 5 N.
- Figure 6.13.** The variation of the COF between Ti and the Graphit-iC DLC 231
coatings in ambient air (59% RH) at 0.02, 0.12 and 0.65 m/s.
- Figure 6.14.** SEM images of **a)** a section of the sliding track of TiB_2 coating 232

tested against Al pin at 0.12 m/s sliding speed in the argon atmosphere. The sliding distance and the applied load were 18 m and 5 N, respectively, **b)** an enlarged view of a part of the sliding track showing the severely smeared Al. The direction of sliding is indicated with an arrow.

Figure 6.15. The variation of the COF between 1100 Al and the TiB₂ coating in argon 0.02, 0.12 and 0.65 m/s. The applied load was 5 N. 233

Figure 6.16. a) SEM image of a section of the sliding track of the TiB₂ coating tested against the 1100 Al pin at 0.12 m/s speed in the argon for 180 m under 5 N load, respectively. **b)** The corresponding COF curve. 234

Figure 6.17. The variation of the COF between 100 Al and the TiB₂ coating in ambient air (43% RH) at 0.02, 0.12 and 0.65 m/s. The applied load was 5N. 235

Figure 6.18. a) SEM image of a section of the sliding track of the TiB₂ coating tested against Al pin at 0.02 m/s sliding speed in ambient air (43% RH) for 3x10² rev. of sliding. A significant amount of loose debris (white) was detected on and along the sliding track, **b)** the EDS analysis of the one of the debris particles showing the extent of oxidation. The applied load was 5 N. 236

Figure 6.19 a) The SEM image of the debris particles gathered along the sliding track when Al was tested against TiB₂ coating at 0.12 m/s sliding speed in ambient air (50.8 % RH) for 180 m of sliding distance, **b)** a closer view of the debris particles in BEI mode. The applied load was 5 N. 237

Figure 6.20. a) SEM image of a section of the sliding track of the TiB₂ coating tested against Cu at 0.12 m/s sliding speed for 180 m of sliding distance in argon. The applied load was 5 N. **b)** an enlarged view of a part of a). The white particles are Cu adhered to the TiB₂ surface. 238

Figure 6.20. SEM images of the corresponding Cu pin in **c)** SEI and **d)** BEI modes. 239

Figure 6.21. SEM images of **a)** a section of the wear track of the TiB₂ coating tested against Cu in ambient air at 0.65 m/s for 3x10² rev., **b)** the corresponding Cu pin showing material transfer to its surface. The applied load was 5 N. 240

Figure 6.21. c) EDS analysis of the location indicated in b). 241

Figure 6.22. The variation of the COF between Cu and the TiB₂ coatings in ambient air at 0.02, 0.12 and 0.65 m/s. 242

Figure 6.23. a) SEM image of a section of the sliding track of the TiB₂ coating tested against Ti pin at 0.02 m/s sliding speed in argon for 3x10² rev. of sliding in argon., **b)** an enlarged view of a part of a). The applied load was 5 N. 243

Figure 6.24. SEM images of sections of the sliding tracks of the TiB₂ coating tested against Ti pin in argon **a)** at 0.12 m/s and **b)** at 0.65 m/s sliding speed for 3x10² rev. of sliding. The applied load was 5 N in all tests. 244

Figure 6.25. The variation of the COF between Ti and the TiB₂ coating in argon 245

at 0.02, 0.12 and 0.65 m/s sliding speeds under a constant load of 5 N.

- Figure 6.26.** The variation of the COF between Ti and the TiB₂ coatings in ambient air (46% RH) at 0.02, 0.12 and 0.65 m/s. 246
- Figure 6.27.** SEM images of sections of the sliding tracks of the TiB₂ coating tested against Ti pin at 0.12 m/s sliding speed in ambient air (49.1% RH), **a)** for 3x10³ rev. of sliding. The applied load was 5 N, **b)** the debris particles generated during the test described in a) showing the two different kinds of debris (rounded small and larger plate-like metallic) generated in ambient air. 247
- Figure 6.28.** SEM images of sections of the sliding tracks of the CrN coating tested against 1100 Al in argon; **a)** and **b)** at 0.65 m/s, **c)** and **d)** enlarged section of b), **e)** and **f)** at 0.12 m/s sliding speed for 300 rev. of sliding. The applied load was 5 N in all tests. 248
- Figure 6.29.** The variation of the COF between 1100 Al and the CrN coating in argon at the sliding speeds of 0.02, 0.12 and 0.65 m/s under a constant load of 5 N. 249
- Figure 6.30.** SEI and BEI SEM images of sections of the sliding tracks of the CrN coating tested against 1100 Al pin in ambient air (42% RH); **a)** and **b)** at 0.65 m/s, **c)** and **d)** at 0.12 m/s, **e)** and **f)** at 0.02 m/s sliding speed for 300 rev. of sliding. The applied load was 5 N in all tests. 250
- Figure 6.31.** The variation of the COF between Al and the CrN coatings in ambient air (42% RH) at 0.02, 0.12 and 0.65 m/s sliding speeds under a constant load of 5 N. 251
- Figure 6.32.** SEM images of **a)** a section of the wear track of the CrN coating tested against Cu in argon at 0.65 m/s for 3x10² rev., **b)** the corresponding Cu pin showing the absence of material transfer to its surface. The applied load was 5 N. 252
- Figure 6.33.** The variation of the COF between Cu and the CrN coatings in argon at the sliding speeds of 0.12 and 0.65 m/s under a constant load of 5 N. 253
- Figure 6.34.** SEM images of sections of the sliding tracks of the CrN coating tested against Cu pin in ambient air (42% RH) **a)** at 0.65 m/s, **b)** at 0.12 m/s, and **c)** at 0.02 m/s sliding speed for 3x10² rev. of sliding. Debris formation in decreasing amount with increasing sliding speed was observed. The applied load was 5 N in all tests. 254
- Figure 6.35.** The variation of the COF between Cu and the CrN coatings in ambient air (42% RH) at the sliding speeds of 0.02, 0.12 and 0.65 m/s under a constant load of 5 N. 255
- Figure 6.36.** SEI and BEI SEM images of contact surfaces of the Cu pins tested against CrN coating in ambient air (42% RH); **a)** and **b)** at 0.65 m/s, **c)** and **d)** at 0.12 m/s, **e)** and **f)** at 0.02 m/s sliding speed for 3x10² rev. of sliding. The applied load was 5 N in all tests. 256
- Figure 6.37.** SEI and BEI SEM images of sections of the sliding tracks of the CrN coating tested against Ti in argon; **a)** and **b)** at 0.65 m/s, **c)** and **d)** at 0.12 m/s, **e)** and **f)** at 0.02 m/s sliding speed for 3x10² rev. of 257

- sliding. The applied load was 5 N in all tests.
- Figure 6.38.** The variation of the COF between Ti and the CrN coatings in argon 258
at the sliding speeds of 0.02, 0.12 and 0.65 m/s under a constant load
of 5 N.
- Figure 6.39.** SEI and BEI SEM images of contact surfaces of the Ti pins tested 259
against the CrN coating in argon; **a)** and **b)** at 0.65 m/s.
- Figure 6.39.** SEI and BEI SEM images of contact surfaces of the Ti pins tested 260
against the CrN coating in argon; **c)** and **d)** at 0.12 m/s, **e)** and **f)** at
0.02 m/s sliding speed for 3×10^2 rev. of sliding. The applied load
was 5 N in all tests.
- Figure 6.40.** SEM images of sections of the sliding tracks of the CrN coating 261
tested against Ti pin in ambient air (51% RH) **a)** at 0.65 m/s, **b)** 0.12
m/s and **c)** at 0.02 m/s sliding speed for 3×10^2 rev. of sliding. The
applied load was 5 N in all tests.
- Figure 6.41.** The variation of the COF between Ti and the CrN coatings in 262
ambient air at 0.02, 0.12 and 0.65 m/s sliding speeds under a
constant load of 5 N.
- Figure 6.42.** Cr-Cu phase diagram [144]. 263
- Figure 6.43.** Ti-Cu phase diagram [145]. 264
- Figure 6.44.** Ti-B phase diagram [145]. 265
- Figure 6.45.** Ti-Cr phase diagram [145]. 266
- Figure 6.46.** Experimental setup to measure the temperature increase of the pins. 267
- Figure 6.47.** The measured increases in the bulk temperatures of the Al and Ti 268
pins while running against non-hydrogenated DLC, CrN and M2
steel at 0.12 and 0.65 m/s under the applied load of 5 N in ambient
air. These values were obtained by subtracting the steady state
temperatures during running from the ones measured before the tests
were started.
- Figure 6.48.** The calculated and measured increases in the bulk temperatures of 269
the Al and Ti pins while running against the 80-V DLC, CrN and
M2 steel at 0.12 and 0.65 m/s under the applied load of 5 N. The
calculations are based on the method developed by Ashby and his
co-workers [143, 159, 160]. The method is described in **Appendix**
A.1.
- Figure A.1.** A typical pin-on-disc configuration from [160]. 278

LIST OF APPENDICES

Appendix 1. Frictional Heating of Sliding Surfaces.....	277
Appendix 2. Impingement Rate (Flux) of Gaseous Species, (J).....	282

LIST OF ABBREVIATIONS

AES	Auger electron spectroscopy
AISI	American Iron and Steel Institute
BEI	Back-scattered Electron Imaging
EDS	Energy Dispersive Spectroscopy
COF	Coefficient of Friction
CVD	Chemical Vapour Deposition
DLC	Diamond-like Carbon
EELS	Electron energy loss spectroscopy
ESCA	Electron spectroscopy for chemical analysis
HSS	High Speed Steel
HV	Vickers hardness scale
PECVD	Plasma-enhanced CVD
PACVD	Plasma-assisted CVD
Ra	Surface Roughness
Rc	Hardness in Rockwell C Scale
Rev.	Revolutions
RH	Relative Humidity
Rpm	Revolutions per minute
SEI	Secondary Electron Imaging
SEM	Scanning Electron Microscope
TEM	Transmission electron microscope
™	Trade Mark
TPD	Temperature Programmed Desorption
XRD	X-Ray Diffraction
WC	Tungsten Carbide

CHAPTER 1

INTRODUCTION

1.1. Driving Force for Dry Machining and Manufacturing: Social and Economic Aspects

Today, one of the main objectives of the manufacturing industry is to reduce and eliminate the use of metalworking fluids in machining operations. There are two main driving forces behind this objective; these are anticipated government regulations and potential economic benefits. For example in United States of America, the National Institute for Occupational Safety and Health (NIOSH) recommends that occupational exposures to cutting fluid aerosols be limited to 0.5 mg/m^3 from its current standard value of 5 mg/m^3 [1]. The reason behind this request is the detrimental effects of the cutting fluid aerosols on machine shop workers and the environment. Cutting fluid aerosol refers to the mist and all contaminants in the mist generated during grinding and machining operations involving products from metal and metal substitutes [1].

NIOSH presented substantial evidence indicating that workers who are constantly exposed to metalworking fluid aerosols have an increased risk of non-malignant respiratory disease and skin diseases [1]. Elimination of the use of metalworking fluids will have a substantial impact towards the improvement of the quality of the working environment. Recycling of the dry chips is also easier since there will be no need for a cleaning operation before their re-use in another form. The cost of fluid filtration, disposal and maintenance of the cutting fluid system is estimated to be around 17% of the overall manufacturing cost [2-4]. Therefore elimination of the metalworking fluids will potentially bring economic benefits to the manufacturing industry.

1.2. Dry Machining of Aluminum and Associated Challenges

North American automotive manufacturers have been constantly seeking new ways of increasing fuel efficiency of their vehicles by reducing the total mass per vehicle. The use of aluminum alloys instead of steel or cast iron brings approximately 66% reduction in weight due to its lower density ($2.7 \text{ vs. } 7.8 \text{ g/cm}^3$). For this reason, automotive companies have been interested in substituting steel or cast iron components

with those made of Al wherever possible. Nowadays, most of the engine components and some chassis parts are made of different aluminum alloys. For example, 319 Al grade cast aluminum alloy is used in engine blocks.

Efforts to machine cast iron and steel without lubricants have been partially successful [5]. However, dry machining of aluminum alloys is a challenging task: In the absence of metalworking fluids, aluminum chips formed during the machining operations adhere to the tool surfaces. The adhesion of aluminum problem also exists in other forming operations like sheet metal forming and deep drawing. Adhesion causes tool failures and leads to products with poor surface quality.

Among the machining operations, dry drilling of aluminum alloys is especially problematic. In the absence of the metalworking fluids, the aluminum chips formed adhere to the surfaces of drill flutes, causing their clogging in a very short time. The process of chip evacuation ceases. The clogged drills do not last long in service; the average number of holes that could be dry drilled in a 319 Al alloy block using an uncoated (high speed steel) HSS drill is less than 50. This is too far from meeting the goal of 1×10^4 holes set by the industry [6]. The severity of aluminum adhesion to an uncoated HSS drill subjected to dry drilling of 319 Al alloy is shown in **Figure 1.1**.

1.3. Metalworking Fluids and Alternative Ways of Cooling

It is useful to emphasize the functions of the metalworking fluids. The metalworking fluids have three main functions: i) they provide lubrication between the cutting tool and the work piece, ii) they assist the removal of the chips from the cutting area (easy chip evacuation), and iii) they cool the work piece which is important for dimensional accuracy and the cutting tool thus preventing its softening by becoming too hot. Metalworking fluids also affect the surface quality of the machined workpieces. For example Haan et al. [7] showed that the surface roughness of the holes drilled on SAE 308 Al alloy doubled in the absence of cutting fluid. For a successful dry machining operation, these points have to be addressed in addition to the adhesion problem.

To help dry machining, alternative ways of cooling have been developed [8]. Some of these are:

i) An under-cooling system where the coolant flows through channels located under the insert, then out to the environment without any direct contact with the cutting zone [ref 9 in [Error! Bookmark not defined.]].

ii) Internal cooling by a vaporization system in which a vaporizable liquid is introduced inside the shank of the tool and vaporized on the underside of the insert [ref 10 in [Error! Bookmark not defined.]].

c) Cryogenic systems, where a stream of cryogenic coolant is routed internally through a conduit inside the tool [ref 11 in [8]].

d) Thermoelectric cooling systems using thermoelectric couples [ref 12 in [8]].

1.4. Optimization of Machining Parameters and Tool Geometry

Machining parameters including feed rate and cutting speed have great influence on the performance of the tools (wear rate and tool life) and the system requirements (force, torque). However, optimization of the machining parameters alone is not enough for dry machining to become a feasible operation. It is the cutting tool (drill bits in drilling) where the major developments need to be made. From their current conditions, the tools have to be transformed into such a condition that adhesion of aluminum chips to the tool surface will be minimized and the chips will be easily evacuated. These are the two additional requirements for cutting tool design.

What can be done to drill bits to achieve these objectives? In addition to optimizing machining parameters, the drill geometry can be optimized to produce chips in such morphology that they can be evacuated easily. Since the assistance of metalworking fluids is not available, generation of chips that are easy to evacuate becomes imperative in dry drilling. Smaller, narrower and curled chips are more ejectable [9]. Therefore, drill geometry should be modified to generate chips in desired morphology. For example, higher helix and points angles produce narrower chips [6].

1.5. Use of Coatings to Reduce Material Adhesion to Tool Surfaces

As long as the chips adhere to the tool surfaces, there is very little to gain with the optimization of tool geometry and machining parameters. Therefore, the main task to be achieved is the reduction or elimination of the adhesion of the aluminum chips to tool

surfaces in dry machining. To achieve this result, either the tool should be made of a material on which Al does not have a tendency to adhere or this material should be applied on the surface of the current industrial tool materials (e.g. high speed steel and cemented carbide). Since the latter is more practical, almost all of the studies on dry machining of aluminum were concentrated on the development of novel coatings that can be applied on the surfaces of cutting tools (inserts, drill bits) rather than developing new bulk tool materials.

1.6. The Need for the Current Study

As explained above, the application of a coating on tool surfaces that does not adhere to aluminum is the primary condition to be satisfied towards the tool design for dry machining of Al alloys. However, the causes, mechanisms, and the factors controlling adhesion and transfer of aluminum to surfaces in sliding contact are not well understood. It is obvious that a better understanding of the adhesion phenomenon will facilitate tailoring a tool coating for dry drilling of aluminum alloys.

Another aspect that requires attention is the evaluation of the dry drilling performance of the currently available industrial coatings. Since performing drilling tests is expensive, there is a need to develop a quick and low cost laboratory method to evaluate the dry drilling performance of a given coating.

1.7. Scope and Objectives

Considering the background and motivation described in the previous sections, the scope and objectives of this work is listed in the following three main groups:

1.7.1. Transfer of 319 Al to Various Coating Surfaces

1. To develop a laboratory evaluation method to rank some of the currently available industrial coatings (DLC, CrN, TiB₂, TiN, TiAlN, and TiCN) according to the transfer tendency of 319 Al alloy to their surfaces.
2. To study the mechanisms of adhesion and transfer of 319 Al alloy to the surfaces of these coatings during dry sliding contact.

3. To elucidate the roles of extrinsic variables, namely environment, temperature and sliding speed on adhesion and material transfer of 319 Al alloy.

1.7.2. Transfer of Al, Cu and Ti to CrN, DLC and TiB₂ Coatings

1. To contribute to the understanding of the mechanisms and factors controlling adhesion and transfer phenomena between surfaces in dry sliding contact.
2. To elucidate the relative roles of material properties and test atmosphere (ambient air vs. argon) on adhesion and material transfer during dry sliding contact.

1.7.3. Tribological Behaviour of Non-hydrogenated DLC Coatings

1. To have a systematic investigation of the tribological behaviour of the DLC coatings against aluminum.
2. To study the effects of test environment, temperature and counterface on the tribological behaviour of DLC coatings.

The Al alloys of interest were 319 Al and 1100 Al. The 319 Al alloy was selected because of its wide application in the automotive industry. The studied coatings included DLC, CrN, TiB₂, TiN, TiAlN and TiCN.

1.8. Organisation of the Dissertation

The next chapter (**Chapter 2**) gives a survey of the open literature on **i)** studies of adhesion and material transfer phenomena, **ii)** performances of coatings in dry and near dry machining of Al alloys, and **iii)** tribological behaviour of DLC coatings and the controlling factors. **Chapter 3** first describes the experimental methods and procedures that were used to manufacture and characterize the test materials used in this study. Then, descriptions of the pin-on-disc machines, test conditions and the procedures that were used to evaluate the test results are given.

The results and discussion of the pin-on-disc tests that were performed to investigate the transfer behaviour of 319 Al alloy to various coating surfaces, namely TiB₂, TiN, TiCN, TiAlN and CrN, are presented in **Chapter 4**. In **Chapter 5**, the details of the investigations of the tribological behaviour of the non-hydrogenated DLC coatings

are described. The effects of the test environment, temperature and counterface material are discussed.

In **Chapter 6**, the adhesion and material transfer phenomena between Al, Cu, Ti and non-hydrogenated DLC, TiB₂ and CrN coatings that were investigated in argon and ambient air environments are given. The general discussion of the results and observations that were originated from this study is also done in **Chapter 6**. Finally, the conclusions are given in **Chapter 7**, the last chapter, where suggestions for future work are also included.

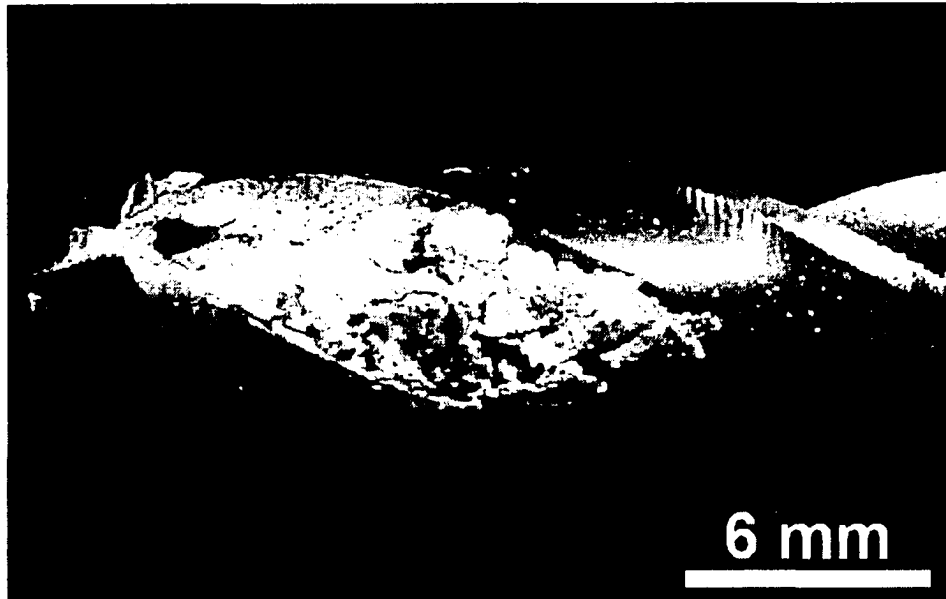


Figure 1.1. The image of an uncoated HSS drill subjected to dry drilling of 319 Al alloy. The severity of aluminum adhesion to drill flutes is clearly seen (courtesy of the GM R&D Center). The drill was 6.35 mm diameter, 2-flute, high helix, 118° point angle, HSS drills from Precision Twist Drill Co., (Crystal Lake, IL). Drilling was done at 61 m/min speed and 0.13 mm/rev. feed.

CHAPTER 2

LITERATURE REVIEW

This chapter starts by giving a summary of the previous studies that investigated adhesion and material transfer phenomena between the surfaces in dry sliding contact. Then studies published in the open literature on the machining and tribological performance of the various tool coatings against aluminum alloys are reviewed. Finally, the studies that investigated the tribological behaviour of DLC coatings are reviewed.

2.1. Terminology

Most of the definitions given in this section are based on the study of Markov and Kelly [10] who reviewed the published English and Russian literature on adhesion initiated wear mechanisms.

Seizure is characterised by plastic deformation of one surface only, by macroscopic adhesive transfer of material from a softer surface onto a harder surface and by formation of widening grooves on the softer surface and protrusions on the harder surface.

Scoring is characterised by plastic deformation of both surfaces, by absence of macroscopic adhesive transfer of material, and by formation of self-organized centres of scoring riders that consist of two mechanically interlocked wedges originated and developed alternately by work-hardening metal on either friction surface.

Scuffing is characterised by friction heating and softening of material of one surface and welding of it onto the other, cooler surface.

Galling is characterised by transfer from a softer surface of cool material by being smeared, before it undergoes significant heating, onto a harder surface.

Work of adhesion is the energy required to separate two surfaces from each other.

2.2. Previous Studies on Adhesion and Material Transfer

The occurrence of adhesion, material transfer and related phenomena (seizure, galling, scuffing, scoring) plays a critical role in determining the performances of many

tribological systems. Many researchers investigated these phenomena to have a better understanding of their fundamental mechanisms [11-30].

Machlin and Yankee [11] compared the COF values of the some freshly cut pure metal pairs (Ag, Al, Cd, Cu, Fe, Mg, Pb, Ti, and Zn). They concluded that solid phase welding is the reason for the static COF (the COF at the start of sliding) in almost all metals tested. Except the Fe-Ag couple, solid phase welding was observed even with insoluble couples such as Fe/Cd pair. They proposed that the occurrence of solid phase welding increases as the ratio of the work of adhesion (energy required to separate two surfaces from each other) to the shear strength of the weaker couple increases.

Ling and Saibel [30] derived a seizure criteria based on considerations of the thermal aspects of sliding contact, which they assumed to be dominating when the two surfaces in contact were smooth enough so that there was no appreciable oscillations in the direction normal to the surfaces. The authors observed that seizure started when the surface temperature of the contact area reached the recrystallization temperature of one of the surfaces. Therefore, they concluded that it was not necessary to reach the melting temperature to observe adhesion.

Rabinowicz [14] found that the average size of loose wear particles (d) generated during the dry sliding of self-mated metals is proportional to the surface energy/hardness ratio (γ/H) as:

$$d = 6 \times 10^5 \times \left(\frac{\gamma}{H} \right) \quad \text{Equation 2.1}$$

The same relation also holds for COF. For example Pb had a γ/H ratio of 2.2×10^{-8} m and gave a COF of 1.2 whereas low carbon steel had a γ/H ratio of 1.2×10^{-9} m and gave a COF of 0.6. He observed that metals with hexagonal structure gave lower COF than the cubic ones.

Sikorski [13] used a twist-compression method to study the adhesion of metals. In this method, samples in the form of cylinders are brought into contact and one of the cylinders is pushed (F_{normal}) and rotated 180° to the fixed sample. Then, a force is applied

in the opposite direction to separate the adhered cylinders (F_{break}). The coefficient of adhesion (COA) is defined as

$$\text{COA} = \frac{F_{\text{break}}}{F_{\text{normal}}} \quad \text{Equation 2.2}$$

Sikorski observed that the COA decreased as the hardness of the metal increased (**Figure 2.1**). Similar to Rabinowicz [14], he suggested that compared to the hexagonal metals, the observed higher COA values of face-centered cubic metals was due to their larger deformation under a given load that increases the area of contact and hence the total adhesion strength. Sikorski proposed that the energy of adhesion ($E_{\text{adh.}}$) between two metal surfaces was roughly equal to the interface energy per unit area (γ) multiplied by the real contact area (A_r) (equation 2.3).

$$E_{\text{adh.}} = \gamma \times A_r \quad \text{Equation 2.3}$$

In other words, the adhesion strength depended on the size of the contact area and the energy per unit contact area. He suggested that there were two aspects of adhesion; a mechanical aspect and a physico-chemical aspect. Mechanical aspect is related to the properties of metals and their oxides that affect the size and cleanliness of real contact areas under normal and tangential loading conditions (crystal structure, work-hardening coefficient, purity, hardness, elastic modulus, melting point, recrystallization temperature and atomic radius). The physico-chemical aspect involves the properties that determine whether adhesion would occur under given conditions (mutual solubility, size-factor, relative positions of the elements in periodic table or type of bonding involved.).

Rabinowicz [15] reviewed studies on the effect of the metallurgical compatibility of metal pairs on their friction, wear and adhesion behaviour. The metals pairs were grouped as “fairly compatible”, “compatible” and “fairly incompatible” when their solid solubility is more than, in the vicinity of, or less than 1%, respectively. He could not find a correlation between the adhesion tests and the material compatibility.

Buckley [17] performed adhesion tests on tungsten, rhodium and iridium against gold. He detected transfer of gold to the surfaces of all three elements although gold does not form compounds and has no or very limited solubility in these metals. Therefore, he suggested that the chemical and physical characteristics of the metallic interfaces do not necessarily follow the behaviour of bulk materials. Buckley [17] also stated that transfer of material occurs from the “cohesively weaker” or softer material (gold in this case) to the “cohesively stronger” or harder material.

It should be noted that adhesion and transfer of material in sliding are more complicated than normal contact because of the additional effects such as plastic deformation by shear stresses and friction induced heating.

Chen and Rigney [19] developed a model based on the thermodynamic behaviour of regular solutions to predict the role of adhesion on transfer and wear during the dry sliding of metal-metal and metal-binary alloy pairs in vacuum. They concluded that at the early stages of sliding, the direction of material transfer can be predicted by comparing the relative energies required for subsurface fracture. In other words, transfer occurs from softer material to the harder material as stated earlier by Buckley [17]. Their calculations also suggested that in tribosystems that involve material transfer, loose wear debris should form from the material that initially transferred to the counterface since the direct generation of wear debris requires more energy than material transfer.

Hwang et al. [23] investigated the relative importance of the material compatibility (in terms of solubility, crystal structure) and hardness ratio (hardness of the disc/hardness of the pin) on the friction and wear behaviour of various metal pairs (Ag, Al, Cr, Cu, Fe, Mo, Pb, Ni, Ti, Sn, Zn) during dry sliding contact. Metal pairs (**Table 2.1**) were grouped as high (e.g. Ag/Al), medium (e.g. Ag/Cu) and low compatible (e.g. Fe/Ag) according to the compatibility chart developed by Rabinowicz [15]. They could not find a relation between material compatibility and static or steady state COF values. They found that material pairs with very large differences in their initial hardness values resulted in high static COF values (**Figure 2.2.**). They also observed that the static COF values had the highest correlation with shear modulus while the steady state COF values had the highest correlation with hardness.

Relative compatibility (compatibility parameter value)	Pin/Flat (Hardness ratio: H_{flat} / H_{pin})
High (compatible: 0.5 or higher)	Ag/Al (0.42), Ni/Cu (0.43), Cu/Al (0.42), Mo/Cr (0.96), Mo/Ni (0.92), Mo/Ti (1.0), Ti/Cr (0.96), Ti/Fe (0.8), Ti/Ni (0.92), Ni/Al (0.18), Ti/Al (0.17), Ag/Sn (0.1), Ti/Pb (0.02), Ti/Sn (0.04)
Medium (partially compatible: 0.32)	Ag/Cu (1.0), Fe/Cu (0.5), Ti/Cu (0.4), Mo/Al (0.17), Mo/Zn (0.14), Ti/Zn (0.14), Zn/Sn (0.29), Cu/Sn (0.1), Ni/Sn (0.04)
Low (partially incompatible or incompatible: 0.125 ~ 0.2)	Cr/Cu (0.42), Fe/Ag (0.5), Mo/Ag (0.4), Mo/Cu (0.4), Ni/Ag (0.43), Al/Pb (0.14), Al/Sn (0.24), Zn/Pb (0.18), Cr/Sn (0.04), Cu/Pb (0.06), Fe/Sn (0.05)
Initial hardness of materials (H_v)	Pb (~ 6), Sn (~ 10), Zn (34), Al (42), Ag (100), Cu (100), Fe (200), Ni (230), Cr (240), Ti (250), Mo (250)

Table 2.1. Metal pairs studied by Hwang [23]

For steels, Hershberger and his colleagues [28, 29] proposed a mechanism that related the initiation of scuffing to adiabatic shear instability. For the scuffing tests, they used SAE 4340 steel samples that were subjected to different heat treatment procedures to obtain different microstructures with hardness values from 29 to 53 R_c. A block-on-ring tribometer lubricated with pure synthetic polyalphaolefin was employed. The applied load was increased at a rate of 8.9 N per one minute step until scuffing occurred. They showed that scuffing occurred when the rate of local thermal softening exceeded that of work hardening. If the shear strength of the junction/contact is more than that of the material with lower shear strength, then the entire shear is taken by that near-surface of the lower shear strength material. The frictional heating builds up in that material. Temperature, strain and dislocation density all increase quickly. Deformation continues until the mechanism of deformation changes (subgrains become smaller until they become nanocrystalline. Then deformation is by grain boundary sliding rather than dislocation motion). They verified their theory by measuring the dislocation densities of the material before, during, and after scuffing was observed using XRD line broadening technique. For example, the respective dislocation density values of the sample with 50 R_c hardness were 1.2×10^{16} , 2.8×10^{16} and $1.1 \times 10^{17} \text{ m}^{-2}$.

Kayaba and Kato [18] investigated adhesive wear process by sliding model asperities (4x20 mm with 15° slope, made of 304 stainless steel, 0.45%C basic carbon steel, and brass) over each other under a normal load of 212.8 N in the SEM chamber. They observed two modes of transfer. In the first mode, successive slip occurs on the slip planes within the prow (the plastically deformed zone which rises ahead of the junction without resulting fracture) and forms an extrusion called “slip-tongue”. A shear crack subsequently propagates from the root of the slip-tongue (schematically shown in **Figure 2.3**). In the second mode, successive ploughing takes place at the head of the wedge by accompanying the shear crack growth at its trailing end (**Figure 2.4**). In both cases, cracks produce a dimpled fracture surface. They also observed that the transfer of fragments occurred from a sharp asperity to a blunt asperity. The adhesive transfer was by shear rupture that forms a shear dimple on the fracture surface of the transferred fragment.

Rooij and Schipper developed [25] and verified [26] a model for material transfer from a soft workpiece to a hard tool surface during deep drawing. They showed that adhering lump growth can be decreased by higher surface hardness of the workpiece, lower roughness of the tool surface, lower nominal contact pressure and lower shear strength of the interface between the adhered lump and the tool. The surface roughness of the sheet material did not affect material transfer.

2.2.1. Effect of Environment on Adhesion and Material Transfer in Normal and Sliding Contact

The effect of the test environment on adhesion and material transfer phenomena during normal [17, 22, 31-34] and sliding contact has been studied [11, 35-45].

Buckley [17] showed that the presence of a very small amount of adsorbed and reacted films on the surface of metals and alloys reduced the strength of interfacial bonding, hence reducing adhesion and material transfer. He tested the self adhesion of Fe with and without a monolayer of sulphur on its surfaces. The force required to separate the two clean Fe surfaces was 4×10^{-3} N. When a monolayer of sulphur was present, this force dropped to 1×10^{-4} N. His observation on adhesion reducing effect of surface-reactive gases was supported by the fact that the static COF values of self mated Cu, Fe and steel decreased as the oxygen and chlorine concentration on their surfaces increased (**Figure 2.5**).

Similarly, Miyoshi [22] observed that contaminated surfaces show reduced adhesion and COF. He performed adhesion and sliding tests of several as-received (contaminated) and sputter-cleaned metals (Co, Cr, Fe, Ni, Re, Rh, Ti, W, V, Zr) against manganese-zinc ferrite in ultrahigh vacuum conditions. The pull-off (adhesion) forces and COF values of the contaminated metal surfaces were low and similar to each other. On the other hand, the cleaned metals showed higher pull-of forces (**Figure 2.6**) and COF values (**Figure 2.7**). Miyoshi observed that adhesion and COF decreased as the elastic and shear moduli of the metals increased. He also showed that, as stated earlier by [13], the COF of metal-ceramic couples was proportional to the multiplication of the surface energy of the metal (γ) with its real area of contact (A_r) against the ceramic (**Figure 2.8**).

Wang and Smith [33] calculated that the Al/Al₂O₃ interface is weaker than bulk Al. However, they showed that the presence of carbon as one third of a monolayer at the Al/Al₂O₃ interface increases the adhesion strength of the interface by a factor of three, making it stronger than bulk Al. The increased strengthening was caused by the extra bonds that carbon makes with both surfaces. For this reason, in the fracture experiments the separation occurs within Al rather than at the Al/Al₂O₃ interface. In another study, the authors showed that hydrogen termination reduces the adhesion strength between Cu and diamond from 1.3 J/m² to 0.21 J/m² [32]. Similarly Qi and Hector [46] showed that hydrogen passivation of the diamond leads to negligible adhesion and no transfer of Al to its surface whereas strong adhesion occurs when hydrogen is not present on the diamond surface.

Hartweck [34] showed that up to a monolayer of foreign atoms such as C, N, S and P increased the adhesion between iron surfaces. However, a significant decrease in adhesion occurred when the coverage was larger than one monolayer. It was suggested that the increased adhesion was due to the bonding of iron with these elements.

Ramboarina and Lepage [31] studied the effect of the co-adsorption of water vapour and oxygen on the self-adhesion of aluminum. In a vacuum tensile test machine, the pre-notched samples were first strained to rupture, then exposed to the chamber gas (oxygen or oxygen + water vapour) in varying amounts (Pressure*time) and then pressed against each other at a compressive force (F_c) equal to the force they were ruptured. The strength of the interface is then measured by straining the sample to rupture again (F_r). The coefficient of adhesion (COA) is defined as the ratio of F_r to F_c . They found that the presence of dry oxygen in the test chamber did not have a reducing effect on COA. However, the adverse effect of water vapour on COA became much more pronounced when oxygen and water vapour co-existed (**Figure 2.9**). The authors proposed that the loss of adhesion in the presence of water vapour was due to the embrittlement of the interface region that contained hydroxyl radicals.

Machlin and Yankee [11] compared the COF values of some freshly cut metals before and after they were exposed to air. They observed that freshly cut titanium solid phase welded to other metals in frictional contact and the degree of welding of Ti was independent of the atmosphere (air, nitrogen or argon) or the time (less than 24 hours) at

room temperature. However with Fe and Cu, less than 5 minutes of exposure to air was sufficient to significantly reduce the degree of solid phase welding. They concluded that the seizebility of titanium is probably due to the lack of resistance of the contaminant film formed on it in air to penetration or wear in frictional contact.

It was shown that humidity, temperature, and working gas all have direct influence on the tribological behaviour of the sliding systems. They affect the system via the chemical reactions, such as oxidation, taking place at the sliding interface and/or via the sorption of species on the surfaces of sliding tracks [47-50]. Oxidation is by far the most commonly encountered chemical reaction in tribological systems [47].

Brendle and coworkers [21, 35] studied the effects of relative humidity, speed and the characteristics of the test equipment on the transfer behaviour of graphite to steel. They observed that the fraction of the area covered by the transferred material increased by increasing relative humidity but decreased with increasing speed. Diss and Brendle [21] related the effect of speed to the occurrence of “stick-slip phenomena”. The source of the stick was the higher static coefficient of friction and slip was due to the lower COF during the slip. It was suggested that the adhesion occurred in the stick stage. When the sliding speed was increased the probability of adhesion decreased since the length of time the surfaces stay together became shorter. Later, Brendle and Stemple [35] attributed the effect of speed to the amount of moisture in the area of contact and its dependence on the kinetics of water adsorption to the surface.

Heimberg et al. [36] performed reciprocating sliding tests on DLC coatings using a ball-on-flat tribometer in dry nitrogen. They were able to correlate the change in friction coefficient caused by different test speeds and time delays with the kinetics of gas adsorption onto carbon. Extremely low COF values in the range of 0.003-0.008 were observed when the exposure time of the DLC coating to dry nitrogen was kept below 5 sec. The time between the two contacts was not enough to adsorb sufficient amount of nitrogen that would change the friction behaviour. When the exposure time was increased using slower sliding speed or a longer time delay, the COF increased to the values typical of DLC coatings under ambient air. Experimental data of [36] was later used to verify the derived frictional coverage models [51, 52].

2.3. Previous Studies on the Machining Performance and Tribological Behaviour of Some Coatings against Aluminum

To date, the research and development of new coatings for the dry machining of aluminum alloys mainly concentrated on three classes of coatings: carbon based coatings, titanium diboride (TiB_2) and other solid lubricant coatings.

2.3.1. Carbon Based Coatings

Hollman et al. [53] investigated the tribological behaviour of CVD-diamond coatings against Al, Al-17%Si and steel using a pin-on-cylinder test. They used ethanol as the lubricant for aluminum whereas commercial cutting oil was used for steel. Low wear rate and low COF were found against aluminum. Decreased diamond surface roughness lowered the initial value of the COF and decreased the amount of material transferred to the counterface.

Lahres et al. [2] investigated the performance of diamond, a-C:H, WC/C, CrC/C, CrN, TiN, TiAlN, MoS_2 , TiN+ MoS_2 coated WC-Co (K10) tools in dry milling of AlZnMgCu1.5 and AlSi10Mg alloys. Diamond and partially crystalline hard coatings with softer morphological parts (WC/C, CrC/C and TiN+ MoS_2) exhibited potential for dry milling. The authors concluded that only the iterative development of the whole system (coating, tool geometry, chip transportation, machine tool adoption) would deliver a successful implementation of dry processes.

Derflinger et al. [5] studied the production and performances of TiN, TiAlN, TiN+WC/C and TiAlN+ WC/C coatings in the dry drilling of X210Cr12 (AISI D3) and 42CrMo4 (SAE 4140H). By performing drilling tests under compressed air, they found that the number of holes drilled per unit worn thickness of the coatings was maximum for TiAlN+ WC/C coated drills (90), followed by TiAlN (60), TiN+WC/C (50) and TiN (30). The beneficial role of low friction layer (WC/C) during machining is explained in **Figure 2.10**. WC/C layer on the top wears out mostly after the running in stage. However, some of it remains on the hard coating due to surface roughness and continues to serve.

Chen et al. [54] observed a significant increase in tool life when drilling SiC particle reinforced aluminum alloy with diamond coated (electron aided hot filament

CVD) WC-Co drills. With diamond coated drill, the flank wear was 73 μm after drilling 25 holes as compared to 113 μm of flank wear after drilling only 13 holes with the uncoated drill. Kim and Kang [55] observed an increase in the surface quality of the Al workpieces using diamond endmills at high speed. No build-up edge and burrs were formed with diamond mills.

Luo et al. [56] studied the performance of cathodic arc deposited DLC coatings against Al- 11%Si alloy and Al_2O_3 under the dry reciprocating sliding contact. The authors divided the tribological behaviour of the DLC film into three regimes: break in stage, strain hardening stage, and fatigue wear stage. In the break-in stage, high COF was observed between Al-Si and the DLC due to the adhesion of the aluminum alloy on the DLC film caused by high hertzian contact stress. In the strain hardening stage, aluminum alloy strain hardens and oxidizes to form a smooth layer which provides a good interface for low friction. Finally in the third wear stage, the hardened layer on the counterface cracks and performs micro cutting on DLC film. This three-stage mechanism is drawn in **Figure 2.11**.

Sakamoto et al. [57] studied the performance of plasma CVD diamond coated tool in cutting A390-T6 alloy. The diamond they deposited at lower temperature (779 K) was much smoother (**Figure 2.12**) and outperformed the one deposited at high temperature (1183 K). The cutting length was 13 times longer for the low temperature deposited diamond. The authors related this to the lower surface roughness and better adhesion strength obtained at 779 K.

Kagiya et al. [58] produced smooth DLC films with low hydrogen content. They performed pin-on-disc, dry milling and dry drilling tests to compare the performance of their DLC with uncoated cemented carbide tools. A5052 and ADC12 (9.5-12 wt.% Si, 1.5-3.5 wt. %Cu, Japanese standard) aluminum alloys were used. The DLC coating had no adhesion of the aluminum alloy in the pin-on-disc test. Tightly curled chips were produced during the milling tests with DLC coated tools (**Figure 2.13**).

For the dry drilling of A5052 alloy, the DLC coatings were applied on drills specially designed for the dry drilling of aluminum. The drills have wide thinning pockets that prevent sticking during high feed cutting. Large thinning angle and minimized negative form cutting flute also help prevent sticking. Compared to conventional

products, the DLC coated drill reduced cutting force and improved surface finish of the holes produced significantly [58].

Nouari et al. [59] studied optimization of the tool geometry and cutting conditions for dry drilling of an aluminum alloy (AA2024 T351). They used diamond (Kennametal) coated and uncoated WC–Co cemented carbide drills. The use of diamond as a coating material extended the tool life. They found that the combination of the optimised tool geometry (high helix and point angles, lower land width and web thickness, and a clearance angle between 6° and 8°) and the cutting conditions (high cutting speeds and small feed rates) brought a high surface quality and a good dimensional accuracy of the machined material. The use of diamond coated drill increased the number of holes with acceptable quality by three times compared to the uncoated drill.

Coldwell et al. [60] examined the dry drilling performances of non-hydrogenated DLC, hydrogenated DLC and Ti containing MoS₂ coatings when drilling British BS L168 : 1978 (ASTM 2014) aluminum alloy (3.9-5 wt. % Cu, 0.5-0.9 wt. % Si). For the Ti containing MoS₂ coated drill, different under layer coatings (CrC, CrTiAlN, ZrN, and MoZrN) were used whereas CrC under layer was used for the non-hydrogenated DLC, hydrogenated DLC coatings. Ti containing MoS₂ coating exhibited highest wear resistance with CrTiAlN under layer. The build up of aluminum became evident even after drilling 30 holes with the Ti containing MoS₂ coating. For the hydrogenated DLC coated drill, aluminum build up was observed after drilling 60 holes. After drilling 100 holes with each coating, they observed that the build up of aluminum on the drill surface was the minimum for the non-hydrogenated DLC coated drill indicating its anti-adhesive property. On the other hand, the quality of the drilled holes (size and out of roundness) did not vary with the use different coatings.

Nouari et al. [61] investigated the wear mechanisms of cemented tungsten carbide (uncoated and coated with TiAlN +WC/C) and HSS tools during dry drilling (up to 70 holes) of the AA2024 aluminum alloy. Their results on the surface quality of the drilled holes in terms of out of roundness and surface roughness showed that HSS tool was not suitable for dry machining of the AA2024 aluminum alloy. Under high pressure and temperature at the contact zone, a material build up was observed on the tool rake face. Increasing the cutting speed from 25 m/min to 165 m/min caused an increase in the

interface temperature (as calculated using a commercial finite element code) from 80 to 175°C that promoted aluminum transfer from the workpiece to the tool by a diffusion mechanism. They found that compared to the uncoated tungsten carbide drills, the use of TiAlN+WC/C coated drills increased the speed at which acceptable quality holes can be produced from 25 to 65m/min at a small constant feed rate of 0.04 mm/rev.

Kishawy et al. [62] investigated the effects of flooding lubrication (CM2 coolant), dry cutting, and minimum quantity of lubrication (MQL) techniques on tool wear, surface roughness and cutting forces for the machining of A356 alloy. For MQL, a synthetic phosphate ester BM2000 with extreme pressure additives was used at rate of 30 ml/h. The authors found that the MQL technology could be a viable alternative to the flooding lubrication application. Due to the high content of silicon in the A356 alloy, the main wear mechanisms encountered were abrasive wear at the tool tip region, and adhesive wear on the flank and rake faces away from the tool tip. The degree of the wear severity was found to be a function of both insert coating and coolant environment. Experimental results showed that the optimal performance of the uncoated carbide inserts was obtained when using MQL. The diamond-coated inserts outperformed the uncoated inserts regardless of the coolant environment. However, random chipping was observed for the diamond coated tools.

Braga et al. [63] compared the drilling performances of the uncoated and diamond coated carbide drills under MQL (10 ml/h of oil in a flow of compressed air) and abundant soluble oil (1 part of oil for 25 parts of water at a flow rate of 2.4 m³/h) lubrication conditions as a lubricant in the drilling of A356 alloy. They found that the performance of the process (in terms of forces, tool wear and quality of holes) when using minimal lubrication was very similar to that obtained using a high amount of soluble oil, with both diamond coated and uncoated drills. Also, the values of flank wear were similar for the two cooling/lubrication systems used, which proves the feasibility of using the MQL technique.

2.3.2. Titanium Diboride (TiB₂) Coatings

Berger and Hogmark [64] investigated the transfer behaviour of AA7075 aluminum alloy to TiN, TiB₂ and uncoated cemented carbide. The TiB₂ coatings were

produced by direct current magnetron sputtering PVD under various bias voltages (0-50V). Crossed cylinders geometry was used to resemble actual metal cutting (**Figure 2.14**). They found that TiB_2 coatings deposited at 50 V bias voltage had relatively low residual compressive stress (measured by beam deflection technique) and performed better than TiN coated and uncoated cemented carbide in term of adhesion of aluminum and wear resistance. Very high and oscillating COF was observed. Under a load of 9 N, the average COF was 1.4 for TiB_2 , 1.7 for TiN and 1.6 for the cemented carbide. Transferred aluminum had a lamellar structure. When an adhered patch of aluminum has reached a critical thickness, it was either transferred to the test pin or left in the sliding path of the Al cylinder. TiN suffered from chemical degeneration and mechanical decohesion and detachment.

In another study Berger and Hogmark [65] compared PVD deposited TiB_2 , TiAlN, TiN and TiCN coatings for their frictional properties and tendency to pick up three different counterface materials (Al 7075, Ti- 6Al- 4V, and Inconel 718) using two crossed cylinder test specimens which are forced to slide against each other at a constant sliding speed. A gradually increasing load was used (**Figure 2.15**).

The authors observed that the TiB_2 coating had lower COF (below 0.3 versus 0.4 and above for the other coatings) and much less aluminum adhesion to its surface compared to the other coatings. However, they found no major difference in the tribological behaviour of TiB_2 against Inconel and titanium alloys compared to other coatings.

Bjork et al. [66] investigated the performance of TiB_2 , TiN, CrN, TiAlN coated and uncoated hot work tool steel extrusion dies against AA 6063 aluminum alloy at 550°C. Block on ring configuration (**Figure 2.16**) was used and the test chamber was filled with argon gas. They observed that TiB_2 , CrN and TiAlN were mechanically, thermally and chemically stable against aluminum. TiN degenerated gradually by cohesive fracture. The order of performance was TiB_2 , TiAlN, CrN and TiN. No wear was observed on TiB_2 . However, they saw that NaOH, which was used to remove aluminum, decomposed TiB_2 indicating that an alternative chemical should be used for periodic cleaning of TiB_2 coated tools.

Lugscheider et al. [67] reamed GG-25 grey cast iron and Al-12%Si aluminum alloy at different speeds using cemented carbide drills coated with TiB₂, TiAlN, Ti-B-N, ZrN and TiZrN coatings. Dry reaming of the Al-12%Si alloy was not possible with any of the coatings due to the large formation of built-up edges which caused tool clogging. Cutting of the Al-12%Si alloy has been achieved only with TiB₂ and TiAlN coated reamers under MQL conditions (fatty alcohol at a rate of 100 ml/h aerosolized in compressed air).

Experimental studies on the adhesion of aluminum on TiB₂ make this coating favourable due to the weak tendency of Al to adhere to its surface. However, to the knowledge of the author, there is no reported study on the dry drilling of aluminum alloys with TiB₂ coated tools. Therefore, dry drilling performance of TiB₂ is yet an area to be explored.

2.3.3. Solid Lubricant Coatings

MoS₂ is a solid lubricant material. It can be both used as a monolithic coating [2, 67] [Error! Bookmark not defined., Error! Bookmark not defined.] or as a top layer coating in a multilayer system [Error! Bookmark not defined., Error! Bookmark not defined.]. However, its machining performance is less than the carbon based coatings [60].

Rechberger et al. [68] evaluated the performance of MoS₂ coated HSS drills in machining wrought Al-Mg alloy, Al-7wt%Si and Pt-5wt%Cu under lubricated conditions. They observed that MoS₂ coated HSS drills produced smoother surfaces and required less torque to drill. The MoS₂ coating performed better at high production rates. In a slotting operation for cast aluminum workpieces (Al-7wt% Si alloy) a tool life improvement of over 50% was obtained with this soft coating.

2.4. Review of the Tribological Behaviour of the Diamond-like Carbon Coatings

As indicated by the studies reviewed in Section 2.3, diamond and DLC coatings seem to be the most promising groups of coatings for dry and MQL machining of Al alloys. For this reason, a detailed review of the studies on the tribological behaviour of DLC coatings will be given in this section.

DLC coatings have been attracting scientific and industrial attention because of their low COF and wear rates. They have found application in a variety of areas like hard discs, bearings, seals, forming and cutting tools. In ambient conditions, aluminum does not tend to adhere to DLC surfaces. For example, using a ball-on-flat reciprocating tester (**Figure 2.17**), Murakawa and Takeuchi [69] tested rf plasma CVD deposited hydrogenated DLC coatings with and without Si (coated on WC-Co balls) against 1100 Al flats in dry sliding conditions in ambient air. The authors showed that adhesion of Al to the DLC coating without Si occurred only at the max applied load of 80 N within the test load range (20-80 N) whereas the Si containing DLC showed Al pickup even at 20 N. The authors suggested that the chemical affinity of Al towards Si was the reason for the observed adhesion at the lower load. Due to the reduced adhesion tendency of aluminum to DLC surfaces, DLC is suggested as a promising tool coating for applications like dry drilling of Al alloys where the adhesion of aluminum chips to the drill surface is a major problem.

The term DLC refers to a large group of carbon-based coatings. DLC coatings can be produced using a variety of deposition techniques such as magnetron sputtering PVD, plasma-assisted chemical vapour deposition (PACVD), ion beam deposition, microwave plasma, pulsed laser, cathodic arc, etc. Depending on the deposition technique and the source materials (e.g. graphite, hydrocarbon gas, metal etc.), DLC coatings with very different structures and mechanical properties can be produced. Examples are amorphous carbon (a-C) with mainly sp^2 bonds and tetrahedral amorphous (ta-C) with mainly sp^3 bonds (**Figure 2.18**). When there is hydrogen in the structure of the DLC film it is denoted as a-C:H and ta-C:H. Similarly metal doped DLCs are shown as Me:C and Me:C:H. Detailed information about the production and characterization and properties of DLC coatings can be found in a recent review by Robertson [70].

A great deal of research has been done to understand the differences in the tribological behaviour of various types of DLC coatings. It has been shown that the friction and wear characteristics of these coatings strongly depend on the bond structure, namely the ratio of sp^2 to sp^3 bonds [70], hydrogen [71-75], and dopant (e.g. N, S, F, Si) contents [76-78]. The tribological behaviour of the DLC coatings is also influenced by

testing conditions, including temperature, applied load, speed [36, 79, 80], water vapour and other gaseous species in the test environment [81-85].

The formation of a carbonaceous transfer layer on the contact surface of the counterface material during sliding against different types of DLC coatings in certain environments has been well documented [80, 81, 86-88]. Friction induced structural changes (such as ordering of the amorphous carbon structure, graphitization) were reported at the sliding interface [89-92]. In his review Donnet [76] showed that proper doping of the DLC films with Si, F, N and various metals improves the tribological behaviour of DLC films. For example, doping with Si decreases the surface energy, the internal stress and COF of the DLC films. Also the humidity dependence of the metal-doped DLC films was found to be less than undoped DLC films.

Most tribological contacts generate frictional heat. In machining operations, much higher heat is released due to extensive plastic deformation during material removal (i.e. chip formation). Therefore, elevated temperature tribological performance of the DLC coatings is also an important selection criterion to be investigated. It has been shown that increasing the test temperature increases the wear rate of DLC coatings and there is a temperature limit above which the DLC coatings graphitize and oxidize heavily [93-97]. This temperature was found to depend on the deposition method, deposition parameters, consequently to the structure and the composition of the DLC coating.

The following sections will give a detailed account of the previous studies on the tribological behaviour of the various types of DLC coatings and the influencing factors.

2.4.1. Effect of Hydrogen Content of the DLC Films

Several studies have shown that the presence of sufficient hydrogen in a DLC film is the most critical intrinsic factor determining its tribological behaviour in various environmental conditions [71, 74, 75, 98-101]. For example in vacuum, the DLC films containing a large amount of hydrogen (about 40 at. % H) have very low COF values (<0.01) and low wear rates ($<1 \times 10^{-8}$ mm³/m) [71, 73-74-101]. On the other hand, the non-hydrogenated DLC coatings (< 5 at. %) exhibit high COF values (0.5-0.6) and high wear rates in vacuum [71, 83]. The origin of the high COF of the non-hydrogenated DLC films in vacuum was attributed to the strong interactions of the “dangling bonds” of

surface carbon atoms with the counterface materials [71, 83, 101]. For the hydrogenated DLC coatings, hydrogen leads to the formation of C-H bonds and hence passivate the dangling carbon bonds on DLC surfaces, leading to low COF in vacuum [71, 102, 103].

The effect of hydrogen content on the tribological behaviour of the DLC coatings was also shown in atmospheres other than vacuum. For example, the non-hydrogenated DLC films showed drastically reduced values of COF and wear rates in the presence of water vapour compared to vacuum test conditions [82, 83, 86]. On the other hand, the presence of water vapour in the test chamber caused higher COF and wear rates of hydrogenated DLC films compared to those in the vacuum environment [82-85, 104-108].

Donnet and his colleagues [71, 98] showed that hydrogen in the test environment could help partially hydrogenated DLC coatings (34 and 40 at. %H) reach very low COF. The authors tested the friction behaviour of the plasma-enhanced CVD (PECVD) deposited DLC coatings with two different hydrogen contents (34 and 40 at. % H) [71]. Tests were done against a steel pin (AISI 52100) in a reciprocating sliding machine under vacuum, hydrogen and argon environments at 25°C and 150°C. Under vacuum, the DLC film with the lower hydrogen content (34 at. %) exhibited a low COF value of 0.01 for 100 cycles after which the COF increased to 0.6, whereas the film with the higher hydrogen content (40 at. %) maintained the very low COF value of 0.03 throughout the test. When the lower hydrogen containing DLC (34 at. % H) was tested under a hydrogen gas pressure of 1000 Pa, the COF did not increase as it did under vacuum and only reached 0.006 at the end of the test. However, the friction behaviour at a lower hydrogen pressure of 100 Pa was similar to the vacuum test, i.e. the COF went to the high value of 0.6 after a short very low COF period. Repeating the same test at 150°C resulted in an even lower COF value of 0.002 at the end of the test. Thus, the authors concluded that a very low COF could be attained only when there is enough hydrogen at the sliding interface and that elevating the test temperature lowers the COF due to the more efficient thermal-assisted diffusion of hydrogen towards the sliding surface.

Erdemir [74] compared the tribological behaviour of PACVD deposited DLC films with different H/C ratios and a hydrogen-free DLC film against steel balls coated with the same type of DLC coating. In dry nitrogen, the hydrogen-free DLC coating (H/C

ratio of 0) had a steady-state COF value of 0.25 whereas the DLC film with the H/C ratio of 10 exhibited a very low COF value of 0.003-0.005. He suggested that the high COF for hydrogen-free DLC film is due to the interaction of the σ bonds of carbon with the counterface material. In hydrogenated DLC film, sigma (σ) bond interaction with the counterface was eliminated since open carbon bonds at the sliding interfaces were filled with hydrogen and hence a very low COF was achieved.

2.4.2. Transfer Layer Formation and Friction-induced Structural Changes

The formation of a carbonaceous transfer layer on the contact surface of the counterface material during the sliding of different kinds of DLC coatings has been well documented [80, 81, 90, 109]. The easy shear of this transfer layer was also quoted as one of the reasons for the low COF and wear rates of the DLC coatings [80, 81, 86-88]. The structure, composition, and thickness of the transfer layer have been found to depend on the loading conditions and the test atmosphere [90, 110, 111].

The change in the structure of the carbonaceous transfer layer is generally attributed to the friction induced structural transformations such as ordering of the amorphous carbon structure, and the graphitization at the sliding interface [89, 90, 92, 99, 110, 111].

Liu and Meletis [**Error! Bookmark not defined.**] were the first to present the evidence of graphitization of DLC coatings during dry sliding. Using a pin-on-disc machine they tested ion-beam-deposited DLC coatings (from methane precursor) against Ti-Al-4V pins in ambient air (30% RH). The transmission electron microscope (TEM) diffraction pattern of the as-deposited films revealed an amorphous structure with short-range sp^3 domains. When the debris collected after 1000 m of sliding distance was examined, the diffraction pattern was similar to that of graphite. Thus, the authors concluded that as-deposited DLC had a distorted diamond cubic structure and transformed into graphite during sliding (friction induced graphitization). It was suggested that low friction observed during sliding is due to the low shear strength of the graphite planes.

The effects of sliding speed (0.06 and 1.6 m/s) and applied load (1 and 10 N) on the friction and graphitization behaviour of ion beam deposited DLC coatings were

studied by Liu et al. [79]. They found that increasing the sliding speed and the applied load decreased the COF and the wear of the DLC coated disc tested against ZrO₂. For example, at a sliding speed of 0.06 m/s and an applied load of 1 N the steady state COF was 0.18 whereas the COF dropped to 0.05 when the sliding speed and load increased to 1.6 m/s and 10 N. The authors suggested that the sliding speed of 0.06 m/s and the applied load of 1 N were not enough to promote graphitization, which is necessary to maintain low steady-state COF. It was suggested that a higher sliding speed eases the hydrogen release from the DLC structure by increasing the temperature at the asperities. The applied load was thought to shear and transform this hydrogen-released DLC layer into graphite [90].

Using an in situ Raman tribometer, Scharf and Singer [110, 111] observed that a transfer film quickly developed on the sapphire surface running against the DLC (C:H:Si:O) coatings deposited from siloxane precursor by PECVD method, and the tribosystem exhibited low COF values in the range of 0.03-0.05. The COF increased when the transfer layer was removed. The Raman data showed that the transfer film was more mostly graphitic compared to the as-deposited coating (**Figure 2.19**).

Sanchez-Lopez et al. [92] studied the structural changes occurring during the dry sliding of DLC coatings with different hydrogen contents (H/C varied from 0 to 10). Examination of the transfer layers on the counterface material (AISI 52100 steel balls) by Raman spectroscopy indicated the presence of a disordered graphite-like structure in the hydrogenated DLC coatings. However, using TEM and electron diffraction, the transfer layer was found to be amorphous just like the as-deposited coating. Therefore, the authors suggested that these graphitic regions must be smaller than 2 nm since they could not detect any of the typical features of nanocrystalline graphite by TEM and electron diffraction.

Voevodin et al. [89] studied the friction behaviour of pulsed laser deposited hydrogen-free DLC films in humid air, nitrogen and vacuum environments against sapphire and steel (440 C) balls. The films were did not contain hydrogen (less than 0.1 at. %) and had mainly sp³ type bonding (ta:C). Raman spectra of the wear debris after 1x10⁵ cycles indicated the transformation from amorphous DLC to polycrystalline graphite. As an indirect proof of friction-induced graphitization, the authors increased the

relative humidity of the test environment after 10^2 and 10^5 cycles. The increase in relative humidity after 1×10^5 cycles reduced the COF as observed typically in graphite-like materials [112-114].

2.4.3. Effect of Test Environment on the Tribological Behaviour of DLC Coatings

In an earlier work, Bowden [113] showed that clean surfaces of diamond, graphite and carbon have high COF. Introduction of oxygen and/or water vapour greatly reduces the COF.

Kokaku and Kitoh [115] studied the effect of exposing DLC films to high atmospheric humidity on their tribological behaviour. RF-PECVD films deposited from benzene (C_6H_6) were exposed to 90% RH at $60^\circ C$ for seven days. Compared to the as-deposited DLC film, the films exposed to high humidity showed higher COF (0.2 vs 0.39) in ambient air (50% RH) for the first 100 revolutions. By performing ESCA and EELS analyses, the authors detected C=O and COOH groups forming on the surface of the film exposed to high humidity.

Miyoshi [104] studied the tribological behaviour of DLC films (with 44.4 at. % H) grown by PACVD method under different power densities (50 and 250 W). He observed an inverse relationship between the argon ion etching rate and the deposition power and concluded that the films deposited at high power were denser than those deposited at lower power. A lower COF of 0.1 was observed in nitrogen than in air with 40% RH where the COF was 0.2. The DLC coating deposited at 300 W power density was annealed at $700^\circ C$ in vacuum. When this coating was tested in nitrogen and in air with 40% RH, the COF under air was initially lower than in nitrogen, different than the as-deposited coating. The author related this observation to the formation of a graphite layer on the surface during annealing. However, as the test continued the COF in air increased and was equal to the value for as-deposited coating. The annealed DLC coating failed after 14,500 passes in ambient air whereas it survived until 35,000 passes in nitrogen. Therefore, the author suggested that the wear and friction behaviour of the DLC coatings was dependent on interactions (mechanical and chemical) between the sliding pairs and the test atmosphere.

Andersson et al. [82, 83] demonstrated the different effect of water vapour pressure on the friction behaviour of hydrogen-free and hydrogenated (39 at.%) DLC coatings tested against DLC coated steel (M 50) balls. Hydrogen-free DLC coatings had a COF of 0.6 under vacuum. Introducing water vapour to the test environment decreased the COF to 0.07. For the highly hydrogenated DLC film the COF was 0.01 under vacuum and increased to 0.07 as water vapour was added to the system.

Donnet et al. [85] studied the role of oxygen and water vapour on the tribology of hydrogenated DLC films (42 at. %). Within the pressure range they worked (vacuum to 6000 Pa), no significant effect of oxygen on the COF value (0.01) of the DLC film was detected. For the effect of water vapour, similar to [83], they observed an increase in COF from 0.01 to 0.1 as the vapour pressure increased from zero to 500 Pa. The authors related the change in the COF with the thickness of the carbonaceous transfer film formed on the counterface material (steel). A considerable amount of transfer film had formed under vacuum whereas it got smaller and smaller as the pressure of water vapour increased. It was suggested that water vapour affects the kinetics of the formation of this carbonaceous transfer layer.

Zhang et al. [81] investigated the tribological behaviour of DLC films, deposited by PACVD method from C_6H_6 , in dry air, O_2 , N_2 and vacuum environments against SiC. The wear rate under O_2 was found to be more than 200 times higher than the wear rate under N_2 . A small contact area covered with a transfer layer was observed on the SiC counterface ball for the test run in N_2 where the COF was 0.06. For the test in O_2 , the COF was 0.1, the contact area was larger and it was rather clean. Therefore, the authors concluded that the friction and wear behaviour of DLC films was controlled by the transfer layer on the opposing surface, formation of which depended on the test atmosphere.

Jiang et al. [84] investigated the effect of relative humidity on the tribological behaviour of DLC films against WC balls using a ball-on-disc machine. The DLC films were produced by a combination of magnetron sputtering and PACVD methods and they were non-hydrogenated with mainly sp^2 type bonding. The authors observed that regardless of the test speed (0.05 and 0.25 m/s), the wear rate of the DLC coatings

decreased as the relative humidity increased (**Figure 2.20**). The role of water vapour was suggested as the passivation of the fresh carbon surfaces via adsorption.

Jiang and Arnell [86] studied the effects of sliding speed and sliding distance on the wear behaviour of magnetron-sputtered DLC coatings. They showed that the variation of the wear rate of DLC coatings with sliding speed followed a U-shaped parabolic curve in the speed range (0.048 to 0.45 m/s) studied. The authors proposed a semi-quantitative relationship between the wear rate and the sliding speed assuming that the generation debris particles from micro-cracks was controlled by chemically activated interactions between environment and the atoms at the crack tip.

Heimberg et al. [36] performed reciprocating sliding tests on DLC coatings that were produced by PACVD method in hydrogen and hydrocarbon rich environment. DLC coated flats were run against DLC coated balls using a ball-on-flat tribometer in dry nitrogen. They were able to correlate the change in friction coefficient caused by different test speeds and time-delays with the kinetics of gas adsorption onto carbon. Extremely low COF values in the range of 0.003-0.008 were observed when the exposure time of the DLC surface to dry nitrogen was kept below 5 seconds. The time period of 5 seconds between the two contacts was not enough to adsorb sufficient nitrogen to change the friction behaviour. When the exposure time was increased using either a slower sliding speed or a longer time delay, the COF increased to the values typical of DLC coatings under ambient air (0.1).

2.4.4. Modelling the Dependency of the Tribological Behaviour of DLC and Graphite on the Sorption of Gaseous Species on Their Surfaces

As shown by the studies described in the previous section, the kinetics of the interaction of the gaseous species with the sliding surfaces had great effect on the tribological behaviour of DLC coatings.

Dickrell et al. [51] developed a fractional coverage model for the adsorption and removal of gaseous species in repeated sliding conditions (unidirectional and reciprocating). Their model relates the COF to the average fractional coverage of gaseous species under the pin contact. The validity of the model was verified with the COF

behaviour of hydrogenated DLC coatings tested under various sliding speeds and time delays reported previously [36].

Similarly, Borodich and Keer [52] examined the applicability of some of the well known adsorption kinetics equations for the modelling the gas adsorption process on DLC films.

Brendle and Stempfle [35] developed a model that successfully simulates the friction and wear of graphite. They proposed a “triboreactor” model that works between the pin the disc at the time of each contact. Their model combines three mechanisms; i) one step embrittlement of graphite governed by the amount of moisture within the contact, ii) the kinetics of water adsorption outside the contact that obeys Elovich equation and iii) the triboreactions between the water and active prismatic surfaces of graphite debris.

2.4.5. Effect of Test Temperature on the Tribological Behaviour of DLC Coatings

In the literature, there are several studies on the elevated temperature behaviour of DLC coatings [93-97, 116, 117]. These studies indicate that DLC coatings do not perform well at high temperatures.

Vanhulsel et al. [97] studied the wear behaviour of PACVD produced a-C:H coatings (containing 35 at.% H) against corundum balls using a low-amplitude oscillatory test machine. They found that the room temperature COF value of 0.13 started to decrease at temperatures higher than 100°C reaching 0.07 at 300°C and the wear scars became larger as the temperature increased. Their room temperature tests on a previously annealed sample (16 h at 300°C) gave similar results to an unannealed sample. Therefore, they concluded that the tribological behaviour of a-C:H coatings would change only when they are exposed to load and heat simultaneously and structural changes (sp^3 - sp^2 change and/or dehydrogenation) are confined only to the top surface layer.

Krumpiegl et al. [96] tested three different DLC coatings (a-C, a-C:H and Ti-doped Ti-C:H) against M2 steel balls at elevated temperatures (up to 450°C) and under vacuum (10^{-3} Pa). The DLC coatings showed low wear rates ($< 2.7 \times 10^{-7}$ mm³/N.m) at room temperature in ambient air. When the test temperature was increased to 450°C, the a-C failed in 10 m and other two failed in 100 m total removal from sliding tracks). The

authors observed a drastic drop in hardness of the coatings after heating them to 450°C in ambient air. This was thought to be related with the severe oxidation of the coating.

Liu et al. [95] studied the high temperature (up to 400°C) tribological behaviour of DLC films grown using CH₄ gas in an RF-PACVD against alumina balls in a reciprocating tester. The wear rate increased by more than 10³ times when the temperature was increased from 200°C to 300°C and the films started to peel off from the Si substrate above 300°C.

Using thermogravimetric and differential thermal analyses and Raman spectroscopy, Wang et al. [94] investigated the high temperature behaviour of DLC films produced by combined PVD and PACVD processes. The authors found that DLC films disintegrated at 350°C due graphitic transformation and heavy oxidation.

Bremond et al. [117] performed elevated temperature pin-on-disc tests (up to 400°C) on a-C:H (10% hydrogen estimated) coatings deposited on 100C6 (AISI 52100 equivalent) steel discs by PACVD technique. They concluded that the failure of the DLC coating was due to the combined effect of the oxidation of the coating and the softening of the substrate.

The effect of vacuum annealing (up to 590°C) on the friction and wear behaviour of DLC films produced by PACVD method at various temperatures and bias was studied by Grill et al. [116]. In humid air, no difference in the COF values between the as-deposited films and the ones annealed at different temperatures was found. However, the DLC films deposited at higher temperatures and biases showed higher wear resistance after annealing.

Gupta et al. [93] studied the friction and wear behaviour of diamond films at 25 and 500°C in ambient air against alumina balls. The COF of the polished film increased from 0.11 at 25°C to 0.28 at 500°C. The authors suggested that the increase in friction might be due to either desorption of the hydrogen from the diamond surface, or formation of tribological layers of alumina surface and/or to the increased fracture of alumina.

2.5. Remarks

The presented literature survey on the tribological behaviour of the DLC coatings showed the following:

1. The friction and wear behaviour of DLC coatings strongly depends on the test environment.
2. The presence of sufficient amount of hydrogen in the DLC film is the most critical intrinsic factor determining the tribological behaviour of DLC coatings in a given environment.
3. Sufficiently hydrogenated DLC coatings exhibit very low COF and wear rates in vacuum and inert gas environments. Introduction of oxygen and especially water vapour adversely affects their tribological behaviour.
4. DLC coatings without sufficient hydrogen generally show high COF and high wear rates in vacuum and inert gas environments. The presence of appropriate reactive gaseous species (such as water vapour in ambient conditions) in the test environment is necessary for them to have low COF and low wear rates.
5. The presence of the easy-to-shear carbonaceous material at the sliding interface is often accounted for the low COF behaviour of DLC coatings.
6. Increasing the test temperature increases the wear rate of DLC coatings regardless of its content and structure.
7. There is a temperature limit above which the DLC coatings graphitize and oxidize heavily. This temperature depends on the deposition method, deposition parameters and consequently the structure and the composition of the coating.
8. The mostly used counterface materials for the study of the tribological behaviour of DLC coatings were different types of steel (52100, 440C, M2, M50 etc.), ceramic based materials (WC-Co, Al₂O₃, SiC, Si₃N₄ etc.) or their DLC coated versions. As stated in the first chapter, the interest of this study is to develop a tool coating to be used during the dry machining of Al alloys. Therefore, the need for a detailed investigation of the tribological behaviour of DLC coatings against aluminum is clear.

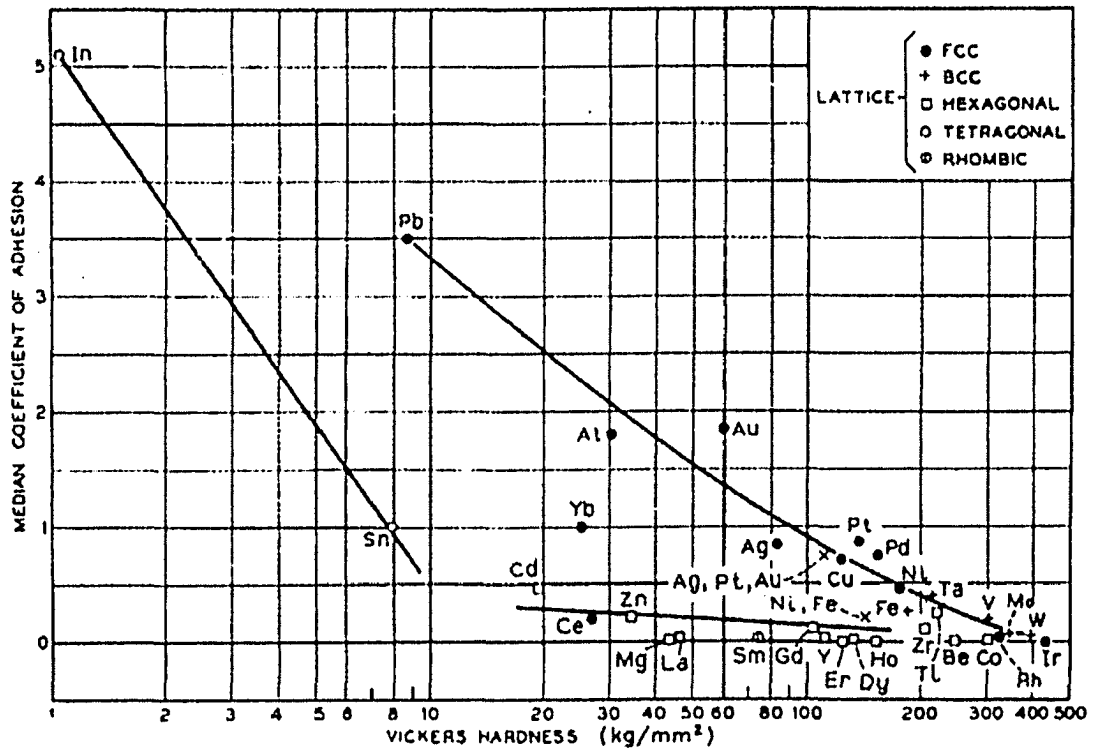


Figure 2.1. The plot of the COA values of the self-mated metal pairs with respect to their hardness [13].

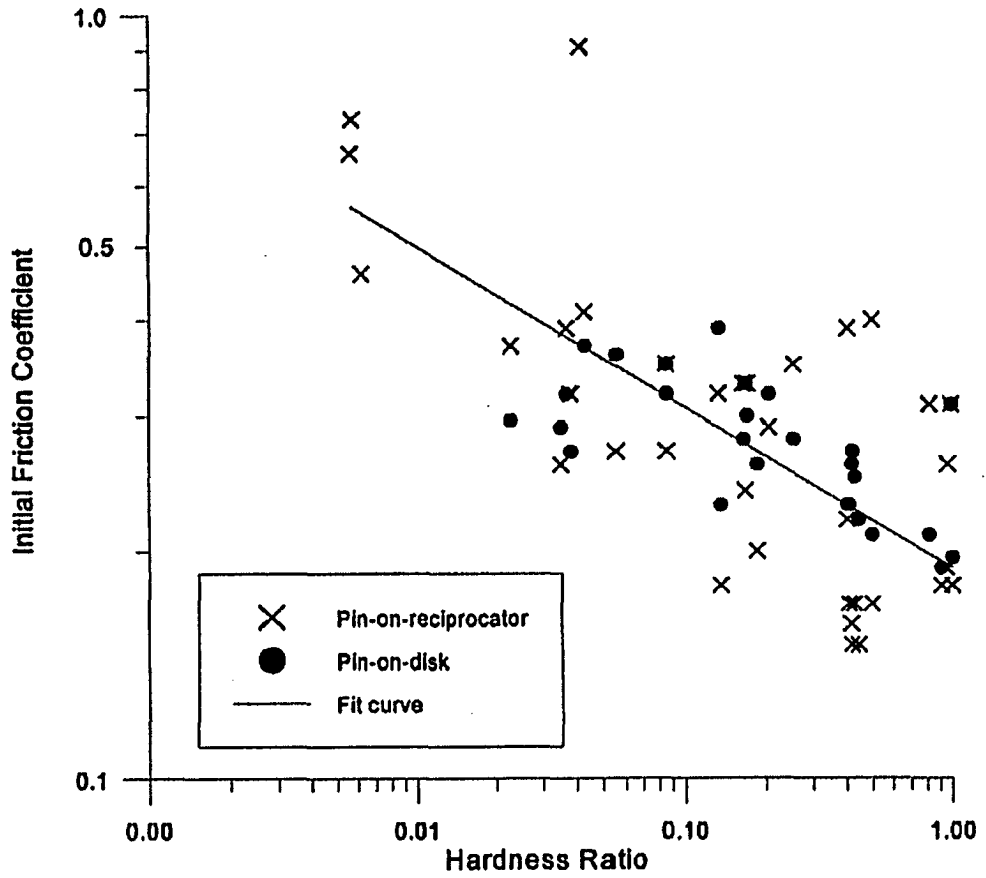


Figure 2.2. The plot of the static (initial) COF values of various metals pairs with respect to their hardness ratios [23].

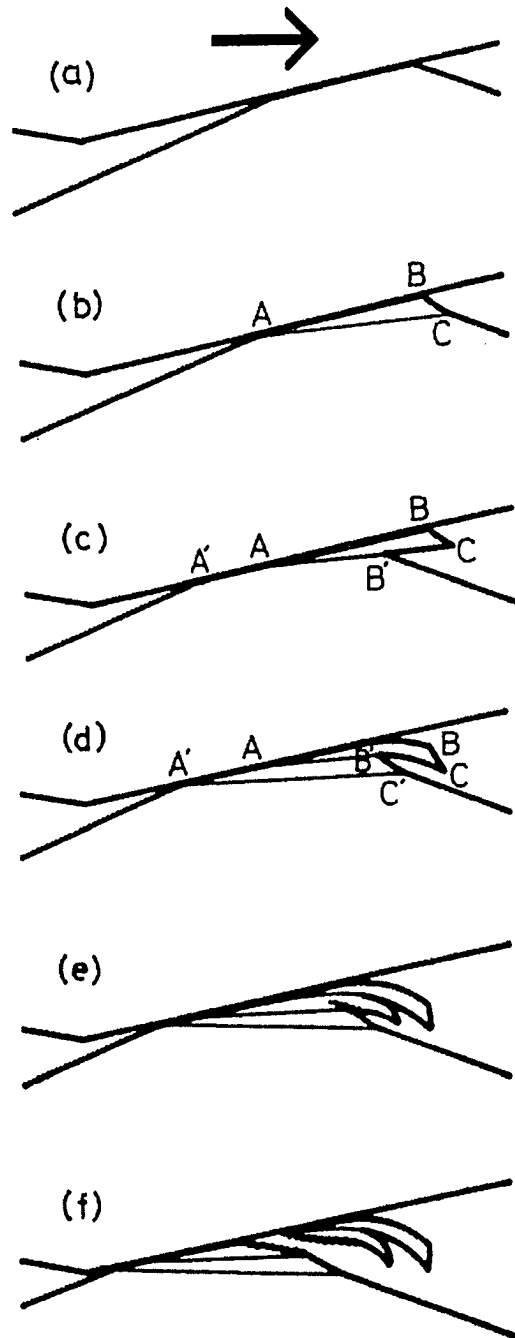


Figure 2.3. Adhesive transfer of the slip tongue [18].

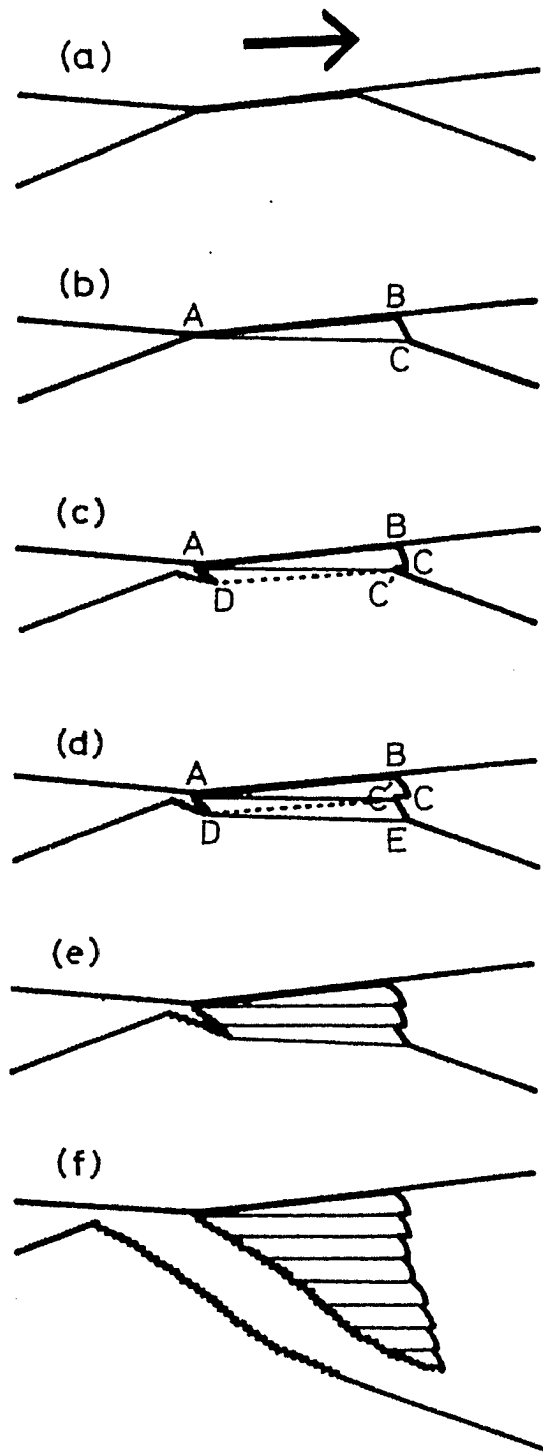


Figure 2.4. Adhesive transfer of the wedge [18].

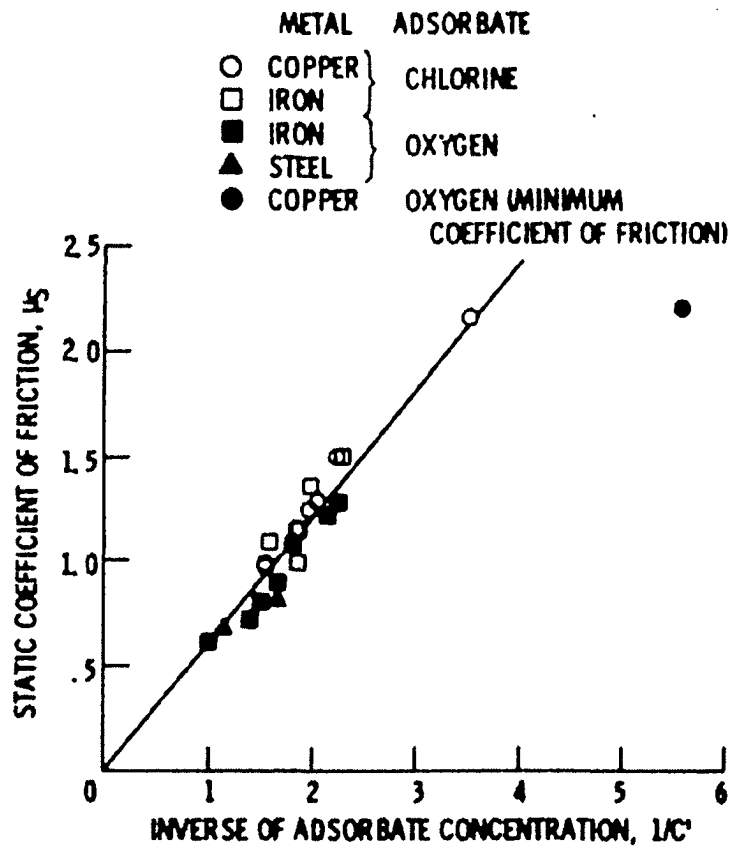


Figure 2.5. The variation of the static COF values of Cu, Fe and steel with respect to inverse of adsorbate concentration (from ref 19 in [17]).

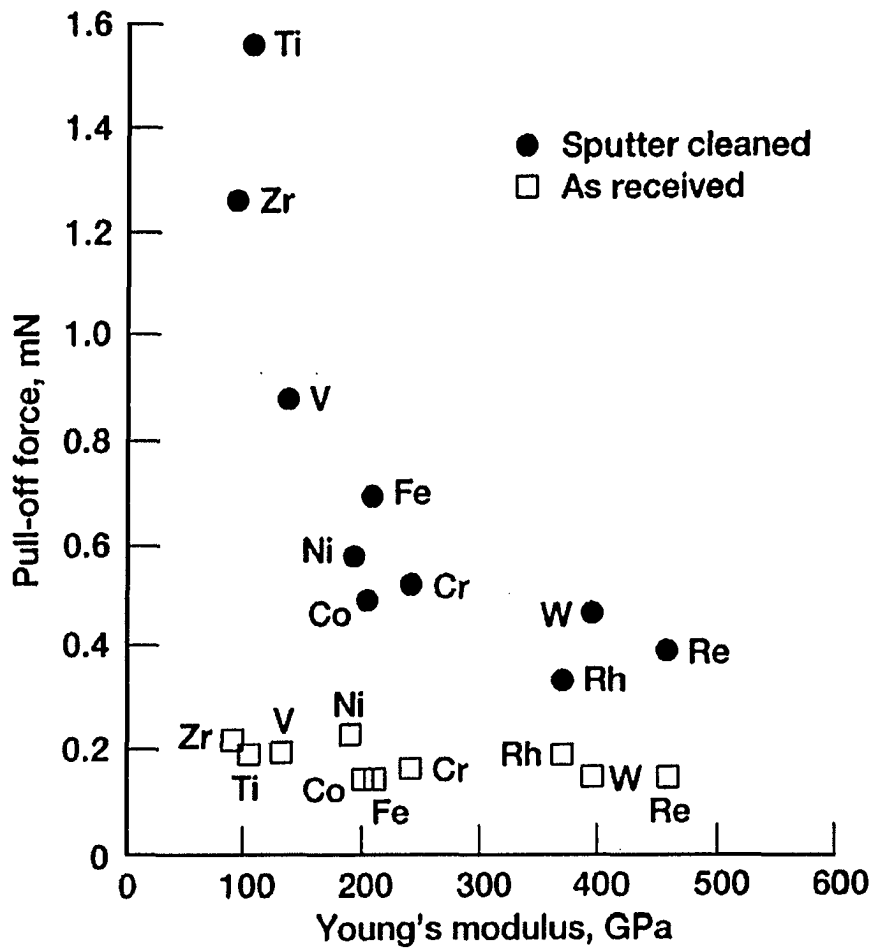


Figure 2.6. The plot of the pull-off forces vs. elastic modulus values of various metals when they were tested against polycrystalline manganese zinc ferrite in ultrahigh vacuum before and after being cleaned [22].

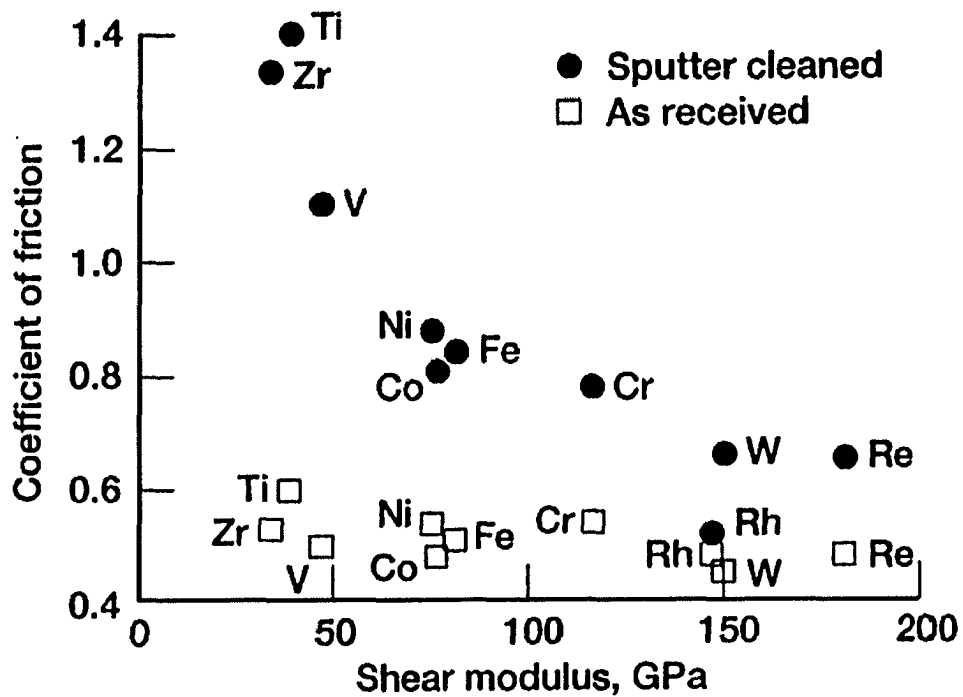


Figure 2.7. The plot of the COF vs. shear modulus values of various metals when they were tested against polycrystalline manganese zinc ferrite in ultrahigh vacuum before and after being cleaned [22].

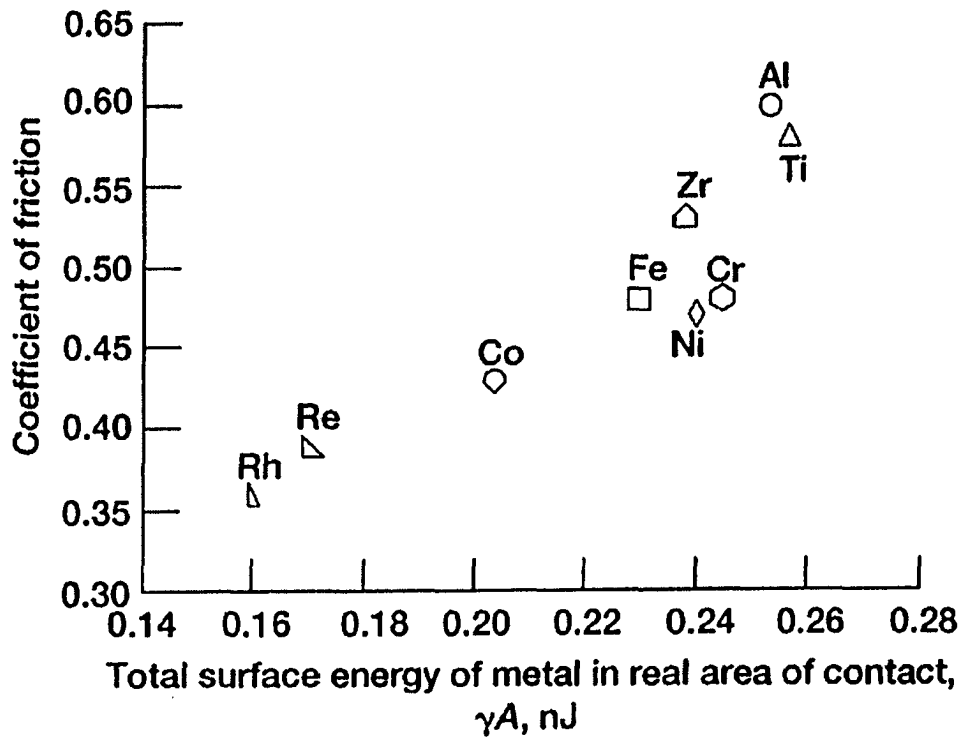


Figure 2.8. The vacuum COF values between various metals and SiC surface as a function of the total surface energy of the respective metal in real area of contact [22].

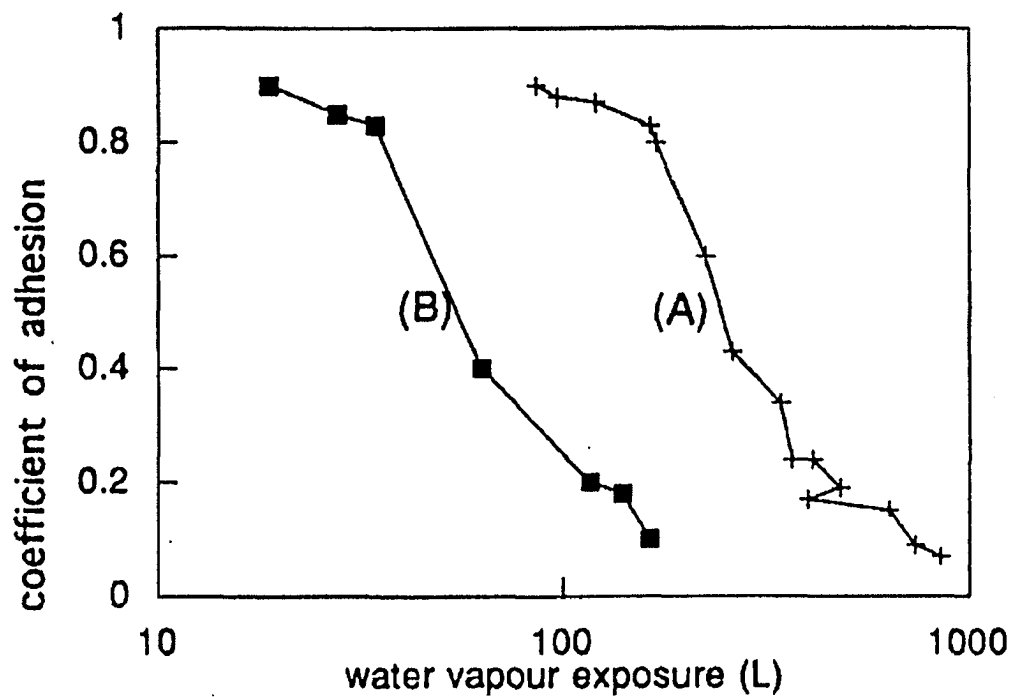
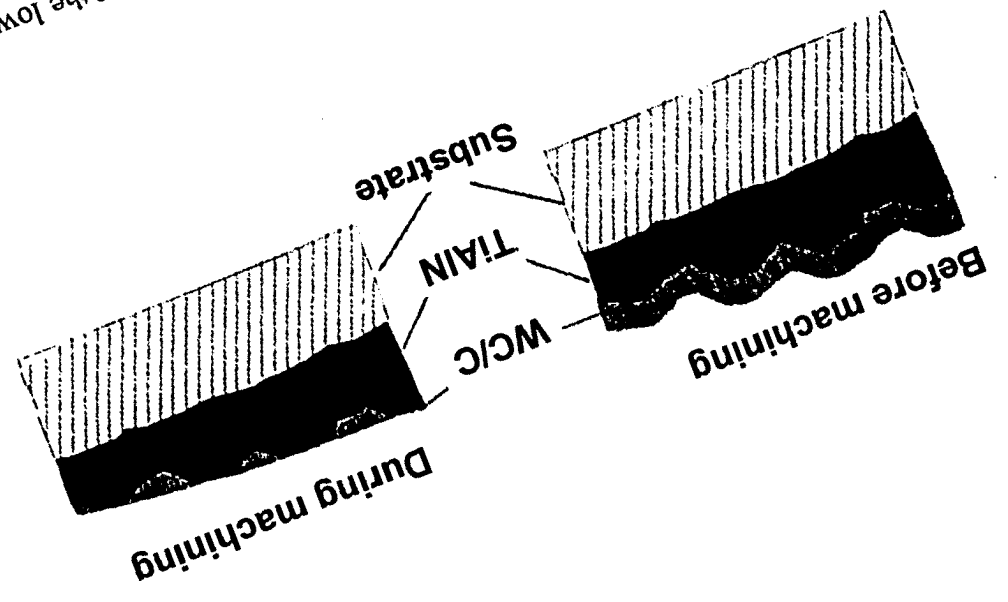


Figure 2.9. The variation of the COA as a function of the exposure to (A) water vapour, and (B) water vapour and oxygen [31]. $1 \text{ L} = 1 \times 10^{-6} \text{ Torr} \cdot \text{sec}$.

Figure 2.10. Illustration of a possible mechanism of the role of the low friction coating during a machining operation [5].



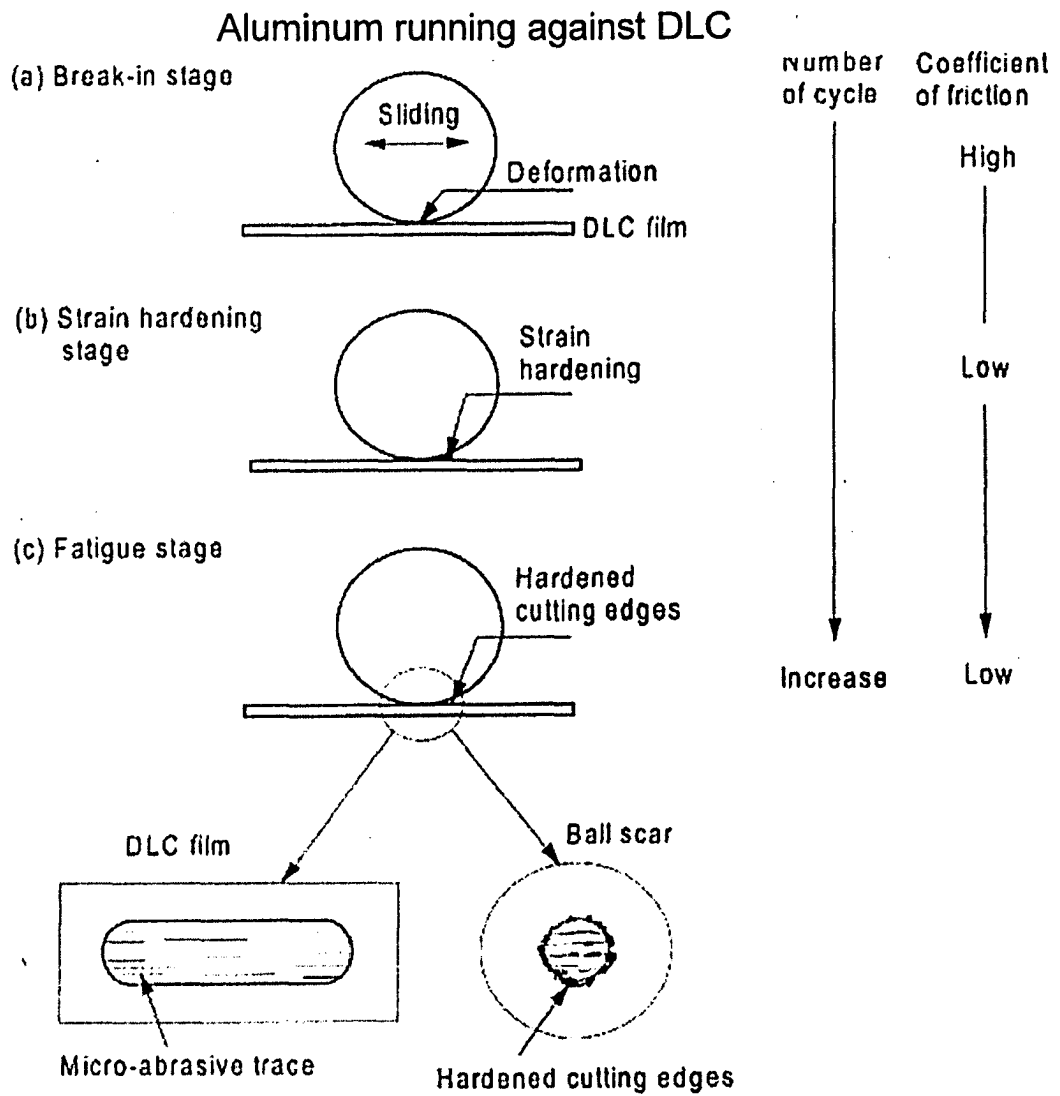
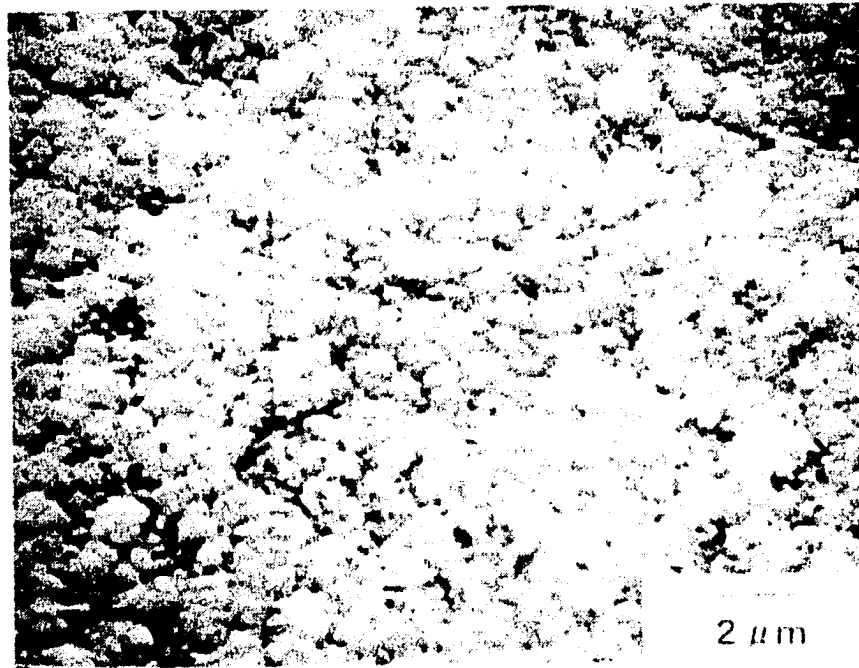


Figure 2.11. Proposed wear mechanism for the counter body against DLC film [56].



a)



b)

Figure 2.12. Diamond coatings deposited at a) 1183 K b) 779 K [57].

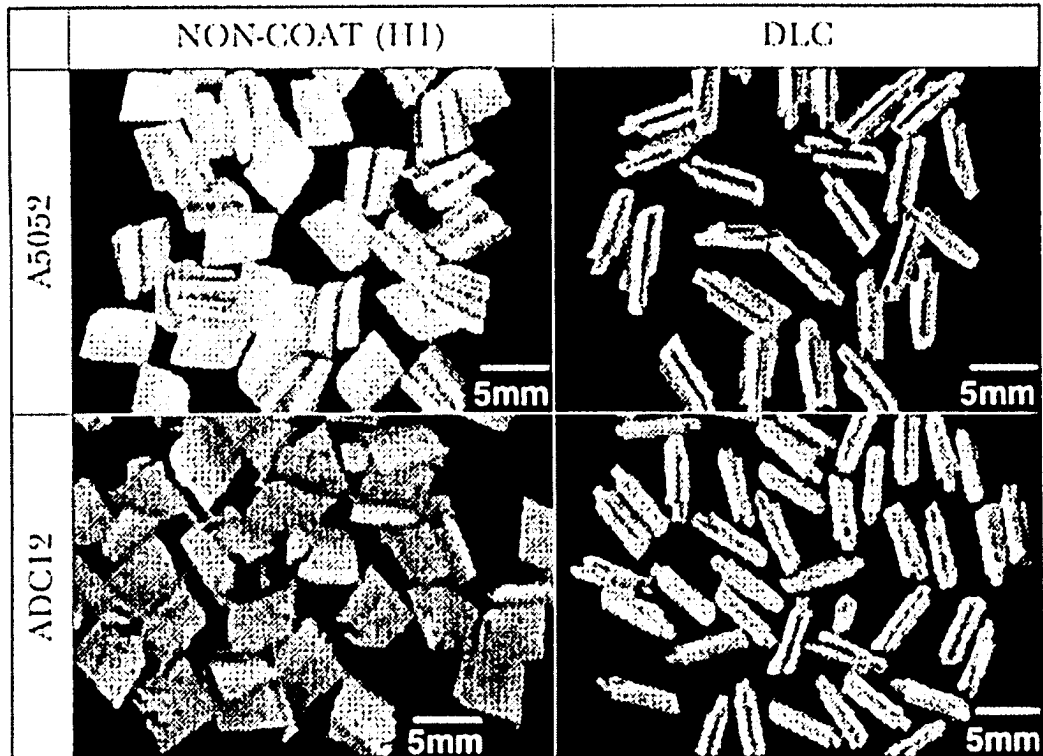


Figure 2.13. Chips produced when cutting with uncoated and DLC coated cemented carbide tools. Small and curled chips are easier to evacuate [58].

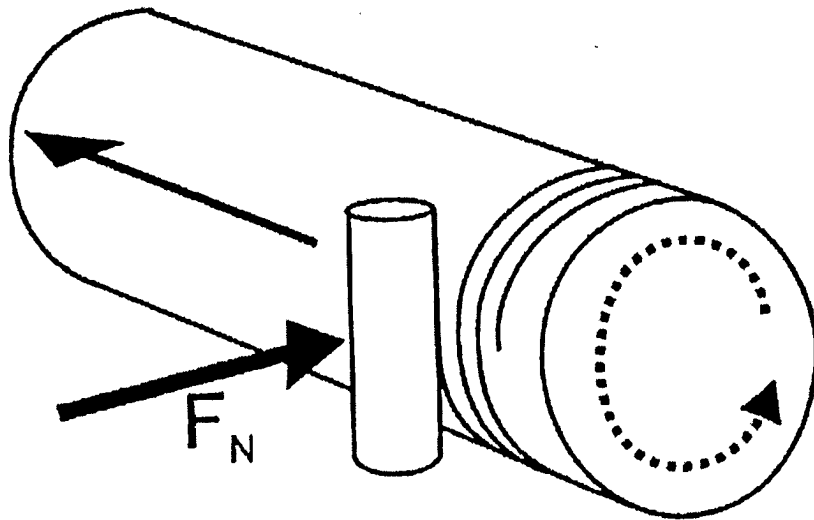


Figure 2.14. Experimental setup [64].

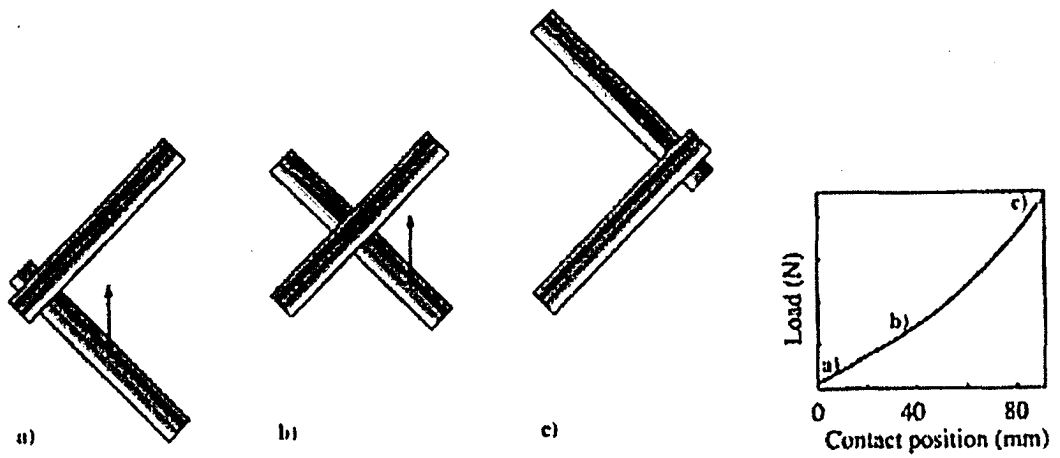
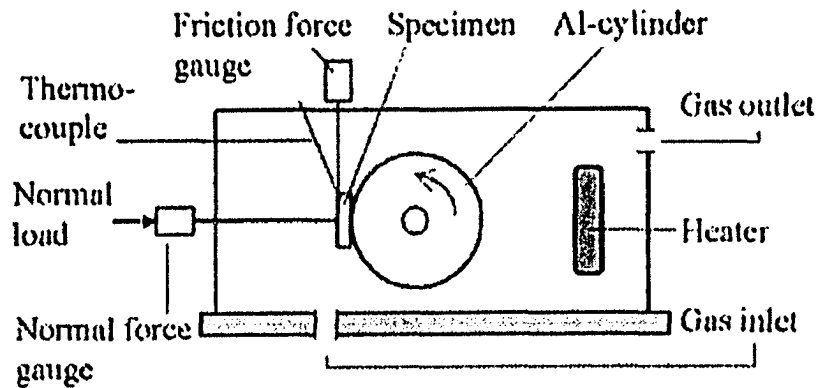
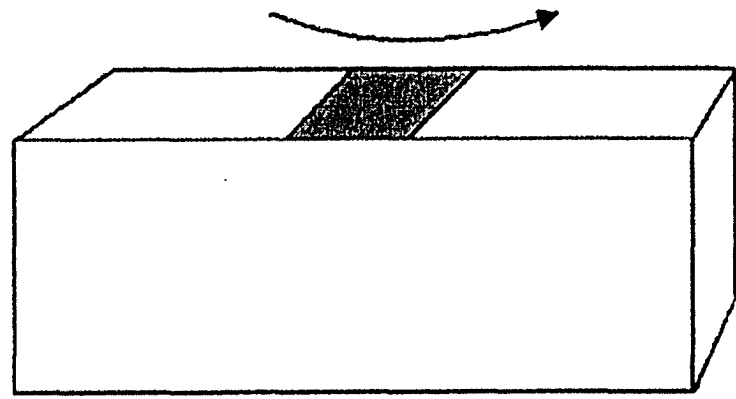


Figure 2.15. Test configuration [65].



(a)



(b)

Figure 2.16. Test configuration [66].

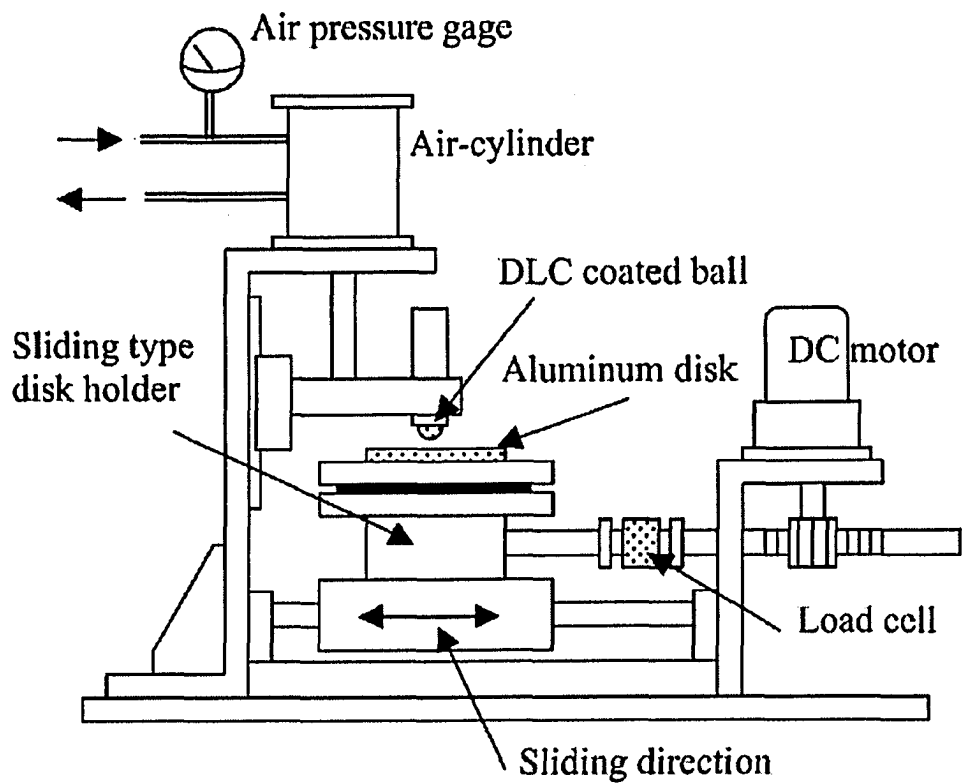


Figure 2.17. Tribometer used by Murakawa and Takeuchi [69].

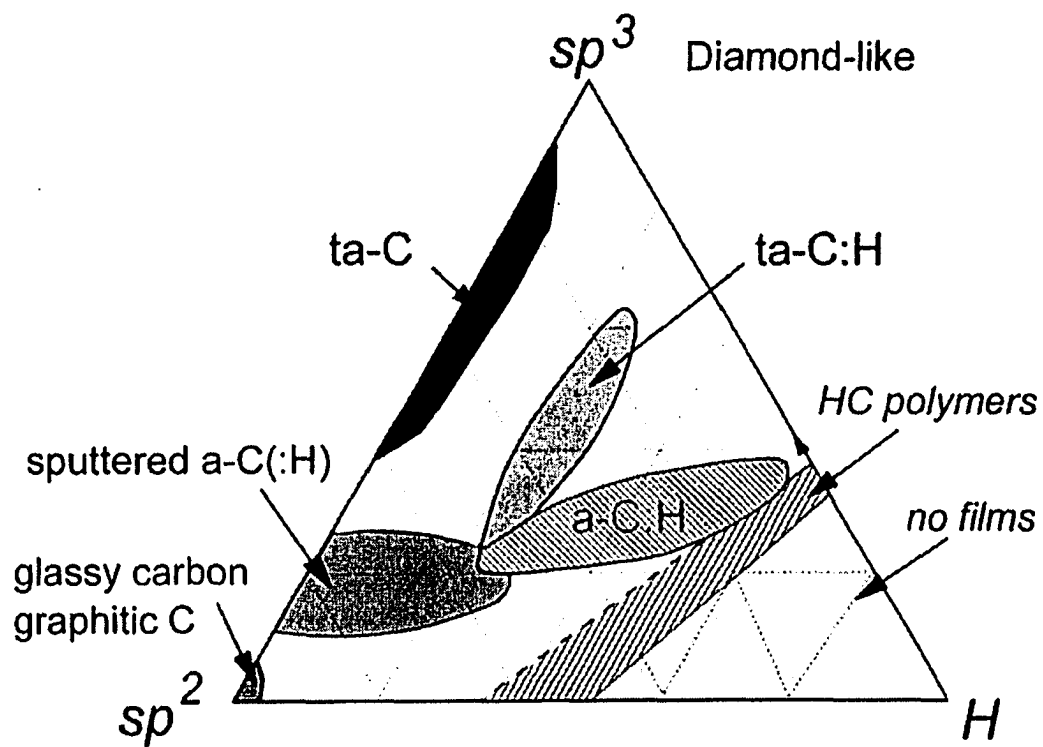


Figure 2.18. Various forms of carbon-hydrogen alloys [70].

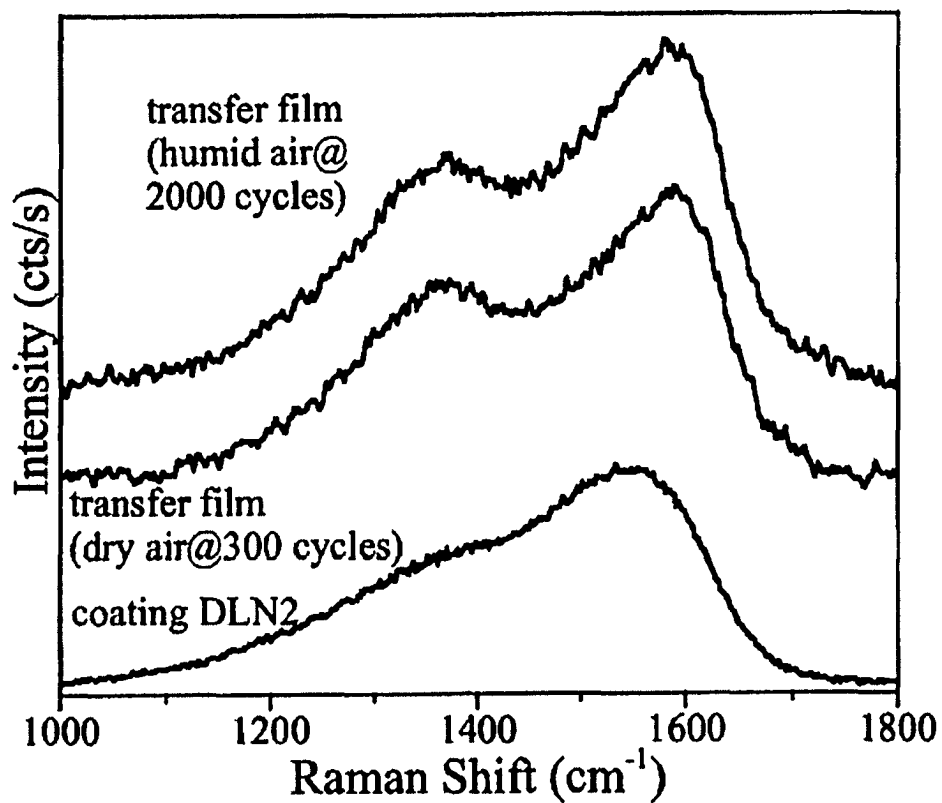


Figure 2.19. Raman spectra of the as-deposited DLC coating (DLN2) and its transfer films after running in humid air for 2×10^3 cycles and in dry air for 3×10^2 cycles [110].

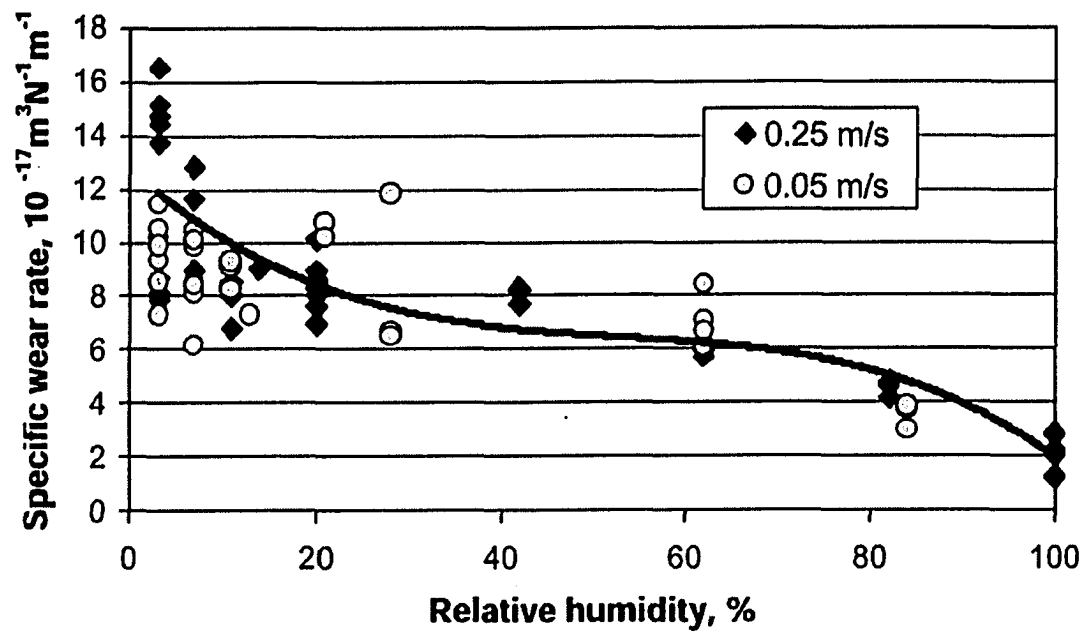


Figure 2.20. The effect of RH in air on wear rate of the DLC coating at sliding speeds of 0.05 and 0.25 m/s. Data for sliding in water is plotted at a RH of 100% [84].

CHAPTER 3

EXPERIMENTAL METHODS AND MATERIALS

In the first part of this chapter, a description of the methods and analysis techniques used to characterize the materials tested throughout this work is given. Then, the coatings used in this work are described: their deposition history, mechanical, structural and surface characteristics are given. This is followed by the description of the counterface materials and their properties. Then, the pin-on-disc tribometers used and the test conditions of the experiments are given. Finally, the tools and procedures used to evaluate the pin-on-disc tests including the calculation of wear rates of the coatings and the quantification of the material adhered to a coated surface are explained.

3.1. Characterization of Test Materials

3.1.1. Thickness Measurements of Coatings Using Radial Sectioning Method

Radial sectioning is a conventional method to measure the thickness of coatings. This method can be applied to all systems where a noticeable colour or reflectivity difference exists between the coating and its substrate. In this technique, the coated surface is subjected to wear by pressing against a rotating sphere of diameter D (**Figure 3.1.a**). Abrasive suspension (usually diamond) is applied to the contact region between the rotating sphere and the coating surface to cause three-body abrasive wear of the coated sample. This process results in a wear crater similar to the one shown in **Figure 3.1.b** for the diamond-like carbon coating deposited at 80 V bias (80-V DLC). By measuring the diameters of the inner (ID) and outer circles (OD), the thickness of the coating (t) can be calculated using the following geometrical relationship,

$$t = \frac{1}{2} \left[\sqrt{4D^2 - ID^2} - \sqrt{4D^2 - OD^2} \right] \quad \text{Equation 3.1.}$$

In this study, both CSM CALOTEST® and Philtec 2015 Sectioner machines located at General Motors Global Research and Development Center in Warren, Michigan, USA (referred as the GM R&D Center thereafter in the text) were used to

measure the thickness of the coatings tested. The CSM CALOTEST® uses hardened steel balls of different diameters. The Philtec 2015 uses abrasive diamond coated discs.

3.1.2. Mechanical Property Measurement Tools

3.1.2.1. Rockwell Hardness Measurements

A Rockwell Macromet® (Model 1800-5100T) hardness tester at the University of Windsor was used for the hardness measurements of the pin materials and M2 tool steel substrates in Rockwell B (R_B) and C (R_C) scales. Rockwell B scale uses a 1.588 mm (1/16 in.) diameter WC ball under a 100 kg load. A conical diamond indenter is used in Rockwell C scale under a major load of 150 kg.

3.1.2.2. Vickers Micro Hardness Measurements

A Buehler Micromet II® (Model 1600-9000) hardness tester at the University of Windsor was used to measure the hardness values of the pin materials in Vickers scale (HV). The indentations were made using a square-base pyramid (Vickers) indenter under a load of 100 g.

3.1.2.3. Nanoindentation of Coatings

An MTS Nano indenter XP located at GM R&D Center was employed to measure the hardness and elastic modulus values of the samples using nanoindentation. In this technique, an indenter is loaded and unloaded in to a sample to a certain depth (h_{max}) or load (F_{max}) in a controlled manner. The most commonly used indenter shape for nanoindentation measurements is a three-sided pyramidal diamond called as the Berkovich indent. The variations of the load and displacement values during the entire loading and unloading processes are recorded. As an example, the indentation load-displacement curve for the diamond-like carbon coating deposited at 60 V bias (60-V DLC) is shown in **Figure 3.2**. The hardness and elastic modulus values of a sample are extracted from its indentation load-displacement curve using the analysis methods developed by Oliver and Pharr [118] and Doerner [119]. The values reported in this dissertation were calculated according to the Oliver and Pharr procedure. This analysis requires the knowledge of the area function of the indent, i.e. the expression of the

contact area (A) of the indent in terms of the distance from its tip (h). The area function of a perfect Berkovich indent is $A=24.5h^2$. Indentation of a sample of known hardness and elastic modulus (for example fused silica) is used to correct the area function for the bluntness of the tip.

The hardness H of the sample can simply be calculated from the ratio of the maximum applied load F_{max} to the contact area of the indent:

$$H = \frac{F_{max}}{A} \quad \text{Equation 3.2.}$$

To calculate the elastic modulus of the sample, the slope of the initial part of the unloading curve is used,

$$\frac{dF}{dh} = \beta \left(\frac{2}{\sqrt{\pi}} \right) E^* \sqrt{A} \quad \text{Equation 3.3.}$$

Here, the expression E^* is generally called as the combined modulus. The elastic modulus of the sample (E_s) is then calculated using the following relation,

$$\frac{1}{E^*} = \frac{(1 - \nu_i^2)}{E_i} + \frac{(1 - \nu_s^2)}{E_s} \quad \text{Equation 3.4.}$$

where E_i and ν_i are the elastic modulus and the Poisson's ratio of the indent and ν_s is the Poisson's ratio of the sample. Detailed information on the analysis and modelling of the indentation process can be found in a recent review by Cheng and Cheng [120]. During the nanoindentation measurements of the coatings, the maximum depth of indentation (h_{max}) was kept less than 10% of the total thickness of the coating in order to minimize the substrate effect.

3.1.3. Structural Characterization Methods

3.1.3.1. X-ray Diffraction

In this study, a Rigaku DMAX-1200 X-ray diffractometer at the University of Windsor and a Siemens D-500 diffractometer at the GM R&D Center, both equipped with Cu K_{α} ($\lambda = 1.5406$ nm) source tube, were used for the X-ray diffraction studies of the test materials.

3.1.3.2. Raman Spectroscopy

Raman spectroscopy is a technique that uses light to obtain structural information of materials. It is the most suited method to investigate the bonding structure of the DLC coatings since X-ray diffraction provides very limited information about these materials [70]. Raman effect can be explained as follows: When a beam of light is sent to a substance, most of the light is elastically scattered, having the same wavelength as the incoming light beam. However, a small portion of the light excites the molecules in the substance and hence is scattered inelastically. The Raman effect is the shift in the energy of the inelastically scattered light from the incident light by the energies of molecular vibrations. Raman spectrum is basically the plot of the intensity of the scattered light versus energy difference between the elastically and inelastically scattered light. Detailed information on Raman effect and its analysis can be found, for example, in [121].

Raman spectra of the DLC coatings tested in this work were obtained using the spectrometer at GM R&D Center. The principle source of excitation for the Raman experiments was a diode pumped, frequency doubled Nd:YVO₄ solid state laser (Spectra Physics Millennia Vs). This laser had an emission wavelength of 532 nm. The power incident on the sample was 100 mW. In order to minimize laser induced heating, the laser was imaged onto the sample with a cylindrical lens; the typical spot size was 50 μm wide by 3 mm tall, which gave a power density of 66 W/cm^2 . The experiments were all done in a backscattered geometry, and the line focus of the laser gave good coupling efficiency to the linear input slits of the spectrometer. The scattered light from the sample was collected with an $f/1.4$ lens and focused onto the slits of a 1 m double grating scanning monochromator with a Czerny-Turner configuration (JY U-1000). The signal was detected with a cooled photomultiplier tube, selected for less than 10 dark counts per second (Hamamatsu R-943). The instrument was set with a 300 μm slit width, giving 2 cm^{-1} resolution at the diamond phonon energy (1332 cm^{-1}).

3.1.4. Surface Profilometry

A Wyko HD 3300 optical surface profilometer at the GM R&D Center was used for the characterization of the surface topographies of the tested and untested samples. This included the measurement of the surface roughness of the samples and width and depth of the wear tracks. The WYKO HD 3300 was used in the vertical scanning interferometry (VSI) mode. In this mode, unfiltered white light reflected from a reference mirror combines with the light reflected from the sample to produce interference fringes where the fringe with best contrast occurs at best focus. The device then measures the degree of fringe modulation to acquire the surface profile.

3.2. Description of the Substrate Material and the Coatings

3.2.1. M2 Tool Steel Substrates

An M2 type tool steel bar of 25 mm diameter and 3.00 m length was received in annealed condition. The nominal composition (wt.%) of M2 steel (AISI type M-2) is 0.83% C, 4% Cr, 2% V, 6% W, 5% Mo, 0.27% Mn, 0.35% Si, and the balance Fe. The M2 steel bar was first cut into 1 cm thick discs (**Figure 3.3**). Then, the discs were subjected to a heat treatment procedure that consisted of austenizing at 1200°C for 3-4 minutes followed by air cooling to 25°C and then tempering at 560°C for 120 minutes. The average hardness of the heat treated M2 steel discs was $60 \pm 2 R_c$.

The grinding of the M2 steel discs was accomplished in running water using SiC emery papers (120, 240, 400 and 600 grit). Water based diamond suspensions of 6 and 1 μm in size were used to polish the M2 steel discs. The final surface roughness of the polished M2 steel discs as measured by the optical surface profilometer was 9 nm R_a . The optical images of the microstructure of the M2 steel disc is given in **Figure 3.4**.

3.2.2. Diamond-like Carbon Coatings

3.2.2.1. 60 and 80-V Diamond-like Carbon Coatings

DLC coatings were deposited on M2 tool steel discs ($60 \pm 2 R_c$) using a Teer UDP 550 unbalanced magnetron sputtering system at the GM R&D Center. The deposition chamber of the Teer UDP 550 machine is 550 mm in diameter and 550 mm in height.

The system has two DC power supplies. The vacuum system consists of a diffusion pump and a mechanical rotary pump.

Argon of 99.999% purity was used to sputter from one Cr and two graphite targets (**Figure 3.5**). The discs were first cleaned with soap and then subjected to ultrasonic cleaning for 10 min before they were placed in the deposition chamber. Once in the deposition chamber, the discs were sputter cleaned for 30 minutes using Argon ions. The base pressure of the chamber before deposition was 1.33×10^{-4} Pa. During the deposition, the chamber pressure was kept around 0.133 Pa. First, a 0.2 μm thick Cr layer was deposited to facilitate bonding. Then, the power on the Cr target was decreased while the power on graphite targets was gradually increased to obtain a coating with a decreasing Cr content with thickness.

One set of samples was produced using a bias voltage of 60 V (60-V DLC coating) and had a thickness of 2.19 μm . The other set of coatings was deposited using a bias voltage of 80 V (80-V DLC coating) and had a thickness of 1.93 μm . The details of the deposition conditions are given in **Table 3.1**.

At an indentation depth of 50 nm, the hardness values of the 60-V DLC and the 80-V DLC coatings were measured as 7.8 and 10.0 GPa, respectively. The elastic modulus values of the 60-V DLC and the 80-V DLC coatings were 100 and 142 GPa, respectively. The surface roughness (R_a) values of the DLC coatings were measured as 34 nm for the 60-V DLC coating, and 39 nm for the 80-V DLC coating.

The Raman spectra of the as-deposited 60-V and 80-V DLC coatings (**Figure 3.6**) did not exhibit any sharp peaks, but had an unresolved broad band between 1000 and 1800 cm^{-1} , indicating that the film had an amorphous structure with mainly sp^2 type bonding. The hydrogen content of the 60 and 80-V DLC coatings is expected to be no more than a few atomic percent as no hydrogen was used during their production. Therefore, 60 and 80-V DLC coatings are defined as Cr containing, sp^2 rich, non-hydrogenated DLC coatings.

Table 3.1. Deposition parameters of the DLC coatings

	60-V and 80-V DLC	Teer Coatings Graphit-iC™
Deposition System	Teer UDP 550 Unbal. Mag. Sput.	Teer UDP 650 Unbal. Mag. Sput.
Targets	One Cr and two graphite	Two Cr and two graphite
Bias (V)	60 and 80	60
Argon flow rate (sccm)	20	10
Current on graphite target during the deposition of the top layer (Amperes)	3.5	3.5
Base Pressure (Pa)	1.33×10^{-3}	$< 2.66 \times 10^{-3}$
Deposition Pressure (Pa)	0.133	0.133
Sputter Cleaning (min)	30	30

3.2.2.2. Teer Graphit-iC™ DLC Coatings

A set of DLC coatings (Teer Coatings Graphit-iC™ DLC) was received from Teer Coatings Ltd. (Worcestershire, UK). The deposition, characterization, and some aspects of the tribological behavior of this DLC coating have been previously reported [122, 123]. A Teer UDP 650 unbalanced magnetron sputtering system that consisted of two Cr and two graphite targets was used to deposit coatings of 1.73 μm thickness following a procedure similar to those employed for the 60 and 80-V DLC coatings (**Table 3.1**). Similar to the 60-V and 80-V DLC coatings, Raman spectrum of the as-deposited Teer Coatings Graphit-iC™ (**Figure 3.6**) had a broad peak around 1500 cm^{-1} , which indicates that the film was amorphous with mainly sp^2 type bonding. Using the elastic recoil detection technique, the hydrogen content of the Teer Coatings Graphit-iC™ was measured to be 1.28 at. %. The hardness and elastic modulus values of the Teer Coatings Graphit-iC™ DLC coatings were measured as 16 and 147 GPa, respectively. The Teer Coatings Graphit-iC™ DLC coatings had a R_a value of 13 nm. This coating served as a benchmark to assess the tribological performances of the 60-V and 80-V DLC coatings and will be referred as “Graphit-iC DLC” thereafter in the text.

3.2.3. TiB₂ Coatings

TiB₂ coatings were received from Argonne National Laboratory, Argonne, IL. They were deposited on M2 tool steel discs by magnetron sputtering ion plating technique. Two TiB₂ coatings with R_a values of 16 and 83 nm were used to examine the effect of surface roughness. The thickness of the TiB₂ coating with 16 nm R_a was 4.18 μm and that of the TiB₂ coating with 83 nm R_a was 3.03 μm . XRD patterns showed that the TiB₂ coatings were crystalline as shown in **Figure 3.7.a**. The hardness and elastic modulus values of the TiB₂ coating with a R_a value of 16 nm were 43.5 and 491 GPa and those of TiB₂ coating with a R_a value of 83 nm were 33.8 and 401 GPa, respectively.

3.2.4. CrN Coatings

2.12 μm thick CrN coatings were deposited using the Teer UDP 550 unbalanced magnetron sputtering system at the GM R&D Center. Two Cr targets were sputtered using a mixture of Ar and N₂ gases (ratio of the N₂ flow rate to that of Ar was 4) to

deposit on M2 steel substrates. A Cr interlayer of 0.2 μm thickness was deposited on M2 steel substrate to facilitate bonding. The crystalline structure of the CrN coatings was confirmed by the XRD (**Figure 3.7.b**). The hardness and elastic modulus values of the CrN coatings were measured as 21.8 and 337 GPa, respectively. The CrN coatings had a R_a value of 22 nm.

3.2.5. TiN Coatings

TiN coatings of 0.79 μm in thickness were received from Chrisbo Inc (Mississauga, Ontario). They were deposited on polished M2 steel discs using cathodic arc evaporation machine. A Ti target and N_2 gas were used for the production. The base pressure of the chamber before deposition was 1×10^{-3} Pa and it was kept at 2.0×10^{-2} Pa during deposition. XRD pattern of the TiN coatings indicated that the coatings were crystalline (**Figure 3.7.c**). The hardness and elastic modulus values of the TiN coatings were measured as 13.9 and 278 GPa, respectively. The TiN coatings had a R_a value of 43 nm.

3.2.6. TiAlN Coatings

TiAlN coatings of 0.82 μm thickness were received from Chrisbo Inc (Mississauga, Ontario). They were deposited on polished M2 steel discs using cathodic arc evaporation technique. A solid Ti-Al target was used in N_2 atmosphere for the production. The base pressure of the chamber before deposition was 1×10^{-3} Pa and it was kept at 5.0×10^{-2} Pa during deposition. XRD pattern of the TiAlN coatings is given in **Figure 3.7.d**. The hardness and elastic modulus values of the TiAlN coatings were measured as 14.2 and 257 GPa, respectively. The TiAlN coatings had a R_a value of 32 nm.

3.2.7. TiCN Coatings

TiCN coatings of 0.87 μm thickness were received from Chrisbo Inc (Mississauga, Ontario). They were deposited on polished M2 steel discs using cathodic arc evaporation technique. For production, a Ti target was used in a mixture of N_2 and C_2H_2 (acetylene) atmosphere. The base pressure of the chamber before the deposition

was 1.0×10^{-3} Pa and it was kept at 1.0×10^{-2} Pa during the deposition. The crystalline structure of the TiCN coatings was confirmed by XRD (**Figure 3.7.e**). The hardness and elastic modulus values of the TiCN coatings were measured as 15.0 and 250 GPa, respectively. The TiCN coatings had a R_a value of 23 nm.

Some of the physical properties of the coatings used in this work are summarized in **Table 3.2**.

3.3. Description of 319 Al Alloy Counterfaces and other Counterface Materials

3.3.1. 319 Al Alloy Pins

Tribological behaviour of non-hydrogenated DLC coatings were investigated against 319 Al alloy because of its wide application in automotive industry. Pins of 319 Al alloy composition were made by drawing the molten alloy at 702°C into 4 and 5 mm diameter glass tubes. Following the solidification, the rods were heat treated in air to T5 condition (200°C for 8 hours). The rods were then cut to pins of 15 mm in length. One end of the each pin was rounded to have a curvature of 4 mm in diameter. The chemical composition of the alloy, determined by inductively coupled plasma-atomic emission spectrometry at the GM R&D Center, is given in **Table 3.3**. The optical images showing the microstructure of the 319 Al pins are given in **Figure 3.8**. Graff-Sargent Reagent consisting of 15.5 ml nitric acid, 0.5 ml hydrofluoric acid, 3.0 g chromium trioxide and 84.0 ml distilled water was used to etch the 319 Al samples for microstructural investigation. The average hardness of the 319 Al pins was 91 HV₁₀₀ (33.87 R_B).

3.3.2. Other Counterface Materials: Al, Cu, Ti, Al₂O₃ and WC

In addition to 319 Al, rods of Al (1100 Al, 99+wt. %), Cu (99.9+ wt. %), and Ti (99.3+wt. %) were also tested against the non-hydrogenated DLC, CrN and TiB₂ coatings. Similar to the 319 Al pins, 5 mm diameter rods of these metals were cut to pins of 15 mm in length and one end of the each pin was rounded to have a curvature of 4 mm in diameter (**Figure 3.9**). The hardness values of the Al, Cu, and Ti pins were 33.9, 110.1, and 209.4 HV₁₀₀ respectively. The optical images revealing the microstructures of the Al, Cu, and Ti pins are given in **Figures 3.10.a-c**.

For comparison purposes, Al₂O₃ (ruby sapphire type) and WC-Co balls of 3.175 mm (1/8 in.) diameter were also used in some tests. The hardness values of the counterface materials used in this work are given in **Table 3.4**.

Table 3.2. Properties of the coatings

SAMPLE	H (GPa)	E (GPa)	R_a (nm)	Thickness (μm)
Teer Coatings Graphit-iC™	16.0	147	13	1.73
60-V DLC	7.8	99	34	2.19
80-V DLC	10.0	142	39	1.93
TiB₂, 16 nm R_a¹	43.5	491	16	4.18
TiB₂, 83 nm R_a¹	33.8	401	83	3.03
CrN²	21.8	337	22	2.12
TiN³	13.9	278	43	0.79
TiAlN³	14.2	257	32	0.82
TiCN³	15.0	250	23	0.87

¹ Argonne National Lab, Argonne, IL, USA

² General Motors R & D Center, Warren, MI, USA

³ Chrisbo Co., Mississauga, ON, Canada

Table 3.3. Chemical composition (wt. %) of the 319 Al pins

% Si	% Cu	% Fe	% Mg	% Zn	% Mn	% Ni	% Ti	% Al
6	3.5	0.26	0.08	0.01	<0.01	<0.01	0.08	Balance

Table 3.4. Hardness values of the counterface materials.

Material	Hardness (HV)
319 Al	91.0
Al	33.9
Al₂O₃ (sapphire)	2300
Cu	110.1
Ti	209.4
WC-Co	1550

3.4. Pin-on-disc Tribometers

3.4.1. High Temperature Tribometer

The high temperature tribometer (CSM, Switzerland) at the University of Windsor was used for most of the pin-on-disc tests in ambient air (**Figure 3.11**). This tribometer is connected to a computer that controls the sliding speed using the number of revolutions per minute of the driving motor. The test duration can be determined as the total number of revolutions, sliding distance or time elapsed. A computer controlled heating element underneath the disc holder provides heating for the elevated temperature tests (up to 800°C).

A typical procedure for a pin-on-disc test is as follows: First the pin and disc materials are cleaned in ultrasonic acetone bath and placed in the appropriate holders. Then, the diameter of the sliding track is adjusted using the gauge. The friction arm is levelled horizontal for precise loading. The test load is applied on top of the pin holder. All test information (sliding speed, test duration, test temperature, file identification etc.) are keyed into the computer program and the test is started (**Figure 3.12**). The friction force is measured from the very small deflections of the friction arm. This tribometer is also capable of measuring the electrical contact resistance between the pin and the disc materials and the depth of the sliding track.

3.4.2. High Temperature Vacuum Tribometer

The high temperature vacuum tribometer (CSM, Switzerland) at the GM R&D Center (**Figure 3.13**) was used for the pin-on-disc tests in vacuum, various gases (Ar, He, N₂, 60 vol. % He- 40 vol. % H₂), and air with controlled humidity (85% RH). This machine is a vacuum configured version of the high temperature pin-on-disc tribometer described in the previous section. The vacuum system consists of turbo and mechanical pumps that could reach vacuum levels down to 1×10^{-5} Pa. Pumping, venting and the vertical motion of the chamber closure/lid operations are controlled via the touch panel on the front face of the tribometer control unit.

3.4.3. ISC 450 Tribometer

The ISC 450 model pin-on-disc tribometer from Implant Sciences (now Falex Co., Sugar Grove, IL, USA) was used for most of the pin-on-disc tests presented in **Chapter 4**, which were done to study the transfer behaviour of the 319 Al alloy to TiB₂, CrN, TiN, TiAlN and TiCN coatings. This machine has a heating module that enables high temperature testing up to 600°C. A plastic cover with a gas inlet was used to define the test atmosphere.

3.5. Conditions

3.5.1. Loading Conditions

A constant load of 5 N was used in all pin-on-disc tests (**Figure 3.14**). The linear sliding speed of 0.12 m/s was commonly used. This was achieved by running tests at a rotational speed of 125 revolutions per minute (rpm) on a 19 mm diameter sliding track. To investigate the effect of sliding speed, linear sliding speeds of 0.02 m/s and 0.65 m/s were also used in some tests. The linear sliding speed of 0.02 m/s was achieved using a rotational speed of 25 rpm on a 13 mm diameter sliding track. A rotational speed of 575 rpm on a 21.6 mm diameter sliding track produced a linear sliding speed of 0.65 m/s.

The total sliding distance used in a particular test depended upon the purpose of that test. For example, a sliding distance of 18 m (3×10^2 revolutions at 0.12 m/s) was used when the main focus of the test was to determine the amount of adhesion and material transfer. Longer sliding distances such as 180 m (3×10^3 rev.) and 600 m (1×10^4 rev.) were chosen when the aim was, for example, to cause a comfortably measurable amount of wear of the coating in that particular test condition.

3.5.2. Control of Test Atmosphere

An aqueous potassium chloride (KCl) solution was placed in the test chamber to create air with 85% RH [124]. For the tests under argon, helium and nitrogen, the chamber was evacuated to 3.99×10^{-3} Pa or lower before the gas was introduced. For the tests in 60% He- 40% H₂, prior to the introduction of the gas, the chamber was evacuated to 3.99×10^{-3} Pa, vented with N₂, and evacuated to the same vacuum level again to

minimize any residual air and water vapour in the chamber. Unless stated otherwise, all non-vacuum tests were performed at 1 atmosphere pressure.

3.6. Evaluation Tools and Procedures

3.6.1. Optical and Scanning Electron Microscopy, Energy Dispersive Spectroscopy

Optical microscopy of the samples was performed using the Zeiss Axiovert 25 CF inverted microscope at the University of Windsor. A scanning electron microscope (SEM, JEOL JSM-5800LV) at the University of Windsor, equipped with an energy dispersive spectroscope (EDS, Kevex Super Quantum) was used to characterize the pin and disc surfaces.

3.6.2. Quantification of the Amount of Adhesion

The following methodology was used to evaluate the material transfer from the pins to the coatings:

- 1) The wear track was examined using SEM. Two SEM images were taken from each location of wear tracks as shown in **Figure 3.15**. One image was taken in secondary electron imaging (SEI) mode and the other in backscattered electron imaging (BEI) mode.

- 2) An image analysis program (Image Pro from Media Cybernetics Inc., Silver Spring, MD) was used to determine the percentage of the area covered by adhered aluminum and debris for each image. For each sample, the reported values are the averages of the values obtained from these images. The contrast difference of the SEI images were used to differentiate the aluminum adhered to the surface from the loose debris particles. In the BEI mode, elements with larger atomic masses appear brighter than elements with smaller atomic masses. Consequently, the BEI images provided a good way to differentiate the substrate material from the adhered aluminum and the debris. The advantage of using the two imaging modes simultaneously is shown in **Figures 3.16.a & b**, which show the SEI (**Figure 3.16.a**) and BEI (**Figure 3.16.b**) SEM images of the sliding track of the M2 tool steel. The debris particles were essentially 319 Al aluminum with some degree of oxidation that occurred during transfer. They are readily distinguished from the adhered aluminum in the SEI mode, while the contrast

between the M2 substrate and the rest (adhered aluminum and debris) is more clearly defined in the BEI mode.

3.6.3. Measurement of Wear Rates

In this work, the wear rate (w) of a sample is expressed as mm^3/m i.e. the volume of material lost per unit sliding length. For a circular wear track, the volume of the material removed can be calculated by multiplying the average cross-sectional area (A_{cross}) of the wear track with the perimeter of a circle ($2 \cdot \pi \cdot R$) passing through the middle of the cross section of the wear track (**Figure 3.17**). Hence:

$$\text{Wear volume} = 2 \cdot \pi \cdot R \cdot A_{\text{cross}} \quad \text{Equation. 3.5}$$

The average A_{cross} is found by measuring the A_{cross} of the wear track at twelve different locations along the wear track using the optical surface profilometer described in section 3.1.4. As an example, the surface and cross-sectional profiles of a region of the wear track on 60-V DLC coating tested against 319 Al at 120°C are given in **Figures 3.18.a** and **b**. The wear rate is,

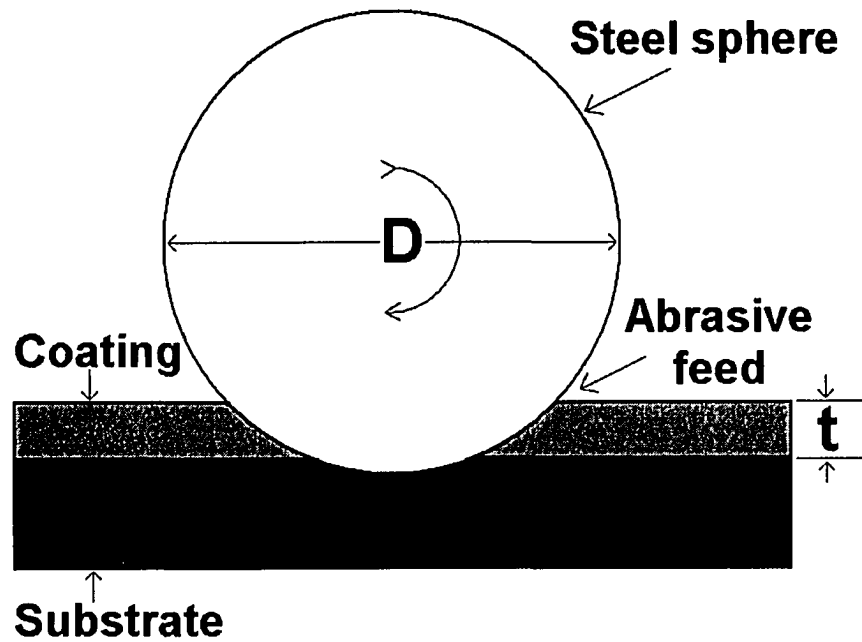
$$w = \frac{\text{Wear volume}}{\text{Sliding distance}}, \text{ where} \quad \text{Equation. 3.6}$$

Sliding distance = $2 \cdot \pi \cdot R \cdot \text{Number of revolutions}$. Then,

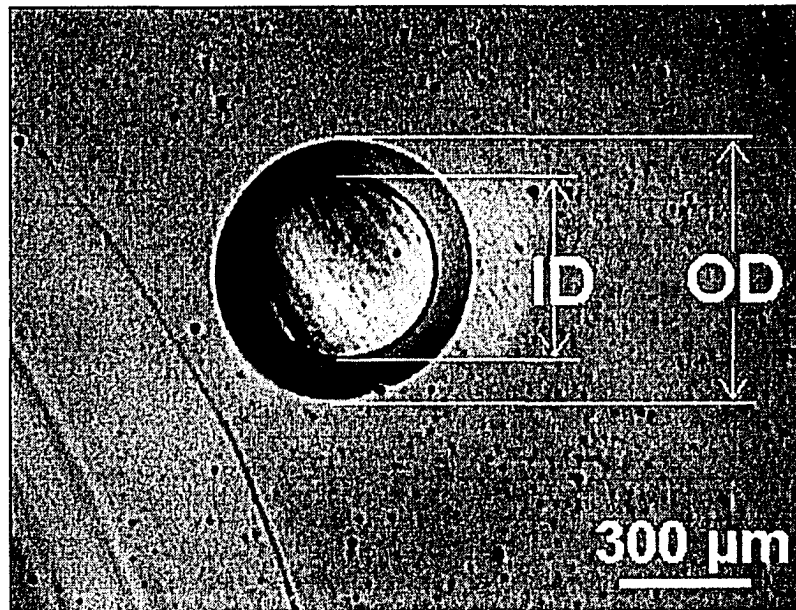
$$w = \frac{2 \cdot \pi \cdot R \cdot A_{\text{cross}}}{2 \cdot \pi \cdot R \cdot \text{Number of revolutions}}$$

Cancellation of the “ $2 \cdot \pi \cdot R$ ” terms gives,

$$w = \frac{A_{\text{cross}}}{\text{Number of revolutions}} \quad \text{Equation. 3.7}$$



a)



b)

Figure 3.1. a) Side view of the radial sectioning configuration. A hard rotating sphere is pressed against the coated sample and abrasive suspension is fed to the contact region to remove material by three-body abrasive wear. b) Top view of the resulting worn area of the diamond-like carbon coating deposited at 80 V bias (80-V DLC). The diameters of the inner and outer circles (ID and OD) are measured to calculate the coating thickness (t) using Equation. 3.1.

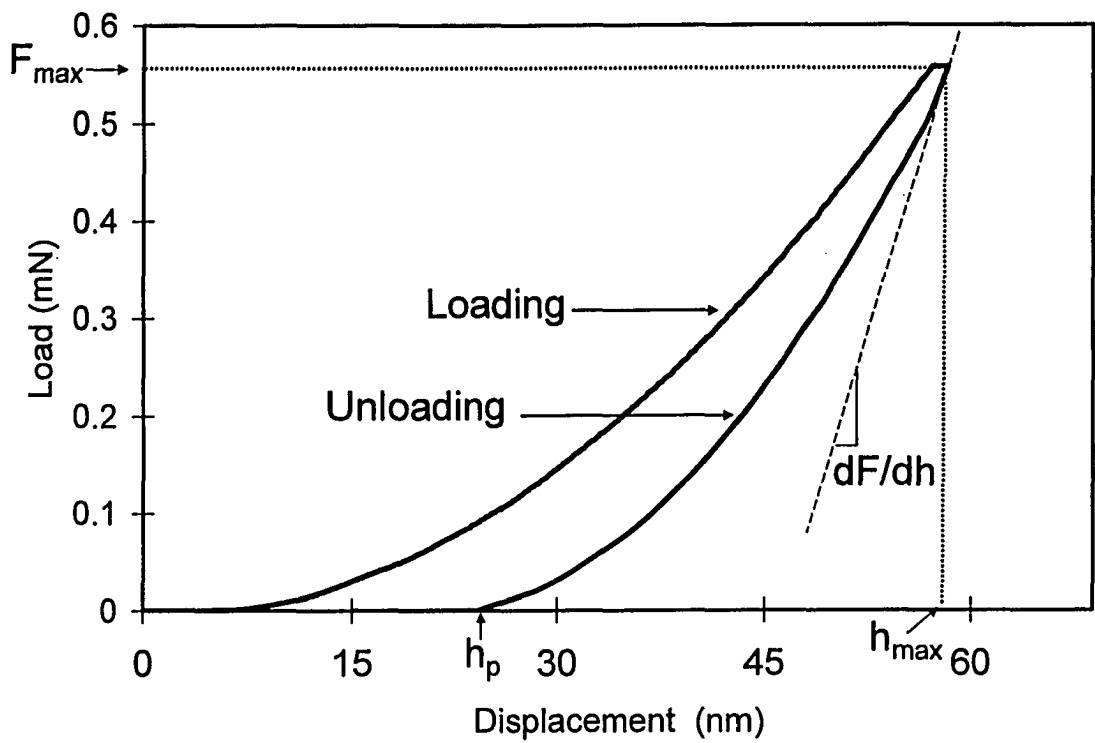


Figure 3.2. The indentation load-displacement curve for the diamond-like carbon coating deposited at 60 V bias (60-VDLC).

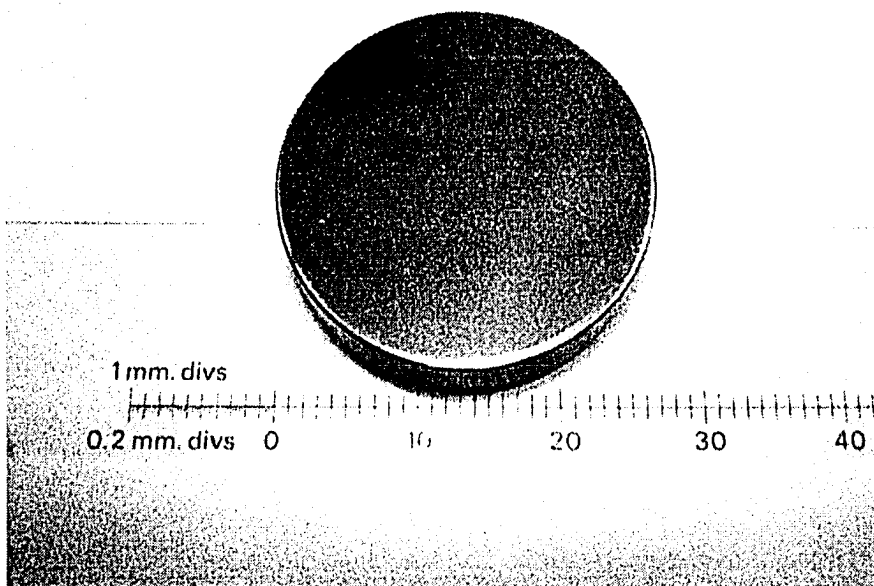
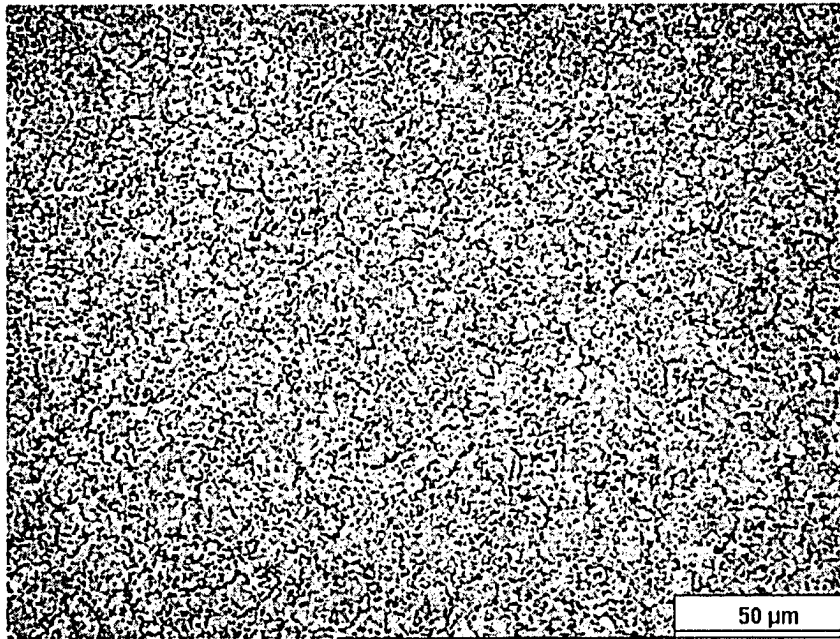
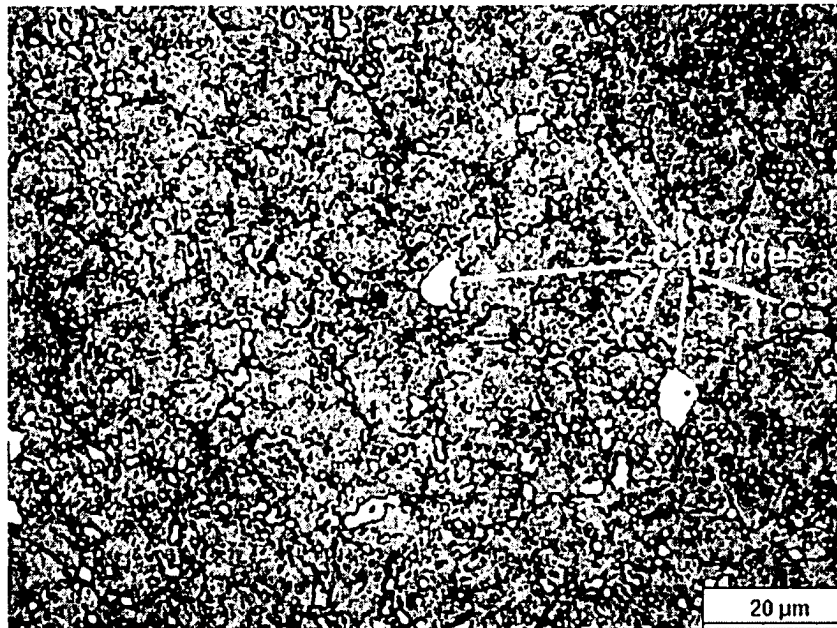


Figure 3.3. Optical image of a typical M2 tool steel disc on which the coatings used in this study were deposited. The diameter and the thickness of the M2 tool steel discs were 25.4 mm and 10 mm respectively.



a)



b)

Figure 3.4. Optical images of the microstructure of the M2 tool steel substrate. The small brighter/whiter particles are various carbides of Cr, V, W and Mo.

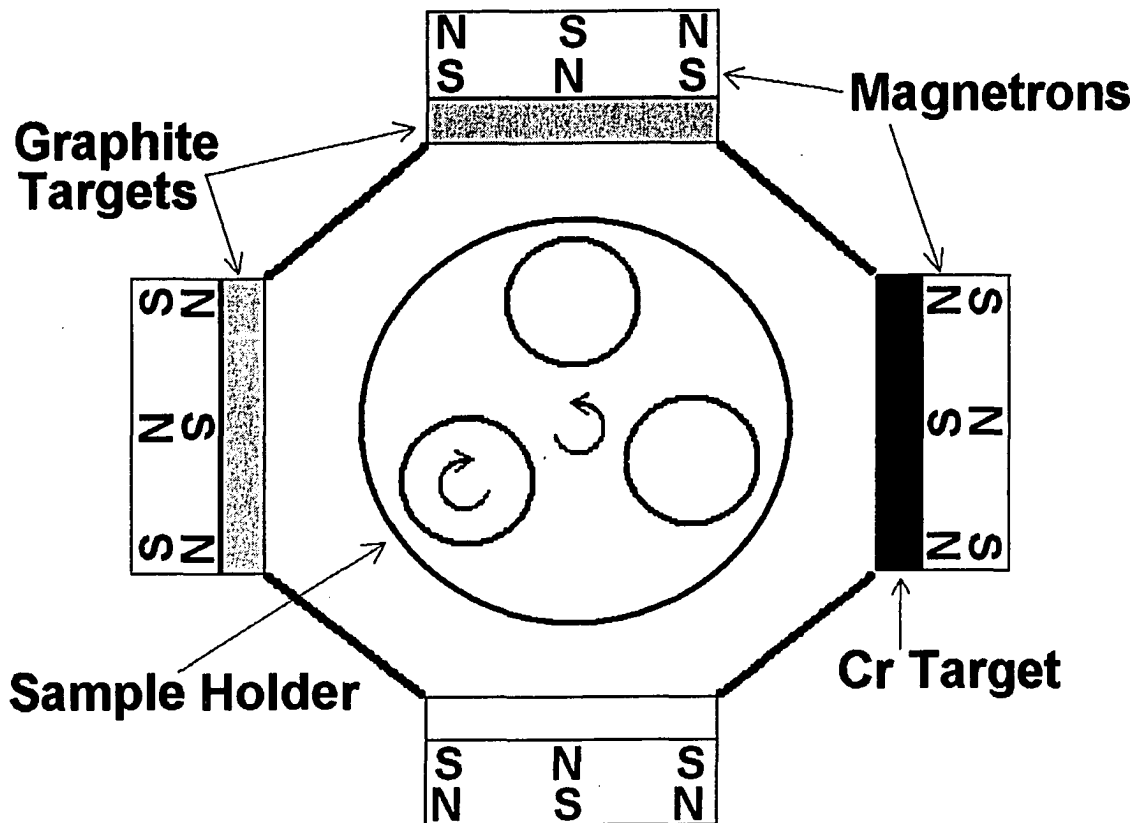


Figure 3.5. A schematic drawing of the configuration of the Teer UDP 550 unbalanced magnetron sputtering system used to deposit DLC coatings. The letters N and S denote the magnets of the sputtering units.

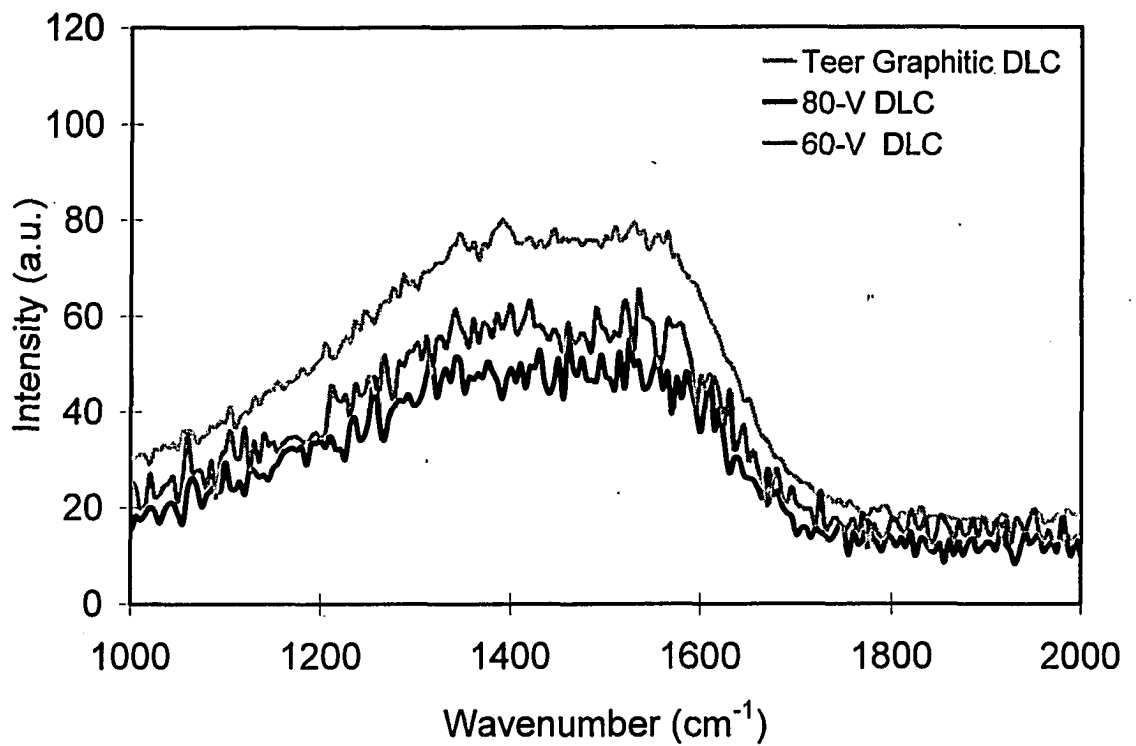


Figure 3.6. The Raman spectra of the as-deposited Teer Graphitic™, 60-V and 80-V DLC coatings.

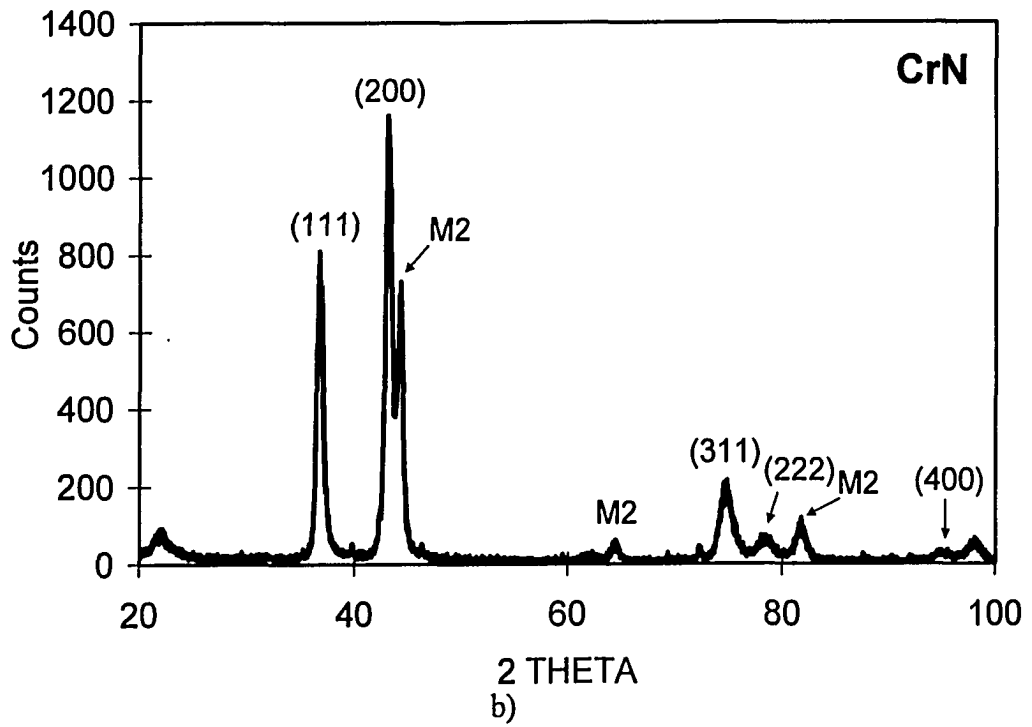
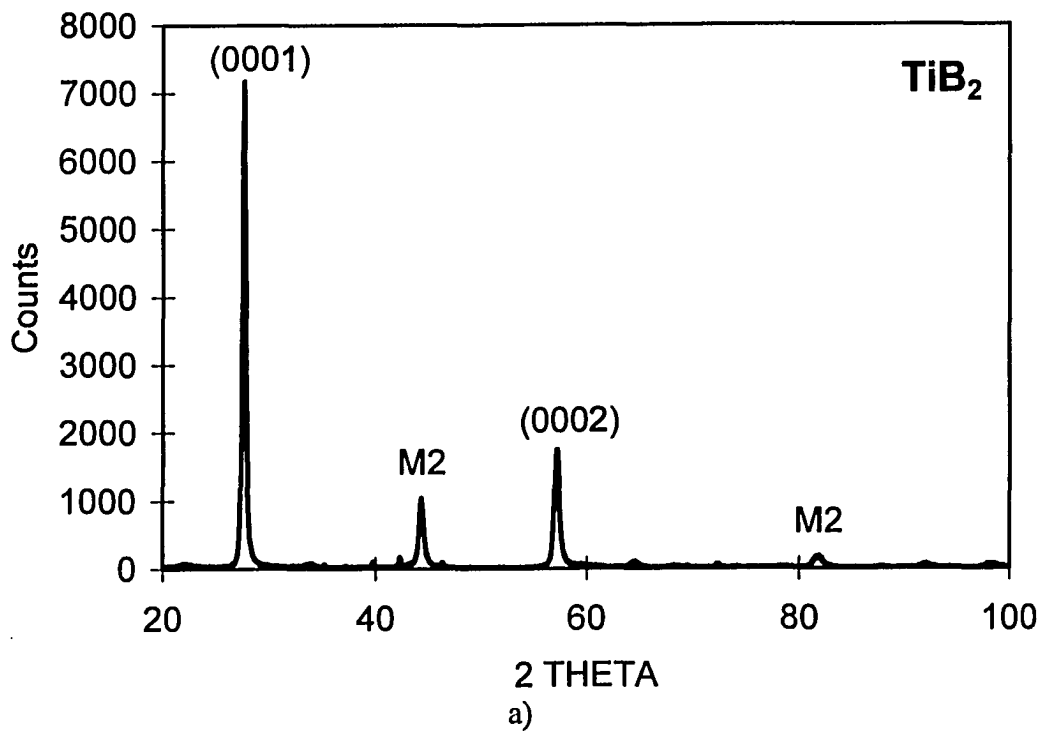


Figure 3.7. X-Ray diffraction patterns of the studied coatings; a) TiB₂, b) CrN.

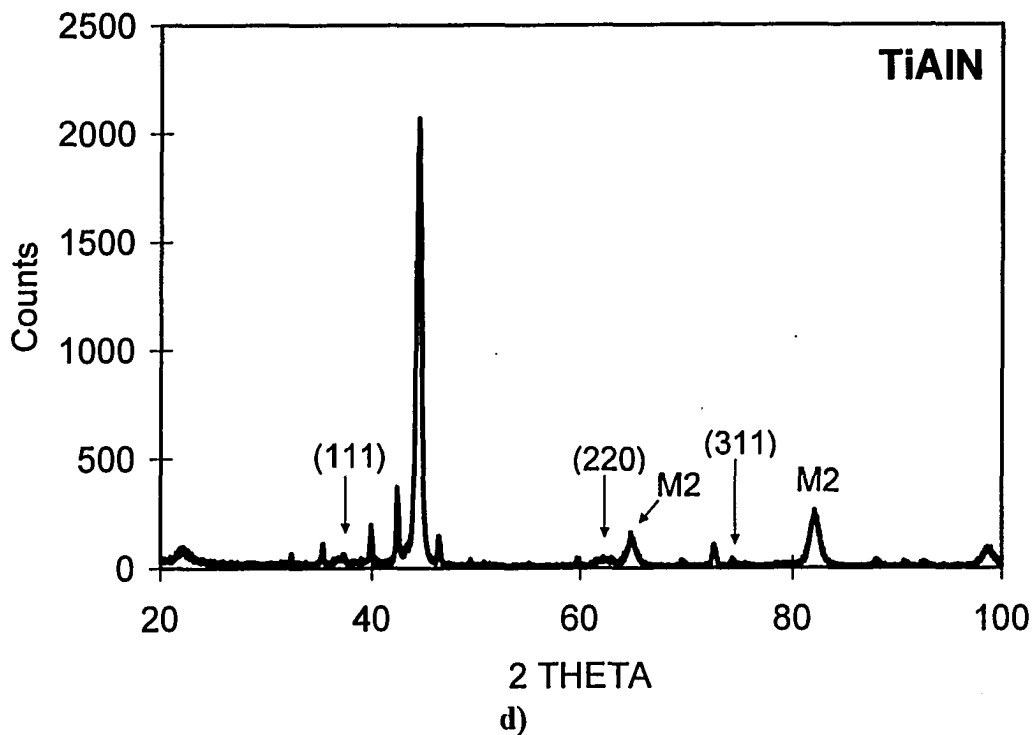
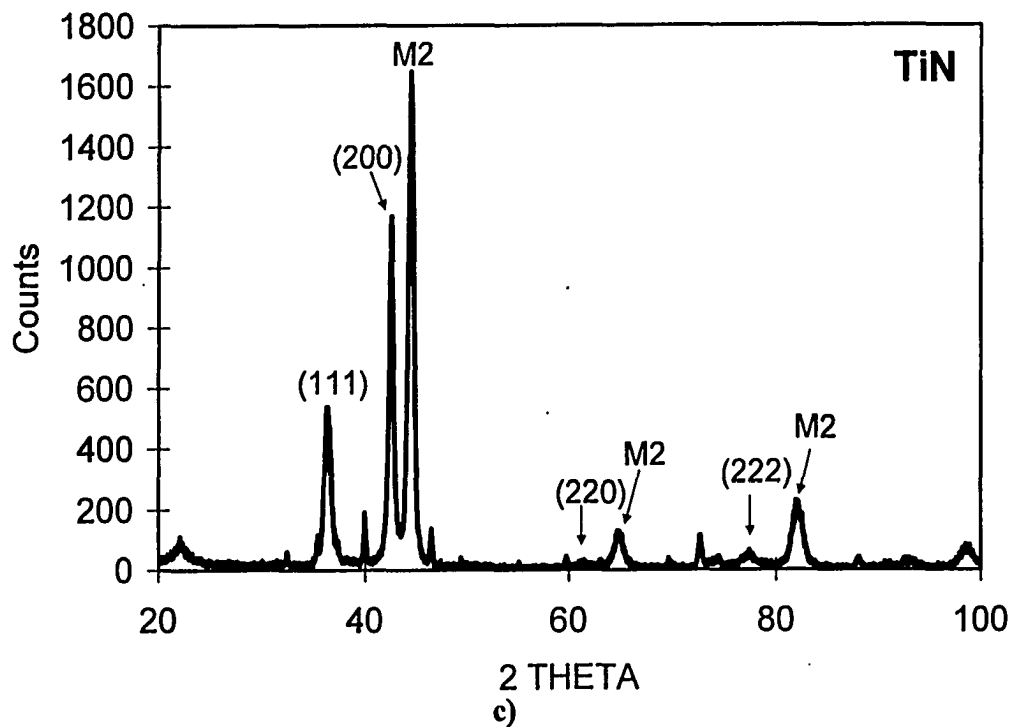
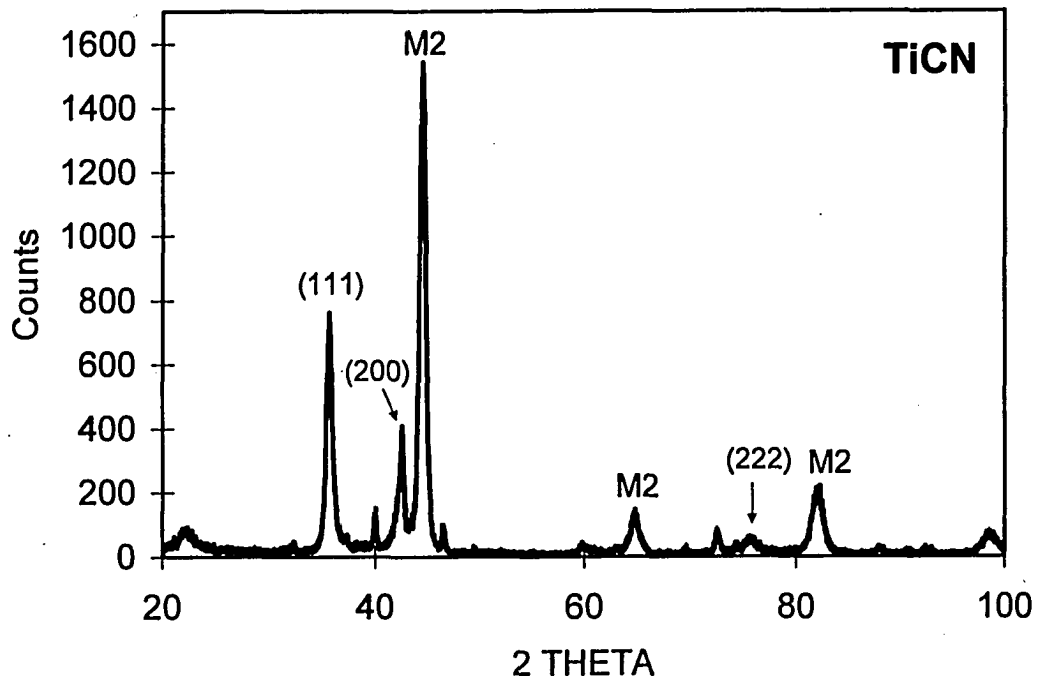


Figure 3.7. X-Ray diffraction patterns of the studied coatings; c) TiN, d) TiAlN.

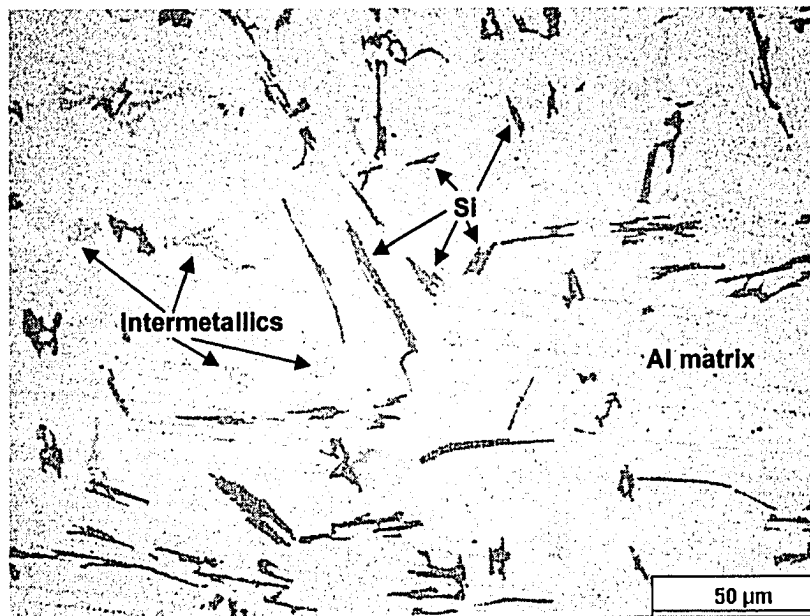


e)

Figure 3.7. X-Ray diffraction patterns of the studied coatings; e) TiCN. Some peaks that belong to M2 steel substrate are also indicated.



a)



b)

Figure 3.8. Optical images of the microstructure of the 319 Al pins.

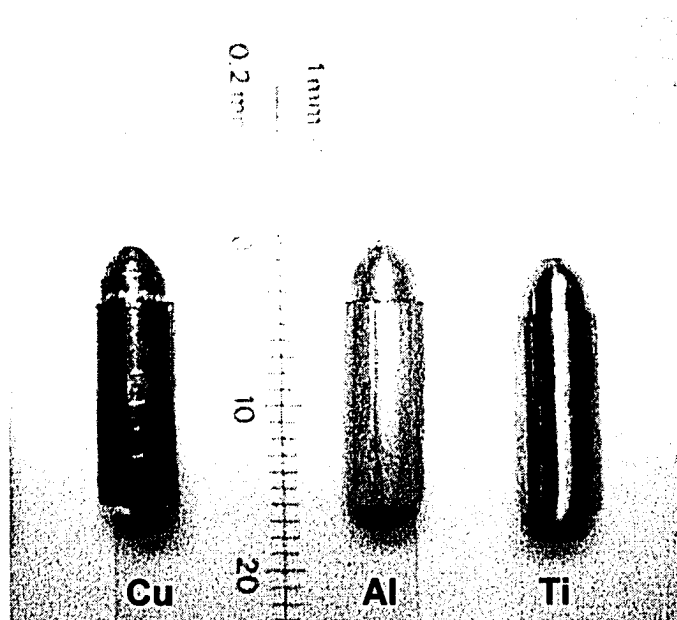
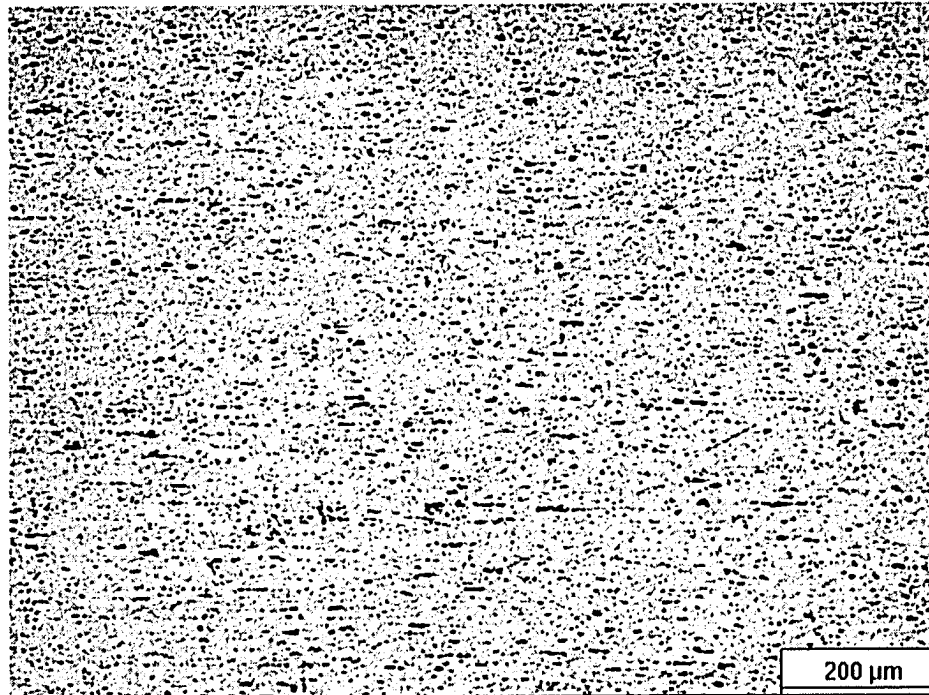
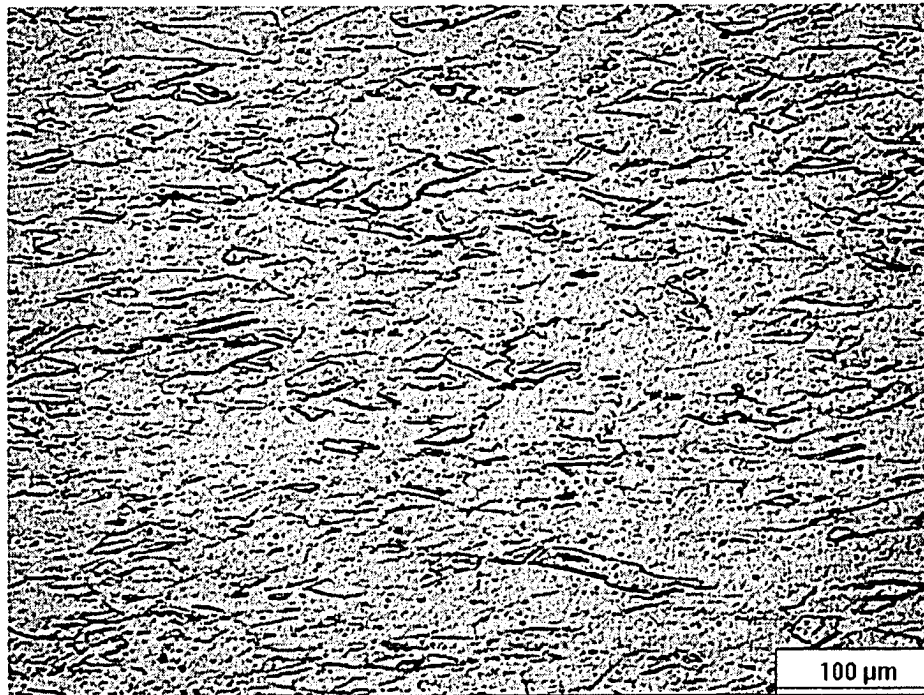


Figure 3.9. Cu, Al and Ti pins used in this study

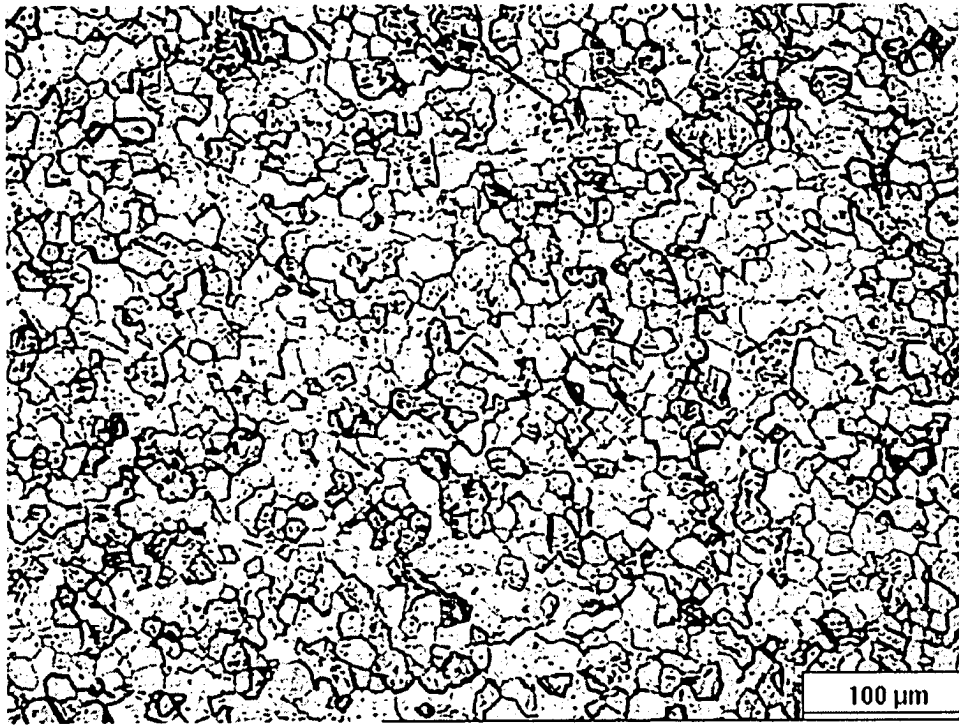


a)



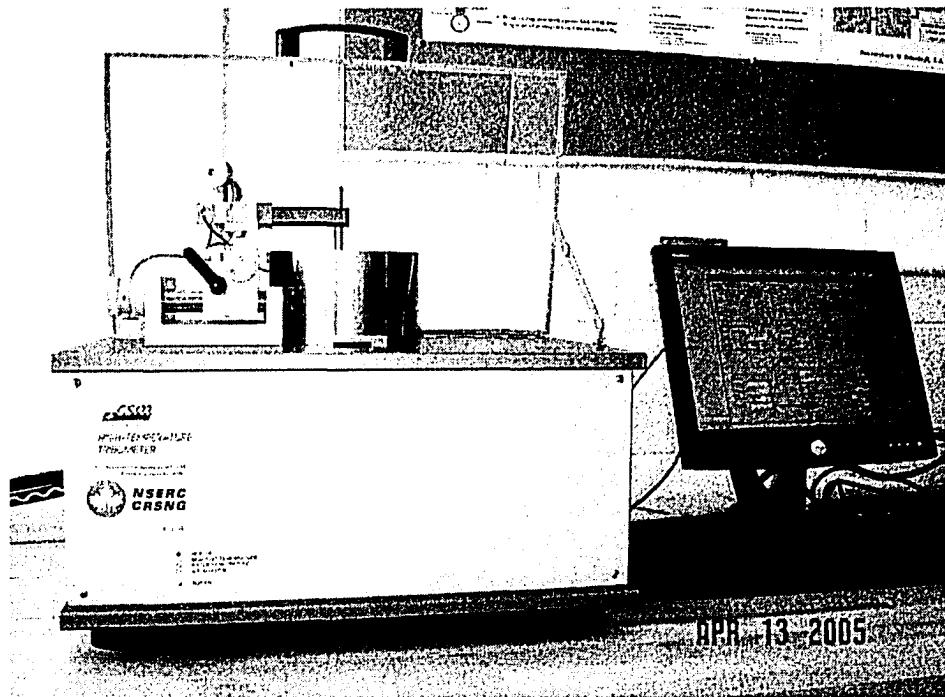
b)

Figure 3.10. Optical images of the microstructures of the a) Al, b) Cu pins.

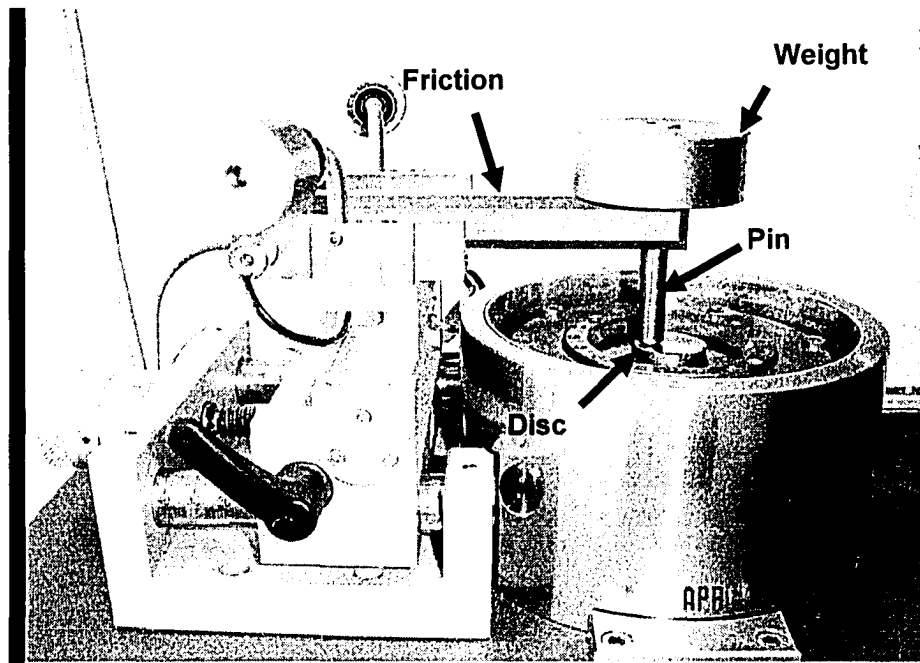


c)

Figure 3.10. c) The optical image of the microstructure of the Ti pins.



a)



b)

Figure 3.11. The high temperature tribometer (CSM, Switzerland) at the University of Windsor.

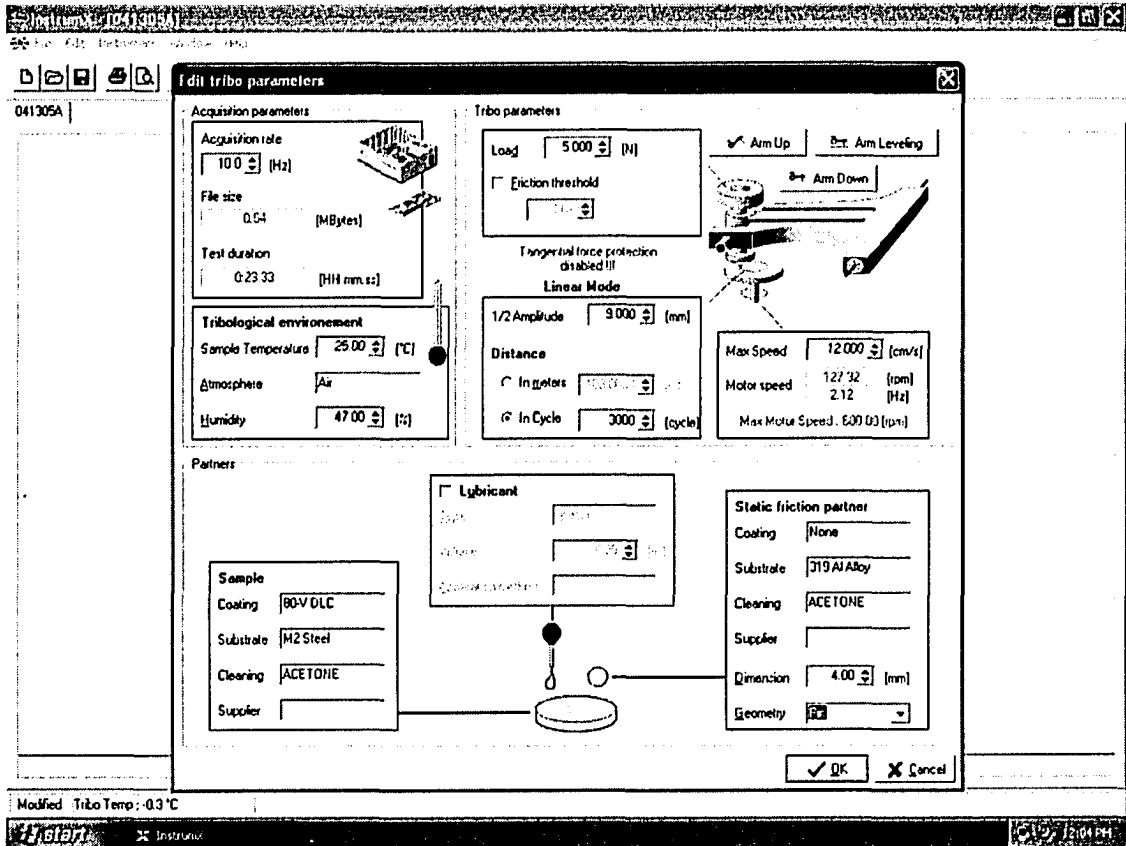
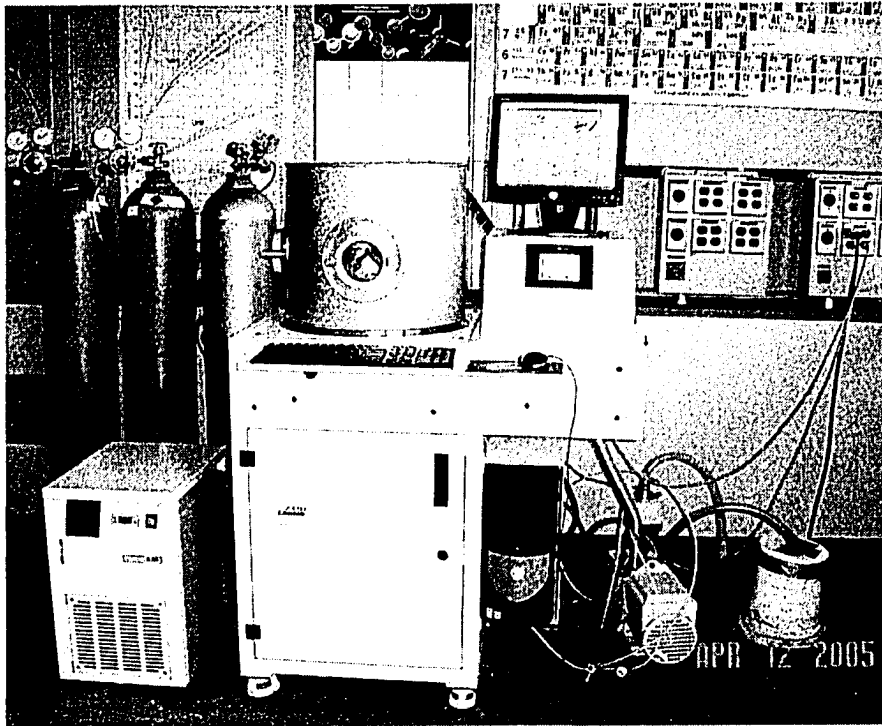
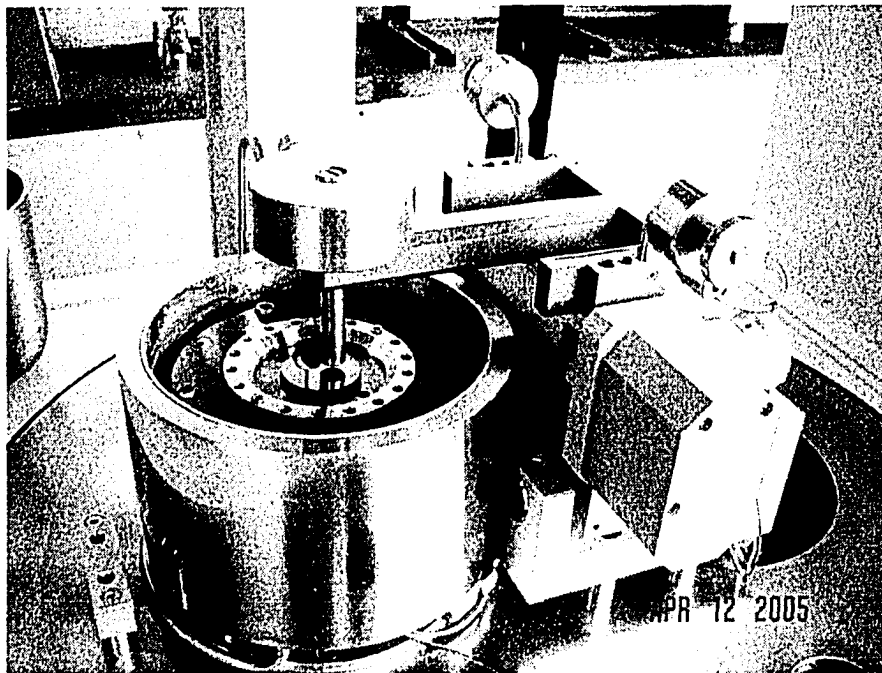


Figure 3.12. Setup screen of the computer program for pin-on-disc tests.



a)



b)

Figure 3.13. The high temperature vacuum tribometer (CSM, Switzerland) at the GM R&D Center.

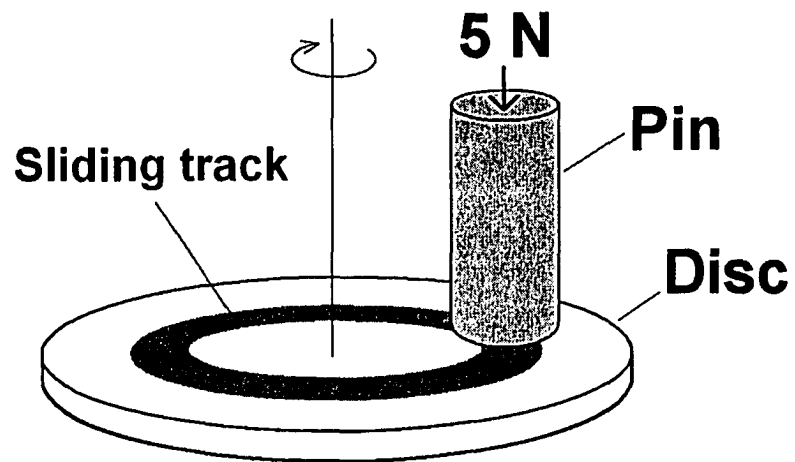


Figure 3.14. Schematic of the pin-on-disc configuration.

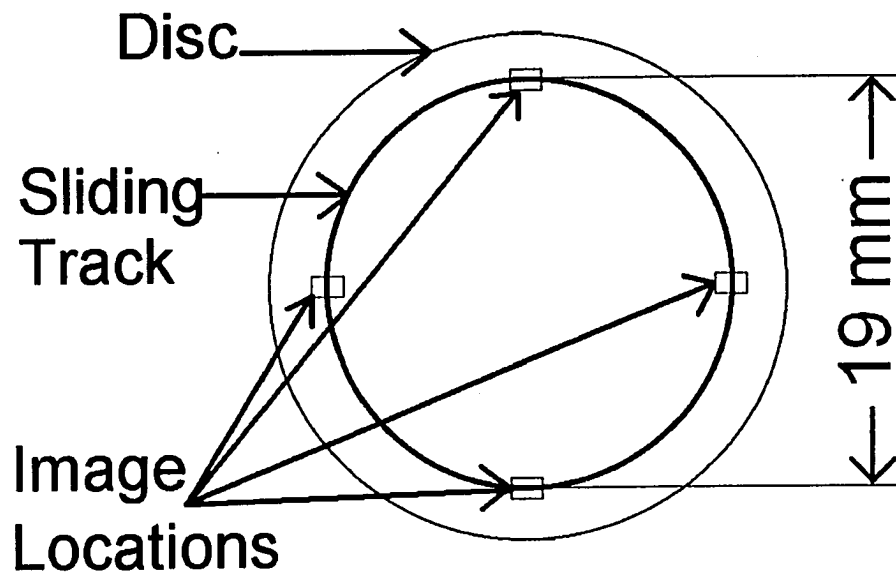
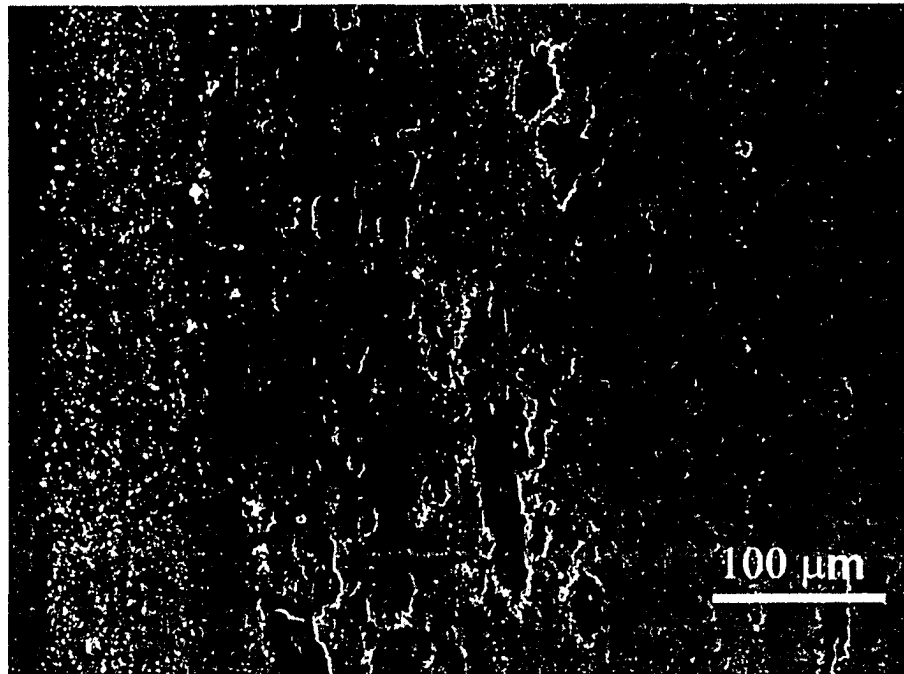
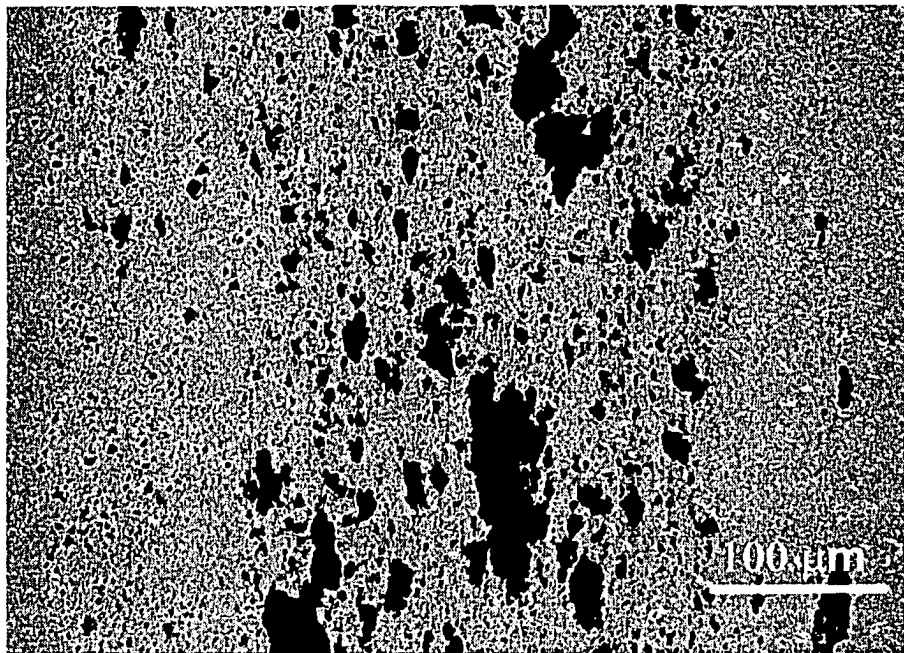


Figure 3.15. SEM images were taken at the locations shown on the sliding track.



a)



b)

Figure 3.16. a) SEI and b) BEI mode SEM images of a section of the sliding track of the M2 steel when tested in ambient air at 0.12 m/s sliding speed for 18 m. Dark particles are the transferred aluminum and the light particles are the debris.

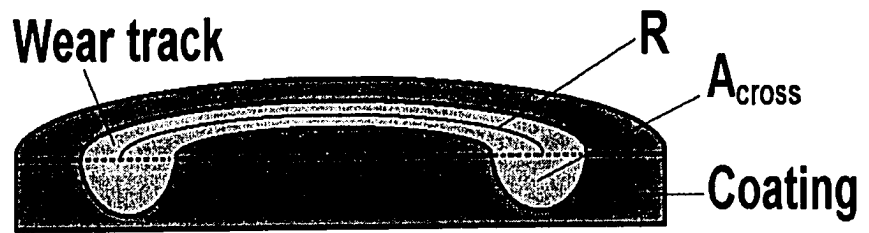
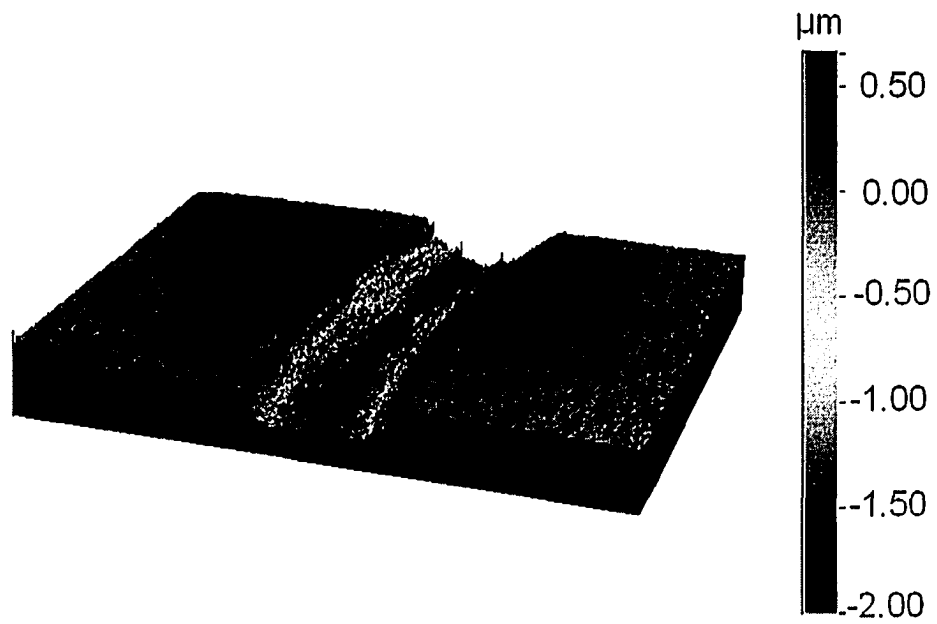
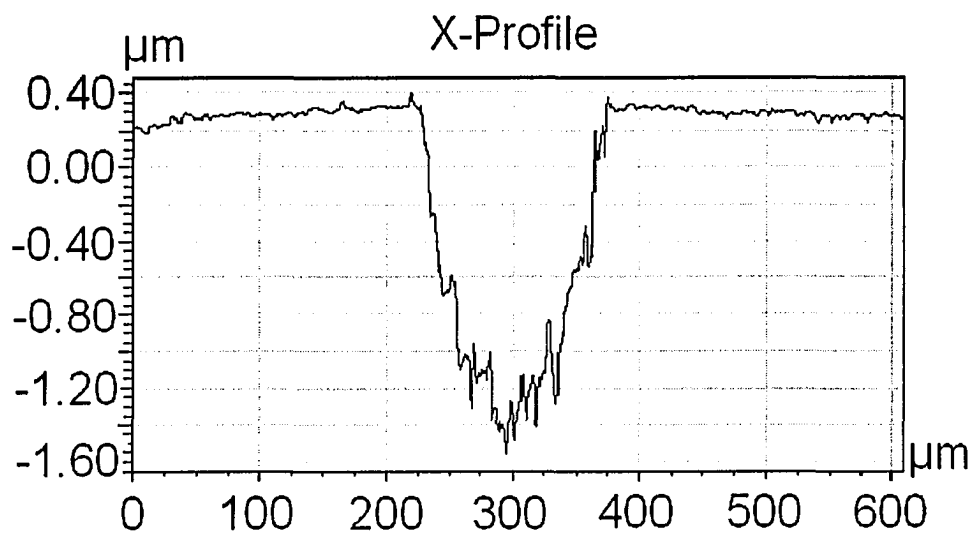


Figure 3.17. Measurement of the wear rates.



a)



b)

Figures 3.18. a) The surface, and b) the cross-sectional profiles of a region of the wear track on the 60-V DLC coating tested against 319 Al at 120°C.

CHAPTER 4

ADHESION AND TRANSFER BEHAVIOUR OF 319 Al ALLOY TO INDUSTRIAL COATINGS

In this chapter, the material transfer and adhesion phenomena during dry sliding contact between 319 Al and some industrial coatings deposited on M2 tool steel substrates were investigated using a pin-on-disc tribometer. The aim was to rank the available industrial coatings according to the adhesion tendency of aluminum to their surfaces. The tested coatings consisted of the following: 1) TiB₂, 2) CrN, 3) TiN, 4) TiCN, and 5) TiAlN. As a reference, uncoated M2 steel discs were also tested. The effects of sliding speed, sliding distance, test temperature and working atmosphere on the adhesion and transfer behaviour of aluminum to these coatings were studied. In order to focus on the initial transfer behaviour, sliding distances were kept short. The effect of surface roughness was examined using two TiB₂ coatings that have the lowest and highest R_a values among the coatings tested in this chapter; one with a R_a value of 16 nm (smooth TiB₂) and the other with a large R_a of 83 nm (rough TiB₂). The morphology of sliding tracks was examined using SEM. Following the procedure described in **Section 3.6.2**, the coatings were ranked according to the amount of aluminum transferred and the loose debris generated in each test condition.

4.1. Pin-on-disc Tests in Ambient air

Under ambient air (33-51% RH), two different test speeds of 0.12 and 0.60 m/s were employed. The details of the experimental setup and test conditions are given in **Sections 3.4.3** and **3.5.1**. The coatings were ranked according to the amount of aluminum transferred to their surfaces. The ranking of the coatings at 0.12 m/s sliding speed is given in **Figure 4.1**. TiB₂ coatings picked up the lowest amount of aluminum among the tested coatings. This was the case for both smooth TiB₂ (2.7% coverage) and rough TiB₂ (3.4% coverage). **Figures 4.2.a** and **b** show the SEM images of the sections of the sliding tracks of TiB₂ coatings with 16 and 83 nm R_a respectively. The wear tracks were covered by loose debris and aluminum adhered. The EDS analyses (**Figures 4.3.a-c**) showed that both the loose debris and the adhered aluminum pieces were significantly oxidized. The

average size of the debris particles was in the vicinity of 3 μm . The TiB_2 coatings were followed by TiCN (5.7%) and uncoated M2 steel (12.2%) in terms of increasing amount of aluminum adhered to their surfaces. TiAlN (23.5%), TiN (24.7%) and CrN (36.4%) picked up more aluminum than the uncoated M2 steel. The wear track of the CrN coating was covered with the largest amount of aluminum (**Figures 4.4.a and b**). The adhered Al pieces had considerable oxygen content as verified by the EDS analysis given in **Figure 4.4.c**.

The TiB_2 and TiCN coatings differed from the rest of the tested materials in terms of the amount of oxidized loose debris generated on the coated surfaces as shown in **Figure 4.1**. For these two coatings, the amount of debris generated on their surfaces exceeded the amount of aluminum transferred, whereas for the other coatings the amount of the debris was always less than the amount of aluminum adhered. It can be noted that for TiN and CrN, which were the two coatings that showed the largest amount of aluminum transfer, the amounts of loose debris formed on their contact surfaces were the smallest (**Figure 4.1**). The mechanism of debris generation will be discussed in **Section 4.5.1**.

4.2. Effect of Speed

When the sliding speed was increased from 0.12 m/s to 0.60 m/s, it is observed that the TiB_2 coatings once more picked up the least amount of aluminum regardless of the surface roughness (1.8% coverage for the smooth TiB_2 coating and 1.3% for the rough TiB_2) coating. A comparison of the coating surface areas covered by transferred aluminum at these two speeds is given in **Figure 4.5**. As shown in **Figure 4.5**, TiB_2 coatings were followed by the TiCN (2.2%), TiAlN (6.2%), TiN (6.6%), M2 steel (8.7%) and CrN (15.1%) coatings in increasing order in the amount of aluminum transferred to their surfaces. The amount of aluminum transferred decreased sharply compared to 0.12 m/s for all materials. For example, for the TiAlN coating, the percentage of the contact area covered by aluminum decreased from 23.5% to 6.2%. For all test materials, the amount of oxidized loose debris generated also decreased considerably with increasing sliding speed as shown in **Figure 4.6**. The effect of sliding speed on the mechanisms of adhesion, material transfer and debris generation will be discussed in **Section 4.5.2**.

4.3. Pin-on-disc Tests in Argon

Under the argon atmosphere, the TiB₂ coating with smaller R_a picked up the least amount of aluminum (0.7%), followed by TiCN (1.7%), CrN (3.5%), rough TiB₂ (6.8%), TiN (6.8%), TiAlN (7.7%), and M2 steel (14.8%) as shown in **Figure 4.7**. More aluminum was transferred onto the M2 steel compared to other test conditions. The CrN coating picked up much less aluminum compared to the ambient condition (36.4% vs. 3.5%). For all materials tested, the amount of debris generated under the argon atmosphere was also less than that in ambient air (**Figure 4.8**).

Figures 4.9.a-g show the COF curves of the samples tested under argon and ambient air. It was observed that the COF curves recorded in argon generally had less fluctuation than those in ambient air.

4.4. Pin-on-disc Tests at 160°C

When the test temperature was increased to 160°C, it was observed that the uncoated M2 steel picked up the lowest amount of aluminum (2.6%) (**Figure 4.10**). The TiB₂ with 83 nm R_a ranked the second with 3.8% aluminum coverage. The other coatings ranked in the following order in terms of contact area covered by aluminum: TiCN (6.0%), CrN (6.2%), smooth TiB₂, (6.9%) and TiN (7.7%). The largest amount of aluminum transfer occurred to the TiAlN surface (9.9%). Except for the TiB₂ and TiCN coatings, the amount of aluminum adhered to the contact surfaces of the coatings was less than that at room temperature (**Figure 4.10**).

4.5. Discussion

4.5.1. Aluminum Transfer and Debris Generation under Ambient Atmosphere

The very small amount of aluminum transfer to the TiB₂ surface can be related to its chemical inertness to aluminum [125, 126]. The reduced tendency of aluminum to adhere to TiB₂ was also observed by Berger and his colleagues [64-66] when they studied material transfer tendency of AA7075 aluminum alloy against TiB₂, TiN, TiAlN, and TiCN coated cylindrical samples (see **Section 2.2.2** for the reviews of these studies). There was either little [64] or no [65] aluminum adhered to the surface of TiB₂ coated cylinders. Other coating surfaces exhibited high amounts of aluminum transfer as well as

higher coefficients of friction. Also, the authors did not detect any wear of TiB_2 when it was tested against the AA6063 aluminum alloy at 550°C under argon atmosphere using a block-on-ring machine [66].

Considering the nitride coatings in **Figure 4.1**, it is evident that TiCN behaves differently than TiAlN, TiN and CrN. The relatively small amount of aluminum transfer to the surface of TiCN compared to the others could be attributed to the presence of carbon.

Formation of oxidized loose debris was the characteristic of the pin-on-disc tests in air with humidity regardless of the coating tested against 319 Al. The mechanism of debris formation could be described in the following way: on each rotation of the coated disc a certain amount of material transfer occurs from the tip of the aluminum pin to the surface of the coating. When the pin reaches the same point at the next rotation, one of the three events may occur. Namely, i) more aluminum can stick on the top of the previously adhered aluminum, or ii) the adhered piece can back-transfer to the pin, or iii) the pin can remove the previously transferred aluminum, forming loose debris. Therefore, the source of the debris could be attributed to the material that was previously transferred to the coating surface. This idea was first proposed by Kerridge and Lancaster [12], and later used by the others [23, 27]. Kerridge and Lancaster [12] studied the transfer and wear of brass against a hard metal surface using radioactive tracers. They concluded that the wear process occurred in two steps: the transfer of metal from the wearing surface to the opposing surface and the formation of wear debris from the transferred layer on the opposing surface.

Based on the explanation provided by Kerridge and Lancaster [12] on the debris formation mechanism, an argument can be proposed to explain as to why the amount of debris formed was very small for the CrN coatings compared to the amount of aluminum adhered to its contact surface (**Figure 4.1**). On the contact surface of CrN, the aluminum particles transferred remained intact as opposed to turning into loose debris. This behavior was in contrast with that of the TiB_2 , which as previously stated is inert to aluminum, and that of TiCN, in which carbon may serve to restrict adhesion. Consequently, the bonding between the adhered aluminum and CrN coating should be relatively strong. Unfortunately, at the present time our knowledge on the composition

and properties of the interface between CrN and the adhered aluminum particles is very limited. A thin layer (1-2 nm) of aluminum oxide (Al_2O_3) always forms on the surface of the aluminum in the presence of oxygen in the atmosphere. On the other hand, aluminum hydroxide ($\text{Al}(\text{OH})_3$) forms on top of this layer when water vapour is present [127]. Therefore, it is possible that a bond is formed between the CrN coating and the aluminum hydroxide or aluminum oxide compounds on the surface of aluminum rather than between CrN and aluminum.

As shown in **Figures 4.9.a-g**, all materials exhibited large fluctuations in the measured values of the COF during sliding in ambient air. The fluctuations in each curve may be due to the debris generation, and back and forth material transfer between the aluminum pin and the coated disc, which involve chemical reactions with the environment, mainly oxidation of the surfaces and the transferred material [64].

4.5.2. Effect of Sliding Speed on Aluminum Transfer and Debris Generation

The decrease in the amount of aluminum transferred to the surfaces of the coatings with increasing sliding speed can be explained by; **i)** the dynamics of the stick-slip behaviour, and **ii)** kinetics of the interaction of the surfaces with the reactive gaseous species in the test environment. As the test speed increases, the probability of sticking should decrease because the length of contact time spent between the pin and any given point on the sliding track decreases. As mentioned in the **Section 2.1.1.**, Diss and Brendle [21] reported a decrease in the amount of material transferred with an increase in the test speed in their study of the transfer of graphite to steel. They attributed this inverse relationship to the kinetics of water adsorption on the sliding track. It was suggested that when the pin travels through a point in the sliding track, it removes the species (water) adsorbed on the surface. Once the pin passes over a certain point, the adsorption begins again and continues until the next visit of the pin. Increasing speed decreases this exposure time and hence less water is adsorbed on the surface. Since adsorbed water on the surface is thought to promote material transfer [43], the amount of material transferred should decrease as the amount of water adsorbed decreases.

4.5.3. Effect of Atmosphere on Aluminum Transfer and Debris Generation

More aluminum was transferred onto the M2 steel surface under argon compared to the test in ambient air (14.8% vs. 12.2%) (**Figure 4.7**). This reveals the positive role of the surface oxide layers on the steel surfaces in reducing the material transfer.

The amount of debris generated under argon atmosphere was also less than that in air for all materials tested (**Figure 4.8**). It can be stated that in general, reducing the oxygen and water vapour in the tribosystem caused a decrease in the amounts of debris formation and the aluminum adhesion to the surface. As shown in **Figures 4.9.a-g**, the COF curves of the samples tested under argon atmosphere were smoother compared to those obtained in ambient atmosphere. This is because under the argon gas atmosphere, there was less environmentally assisted chemical interaction between the sliding pairs. To elucidate this idea, the BEI SEM images of the contact areas of the 319 Al pins, which were tested against TiCN coating under ambient air and under the argon gas are given in **Figures 4.11.a** and **b** respectively. Considering that the BEI SEM images reflect the atomic mass differences so that the light elements appear darker, the darker areas in **Figures 4.11.a** and **b** indicate the presence of oxygen in aluminum. Contact area of the pin tested in ambient air (**Figure 4.11.a**) is darker than that tested under argon gas (**Figure 4.11.b**). Therefore, it is reasonable to conclude that less oxygen was gathered on the contact area of the pin tested under argon gas. The EDS spectra (**Figures 4.12.a-d**) obtained from the locations indicated on the SEM images (**Figures 4.11.a** and **b**) show the presence of oxygen and titanium on the contact surface of 319 Al pin. Higher oxygen to aluminum signal ratios, 0.098 at location 1 and 0.096 at location 2, were obtained for the pin tested in ambient air compared to that tested in argon gas (0.061 at location at 3 and 0.01 at location 4). Hence, the presence of smaller amount of oxygen on the contact surface clearly indicated that there was less interaction of the sliding surfaces with the environment under the argon atmosphere.

4.5.4. Effect of Temperature on Aluminum Transfer and Debris Generation

Compared to 25°C, the sharp decrease in the amounts of material adhered to the surfaces of M2 steel, TiAlN, TiN and CrN coatings at 160°C is thought to be related with the change in the water adsorption behaviour of these materials. With increasing temperature, the amount of water staying adsorbed on the surfaces of the coatings

decreases [139]. Since the previous tests in ambient air and argon showed that water vapour and oxygen promote the adhesion of Al to these materials, the less amount of adhesion at 160°C should be due to the less amount of adsorbed water on the coating surfaces at this temperature.

4.5.5. Effect of Surface Roughness on Aluminum Transfer and Debris Generation

No correlation could be established between the surface roughness of a coating and the amount of aluminum transferred to its surface. For example CrN and TiCN coatings had similar surface roughness values of 22 and 23 nm R_a respectively, as shown in **Table 3.2**. However, the percentage of the area covered by aluminum at 18 m of sliding at 0.12 m/s sliding speed in ambient air was 36% and 6% respectively.

Somewhat surprisingly, TiB₂ coatings with very different surface roughness values (16 and 83 nm R_a) picked up almost the same amount of aluminum namely, 2.7 and 3.4%, at the end of 18 m of sliding in ambient air. The transfer behaviour of 319 Al to the TiB₂ coatings with two different R_a values was investigated in more detail to gain more insight about the role of surface roughness. **Figure 4.13** shows the change in the area covered by the aluminum alloy as the number of revolutions increased from 50 to 1000 for smooth and rough TiB₂. As the number of revolutions increased from 50 to 300, corresponding to sliding distances of 3 m to 18 m, the amount of aluminum picked up by the TiB₂ coating with the low R_a increased only slightly from 1.2% to 2.7% (**Figure 4.13**). The surface morphology of this coating tested for 50 rotations was almost featureless as shown in **Figure 4.14.a**. The rough TiB₂ coating showed an interesting behaviour. When it was tested for 50 revolutions, about 60% of the sliding track was covered with a thin layer of aluminum as shown in **Figures 4.14.b and c**). However, after testing for 300 revolutions, only 3.4% of the track was covered with aluminum (**Figure 4.2.b**). Therefore, aluminum particles, which were initially transferred to the coating were released and turned into loose debris as the test continued from 50 to 300 rotations. It is obvious that the cause of the initial large material transfer was the high surface roughness of the TiB₂ coating. Since the bonding between the TiB₂ coating surface and the aluminum is weak, the adhered thin layers of aluminum were turned into loose debris

particles as the sliding continued from 50 to 300 revolutions. At the end of 300 revolutions, the percentage of the area covered by debris was 7.1% for the rough TiB₂.

The COF curves of the tests mentioned above also indicate this interesting behaviour (**Figures 4.15.a & b**). For the rough TiB₂ coating, the initial friction COF of 0.5 dropped to 0.30-0.36 after 70 revolutions (**Figure 4.15.a**). It then started to increase and reached 0.6-0.8 at 300 revolutions, which is similar to the COF of smooth TiB₂ (**Figure 4.15.b**) at the same number of revolutions. At this point, the surfaces of both smooth and rough coatings were covered by similar amount of aluminum (2.3-3.5 %). The type of COF dependence depicted for smooth and rough TiB₂ at 0.12 m/s was also observed for the tests performed at a higher velocity of 0.60 m/s and those at 160°C.

4.6. Summary and Remarks

In general, the TiB₂ and TiCN coatings exhibited the least amount of aluminum transfer to their surfaces compared to the other coatings (CrN and TiN, TiAlN). Some of them performed worse than the uncoated M2 steel including TiN and CrN that exhibited the largest amount of aluminum transfer. However, the amount of loose debris generated on the surfaces of these two coatings was small. Increasing the sliding speed from 0.12 to 0.6 m/s led to a decrease in the amount of aluminum transferred to the surfaces of all the coating tested.

Increasing the test temperature to 160°C did not significantly change the amount of aluminum transferred to TiB₂ and TiCN coatings. However TiN, TiAlN, CrN and M2 steel picked up significantly less aluminum compared to that at room temperature.

When tested under argon atmosphere, all coatings with the exception of TiB₂ exhibited a sharp decrease in the amount of aluminum adhered to their surfaces. This suggested that the interaction of oxygen and water vapour with 319 Al and these coatings at the sliding interface promoted aluminum adhesion to these coatings. Debris formation mainly occurred in ambient air but not in an argon atmosphere.

The amount of aluminum transfer to the TiB₂ coating was a weak function of the environment. This behaviour was attributed to the high chemical stability of TiB₂. The surface roughness played a critical role in aluminum transfer in the early stages of sliding

of TiB₂. The TiB₂ coating with a higher surface roughness had more aluminum transfer to its surface.

4.7. Outlook

The tests presented in this chapter showed that although there are significant differences among the coatings tested, none of them totally prevented aluminum adhesion and transfer to their surfaces. These observations suggested that the coatings studied in this part of the work were not the most promising ones for implementation as tool coatings for dry machining of aluminum. As anticipated, drilling of 319 Al alloy blocks using drills bits coated with these coatings at the GM R&D Center did not improve the tool life significantly [128]. As a result, the focus of the study were directed to a new potentially promising class of coatings namely, diamond-like carbon (DLC) coatings.

In ambient conditions, transfer of aluminum to the surfaces of DLC coatings is generally not observed during dry sliding, which makes them more promising compared to the coatings studied in this chapter. The studies reviewed in **Section 2.3** also indicate that carbon based coatings including DLC carry the highest potential to be implemented as tool coatings for dry and MQL machining of aluminum alloys.

As described in the **Section 2.4**, the tribological behaviour of DLC coatings varies enormously depending on their sp²/sp³ bond structure, hydrogen and dopant content. The information in open literature on the tribological performance of DLC coatings against aluminum is very limited. In addition, some of published studies lead to confusion due to the incomplete characterization of tested DLC coatings in terms of, for example, hydrogen content. Therefore, the need for a systematic investigation of the tribological behaviour of well defined DLC coatings against aluminum was clear. **Chapter 5**, will present a comprehensive investigation of the tribological behaviour of DLC coatings against aluminum.

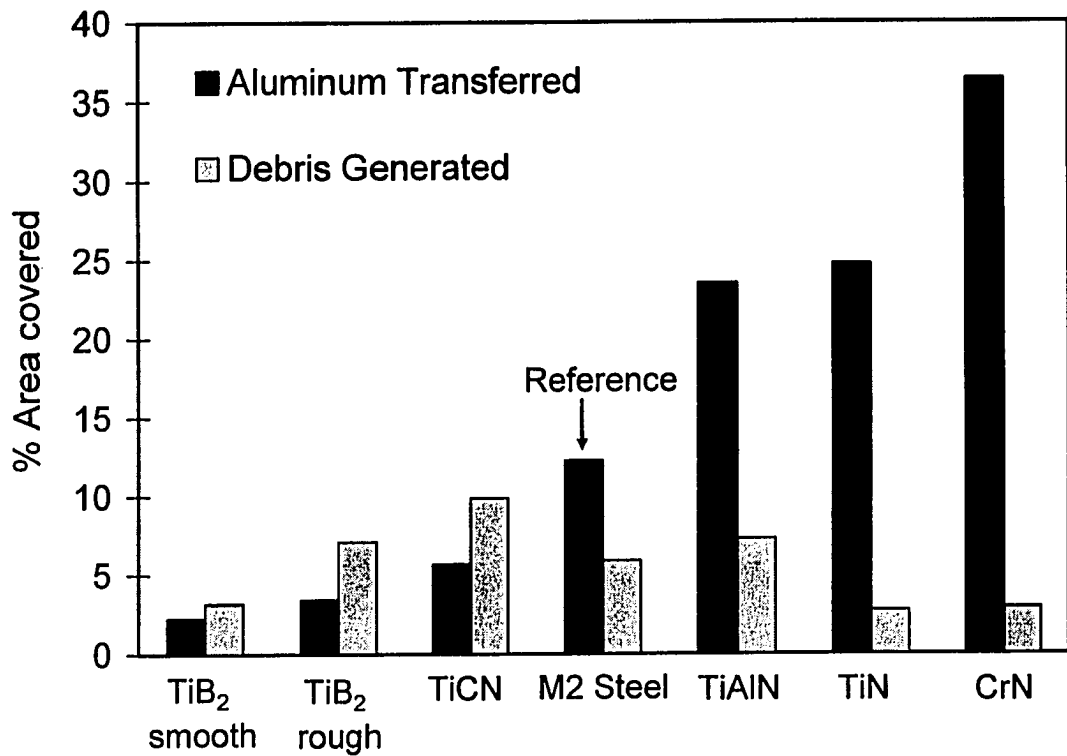
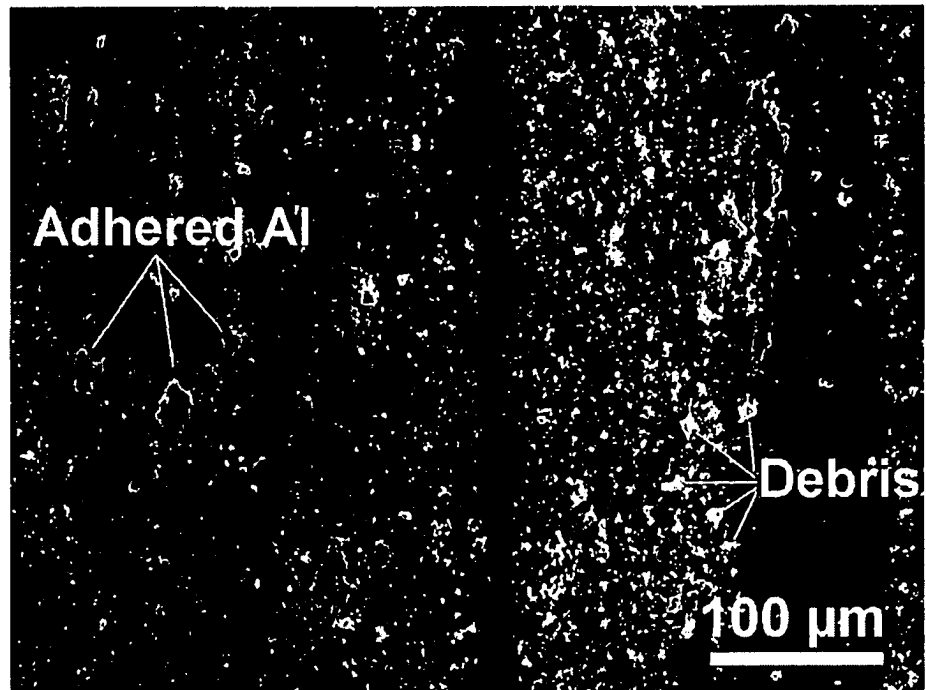
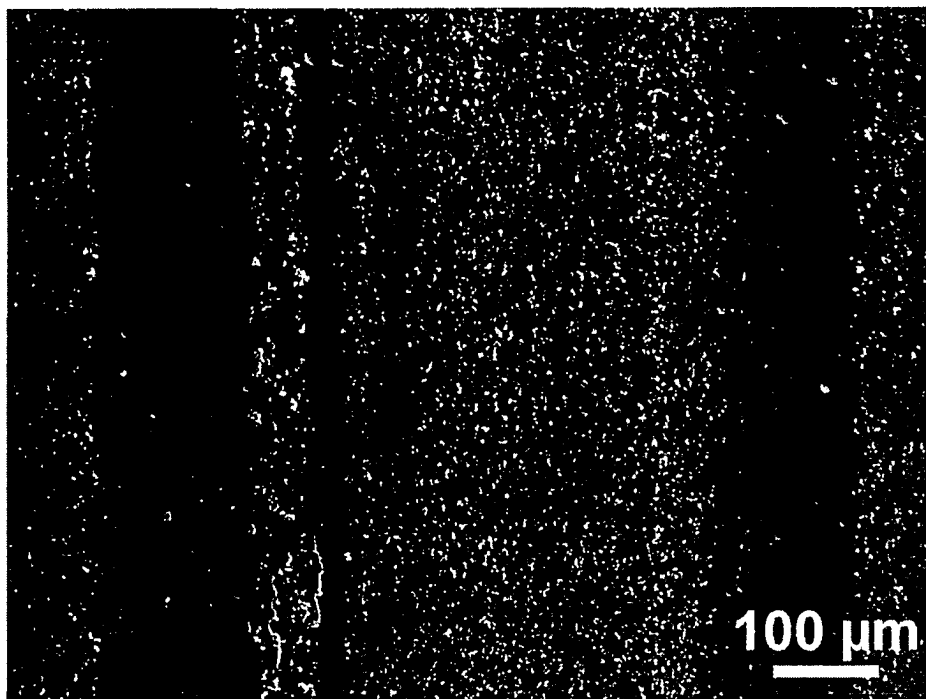


Figure 4.1. Percentages of the surface areas of the coating sliding tracks covered by aluminum and loose debris when tested in ambient air (33-51% RH) at a sliding speed of 0.12 m/s for 18 m of sliding distance. The applied load was 5 N.

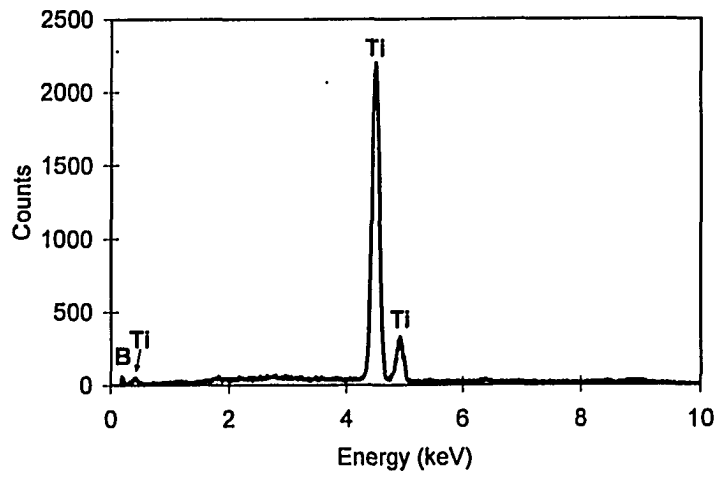


a)

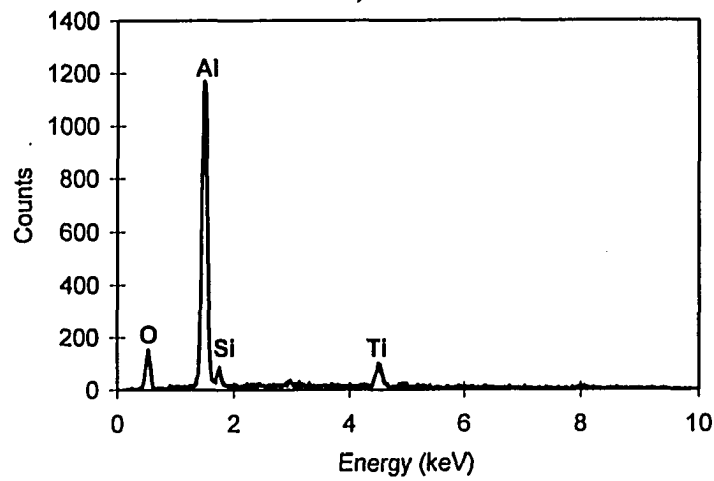


b)

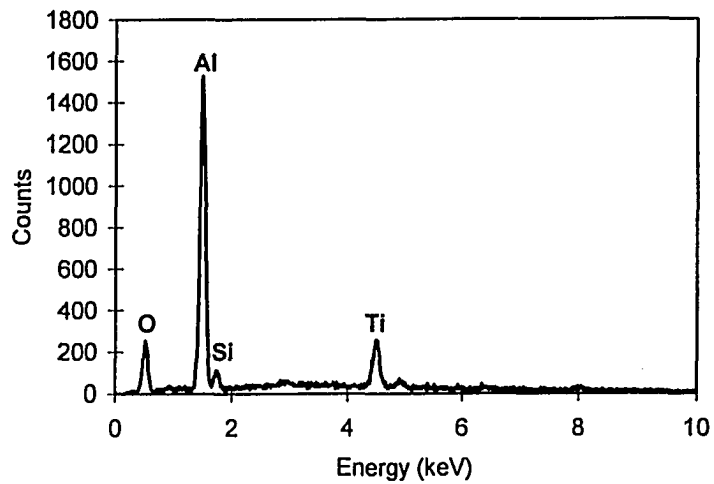
Figure 4.2. SEM images of sections of the sliding tracks of a) smooth ($R_a = 16$ nm) and b) rough ($R_a = 83$ nm) TiB_2 coatings tested against 319 Al for 300 revolutions (18 m) in ambient air (43% RH) at 0.12 m/s sliding speed. The applied load was 5 N. The white particles are the loose debris generated during sliding.



a)

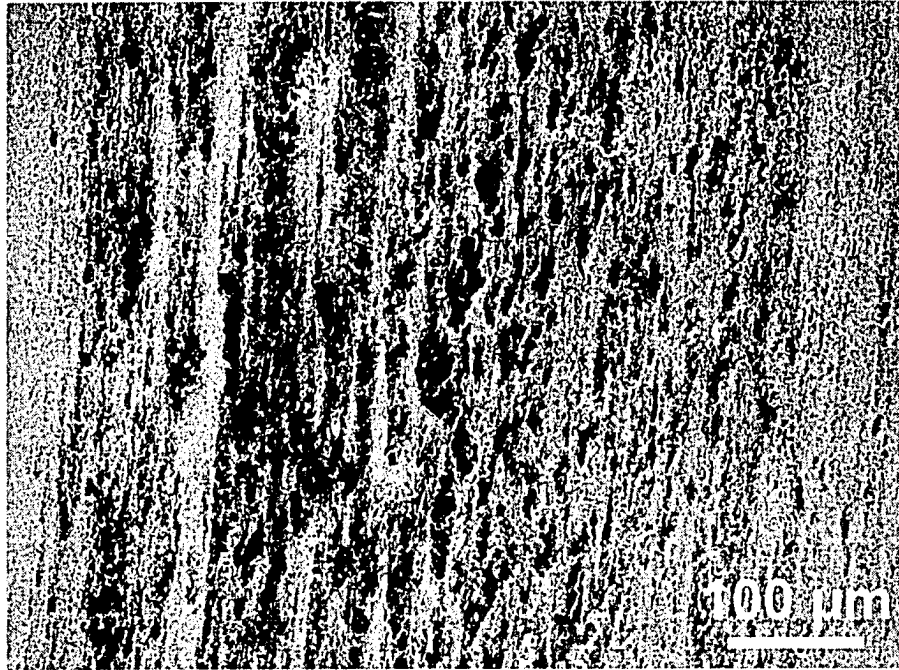


b)

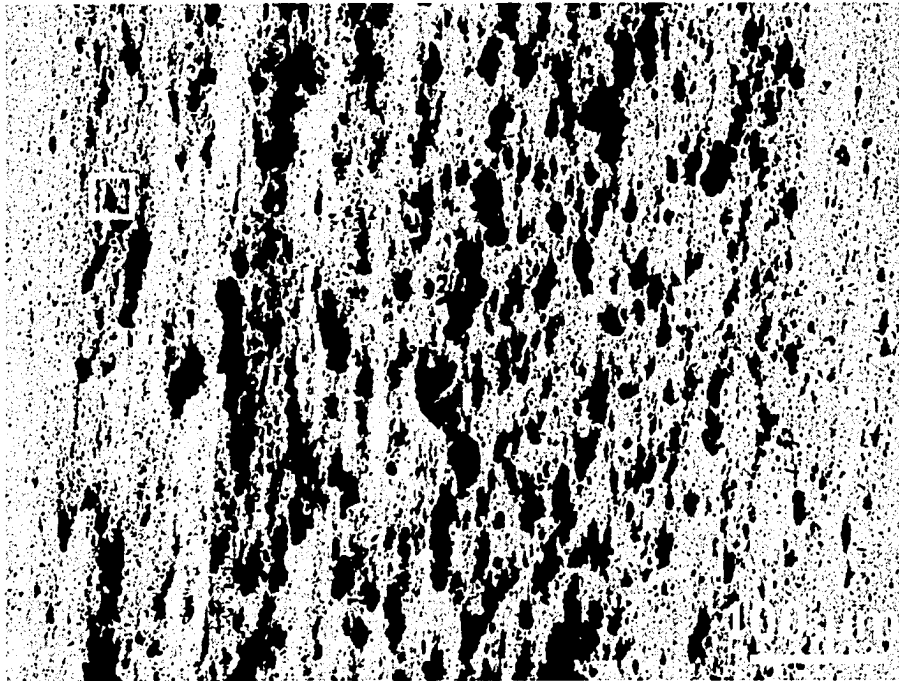


c)

Figure 4.3. EDS analyses of a) the smooth TiB_2 coating, b) a typical loose debris particle indicated in Figure 4.2.a, and c) an adhered Al piece on the TiB_2 shown in Figure 4.2.a.



a)



b)

Figure 4.4. a) SEI and b) BEI SEM images of a section of the sliding track of the CrN coating when tested in ambient air (41% RH) at 0.12 m/s sliding speed for 18 m. The applied load was 5 N. Significant amount of Al transfer to the CrN coating surface occurred.

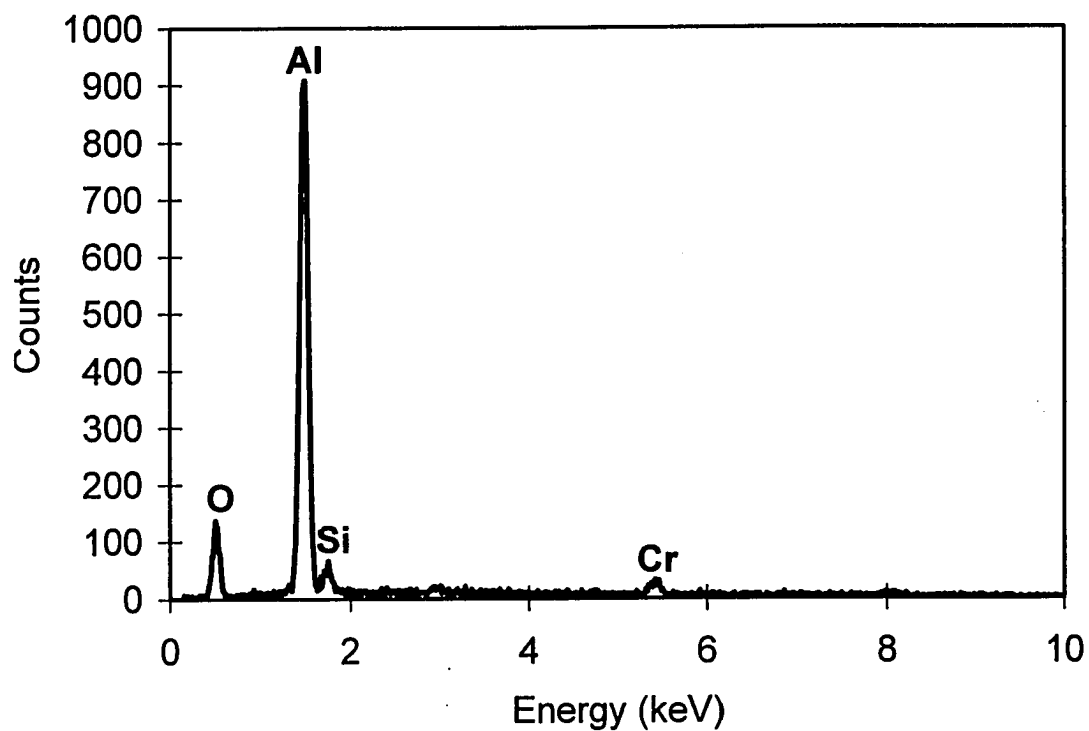


Figure 4.4. c) EDS analysis of the location shown in b). The adhered Al pieces were significantly oxidized.

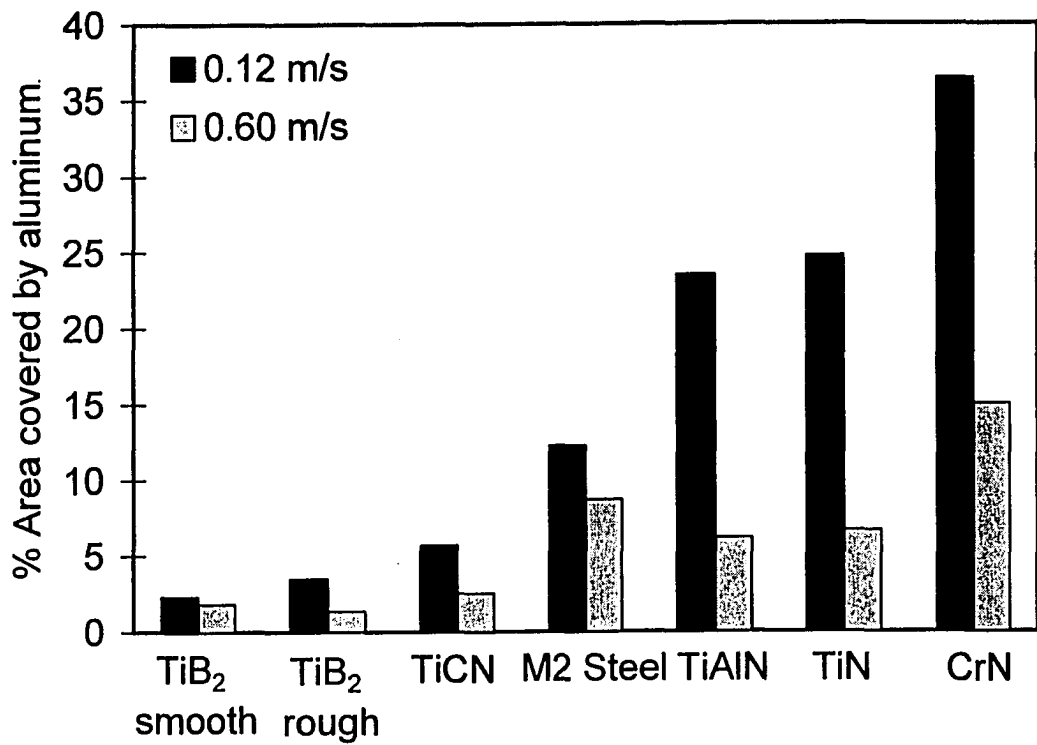


Figure 4.5. Effect of test speed on the percentage of the coating surface area covered by aluminum. Tests were done at sliding speeds of 0.12 and 0.60 m/s for 18 m of sliding distance under 5 N of load in ambient air.

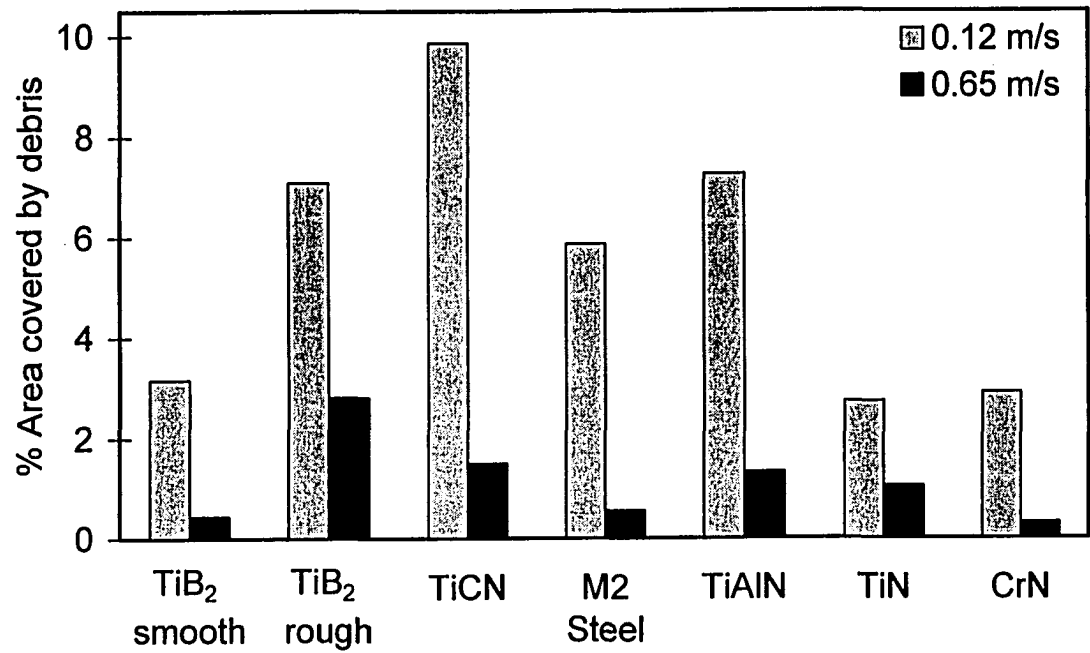


Figure 4.6. Effect of test speed on the percentage coating surface area covered by debris. Tests were done at sliding speeds of 0.12 and 0.60 m/s for 18 m of sliding distance under 5 N load in ambient air.

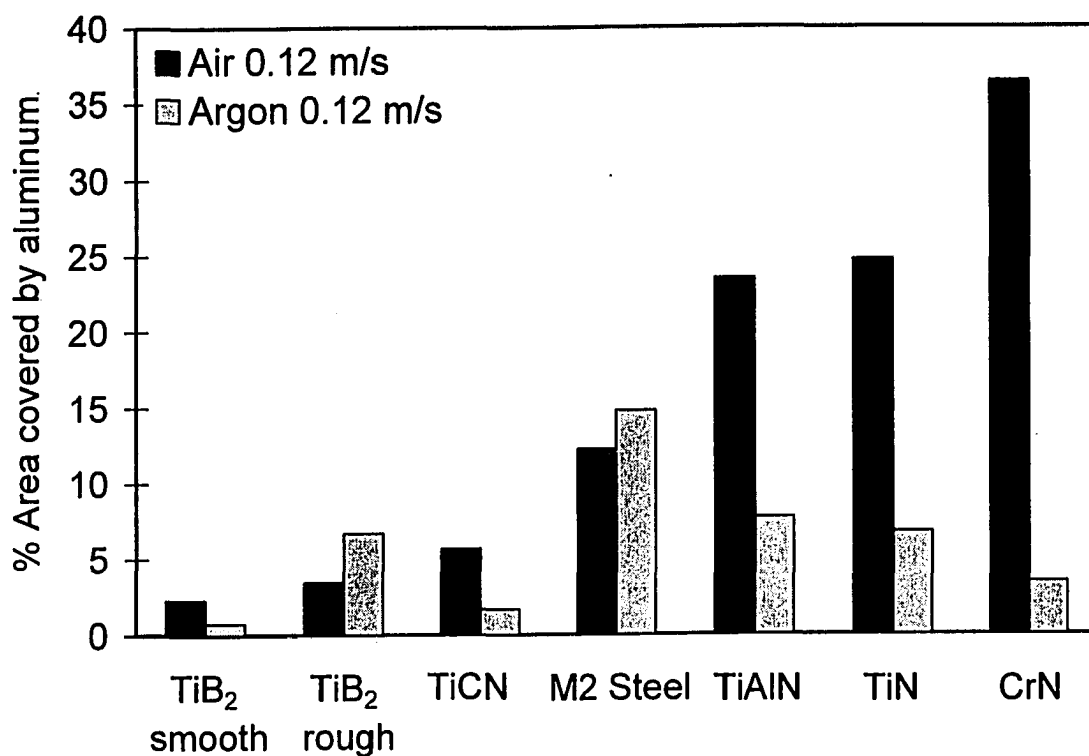


Figure 4.7. Effect of test atmosphere on the percentage of the coating surface area covered by aluminum. Tests were done under ambient air and argon gas at a sliding speed of 0.12 m/s for a sliding distance 18 m under 5 N load.

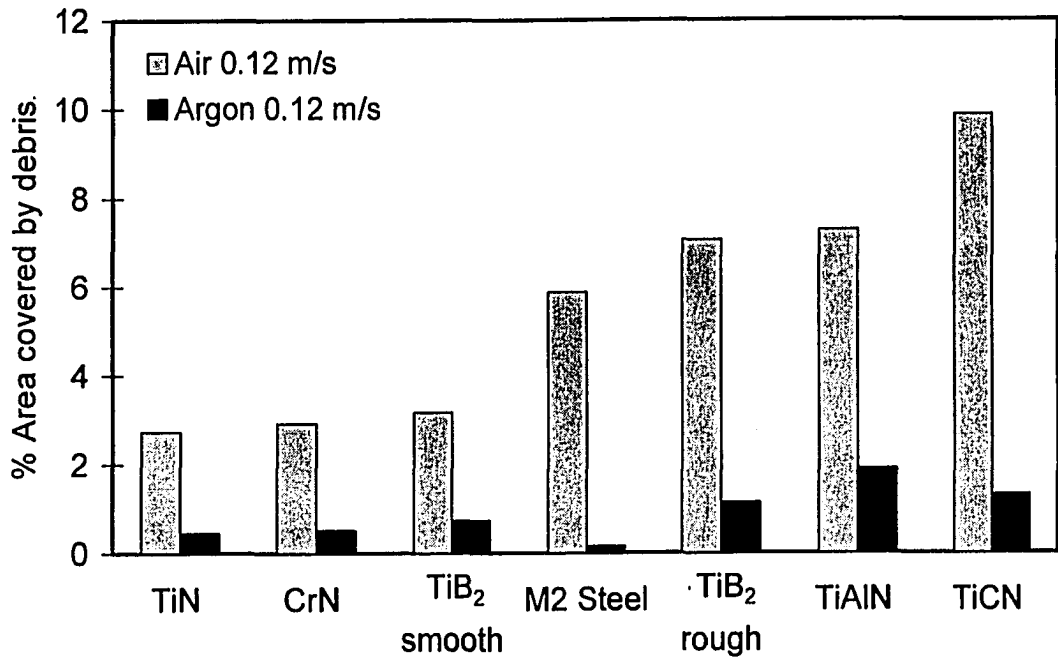
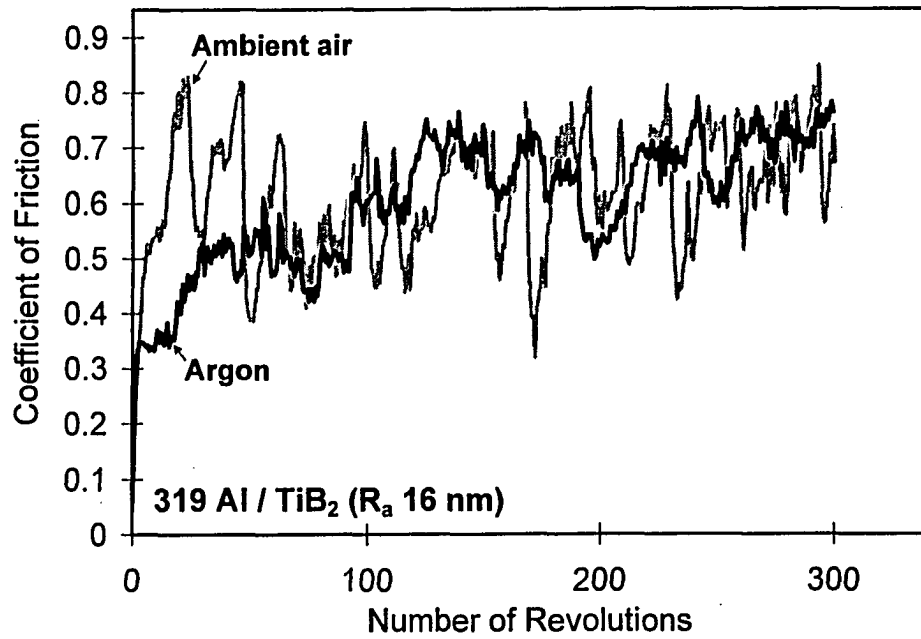
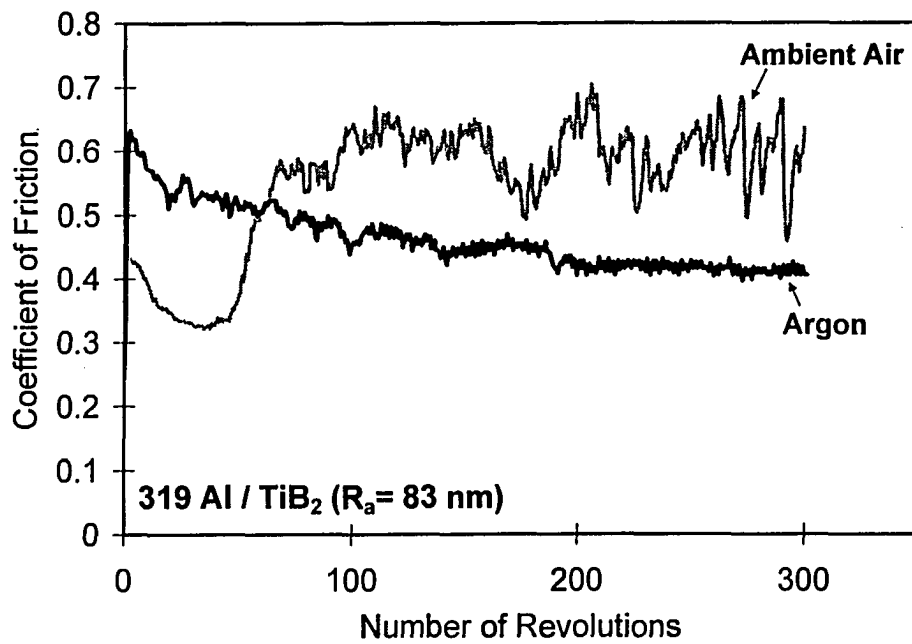


Figure 4.8. Effect of test atmosphere on the percentage of the coating surface area covered by debris. Tests were done under ambient air and argon at a sliding speed of 0.12 m/s for a sliding distance 18 m under 5 N load.

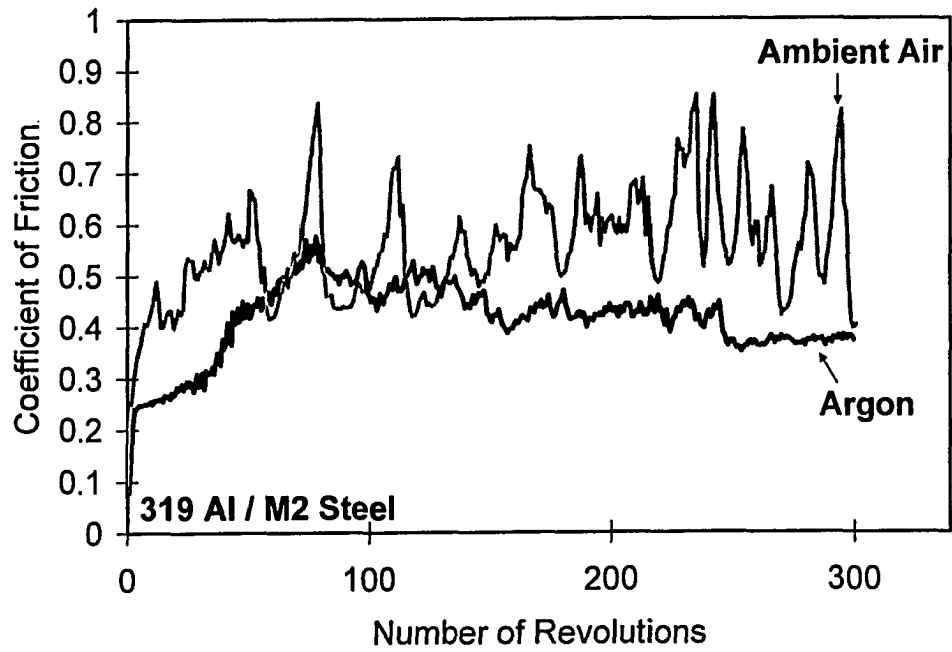


a)

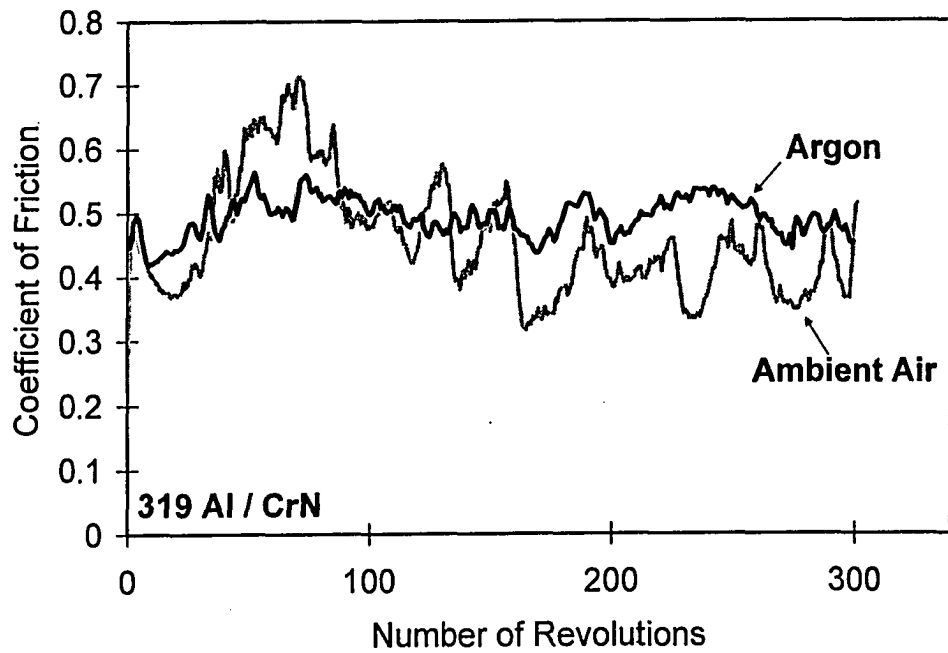


b)

Figure 4.9. The COF curves of the samples tested against 319 Al under argon and ambient air; a) TiB₂ (16 nm R_a), b) TiB₂ (83 nm R_a).

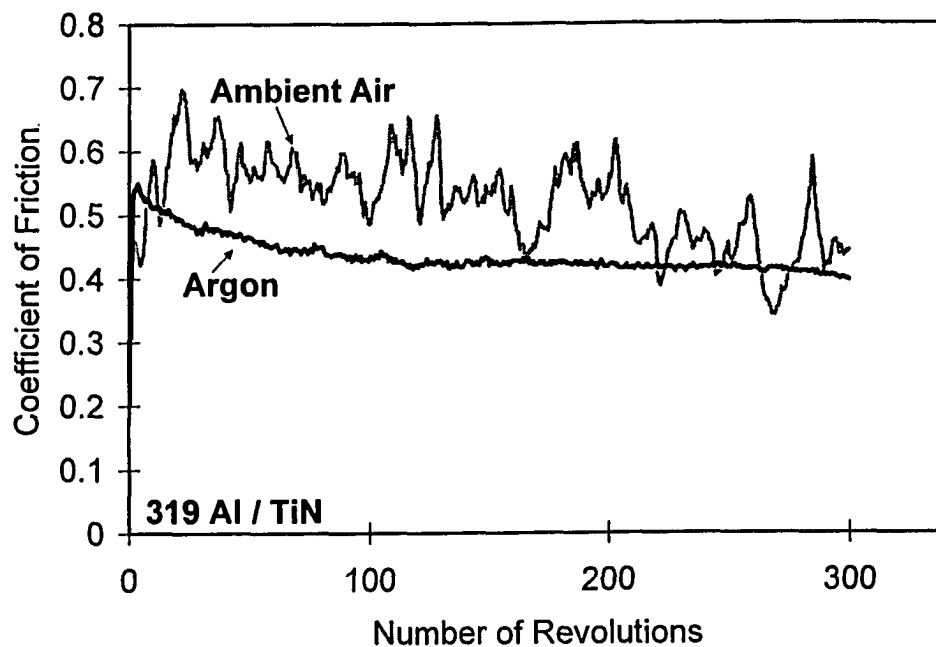


c)

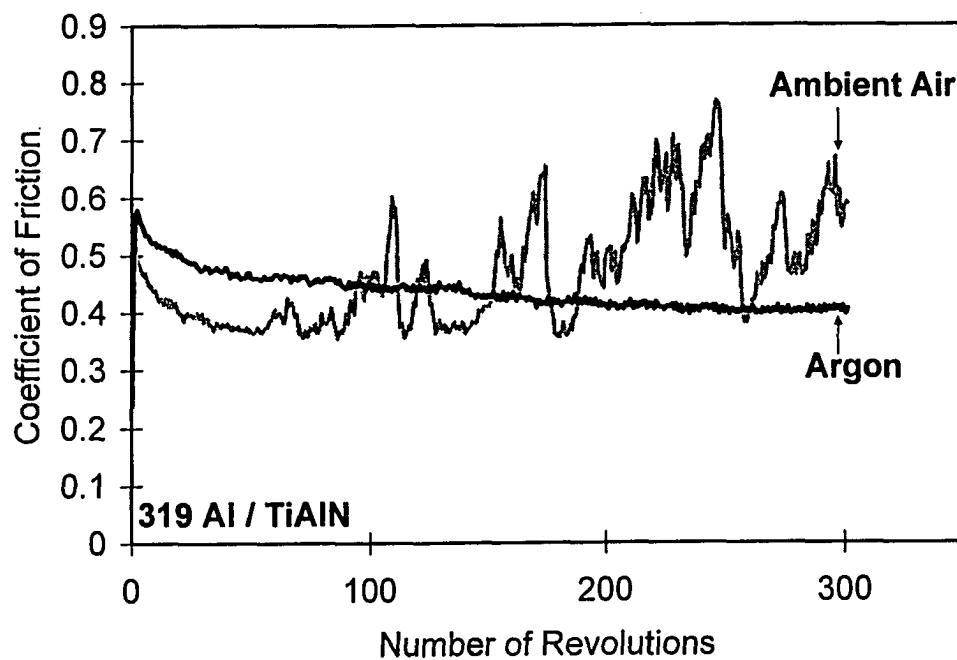


d)

Figure 4.9. The COF curves of the samples tested against 319 Al under argon and ambient air; c) M2 steel, d) CrN.

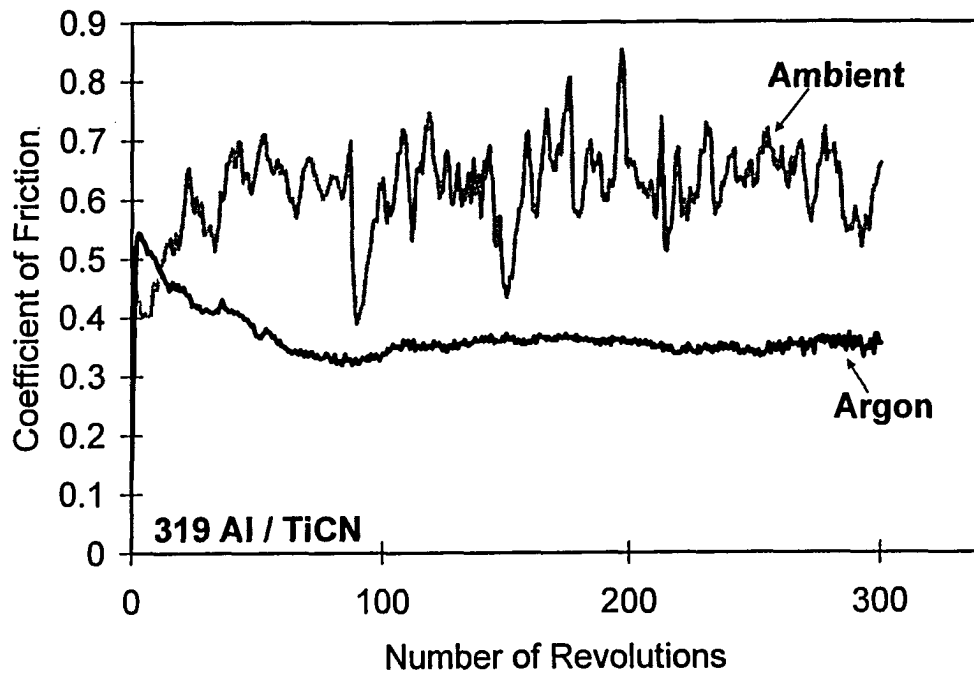


e)



f)

Figure 4.9. The COF curves of the samples tested against 319 Al under argon and ambient air; e) TiN, f) TiAlN.



g) TiCN

Figure 4.9. The COF curves of the samples tested against 319 Al under argon and ambient air; g) TiCN. Tests were done at a sliding speed of 0.12 m/s under an applied load of 5 N. The COF curves recorded in argon generally had less fluctuation than those recorded in ambient air.

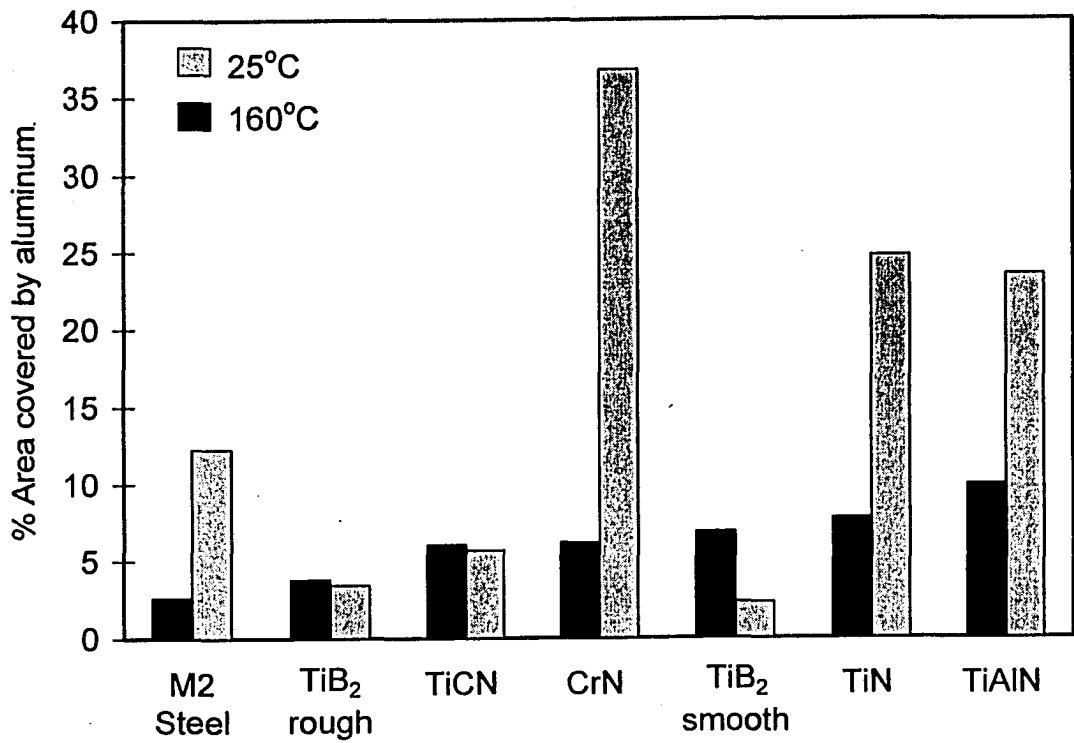


Figure 4.10. Effect of test temperature on the percentage of the coating surface area covered by aluminum. Tests were done at 25 and 160°C at a sliding speed of 0.12 m/s for 18 m of sliding distance under 5 N load.

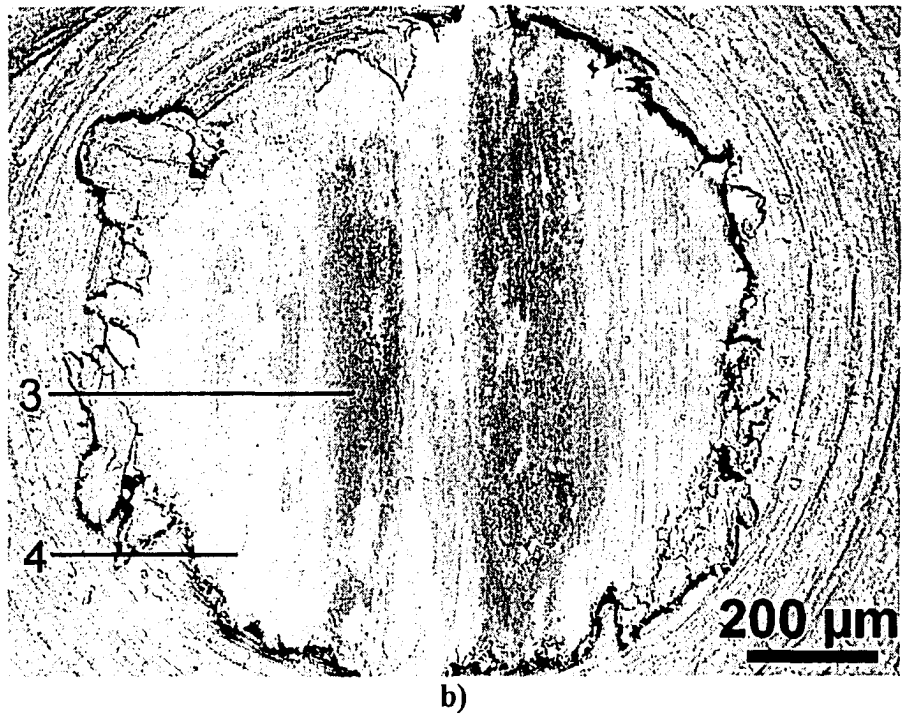
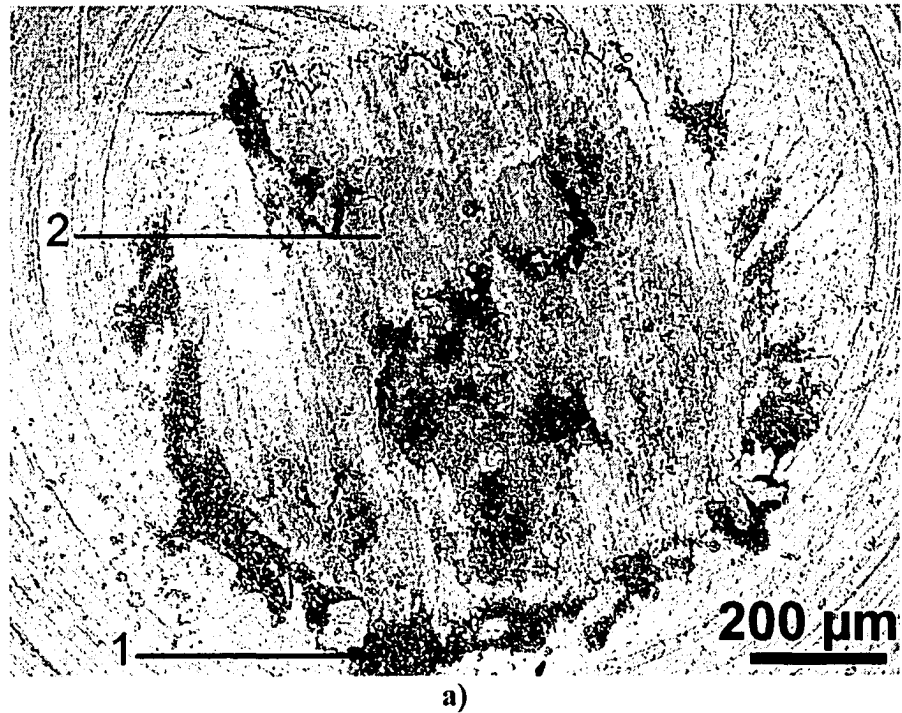


Figure 4.11. BEI SEM images of the contact surfaces of the 319 Al pins tested against TiCN coatings under a) ambient air and b) argon gas. The tests were performed at 0.12 m/s sliding speed under an applied load of 5 N for a sliding distance of 18 m.

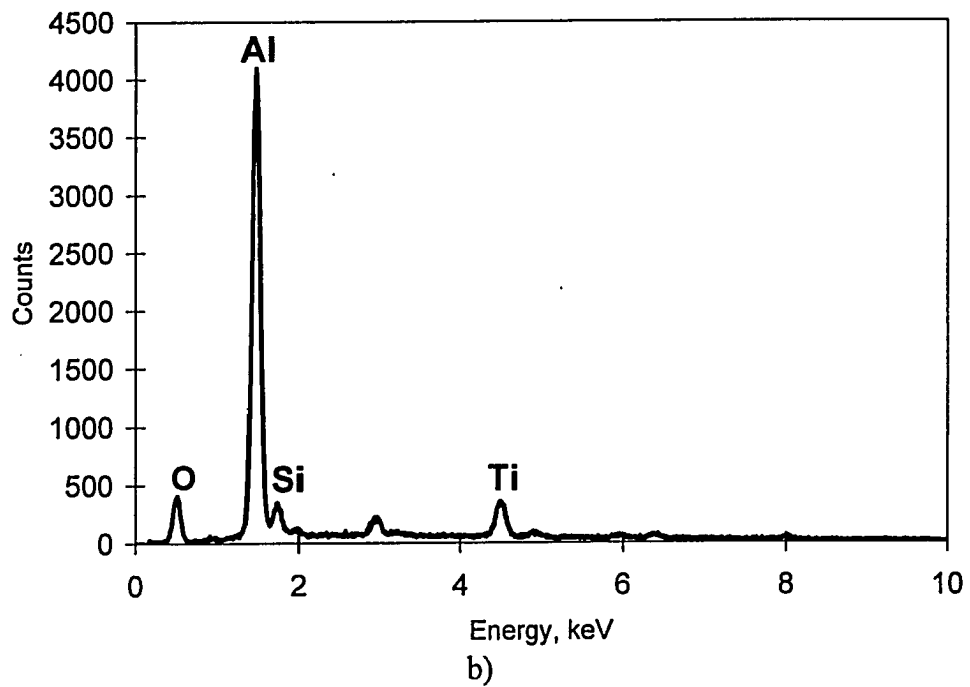
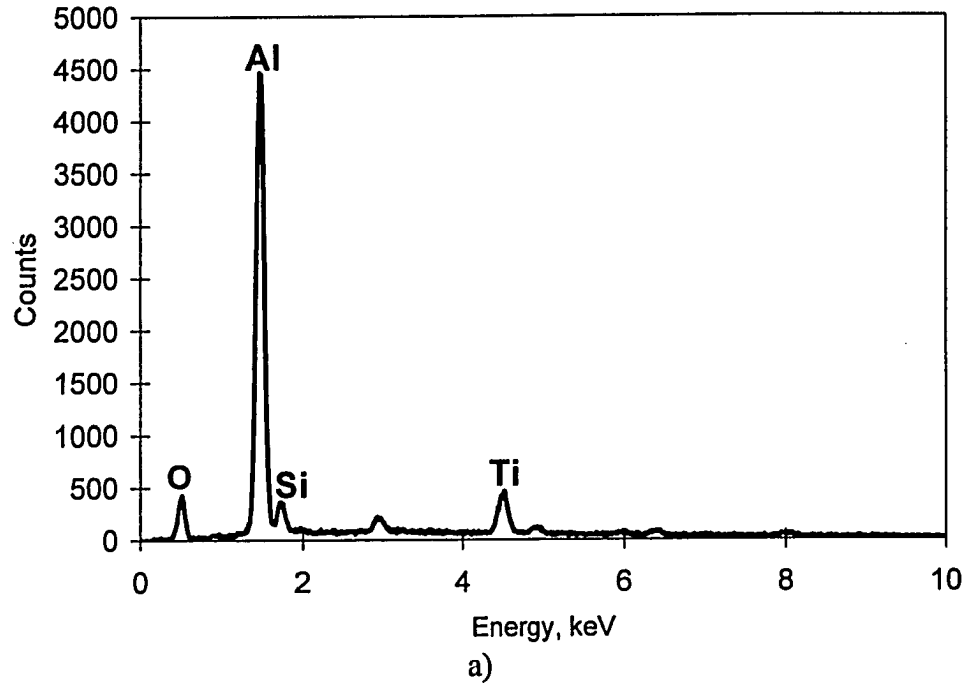
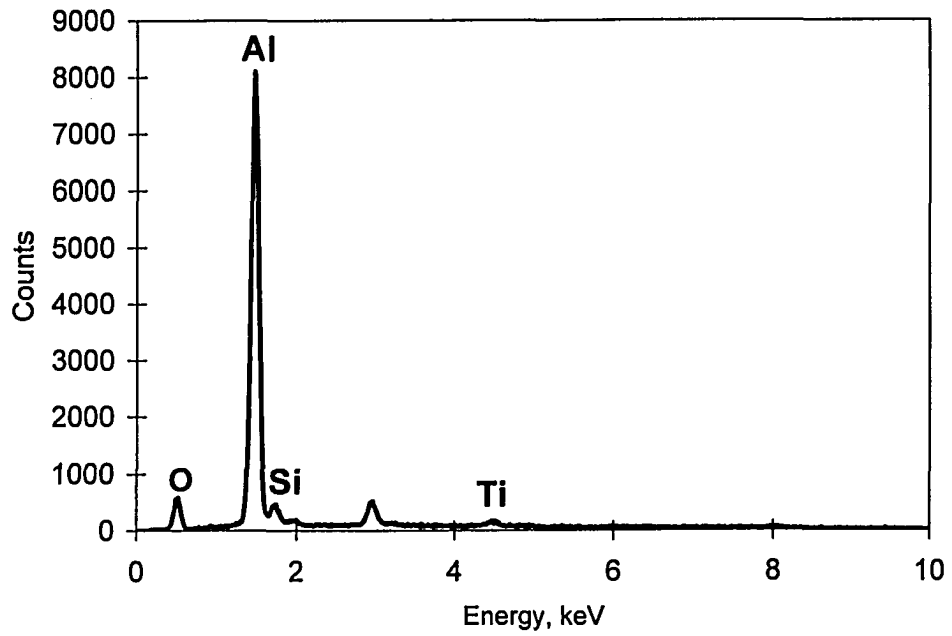
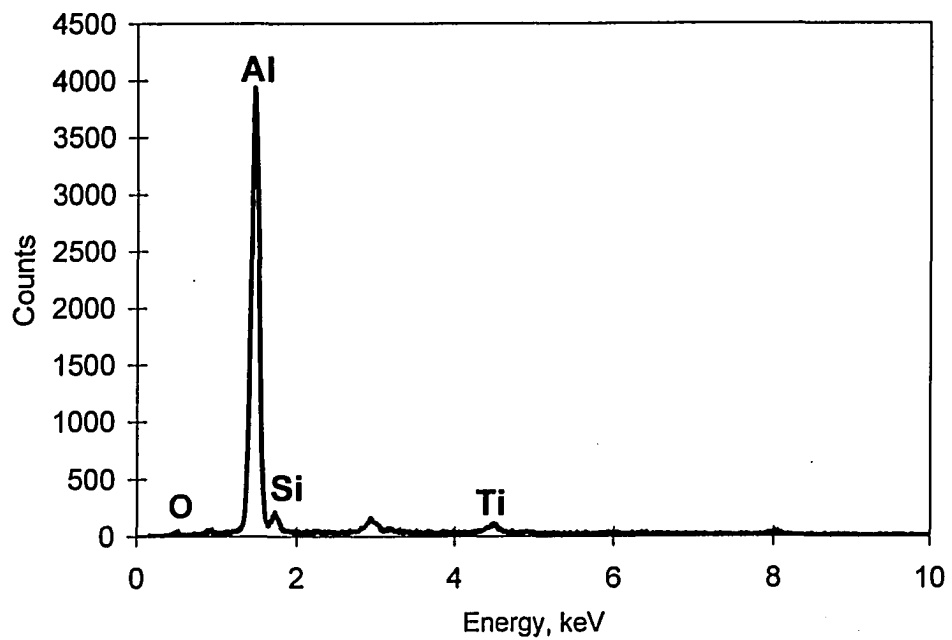


Figure 4.12. EDS analyses of selected locations indicated in Figures 4.11.a&b: a) Location 1 in Figure 4.11.a. b) Location 2 in Figure 4.11.a.



c)



d)

Figure 4.12. EDS analyses of selected locations indicated in Figures 4.11.a&b: c) Location 3 in Figure 4.11.b., d) Location 4 in Figure 4.11.b.

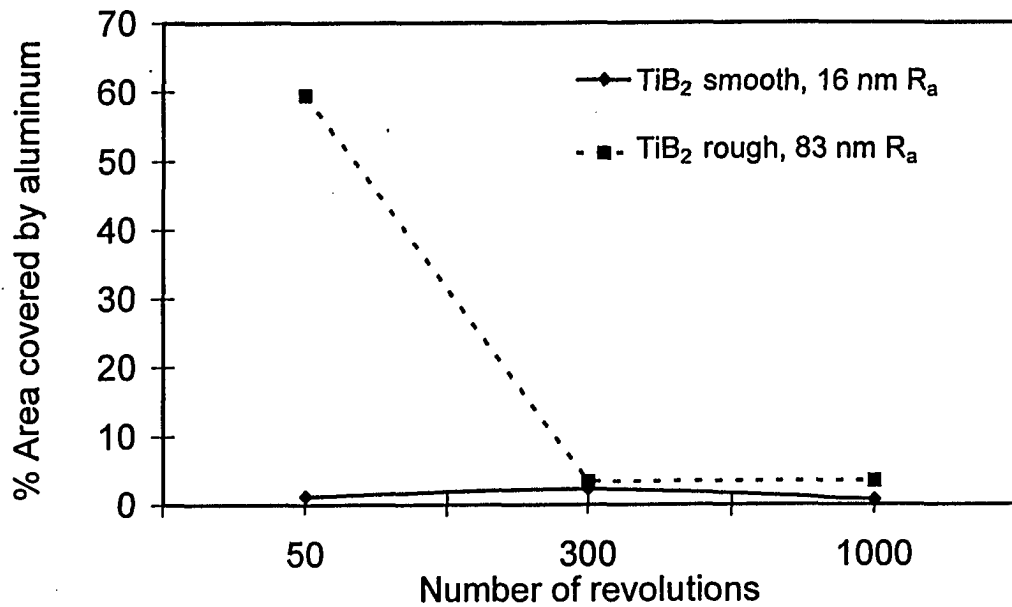
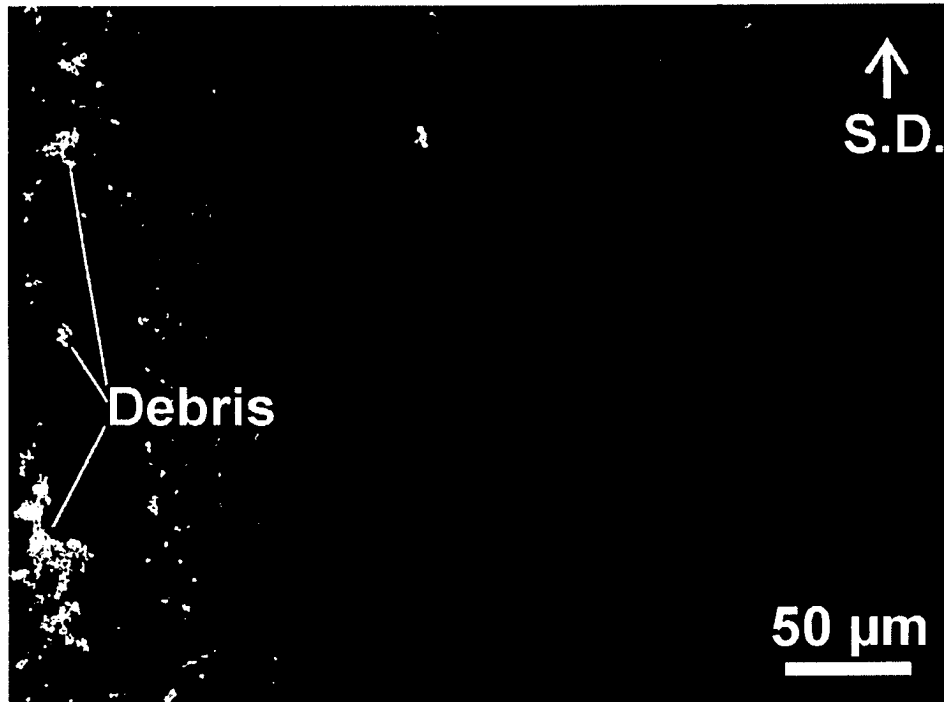
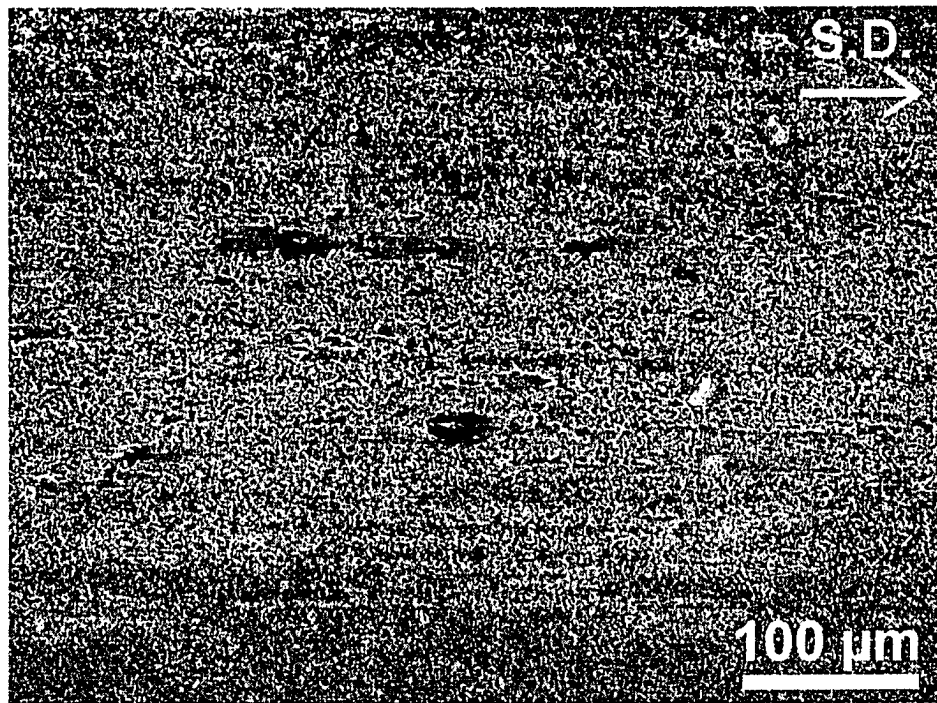


Figure 4.13. Percentage of the area covered by aluminum versus sliding distance for smooth ($R_a=16$ nm) and rough ($R_a=83$ nm) TiB₂. Tests were done in ambient air at 0.12 m/s sliding speed under 5 N load.

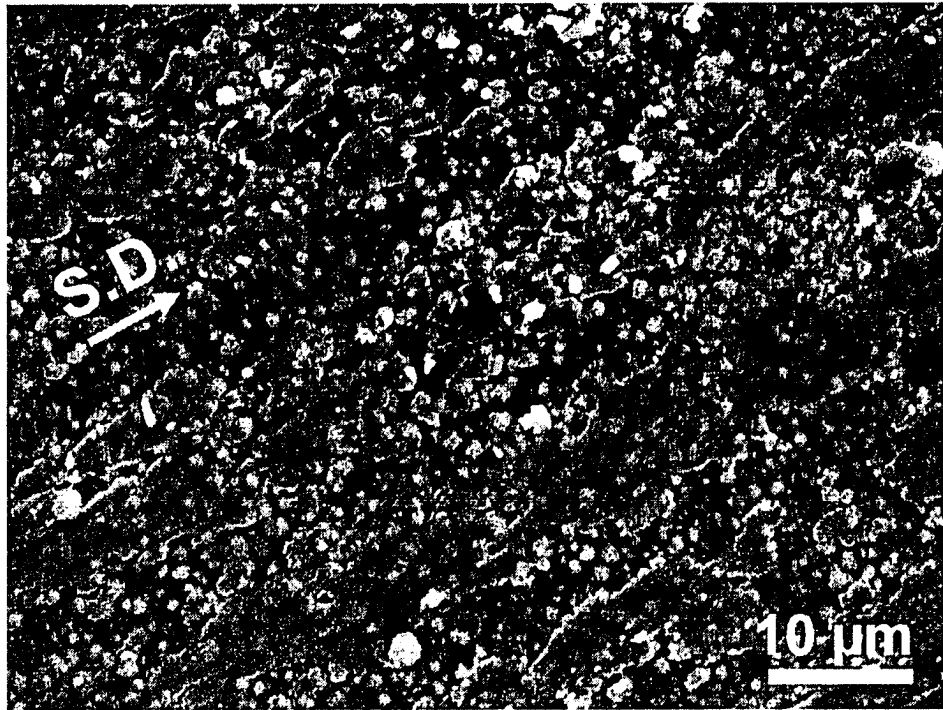


a)



b)

Figure 4.14. SEM images for **a)** smooth ($R_a= 16$ nm) and **b)** rough ($R_a= 83$ nm) TiB₂ at 50 revolutions (3 m) when tested against 319 Al in ambient air at 0.12 m/s sliding speed under 5 N of applied load.



c)

Figure 4.14. c) Enlarged view of a region in Figure 4.14.b). 60 % of the surface area of the rough TiB_2 was covered with mostly thin layers of aluminum.

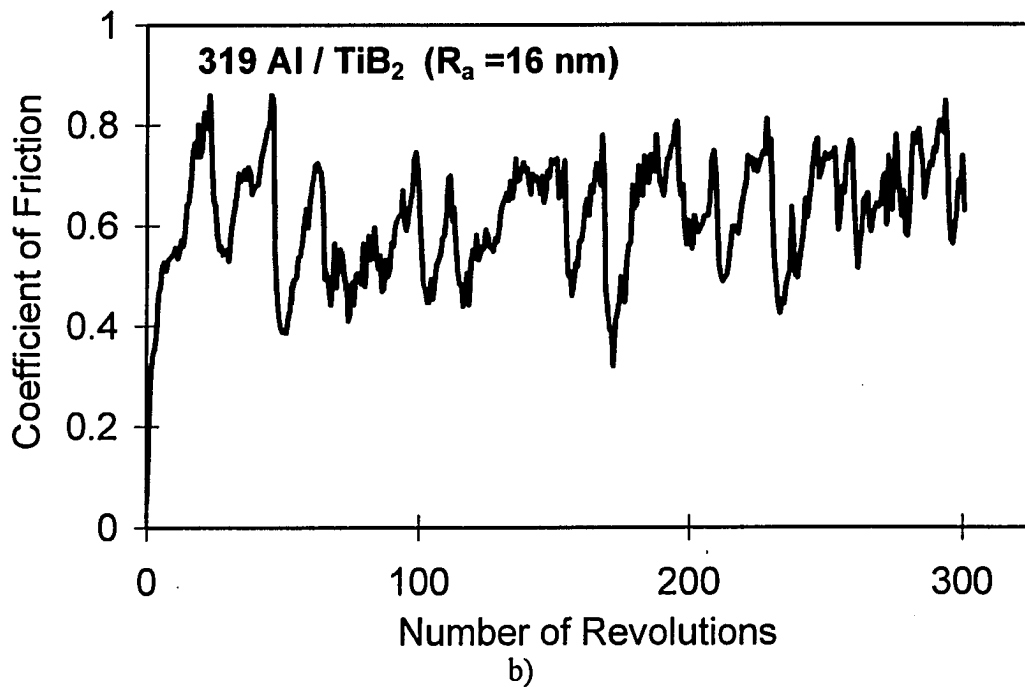
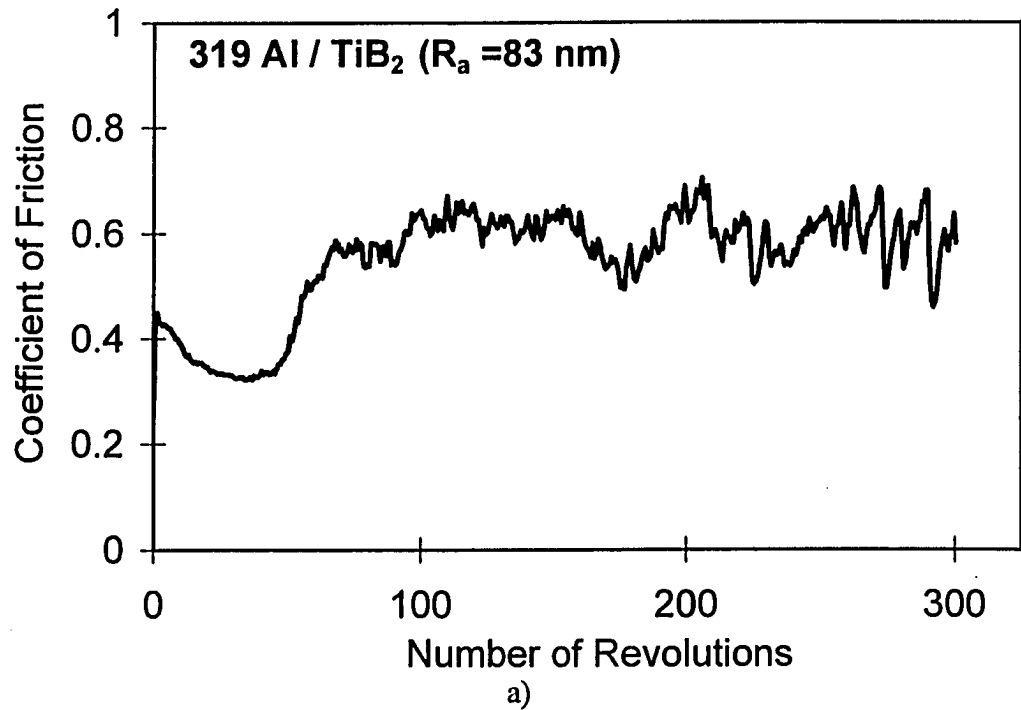


Figure 4.15. COF curves for a) rough ($R_a = 83$ nm) and b) smooth ($R_a = 16$ nm) TiB₂ coatings when tested in ambient air at 0.12 m/s sliding speed for 18 m of sliding distance under an applied load of 5 N.

CHAPTER 5

TRIBOLOGICAL BEHAVIOUR OF THE NON-HYDROGENATED DLC COATINGS AGAINST 319 AL ALLOY

The results of the previous chapter showed that the coatings studied in that part of the work (CrN, TiB₂, TiN, TiAlN and TiCN) were not the most promising ones for implementation as tool coatings for dry machining of aluminum since none of them totally prevented aluminum adhesion and transfer to their surfaces. Compared to other coatings, the much reduced adhesion tendency of aluminum to DLC coating surfaces in ambient conditions warrants a closer look at the tribological behaviour of these coatings against aluminum.

In an attempt to better understand the tribological properties of the DLC coatings for cutting tool coating applications, 60-V DLC, 80-V DLC and commercially available Graphit-iC DLC coatings were tested against 319 Al alloy, WC and Al₂O₃ under various test atmospheres and at elevated temperatures. The production and characterization details of the DLC coatings are given in **Section 3.2.2**. Basically, they were amorphous, sp² bond rich, non-hydrogenated DLC coatings.

The coatings were tested in air (0-85 % RH), vacuum, inert gas (Ar, He and N₂) and 60% He- 40% H₂ mixture. The effect of temperature was investigated at 120, 300 and 400°C. Static oxidation behaviour of the DLC coatings by annealing them at 300°C in air was used as a method to assess the stability of their structures. The observed results are explained in terms of interactions of the DLC coating surface with the gaseous species in the environment and material transfer to counterfaces.

5.1. Tribological Behaviour of the 80-V DLC Coatings against 319 Al under Various Test Environments

5.1.1. Tests in Vacuum

The 80-V DLC coatings suffered severe wear damage against 319 Al in vacuum (6.65x10⁻³ Pa). The average COF and wear rate of the 80-V DLC coating against the 319 Al pin were 0.46 and 2.48x10⁻⁴ mm³/m under vacuum, respectively. The COF curve had large fluctuations (**Figure 5.1.a**). **Figure 5.1.b** shows a region of the wear track on the

80-V DLC coating tested against 319 Al in vacuum for 8.5×10^3 revolutions (i.e., 5.07×10^2 m of sliding). Most of the coating was removed leaving the M2 steel substrate exposed. Transfer of 319 Al to the wear track was also observed.

5.1.2. Tests in Nitrogen

Similar to the tests under vacuum, the 80-V DLC coatings had severe wear damage against 319 Al in the nitrogen environment (**Figures 5.2.a and b**). The average COF and the wear rate of the 80-V DLC coating against 319 Al was 0.47 and 3.63×10^{-4} mm³/m under nitrogen.

5.1.3. Tests in Dry air

In dry air, the average COF of the 80-V DLC coatings against 319 Al slightly decreased to 0.44 (**Figure 5.3.a**). The wear rate in dry air was 6.64×10^{-5} mm³/m, which corresponds to a 81% decrease from the vacuum test. In contrast to the tests in vacuum and nitrogen, there was no adhered Al in the wear track of the 80-V DLC coatings tested in dry air (**Figure 5.3.b**). Some fine debris, consisting of mainly oxidized Al, was observed along the wear track (**Figures 5.3.c-e**).

The size of the width of the wear track was of the 80-V DLC coatings tested in dry air was smaller than the corresponding ones in vacuum and nitrogen. Again, the contact surface of the 319 Al pin contained some of the material removed from the coating. This time, however, the EDS analysis of the contact surface indicated that it was significantly oxidized (**Figure 5.3.f and g**).

5.1.4. Tests in Air with 20 - 85% Relative Humidity

The COF and the wear rates of the 80-V DLC coatings against 319 Al were drastically reduced in air with humidity levels exceeding 20% RH. In air with 20% RH, the steady state COF and the wear rate of the DLC coatings were 0.16 and 2.31×10^{-6} mm³/m. With increasing humidity, the COF and the wear rate further decreased to 0.09 and 5.59×10^{-7} mm³/m at 50% RH and to 0.085 and 4.38×10^{-7} mm³/m at 85% RH.

The COF curves recorded in air with 22% humidity (**Figure 5.4.a**) showed much smaller fluctuations compared to the vacuum and nitrogen environments. Again, similar

to the tests in dry air, there was no adhered Al on the wear track of the DLC coating at the end of the tests (**Figure 5.4.b**). The sliding track on the DLC coating had a polished appearance compared to the unworn coating surface.

On the other hand, a well defined tribolayer was observed on the contact surface of the 319 Al pins tested in air with $RH \geq 20\%$ (**Figure 5.4.c**). The EDS analysis of this layer (**Figure 5.4.d**) showed C, Cr and O peaks.

5.2. Tribological Behaviour of the 80-V DLC Coatings against WC

In addition to the 319 Al pins, WC balls were also used as the counterface material running against the 80-V DLC coatings. The purpose of these tests was to investigate the tribological behaviour 80-V DLC coatings against a material that is much harder than 319 Al and also the coating itself.

5.2.1. Tests in Vacuum and Nitrogen Atmospheres

The 80-V DLC coatings showed high COF (0.50 and 0.56) and high wear rates (3.74×10^{-5} and 1.09×10^{-4} mm³/m) against WC in vacuum (6.65×10^{-3} Pa) and nitrogen environments. The SEM image of a region of the wear track formed on the 80-V DLC coated surface tested in vacuum for 1.2×10^3 revolutions (71.6 m of sliding) shows the severity of the damage (**Figure 5.5.a**). The corresponding WC ball had a ring shaped flat contact area that contained materials removed from the coating (C and Cr) as shown in **Figure 5.5.b**. For a longer sliding distance of 3.5×10^3 revolutions in vacuum, significant adhesion and transfer of material from the WC ball to the DLC coating surface took place as shown in **Figure 5.5.c** and verified by EDS (**Figure 5.5.d**).

5.2.2. Tests in Dry Air (0% RH)

The WC ball still caused high wear rates (3.28×10^{-5} mm³/m) when tested against the 80-V DLC coating in dry air (0% RH). The average steady state COF value was 0.50, i.e. the same as the vacuum test. The SEM image of a section of the wear track on the 80-V DLC coating tested in dry air for 1.2×10^3 revolutions is given in **Figure 5.6.a**. Oxidized coating material containing C and Cr was accumulated as debris along the edges of the wear track on the DLC coating. The WC ball tested against the 80-V DLC

coating experienced much less wear in dry air compared to the vacuum and nitrogen environments (**Figure 5.6.b**). The contact surface of the WC ball was bare and some material removed from the DLC coating, which was oxidized during sliding (**Figure 5.6.c**), was deposited along the contact area as fine powdery debris.

5.2.3. Tests in Air with 20 - 85% Relative Humidity

The tribological behaviour of the 80-V DLC coatings against WC has shown significant improvements with increasing relative humidity of air. The steady state COF and the wear rate of the 80-V DLC coating were 0.08 and 1.03×10^{-6} mm³/m in air with 20% RH. These correspond to 84% and 96% drop in the COF and wear rates as compared to the tests in vacuum. The material removed from the DLC coating was oxidized and accumulated uniformly along the wear track as shown in **Figure 5.7.a**. The contact area of the WC ball tested against the 80-V DLC coating in ambient air was much smaller compared to the tests performed in vacuum and nitrogen environments (**Figure 5.7.b**). A transfer layer that covered most of the contact surface of the WC ball was observed when the pin-on-disc tests were performed in humid air. The EDS analysis of the transfer layer (**Figure 5.7.c**) revealed that it was composed of oxidized coating materials, namely C and Cr. Therefore, in air with humidity levels exceeding 20% RH, the 80-V DLC coating was essentially running against this transfer layer instead of the WC ball after the first few revolutions of sliding.

At higher humidity levels ($RH \geq 50\%$), the COF and the wear rate of the 80-V DLC coating run against the WC ball increased. At 85% RH, the steady state COF and the wear rate were 0.19 and 4.19×10^{-6} mm³/m, respectively. The debris was non-uniformly accumulated at certain locations along the wear track.

The test results presented in **Sections 5.1** and **5.2** showed that the 80-V DLC coatings experienced high COF and high wear rates in vacuum and nitrogen gas environments. Introduction of water vapour to the test chamber drastically reduced the COF and wear rates. The measured wear rates and the steady state COF values of the 80-V DLC coatings against 319 Al and WC under various environments are summarized in **Figures 5.8.a** and **b**.

5.3. Tribological Behaviour of the Graphit-iC DLC Coatings against 319 Al under Various Test Environments

In this study, Graphit-iC DLC coatings served as a benchmark to help assess the tribological performances of the experimental coatings (60 and 80-V DLC).

5.3.1. Tests in Vacuum, Argon, Helium and Nitrogen

In addition to the vacuum and nitrogen environments, the tribological behaviour of Graphit-iC DLC coatings were also investigated in other inert environments namely, argon and helium. The Graphit-iC DLC coating exhibited high COF and high wear rates against the 319 Al alloy in vacuum, argon, helium and nitrogen environments. At a sliding of 0.12 m/s, the average COF was 0.56 in vacuum (6.65×10^{-4} Pa), 0.72 in argon, 0.74 in helium, and 0.69 in nitrogen. The COF curves of the Graphit-iC DLC in these environments are plotted in **Figures 5.9.a-d**.

Figure 5.10.a shows a region of the wear track on the Graphit-iC DLC coating tested against 319 Al in vacuum for 1×10^4 revolutions (i.e., 5.97×10^2 m of sliding). A significant amount of material was removed from the 319 Al pin, which was transferred and adhered to the Graphit-iC DLC coating surface. The transfer of Al to the Graphit-iC DLC coating surface occurred in the form of i) large chunks of Al deposited as discrete patches and ii) very small smears of Al (**Figure 5.10.b**). The BEI SEM image of the contact surface of the 319 Al pin tested against the Graphit-iC DLC coating in vacuum is shown in **Figure 5.10.c**. The EDS analysis of the contact surface of the 319 Al pin showed that, in addition to Al, the contact surface contained C and Cr that were removed from the DLC coating (**Figure 5.10.d**).

5.3.2. Tests in Dry Air (0% RH)

In dry air, the Graphit-iC DLC coatings showed lower COF and wear rates compared to the tests in the vacuum and inert environments. After reaching a peak value of 0.68 at 60 revolutions, the COF decreased to a steady value of 0.28 (**Figure 5.11**).

5.3.3. Tests in Ambient Air

When the 319 Al alloy pin was run against the Graphit-iC DLC coating at 0.12 m/s sliding speed in ambient air (47% RH), the average COF was 0.12 as shown in **Figure 5.12**. The COF curve was significantly smoother and its average value was much lower than the values obtained in vacuum, argon, helium, and nitrogen (**Figures.5.9.a-d**).

5.3.4. Tests in H₂-He Mixture against 319 Al

The results of the pin-on-disc tests in vacuum, inert gas, dry air and air with varying humidity levels showed that the tribological behaviour of the DLC coatings under investigation is quite sensitive to the presence of reactive gaseous species (oxygen and water vapour) in the test environment. In addition to this, the literature survey (**Section 2.4**) indicated that the presence of sufficient hydrogen in the film structure can drastically change the COF and wear behaviour of the DLC coatings. Together with the experimental observations, this finding generated the idea of testing non-hydrogenated DLC coatings in a hydrogen rich test environment. A 40% H₂-60% He mixture was used for these tests.

The typical variation of the COF between the Graphit-iC DLC coating and the 319 Al alloy during sliding in H₂-He mixture at 0.12 m/s sliding speed is given in **Figure 5.13.a**. The recorded COF curve had three sections. Initially, a high COF (0.70±0.10) regime (**Figure 5.13.b**) that lasted 50-300 revolutions was observed at the beginning of the test. This was followed by a very low COF period where the COF dropped to the very low value of 0.15. After staying at this very low COF value for some time (about 2000 revolutions), the COF gradually increased to 0.025-0.040 range and fluctuated in this range for the rest of the test (about 1x10⁴ revolutions). Compared to the other test conditions, the Graphit-iC DLC coatings had the lowest COF and the least amount of wear during sliding in He-H₂ mixture.

5.3.5. Tests in H₂-He Mixture against WC

The COF behaviour of the Graphit-iC DLC coatings against the WC ball in He-H₂ mixture (**Figure 5.14.a and b**) was similar to that against 319 Al. With the start of sliding, the COF quickly reached to high values about 0.67. This high COF period ended around 450 revolutions and the COF drastically dropped to 0.015. Further sliding did not

caused a change in COF. The measured wear rates and the steady state COF values of the Graphit-iC DLC coating against 319 Al under various environments are summarized in **Figures 5.15.a and b.**

5.4. Elevated Temperature Testing of 80-V DLC Coatings against 319 Al, WC and Al₂O₃

To investigate the effect of temperature on the tribological behaviour of DLC coatings, first 80-V DLC coatings were run against 319 Al at 25, 120, and 300°C. The COF curves generated during the course of sliding contact between the 319 Al pins and the 80-V DLC samples at 25, 120, and 300°C are given in **Figure 5.16.** The COF curves obtained at 25 and 120°C were characterized with an initial running-in period where the COF values were high (0.4-0.5) but then decreased to steady state values in less than 1×10^2 revolutions. On the other hand, the COF curve obtained at 300°C did not have a steady state value; it increased from 0.20 to at 2×10^2 revolutions to 0.56 at 1×10^3 revolutions and displayed larger fluctuations compared to the ones at 25 and 120°C.

The steady state COF between the 319 Al pin and the 80-V DLC coating was 0.17 at 25°C in ambient air with 15% RH. At the end of 2.5×10^4 revolutions (sliding distance of 1.5×10^3 m), the wear rate of the 80-V DLC coating was 1.25×10^{-6} mm³/m. There was no transfer of material from the 319 Al pin to the coating surface at 25°C. The sliding track on the 80-V DLC coating had a polished appearance compared to the unworn coating surface.

At 120°C, the 80-V DLC exhibited high COF and high wear against 319 Al. The steady-state COF during the test was 0.30, about two times higher than that at 25°C. The wear rate increased to 3.08×10^{-5} mm³/m, which is an order of magnitude higher than the wear rate at 25°C.

The 80-V DLC coating suffered the highest amount of wear at 300°C as compared to the 25 and 120°C tests. The wear rate was 3.36×10^{-4} mm³/m at this temperature. Initially, the COF was 0.2 but increased to 0.55 after 7×10^2 revolutions (**Figure 5.16**). The coating was worn in such a way that the M2 tool steel substrate surface became exposed and the contact took place mostly between the M2 tool steel substrate and the 319 Al pin after about 10^3 revolutions. Because of the continuously

increasing COF values of the coating at 300°C compared to steady state COF values obtained at lower temperatures (**Figure 5.16**), the wear behaviour of the coating at this temperature was investigated in more detail at longer sliding distances. Comparison of the SEM images of the wear tracks of the 80-V DLC coating tested against 319 Al for 1×10^3 and 1×10^4 revolutions at 300°C showed that considerable amount of material transfer occurred from the 319 Al pin to the disc surfaces once the DLC coating was removed from the disc surface as a result of wear (**Figures 5.17.a and b**). Also, it was observed that the width of the wear tracks more than doubled during sliding from 1×10^3 to 1×10^4 revolutions at this temperature.

5.4.1. Effect of Counterface Material

In addition to the 319 Al pins, the elevated temperature friction and wear behaviour of the 80-V DLC coating was also investigated against the harder counterface materials namely, tungsten carbide (WC) and sapphire (Al_2O_3) balls.

In ambient air (15% RH) at 25°C, the 80-V DLC coating exhibited low COF values against the tungsten carbide (COF = 0.10) and sapphire (COF = 0.09) balls during 2.5×10^4 revolution-tests. The wear rates of the 80-V DLC against these two counterface materials were also low; 9.73×10^{-7} mm³/m against the WC ball and 6.38×10^{-7} mm³/m against the sapphire ball. The variation of the wear rates of the 80-V DLC coatings worn against 319 Al, WC and sapphire at 25, 120, and 300°C is given in **Figure 5.18**.

At 120°C the wear rate of the 80-V DLC coating increased to 2.06×10^{-6} mm³/m against the WC ball and to 1.03×10^{-5} mm³/m against the sapphire ball. The COF between the 80-V DLC coating and WC reached 0.46 for a short time at the beginning of the sliding and then decreased to a steady state value of 0.05. Against sapphire, the COF started at 0.15 and then quickly went down to the steady state value of 0.06.

When the temperature was increased to 300°C, the wear rate of the 80-V DLC coating increased to 4.48×10^{-5} mm³/m against the WC ball and to 2.22×10^{-4} mm³/m against the sapphire ball. Therefore, the interesting result that emerged from these observations is that at all three test temperatures, the wear rate of the 80-V DLC coating was the highest when worn against the 319 Al alloy pin.

At 300°C, for the 80-V DLC/WC pair, the average COF was 0.10 throughout the test. For the 80-V DLC/Sapphire pair, the COF was 0.04 at the beginning but increased to 0.30 around 800 revolutions, suggesting that the coating was worn down to substrate level at this sliding distance. As opposed to the DLC/319 Al pair, the DLC/WC and DLC/Sapphire pairs exhibited lower COF with increasing test temperature.

5.4.2. Effect of Deposition Conditions

The tribological behaviour of the 80-V DLC coatings was compared with that of the 60-V DLC and Graphit-iC DLC coatings using 319 Al alloy pins (see Table 3.1 and 3.2). At 25°C, the wear rates of the 60-V DLC and the Graphit-iC DLC coatings were similar to that of the 80-V DLC coating (**Figure 5.19**). When the tests were done at 120°C, the 60-V DLC coating exhibited an order of magnitude higher wear rate ($2.41 \times 10^{-4} \text{ mm}^3/\text{m}$) and the Graphit-iC DLC had an order of magnitude lower wear rate ($5.51 \times 10^{-6} \text{ mm}^3/\text{m}$) than the 80-V DLC coating ($3.08 \times 10^{-5} \text{ mm}^3/\text{m}$) tested at the same temperature. At 120°C, the 60-V DLC coating was significantly worn down so that the substrate was exposed as seen in **Figure 5.20**. Therefore, compared to the 80-V DLC coating, higher amount of damage was inflicted on the surface of the 60-V DLC coating at this temperature.

At 300°C, the 60-V DLC coating was totally removed from the contact surface. Material transfer from the 319 Al pin to the M2 steel disc surface took place. The wear rate of the 60-V DLC coating was $5.26 \times 10^{-4} \text{ mm}^3/\text{m}$ and that of the Graphit-iC DLC coating was $4.47 \times 10^{-4} \text{ mm}^3/\text{m}$ and thus all three wear rates were comparable. Although the wear rate of the Graphit-iC DLC coating was similar to the 60-V DLC and 80-V DLC coatings (**Figure 5.19**) because of the wider wear track caused by the deformation of the 319 Al pin, the Graphit-iC DLC coating was only partially worn, as opposed to the complete removal of the 60-V DLC and 80-V DLC coatings at 300°C. The average depth of the wear track in the Graphit-iC DLC was around 0.9 μm , indicating that about half of the coating still remained intact on the substrate.

The test temperature was further increased to 400°C and at this temperature only the Graphit-iC DLC coating was tested since the 60-V DLC and 80-V DLC coatings were already completely worn at 300°C. At 400°C, the pin-on-disc test was stopped at 250

revolutions since a large amount of adhesion and aluminum transfer occurred to the Graphit-iC DLC coating surface. A significant portion of the coating surface was covered by the adhered aluminum (**Figure 5.21**). The colour of the uncontacted area of the Graphit-iC surface changed from dark brown, the colour of as-deposited DLC, to black indicating the deterioration of the coating.

5.5. Discussion

5.5.1. Tribological Behaviour of the Non-hydrogenated DLC Coatings against 319 Al in Vacuum and Inert Gas Environments

For all three DLC coatings tested, higher COF values and wear rates occurred under vacuum and inert gas environments compared to those obtained in ambient air (**Figures 5.8.a-b** and **Figures 5.15.a-b**). These observations on the tribological behaviour of the non-hydrogenated DLC coatings against 319 Al were in agreement with the previous studies where other counterface materials (steel, ceramic) were employed [74, 82-84].

The high COF and wear rate of the non-hydrogenated DLC coatings in vacuum and inert gas environments are commonly attributed to the bonding interactions of the carbon atoms on the DLC coating surface with the atoms on the counterface material [21, 82, 83]. It has been suggested that when the pin passes through a certain point on the sliding track, it destroys the passivated surface state by friction and possibly by frictional heating, creating a fresh surface with dangling carbon bonds. If the carbon atoms do not fulfill their bonding requirements by the return of the pin, strong adhesive interactions occur between the surface carbon atoms and the atoms on the pin surface, causing high fluctuating COF and severe adhesive wear (**Figure 5.22.a-c**). The degree of adhesive interaction is expected to increase with the increasing chemical affinity of the pin material towards the DLC coating (C and Cr). The high chemical affinity of Al towards C to form Al_4C_3 (Equation 5.1) could lead to strong adhesion between the 319 Al and the non-hydrogenated DLC coating.



The standard Gibbs free energy of formation of Al_4C_3 is -203 kJ/mole at 300K [129]. Consequently, Al pieces became strongly adhered to the wear track of the non-hydrogenated DLC coating as shown in **Figures 5.10.a** and **b**.

319 Al (91 HV) itself is too soft to cause abrasive wear of the DLC coating unlike the hard counterface materials such as WC (1500 HV) and Al_2O_3 (2300 HV). Tribochemical wear of the DLC coating involving surface oxidation is unlikely for the tests performed in vacuum and nitrogen. Therefore, adhesive wear, as qualitatively described above, remains as the most plausible wear mechanism for the 319 Al pin / non-hydrogenated DLC coating tribo-pair in the vacuum and nitrogen environments.

5.5.2. Tribological Behaviour of the Non-hydrogenated DLC Coatings in Dry Air against 319 Al: Interaction of DLC Coating Surface with O_2

Although the introduction of dry air (0% RH) into the test chamber caused some reduction in the wear rate and the COF values of the non-hydrogenated DLC coatings, they were still high (**Figures 5.8.a** and **b**). The absence of adhered Al pieces on the wear track of the non-hydrogenated DLC coating at the end of the tests suggested that the adhesive wear of the non-hydrogenated DLC coating did not occur in dry air. Interaction of the oxygen molecules in dry air with the sliding surfaces is thought to prevent adhesion. It has been shown that, the oxygen molecules on the DLC coating surface become adsorbed, creating C=O bonds [105, 130, 131]. On the opposite side, the 319 Al pin quickly oxidized because of the very high tendency of aluminum oxidation (Equation 5.2). The Gibbs free energy of Al_2O_3 formation, ΔG° is -1582.3 kJ/mole at 300K [129].



Thus, while oxygen could prevent adhesive wear of the DLC coating, it is likely that it triggered a tribochemical wear process on the surfaces of the DLC coatings by oxidation [81, 88, 105, 130-133]. On each return of the pin to the same location on the DLC coating, it caused desorption of CO_2 by frictional and/or thermal means leading to progressive material loss.

It can be suggested that the major wear mechanisms of the non-hydrogenated DLC coatings against 319 Al in dry air are:

- i) The oxidational wear of the DLC coating during sliding, and
- ii) The abrasive wear of DLC caused by the hard, oxidized Al layers on the contact surface of the 319 Al pin (**Figure 5.23**). The formation of an oxidized tribolayer on the contact surface of the 319 Al pin was shown in **Figures 5.3.f** and **g**.

5.5.3. The Effect of Water Vapour on the Tribological Behaviour of Non-hydrogenated DLC Coatings against 319 Al

In comparison with the tests in vacuum, nitrogen, and dry air, the COF and the wear rate of the non-hydrogenated DLC coatings tested against 319 Al were significantly reduced in the ambient air with $\geq 20\%$ RH (**Figures 5.8.a** and **b**). It is well established that, similar to the graphite surfaces [112, 113], the improved tribological behaviour of the non-hydrogenated DLC coatings in ambient air is controlled by water molecules in the environment. It is generally agreed that water vapour in the air can passivate the “dangling carbon bonds” on the contact surface of the non-hydrogenated DLC coatings via adsorption and/or dissociation of water molecules [82, 83, 101].

The water in the test environment adsorbed by the non-hydrogenated DLC coating surface provides protection to the DLC coating and thus reduces the adhesive interactions with the counterface. Together with the formation of the easy-to-shear transfer layer, the adsorption of water vapour causes the COF to drop to values around 0.07-0.20 from 0.55-1.0 that were typically observed in vacuum and inert gas environments [74, 76, 84, 105].

As explained above, adhesive wear is not expected to be operative in air with humidity levels greater than 20%. Similar to the dry air tests, the possible operating wear mechanisms in ambient air are:

- i) Oxidational wear of the DLC during sliding,
- ii) Abrasive wear caused by the oxidized Al layer and debris.

Compared to the tests in dry air, the much reduced wear rate of the non-hydrogenated DLC coatings in ambient air is due to presence of water vapour, which passivates the non-hydrogenated DLC surface via adsorption and also promotes the

formation of an easy-to-shear carbonaceous layer covering most of the contact surface of the 319 Al pin, further reducing abrasive wear (**Figure 5.24**).

5.5.3.1. The Role of Material Transfer to the Counterface on Very Low COF

To provide a better understanding of the role of the transfer layer in reducing the COF of the non-hydrogenated DLC coatings, vacuum pin-on-disc tests were performed after some initial sliding in ambient air. The principal hypothesis was that the transfer layer formed in ambient air would help reduce the COF in vacuum. **Figure 5.25.a** shows the COF between the 319 Al pin and the 80-V DLC coating where a running-in period of 8.5×10^2 revolutions in ambient air (52% RH) was allowed prior to pumping down the test chamber to 1.07×10^{-2} Pa. The COF decreased from 0.15 in ambient air (regime 1 in **Figure 5.25.a**) to very low values of 0.006 with decreasing chamber pressure and maintained its low value for some period of time (regime 2 in **Figure 5.25.a**). This very low COF period came to an end with an increase in COF to 0.55 accompanied by large fluctuations (regime 3 in **Figure 5.25.a**).

The very low COF values can be explained as follows: The transfer layer formed in air with 52% RH (**Figure 5.4.c**) was continuously consumed and re-generated maintaining a certain equilibrium thickness during sliding in air. At the time the pumping down of the chamber was started, the DLC coating was running against this transfer layer. At pressures of 0.173 Pa (1.297×10^{-3} Torr) and lower, the atmosphere in a typical vacuum chamber consists of mainly water vapour due to the desorption of the water that was previously adsorbed by the stainless steel chamber walls [134]. In this case, the passivation of the coating surface by the adsorption of water vapour is still possible. Together with the tribolayer formed on the contact surface of the 319 Al pin, this passivation results in very low COF values.

Examination of several COF curves showed that the very low COF values were reached and stabilized around 0.173 Pa and further decrease in pressure did not cause any further significant drop in the COF values. The very low COF regime lasted until the tribolayer became consumed. When the test was started directly in the vacuum environment, the very low COF was not observed because of the absence of the carbonaceous tribolayer on the contact surface of the 319 Al pin.

The same test procedure was implemented for the 80-V DLC coating tested against the WC ball. First, the WC ball was tested against the 80-V DLC coating for 3×10^3 revolutions in ambient air (22% RH) to form a transfer layer similar to that shown in **Figure 5.7.b**. The resulting shape of the COF curve shown in **Figure 5.26** was similar to the one in **Figure 5.25**. During chamber evacuation, the COF decreased from 0.09 to 0.006. The low COF period ended around 5.2×10^3 revolutions and the COF rapidly increased to the values (0.52) typically encountered in the vacuum tests without first running-in in ambient air. Therefore, the test with WC has provided additional proof that the COF of DLC coatings was controlled by the formation of transfer layers on the counterface.

5.5.4. Tribological Behaviour of the Non-hydrogenated DLC Coatings in an H₂-He Environment

As shown in **Figures 5.13.a-b**, and **5.14.a-b**, the low COF values of 0.015 were observed when the Graphit-iC DLC was run against 319 Al and WC in the H₂-He environment. The hydrogen in the test environment is responsible for the low COF values since the helium alone caused high COF and high wear as shown previously (**Figure 5.9.c**). It is well known that the non-hydrogenated DLC coatings can have low COF only when there is a species in the test atmosphere that can decrease the interactions between the sliding surfaces by passivating them. Hydrogen molecules must have created this passivation by meeting the bonding requirements of the carbon atoms on both surfaces.

5.5.4.1. Material Transfer to the Contact Surface of the 319 Al Pin

The examination of the sliding tracks of the DLC coating tested in the H₂-He environment revealed that the sliding tracks were smooth and there was only a minute amount of wear, which probably occurred during the initial high COF period (**Figures 5.13.a-b**, and **5.14.a-b**). The SEM image of the contact surface of the 319 Al pin that was run against the Graphit-iC DLC in H₂-He at 0.12 m/s showed the presence of a transfer layer (**Figures 5.27.a** and **b**). The EDS analysis of the transfer layer (**Figure 5.27.c**) showed that it was essentially composed of carbon and chromium. Therefore, it is clear

that when the COF was very low in H₂-He environment, the non-hydrogenated DLC was running against a carbonaceous counterface, not the bare 319 Al pin surface.

It is concluded that the occurrence of the high COF period at the beginning of the tests in hydrogen can be attributed to the process of transfer layer formation on the counterface. In order to confirm this idea, two different tests were performed.

In the first test, after the system reached the very low COF state in H₂-He environment, the sliding was paused for 30 seconds and then resumed. There was no high COF period when the test was re-started (**Figure 5.28**). This procedure was repeated several times and the results were the same. Therefore, this test showed that the carbonaceous transfer layer, once formed, was able to maintain itself during sliding.

In the second test, prior to testing in H₂-He environment, the 319 Al pin was run against the non-hydrogenated DLC for 1×10^3 revolutions in ambient air (32% RH) in order to form a transfer layer on the contact surface of the 319 Al pin. Then, the test was stopped and the chamber was evacuated to 5.45×10^{-3} Pa. After flushing with nitrogen, the chamber was evacuated to 5.45×10^{-3} Pa again. Finally the H₂-He environment was introduced and the test was re-started. As seen in the corresponding COF curve (**Figure 5.29**), there was no occurrence of the high COF regime in H₂-He environment this time and the COF decreased to the very low values immediately. Therefore, these tests have proven that i) the observed initial high COF regime in H₂-He environment corresponded to the process of the transfer layer formation on the counterface, ii) a carbonaceous counterface was essential to achieve very low COF values with non-hydrogenated DLC coatings, iii) the transfer layers forming in ambient air and H₂-He environment have similar properties.

5.5.4.2. The Role of Hydrogen Pressure on the Very Low COF Behaviour

To investigate the stability of the very low COF regime of the non-hydrogenated DLC coatings under H₂-He environment, the following pin-on-disc test was performed: First the test was started in the hydrogen environment and was allowed to run in the very low COF period for a certain amount of sliding (5×10^3 revolutions). Then the chamber was pumped down to 9.5×10^{-3} Pa while the sliding continued. When the COF increased to the high values (around 0.75), the chamber was refilled with hydrogen (101.3 kPa) and

the test was allowed to continue until the very low COF state was restored. This procedure was repeated several times. The change in the total pressure of the chamber and the variation of the COF with respect to number of revolutions is given in **Figure 5.30**. It was observed that the COF started to increase as soon as the pressure was decreased. Similar to the beginning of the test, a high COF regime was observed each time the H₂-He mixture was re-introduced into the chamber, which is followed by the very low COF (0.010-0.015) values. This test showed that the easy-to-shear carbonaceous material at the sliding interface was very thin as it was consumed quickly in the absence of significant amount of hydrogen in the test environment.

To explore the dependency of COF to the amount of hydrogen, the test described above was modified such that the chamber was refilled with a lower amount of gas after each pumping down cycle rather than filling to 101.3 kPa. It was found that the tribosystem was able to reach very low COF (0.015) values at H₂-He pressures as low as 4.7 kPa (**Figure 5.31**). The technical difficulties prevented testing at pressures lower than 4.7 kPa. It was observed that the number of revolutions needed to reach the very low COF regime increased with decreasing back-fill pressure of H₂-He. For example, restoring the very low COF regime took 1,130 revolutions at 4.7 kPa as compared to 300 revolutions at 101.3 kPa. In other words, higher amount of hydrogen in the test environment accelerated the creation of the very low COF regime but, once created, very low COF regime can still be maintained at much lower pressures of hydrogen.

5.5.4.3. Interaction Mechanisms of Hydrogen with the Sliding Surfaces

To learn more about the nature of the interactions between the sliding surfaces and the hydrogen, the worn and unworn sections of the non-hydrogenated DLC and the contact surface of the 319 Al alloy pin that were run in hydrogen were analyzed using the Micro-Raman technique (see Section 3.1.3.2). Micro-Raman analysis is an ideal way to detect the presence of hydrocarbons in a given material. No sign of C-H stretching (hydrocarbon formation) was detected on the sliding track of the DLC coating or on the contact surface of the 319 Al pin (**Figure 5.32**). This can be due to i) there was no chemisorption (and thus no hydrocarbon bond formation), or ii) the amount of chemisorption was so little that it could not be detected. The fact that the COF increased

immediately with lowering the hydrogen pressure (**Figures 5.30 and 5.31**) supports the latter. If there was an accumulation of C-H bonds, then the COF should have stayed at the low COF region for a longer duration even if there was no further C-H bond production.

Compared to the spectrum obtained from the unworn section of the DLC coating, the only observed difference of the spectra obtained from the edge of the wear track and that of the transfer layer formed on the 319 Al pin was the increase in the peak intensities around 1370 and 1550 cm^{-1} . This change corresponds to the friction-induced graphitization, which is a well-known structural transformation, observed as a result of dry sliding of DLC coatings [79, 89, 90, 92, 99]. The transfer layer is, therefore, more crystalline and graphite-like compared to the original coating. The destruction of the cross-linked graphite domains during sliding has probably increased the graphitic character of the transfer layer.

Since the transfer layer is graphite-like, it is reasonable to assume that the mechanisms of the interactions between hydrogen and graphite can help understand the interactions between hydrogen and the non-hydrogenated DLC. The adsorption of atomic and molecular hydrogen on graphite surfaces has been studied both experimentally and theoretically. It was shown that the dissociation of the molecular hydrogen into two hydrogen atoms and their chemisorption by the edge carbon atoms of the graphite planes is thermodynamically favourable [135-137]. It requires 436 kJ of energy to break one mole of H-H bonds (Equation 5.3) and approximately 831.6 kJ of energy is released when two moles of C-H bonds are formed (Equation 5.4) [138].



Therefore, the reaction of breaking of an H-H bond and forming two C-H bonds is energetically favoured. This shows that the friction-assisted creation of C-H bonds at the sliding surfaces is feasible (**Figure 5.33**).

5.5.5. Elevated Temperature Tribological Behaviour of Non-hydrogenated DLC Coatings

As shown in Sections 5.1.4., 5.2.3, and 5.3.3, the all three DLC coatings (60-V, 80-V and Graphit-iC) showed low friction and wear rates at 25°C in ambient air (15% RH). However, upon heating to 120°C both the 60-V DLC and 80-V DLC coatings suffered high friction and wear (**Figure 5.19**). The amount of wear was higher for the 60-V DLC coating compared to that of the 80-V DLC coating. When the temperature was increased to 300°C, the wear of the Graphit-iC also increased dramatically. This observation is consistent with the previous studies in that the wear rate of various types of DLC coatings (a-C and a-C:H) increases with increasing test temperature [95-97].

Two reasons are suggested to explain the observed accelerated wear of the DLC coatings with an increase in the test temperature (**Figures 5.19**). The first one is the inefficiency of the passivation mechanism of the DLC coating surfaces with water vapour at elevated temperatures. Similar to graphite [112, 113] the low friction and wear behaviour of non-hydrogenated DLC coatings is due to the adsorbed species (water vapour in ambient air, and other polar gas molecules) on the surface. In the absence of adsorbed species (e.g. in vacuum or in inert gas environment), the carbon atoms on the non-hydrogenated DLC coating surface interact with the counterface causing high wear rates and friction [82, 83, 101].

As the test temperature increased, the amount of water remaining adsorbed on the coating surface decreased [139] and hence the efficiency of the coverage of the coating surface by water molecules decreased. In this case, the DLC coating surface became unprotected and the surface carbon atoms started interacting with the counterface atoms to meet their bonding requirements rather than being passivated through the water adsorption mechanism. Then, in each rotation, the pin removed a certain amount of carbon from the coating by breaking the bonds at the point of contact. The removed carbon either i) became oxidized to CO₂, or ii) transferred to the counterface, or iii) turned into loose debris. Therefore the depth of the wear track increased with each revolution.

The second cause for the poor elevated temperature tribological behaviour of the non-hydrogenated DLC coatings was the loss of the room temperature stability. It was

suggested that the high hardness of this type of DLC coating was due to some cross-linking between graphite planes [140, 141]. Heating the 60-V DLC and 80-V DLC coatings to a relatively low temperature of 120°C could be sufficient to weaken the cross-linking between the graphite planes. Compared to the 60-V DLC coating, the higher wear resistance of the 80-V DLC coating at this temperature suggests that increasing the bias voltage during deposition was helpful in stabilizing the structure of the DLC coating. For the Graphit-iC, the abrupt increase in the wear rate did not occur before 300°C rather than 120°C indicating that the Graphit-iC DLC had a more thermally stable structure compared to the 60-V DLC and 80-V DLC coatings. This should be due to the better optimization of its deposition conditions.

The effect of bias voltage can be explained as follows: It is difficult to obtain a dense film if the sputtered carbon atoms do not hit the substrate with sufficient velocity. Increasing the kinetic energy (i.e. velocity) of the sputtered carbon atoms is possible by increasing the bias voltage. The 80-V DLC is thought to have higher density than 60-V DLC since the kinetic energy of the carbon atoms was higher under higher bias (60 V vs. 80 V). An increase in density resulted in a higher stability of the coatings and also provided higher resistance against high temperature oxidation as previously shown by Miyoshi [104].

5.5.5.1. Stability of the Coatings at High Temperature

Investigation of the static oxidation behaviour of the DLC coatings by annealing them at 300°C in air was used as a method to assess the stability of their structures. For this purpose, EDS analyses were made on the 60-V DLC and 80-V DLC coatings at three different states; i) as-deposited, ii) annealed at 300°C for 7.7 minutes and iii) annealed at 300°C for 77 minutes. All EDS curves were taken from the unworn portions of the coatings. The EDS spectrum of the as-deposited coatings mainly consists of C, Ar and Cr peaks. The argon was present in the coatings since it was used as the sputtering gas. After annealing at 300°C for 7.7 minutes, the oxygen peak of the annealed 60-V DLC coating became somewhat higher than that of the as-deposited coating. For the 80-V DLC, there was no difference between the EDS curves taken from as-deposited coating and the one annealed for 7.7 minutes.

To study the effect of this short time annealing on the wear behaviour, 60-V DLC and 80-V DLC samples annealed at 300°C for 7.7 min were tested against 319 Al at 25°C in ambient air. The wear rates of the annealed samples were higher than those of the as-deposited coatings tested at 25°C, but much lower than those of tested at 300°C (**Figure 5.34**). This suggests that any change in the DLC film (structural and/or oxidational) as a result of this short time annealing was confined to the top portion of the coating.

Figure 5.35.a shows the EDS curves taken from the unworn areas of the as-deposited 60-V DLC and the one annealed at 300°C for a longer period of 77 min (1×10^4 revolution-test duration). **Figure 5.35.b** shows the curves for the 80-V DLC coating at the same conditions. Compared to the as-deposited coatings, the EDS curves of the both 60-V DLC and 80-V DLC coatings annealed at 300°C for 77 minutes showed reductions in Ar signals, and increases in O, Cr and Fe signals. The reduction in carbon signal was more clearly observed in 60-V DLC and this suggests that some of the carbon left the disc surface by oxidation to CO₂ during annealing. The sharp decrease in the ratio of Ar to Cr signals (from 1.08 for as-deposited coating to 0.38 for the annealed coating) indicates that some Ar was also released from the coating structure during annealing. Comparison of the **Figures 5.35.a** and **b** shows that changes (oxidation and Ar release) due to annealing were more pronounced for the 60-V DLC coating. Therefore it can be said that the structure of the 60-V DLC coating was less stable and less dense compared to 80-V DLC coating, which allowed a higher degree of oxidation.

5.5.5.2. Comparison of the Wear Mechanisms of DLC Coating against 319 Al with WC and Al₂O₃

In their initial conditions (at the onset of the wear test), the calculated maximum Hertzian contact pressure exerted on the 80-V DLC coating was 0.88 GPa by the 319 Al pin (4 mm diameter), 1.84 GPa by the WC ball (3.18 mm diameter) and 1.71 GPa by the sapphire ball (3.18 mm diameter) under the applied load of 5 N. Once the test started, the tip of the 319 Al pin deformed plastically and its contact surface area increased, and hence the contact pressure exerted by the 319 Al pin decreased. The SEM images of the WC ball and the 319 Al pins showed that the 319 Al pin had a larger contact area (0.061 mm²) than the WC ball (0.009 mm²) at 25°C. The contact area increased as the test

temperature was increased from 25 to 300°C (**Figure 5.36.a-c**). Therefore, the contact pressure exerted by the 319 Al pin on the non-hydrogenated DLC coatings continued to decrease with increasing test temperature. The increase in the contact area of the 319 Al pin was due to the combined effect of temperature and the applied load (softening and deformation). In the temperature range studied, no softening due to thermally activated plastic deformation of the WC (WC-Co eutectic at 1558 K, $T_m(\text{Co})=1767$, $T_m(\text{W})=3052$) or sapphire ($T_m = 2323$ K) balls can be expected. Although the pressure exerted by the 319 Al pin was lower than the pressures exerted by the WC and sapphire, and the pressure decreased even more during the elevated temperature tests, the 319 Al pin (91 HV) caused higher wear of the 80-V DLC coating than the harder materials WC (1500 HV) and sapphire (2300 HV) as shown in **Figure 5.18**. For example, the average depth of the wear track created on the 80-V DLC coating at 120°C was 0.67 μm when tested against 319 Al, 0.09 μm against WC and 0.12 μm against sapphire. The three-dimensional surface profiles of the sections of the wear tracks of the 80-V DLC coating tested against 319 Al and WC at 120°C, given in **Figures 5.37.a** and **b**, show that more damage was inflicted by 319 Al.

The observation that the sapphire ball caused a higher wear rate than the WC ball at 120 and 300°C (**Figure 5.18**) was not unusual since the sapphire ball is harder than the WC ball and hence caused more wear. However, it was rather unexpected to observe that 319 Al, which is 23 times softer than sapphire and 15 times than WC, caused more wear of the DLC coatings than sapphire and WC. It is clear that the difference in the contact stress values cannot explain the observed differences in the wear behaviour of the DLC coatings.

To account for the relatively high wear rate caused by the soft aluminum alloy, a two- and three-body abrasive wear model is proposed as schematically illustrated in **Figures 5.38.a-f**: The surface of the aluminum became oxidized (**Figures 5.38.b** and **c**). During the initial stage of the experiment, the wear of the DLC coating occurs by the oxidation of the DLC and the abrasive action of the Al_2O_3 layer. The wear rate is thus expected to be similar to by the sapphire ball. As the wear and oxidation of the 319 Al progress, the oxide layer on 319 Al surface cracks, delaminates, and fragments into loose debris (**Figures 5.38.d** and **e**). Some of the debris acts as abrasive particles at the sliding

interface, others are embedded on the 319 Al pin surface (**Figure 5.38.f**). Therefore, a three-body abrasion mechanism becomes operative. Since the mechanisms of oxidation and debris generation are continuous throughout the pin-on-disc test, there is a continuous supply of freshly made abrasive aluminum oxide particles at the sliding interface, causing severe wear of the non-hydrogenated DLC coating. In the case of the sapphire ball, only a negligible amount of debris was generated from it due to its high hardness. Therefore, there was no three-body abrasive wear mechanism operating. The two-body abrasive wear caused by the sapphire ball was also limited due to its starting smooth surface. This explains why the 319 Al pin created a deeper wear track than the sapphire (Al_2O_3) ball (0.67 versus 0.12 μm at 120°C). The formation of oxidized tribolayer on the contact surface of the 319 Al pin and the presence of debris are visible in **Figures 5.3.f** and **5.32.c**. The EDS analysis of the tribolayers (**Figure 5.3.g** and **5.32.d**) clearly shows the extent of oxidation, in support of the proposed mechanism. Since the non-hydrogenated DLC coatings started to deteriorate with increasing temperature, the 319 Al pin with a much larger contact area was able to cause higher wear of the DLC coating by the abrasive action of the generated debris particles although it exerted much less contact stress compared to the other counterface materials.

5.6. Summary and Remarks

5.6.1. Effect of Test Atmosphere

1. The non-hydrogenated DLC coatings (60-V, 80-V DLC and Graphit-iC DLC) experienced high COF (≥ 0.44) and high wear rates ($\geq 3.28 \times 10^{-5} \text{ mm}^3/\text{m}$) in vacuum, nitrogen and dry air (0% RH) against 319 Al and WC.

2. The non-hydrogenated DLC coatings tested against the 319 Al alloy showed higher wear rates than the ones tested against WC. For example, the wear rates of the 80-V DLC coatings tested in nitrogen were $3.63 \times 10^{-4} \text{ mm}^3/\text{m}$ against 319 Al and $1.09 \times 10^{-4} \text{ mm}^3/\text{m}$ against WC.

3. Low COF (≤ 0.16) and low wear rates ($\leq 2.31 \times 10^{-6} \text{ mm}^3/\text{m}$) of the DLC coatings were observed against 319 Al in air with relative humidity $\geq 20\%$. The same observation was also done against WC. This indicated that the presence of water vapour

in the test environment was essential to reach the low COFs and wear rates of the non-hydrogenated DLC coatings except testing in hydrogen gas environment.

4. Increasing the relative humidity from 20 to 85% slightly decreased the COF and wear rates against 319 Al, but increased that against WC.

5. In ambient air with $\geq 20\%$ RH, a carbonaceous easy-to-shear transfer layer formed on both counterface materials. Sliding in other environments namely in vacuum, nitrogen and dry air, did not cause the formation of this carbonaceous tribolayer.

6. The formation of the carbonaceous easy-to-shear tribolayer on the counterface material and the passivation of the non-hydrogenated DLC coating surface by adsorption and dissociation of the water molecules were suggested as the two possible mechanisms responsible for the low COF and wear rates of the non-hydrogenated DLC coatings in air with humidity. Formation of tribolayers on both 319 Al and WC had an overwhelming influence compared to the hardness of the counterface material which was not the main factor determining the tribological behaviour of non-hydrogenated DLC coatings in humid air.

7. A very low COF (0.006) was observed under vacuum after an initial running-in period (COF = 0.6-0.8) in ambient air during which a transfer layer was formed on the counterface materials.

8. The non-hydrogenated DLC coatings exhibited low COF values (0.01-0.02) against aluminum when molecular hydrogen was present the test environment. The very low COF values were reached after an initial high COF (0.70 ± 0.15) period.

9. The initial high COF period in hydrogen environment corresponded to the formation of a carbonaceous transfer layer on the contact surface of the 319 Al pin. The presence of this carbonaceous transfer layer on the counterface was found to be essential to reach the very low COF state in the presence of hydrogen.

10. It was proposed that the very low COF state was maintained by the instantaneous passivation of available carbon bonds by the hydrogen molecules. The chemisorption of the hydrogen molecules, which consist of the breaking of the H-H bonds and the formation of C-H bonds, is suggested as a possible mechanism for the passivation. When C-H bonds broke due to frictional and/or thermal processes, hydrogen molecules are instantaneously chemisorbed forming C-H bonds.

11. Changing the test environment from a 40% H₂ – 60% He atmosphere (101.3 kPa) to vacuum caused the COF to increase immediately to 0.65-0.80, suggesting that the production of the C-H bonds was limited to the very top layers of the both sliding surfaces.

12. Adhesive wear was the dominant wear mechanism in vacuum and nitrogen atmospheres, i.e. when the materials in contact did not have other appropriate species, such as O₂ and H₂O in the test environment, to meet their bonding requirements. Chemical affinity of the counterface material towards the DLC coating promoted adhesive wear.

5.6.2. Effect of Temperature:

1) The wear resistance of the non-hydrogenated DLC coatings is poor at elevated temperatures. The mechanisms that provide the high wear resistance of the coating in ambient temperature cease to operate at temperatures as low as 120°C. Annealing at elevated temperatures in air causes the loss of the stability and the significant oxidation of the coating.

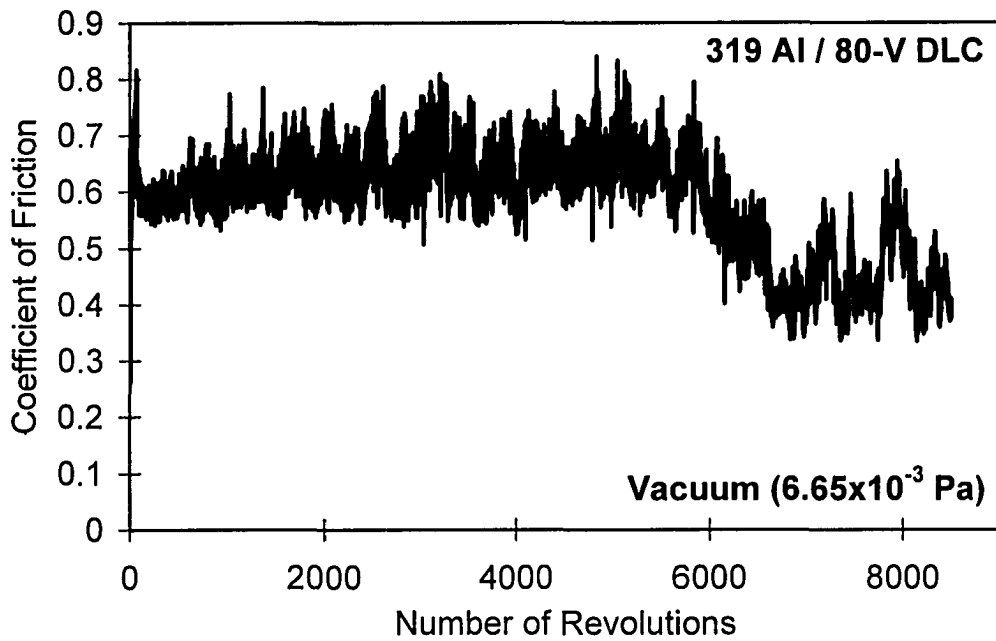
2) The tribological performance of the DLC coatings may be improved by optimizing the deposition parameters. For example, increasing the bias voltage improves the coating stability and wear resistance.

3) Different counterface materials caused differences in the wear behaviour of the DLC coatings. Although much softer than WC and sapphire, the 319 Al alloy inflicted more severe wear damage to the DLC coatings both in terms of wear volume and depth of the wear track especially at elevated temperatures. A two- and three-body abrasive wear model, which considers the continuous generation of highly oxidized aluminum layer and particles at the sliding interface, is proposed to explain this observation.

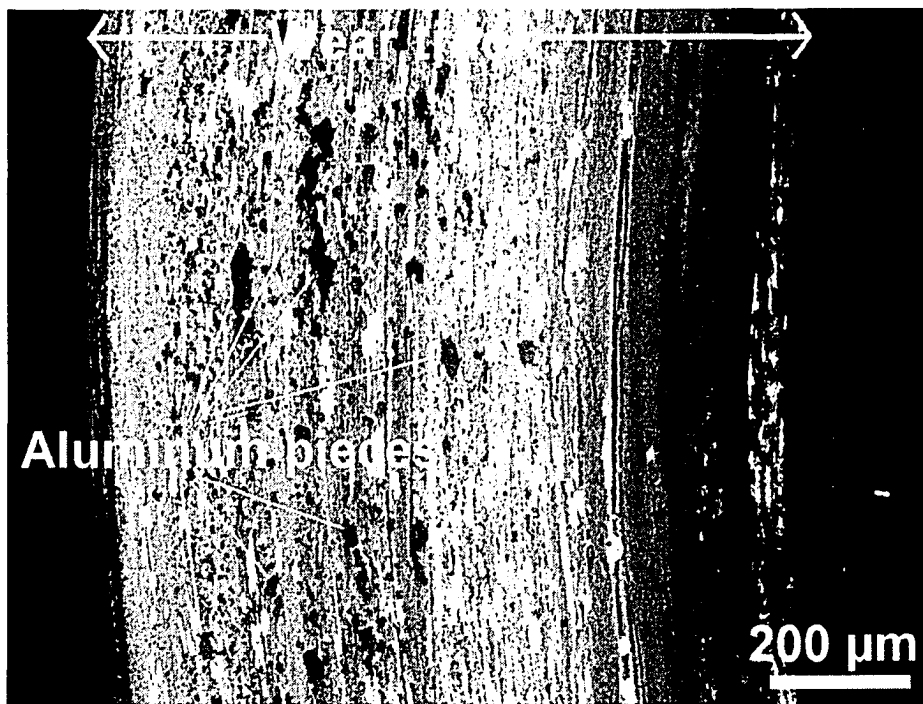
5.7. Outlook

This chapter showed that the extrinsic factors such as the composition of the testing environment and the temperature have dramatic effects on the adhesion and transfer behaviour of 319 Al to DLC surfaces. On the other hand, the effects of intrinsic factors on adhesion and material transfer, i.e. effect of the material properties of the

sliding pair, were not very clear. **Chapter 6** is devoted to studying of the role of material properties of the sliding pair on the adhesion and transfer phenomena. The hardness and thermal conductivities of the sliding materials, the chemical affinities of the sliding materials against each other and to the species in the environment were put under investigation. In addition to 319 Al examined in this chapter, commercial purity Al, Cu and Ti were tested against the non-hydrogenated DLC, TiB₂, and CrN coatings in ambient air and argon atmospheres. TiB₂ and CrN were selected because of their different adhesion and transfer behaviour of 319 Al to their surfaces as presented in **Chapter 4**.

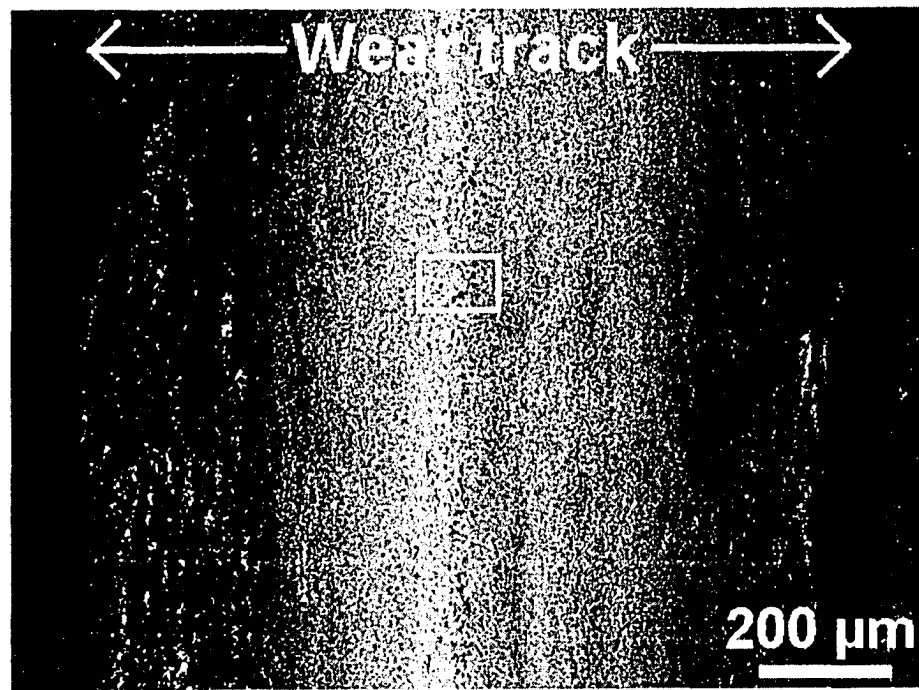


a)

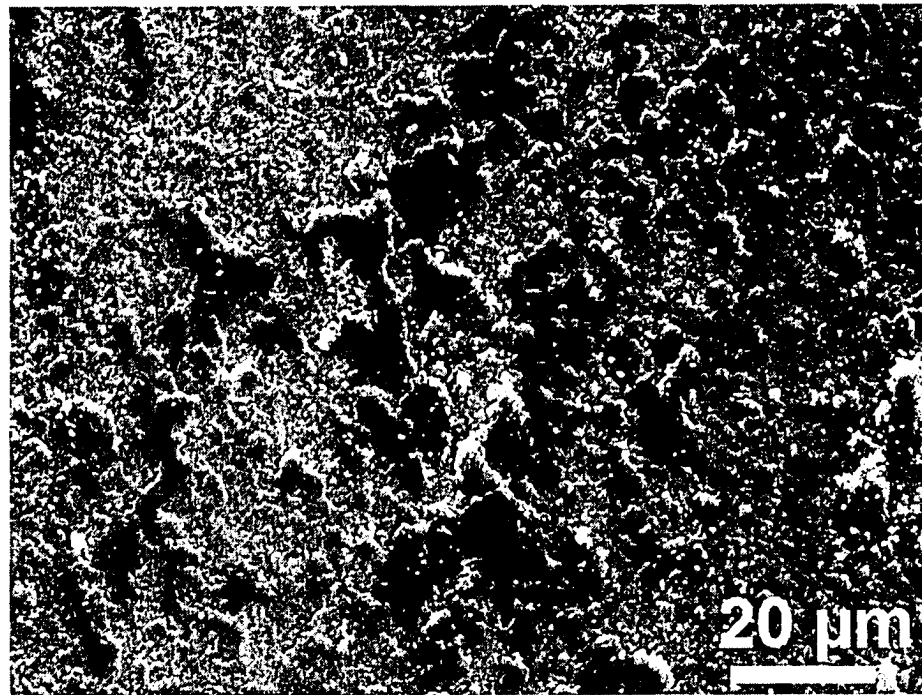


b)

Figure 5.1. a) The COF curve between the 80-V DLC coating and 319 Al during sliding in vacuum (6.65×10^{-3} Pa) for 8.5×10^3 revolutions, b) The SEI SEM image of a section of the wear track of the 80-V DLC coating. The DLC coating was heavily worn. Adhered Al pieces were observed on the wear track. The applied load and sliding speed were 5 N and 0.12 m/s.



a)



b)

Figure 5.2. SEI SEM images of a) a section of the wear track of the 80-V DLC coating tested against 319 Al in nitrogen (101.3 kPa) for 3.5×10^3 revolutions, and b) enlarged view of the location indicated in a) showing the aluminum transfer. The applied load and sliding speed were 5 N and 0.12 m/s.

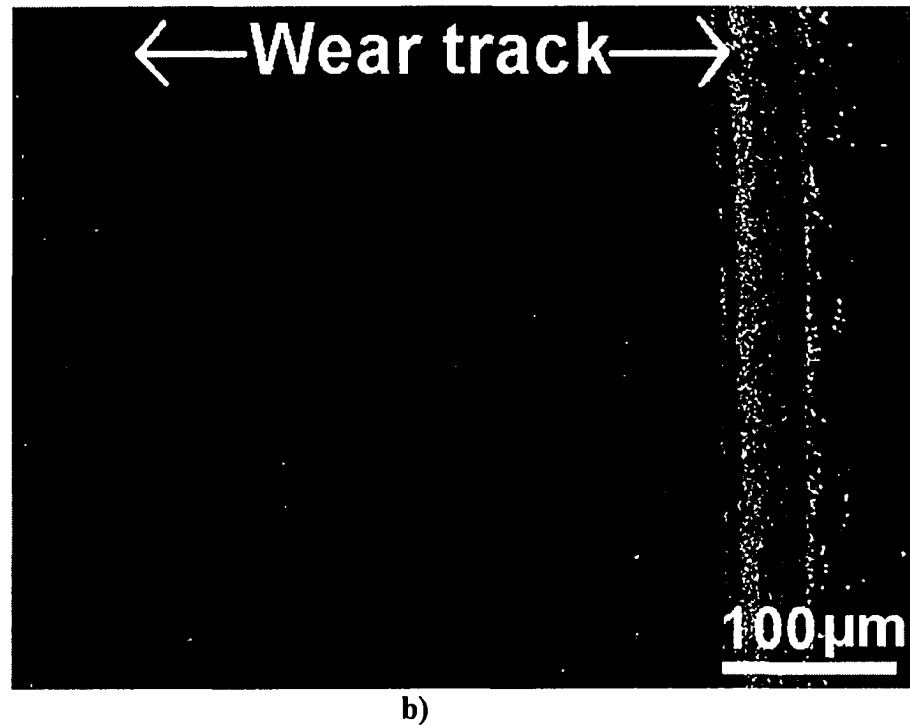
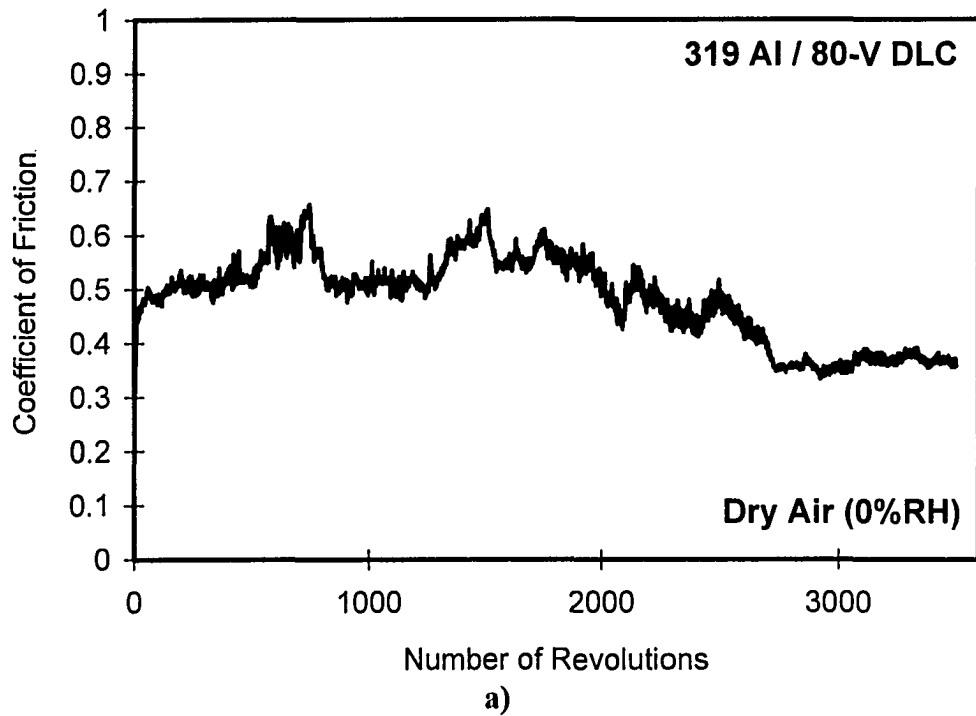
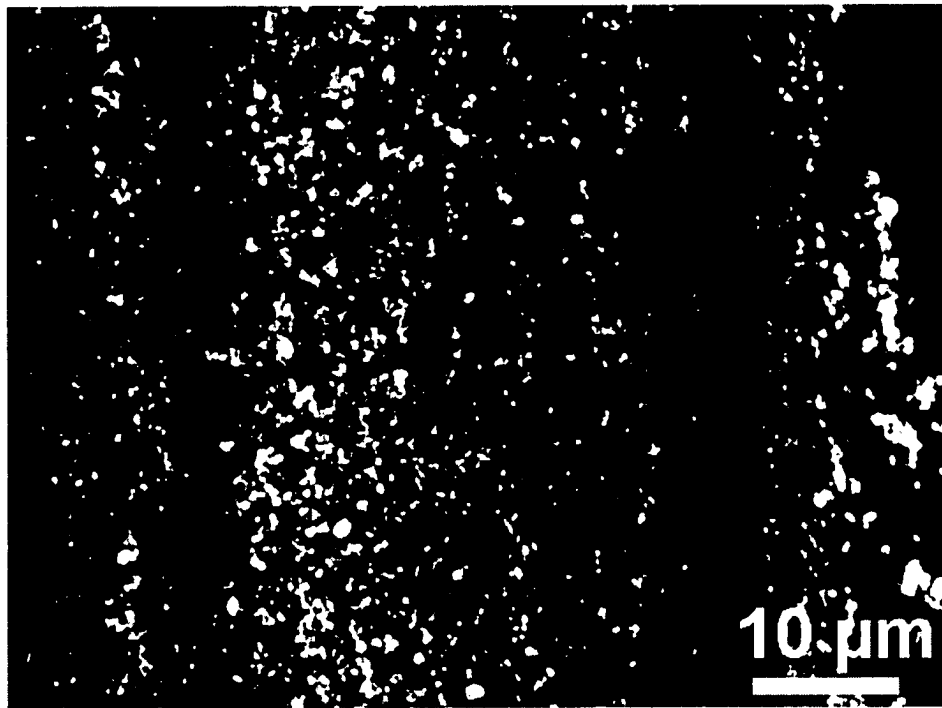
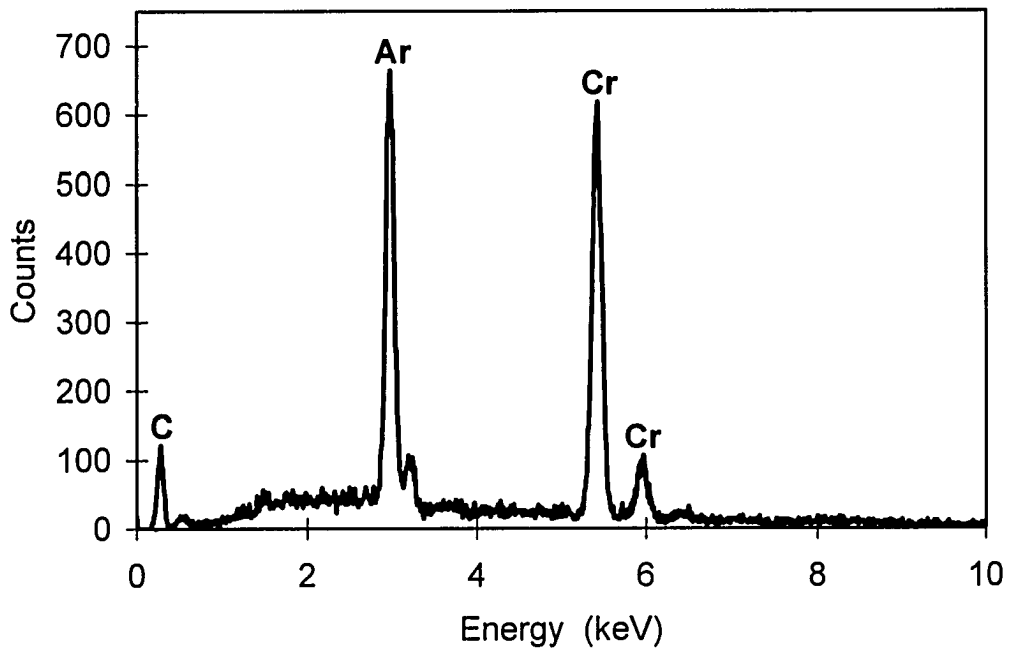


Figure 5.3. a) The COF between the 80-V DLC coating and 319 Al during sliding in dry air for 3.5×10^3 revolutions, b) the SEM image of a section of the wear track of the 80-V DLC coating.



c)



d)

Figure 5.3. c) A closer look at the debris generated during sliding between 319 Al and 80-V DLC coating in dry air, d) EDS analysis of the 80-V DLC coating surface.

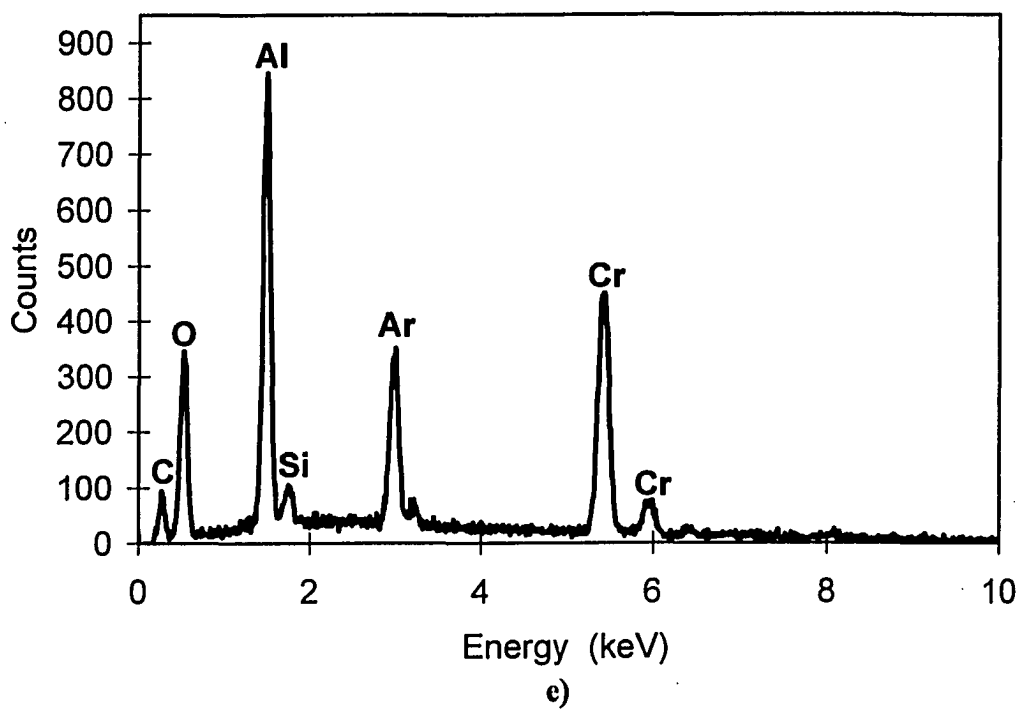
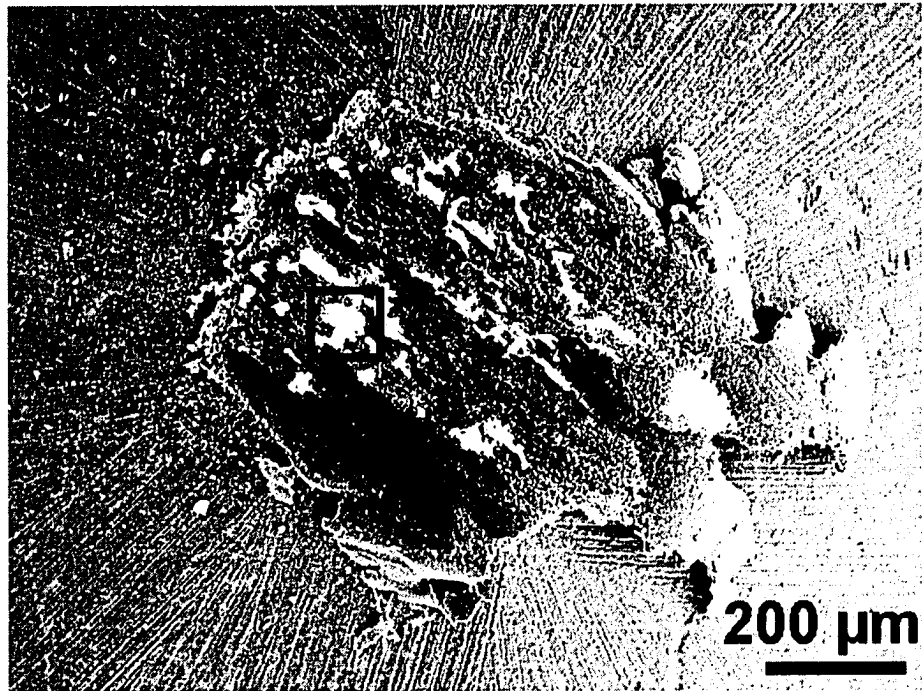
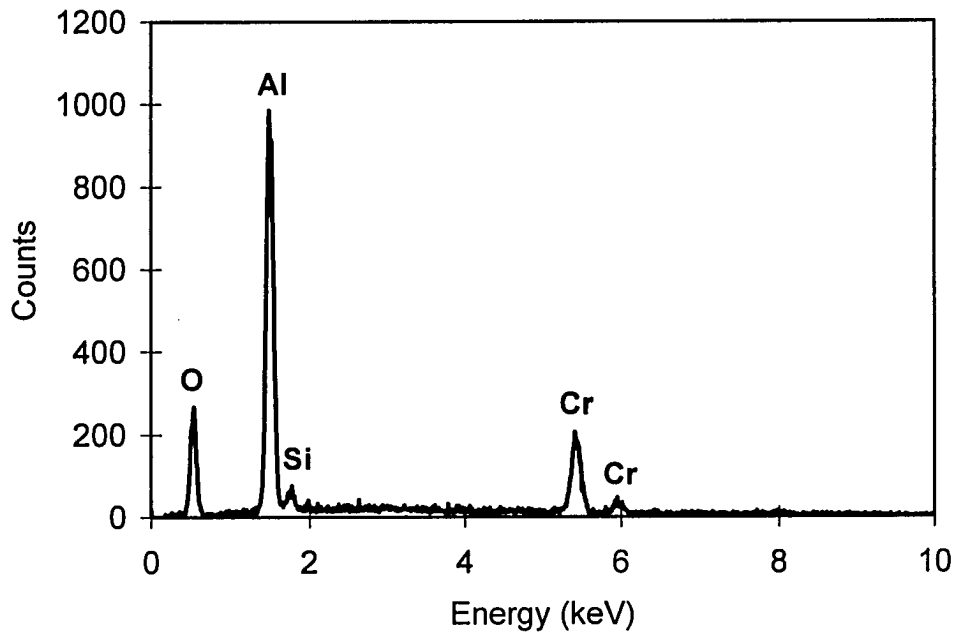


Figure 5.3.e) EDS curve of a typical debris particle while it is analysed on the coating surface. The applied load and sliding speed were 5 N and 0.12 m/s.

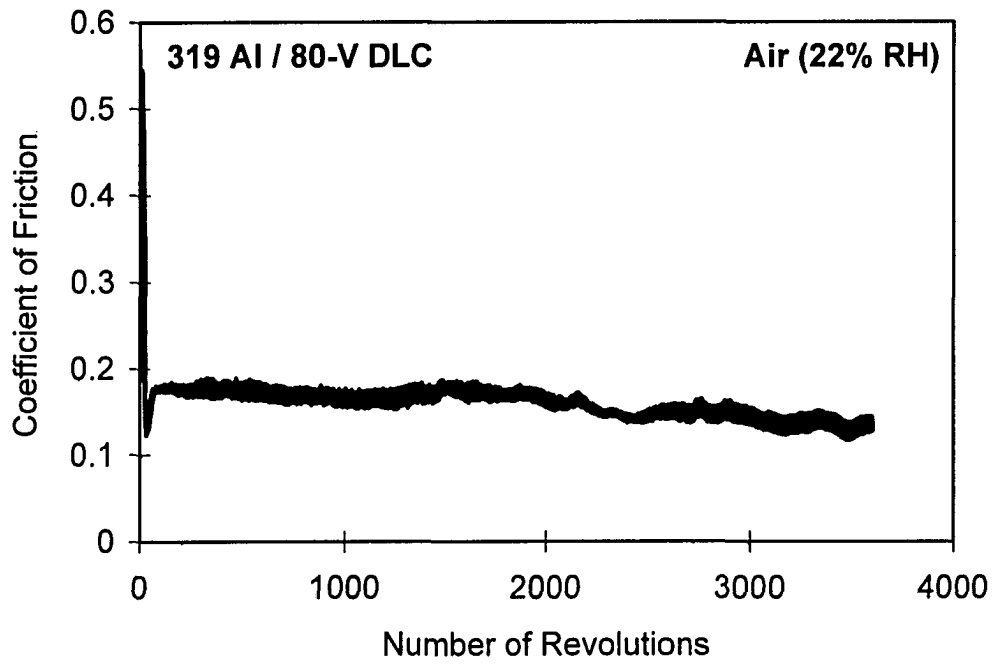


f)

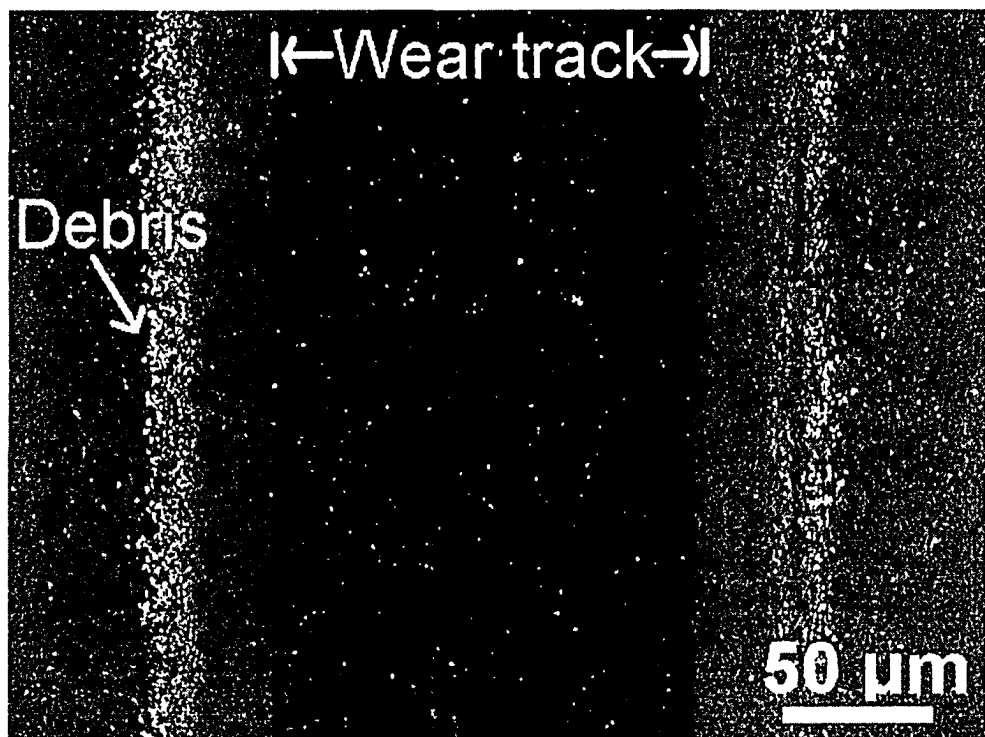


g)

Figure 5.3. f) SEM image of the contact surface of the corresponding 319 Al pin, and g) the EDS analysis of the location indicated in b).

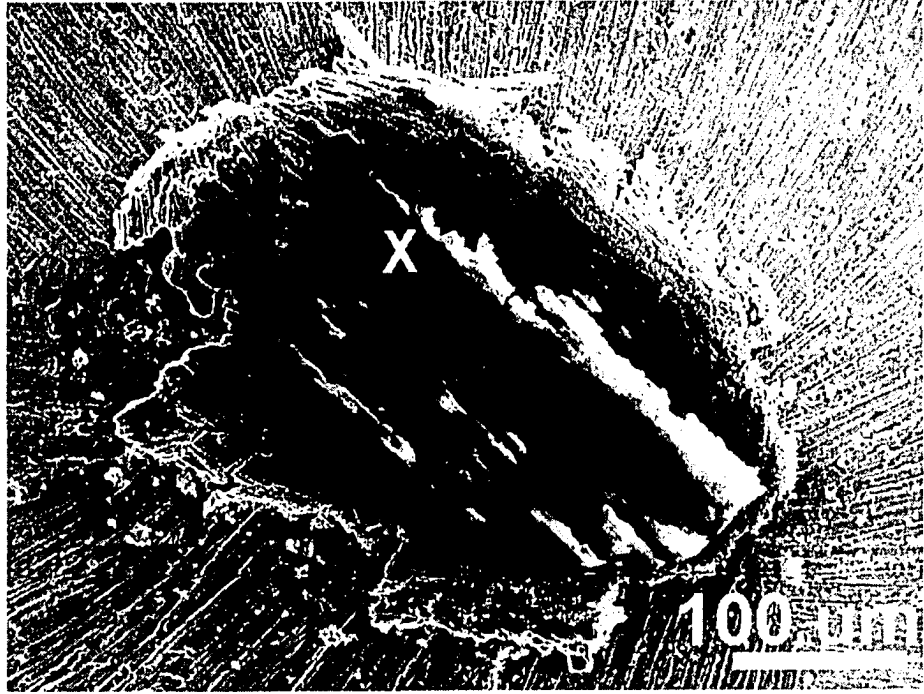


a)

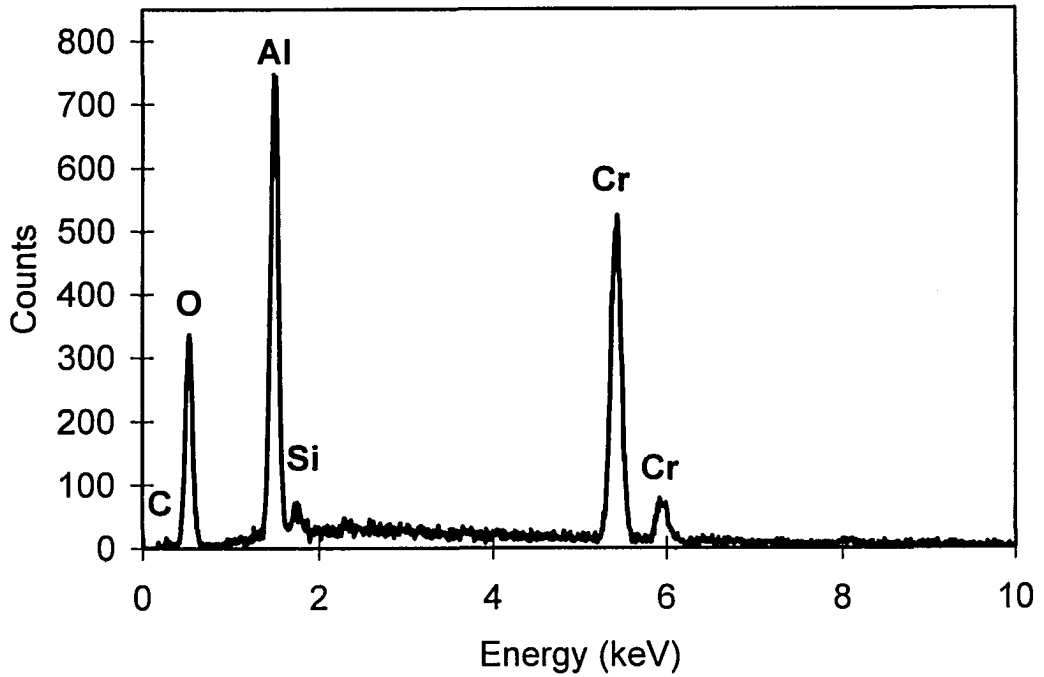


b)

Figure 5.4. a) The COF curve, b) SEM image of a section of the wear track of the 80-V DLC coatings tested against the 319 Al pin in air with 22% RH for 3.5×10^3 revolutions.

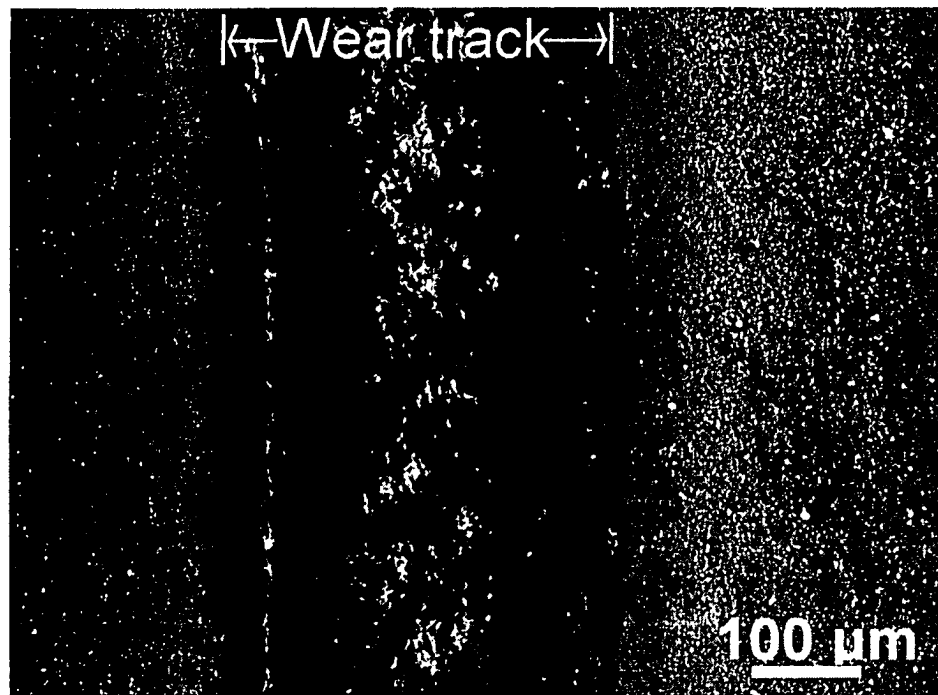


c)

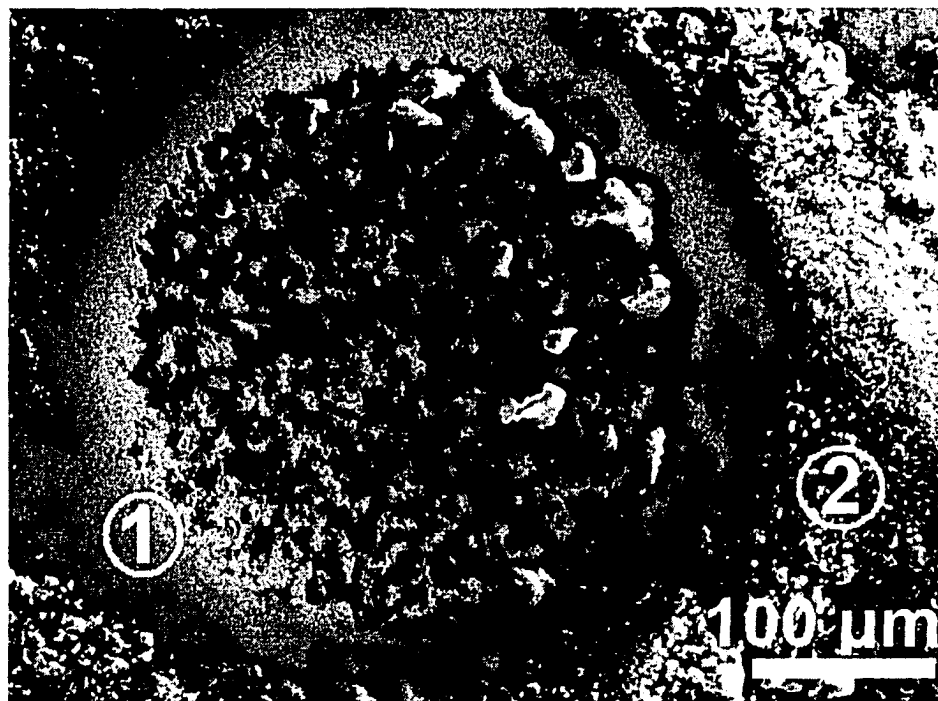


d)

Figure 5.4. c) SEM image of the contact surface of the corresponding 319 Al pin, d) EDS analysis of the location indicated in c).



a)



b)

Figure 5.5. SEM images of **a)** a region of the wear track of the 80-V DLC coating tested against the WC ball in vacuum for 1.2×10^3 revolutions and **b)** the contact surface of the corresponding WC ball (1) with coating material around (2).

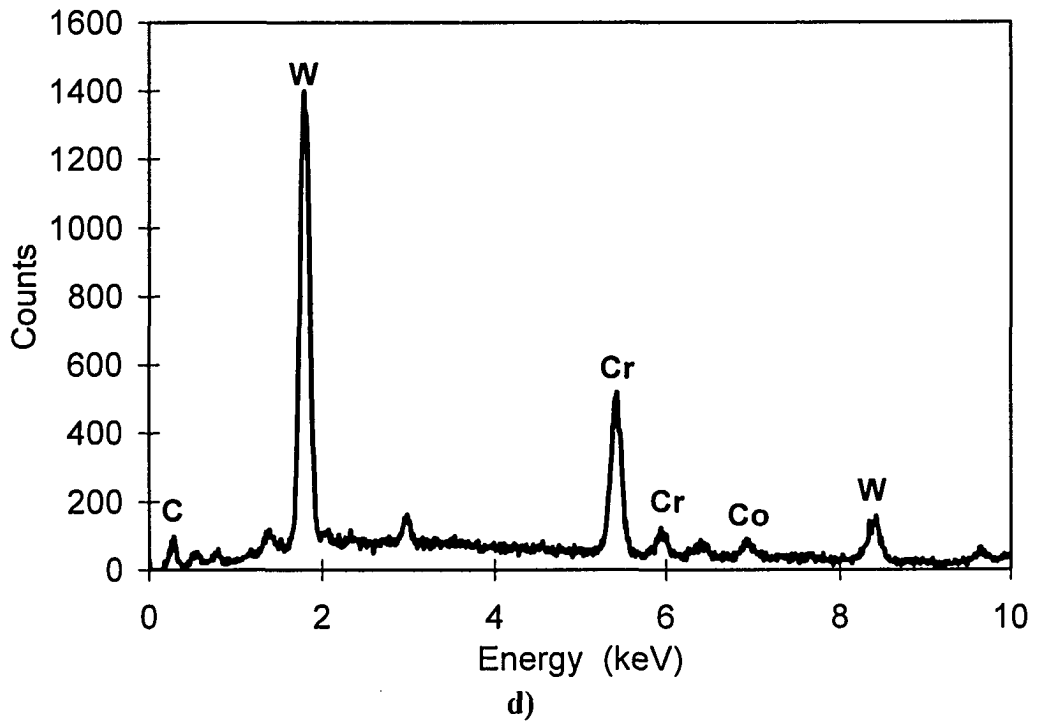
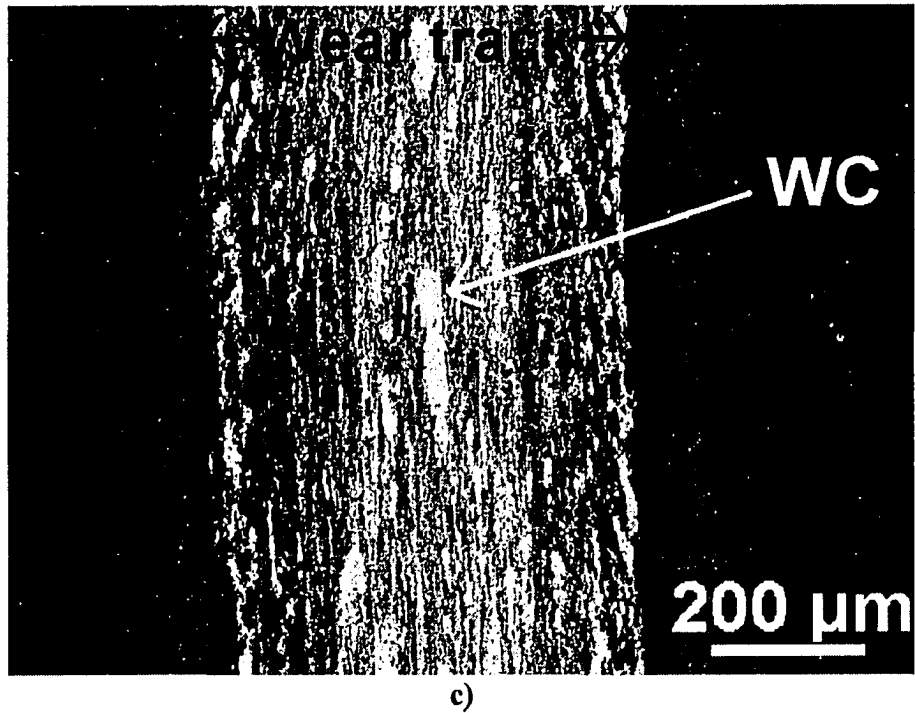
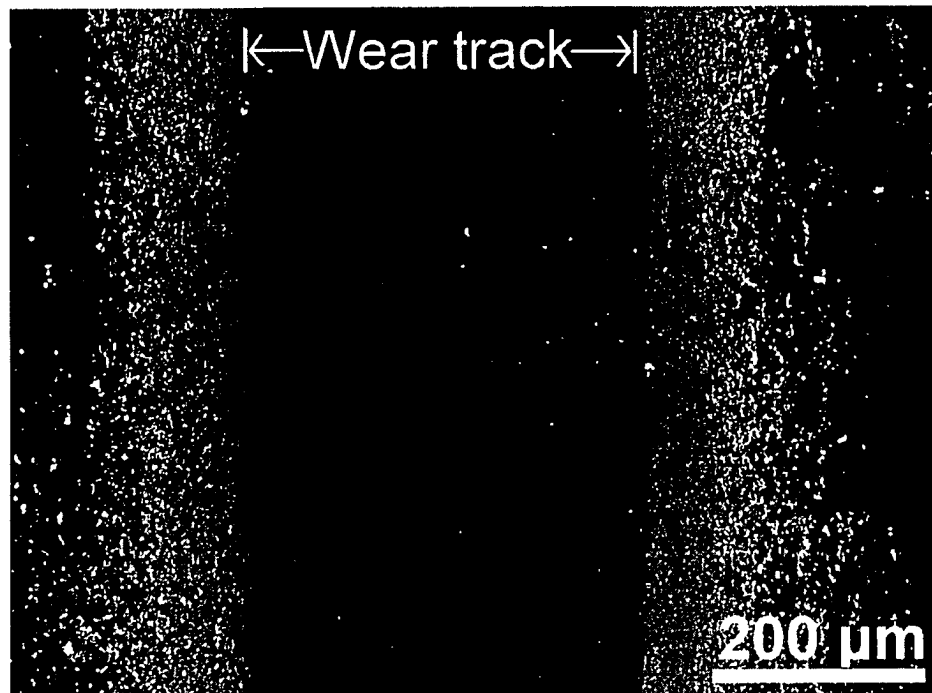
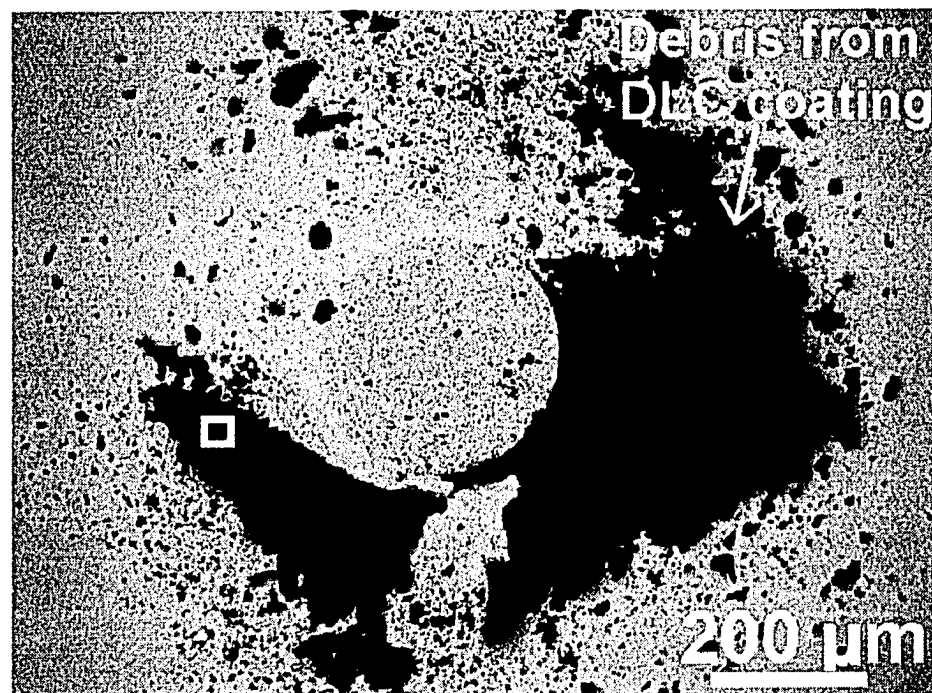


Figure 5.5. c) SEM image of a section of the wear track of the DLC coating tested against the WC ball in vacuum for 3.5×10^3 revolutions, and d) the EDS analysis of the location indicated in c). A significant amount of WC transfer to the 80-V DLC coating surface was observed as verified by EDS. The applied load and the sliding speed were 4.9 N and 0.12 m/s.



a)



b)

Figure 5.6. SEM images of a) a region of the wear track of the 80-V DLC coating tested against the WC ball in dry air (0% RH) for 1.2×10^3 revolutions and b) the contact surface of the corresponding WC ball.

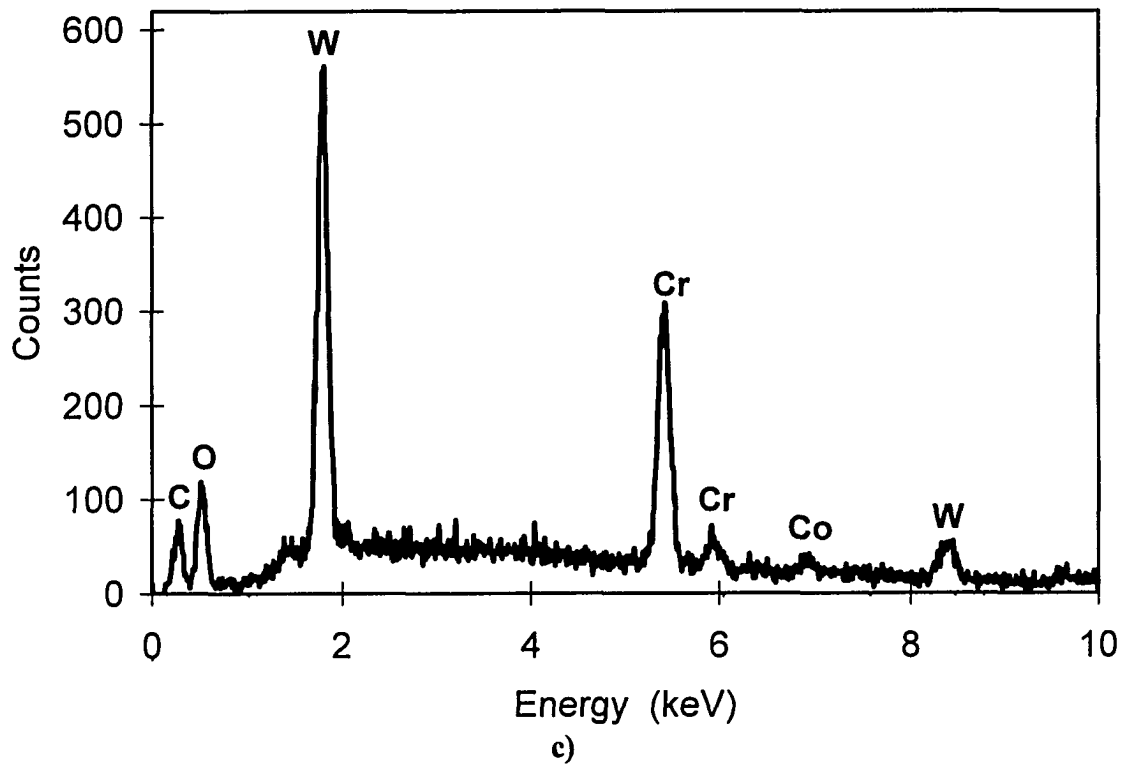
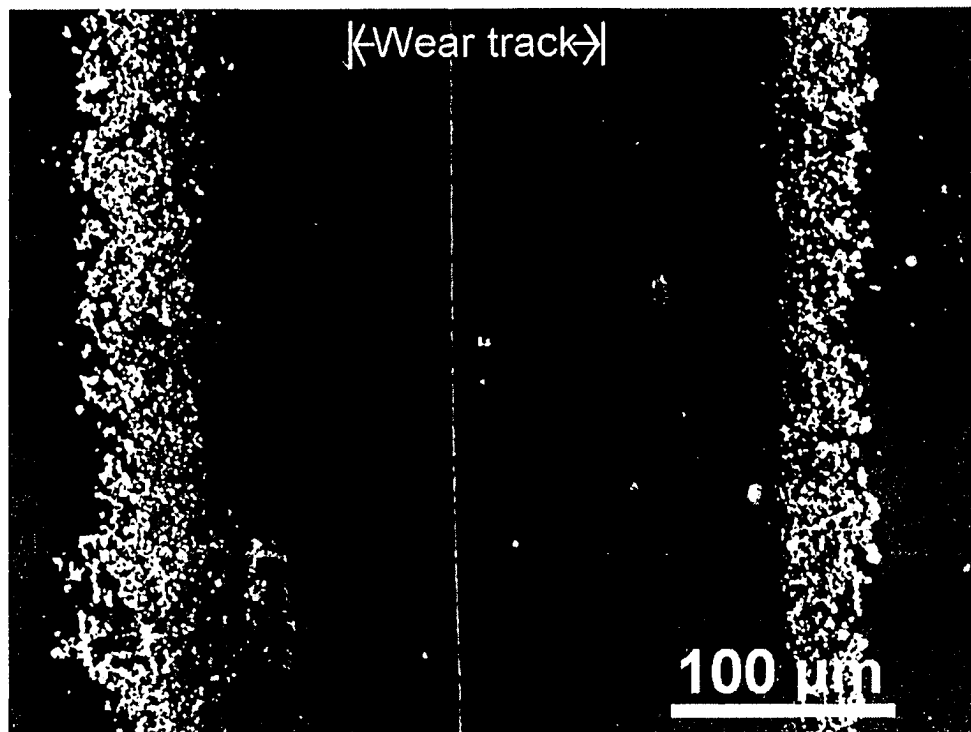
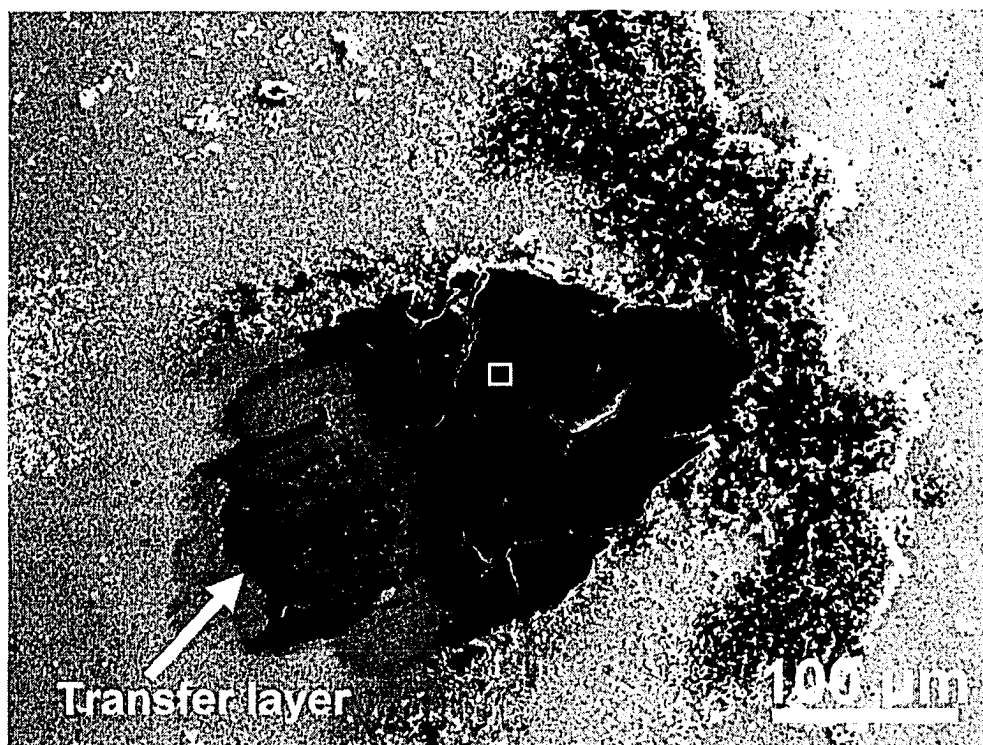


Figure 5.6. c) EDS analysis of the location indicated in b). The applied load and the sliding speed were 5 N and 0.12 m/s.



a)



b)

Figure 5.7. SEM images of a) a region of the wear track of the 80-V DLC coatings tested against the WC ball in air with 50% RH for 1.2×10^3 revolutions and b) the contact surface of the corresponding WC ball.

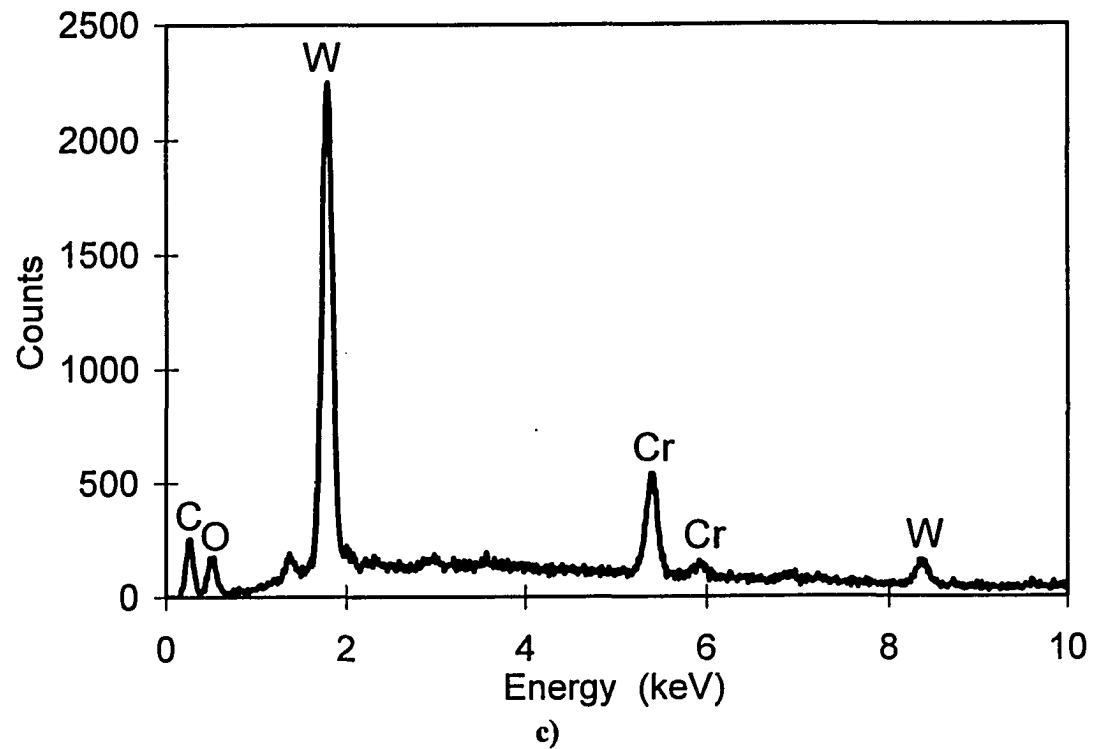


Figure 5.7. c) The EDS analysis of the location indicated on the transfer layer formed on the contact surface of the WC ball. The applied load and the sliding speed were 5 N and 0.12 m/s.

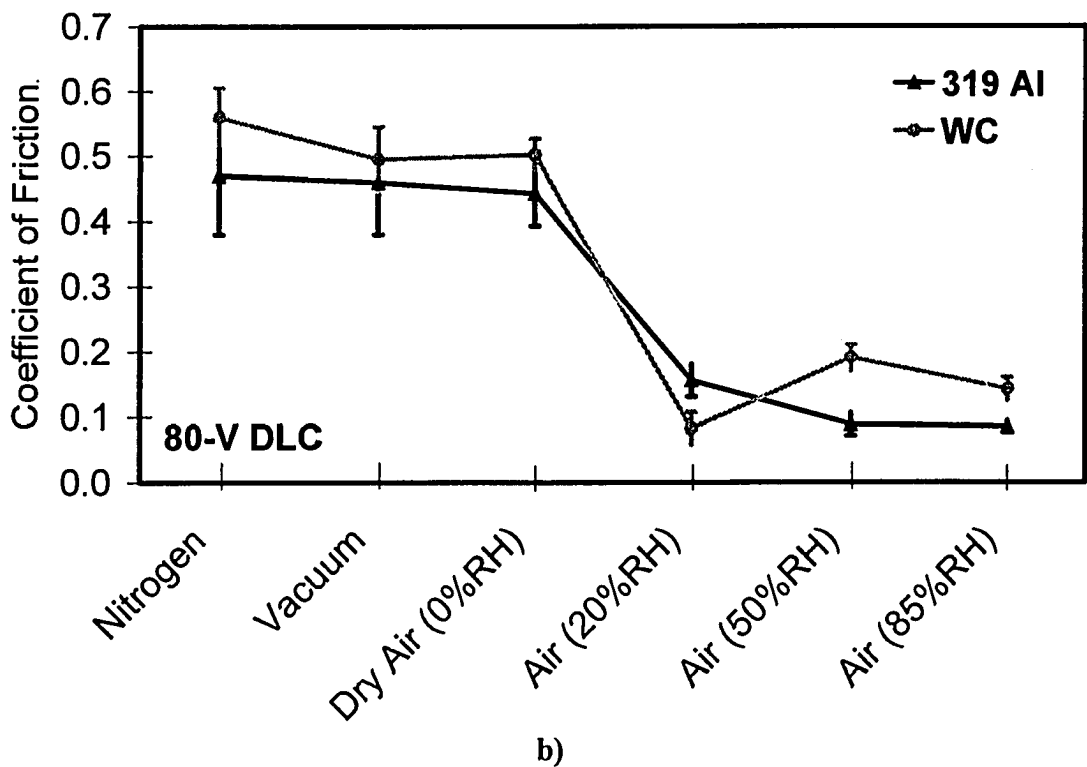
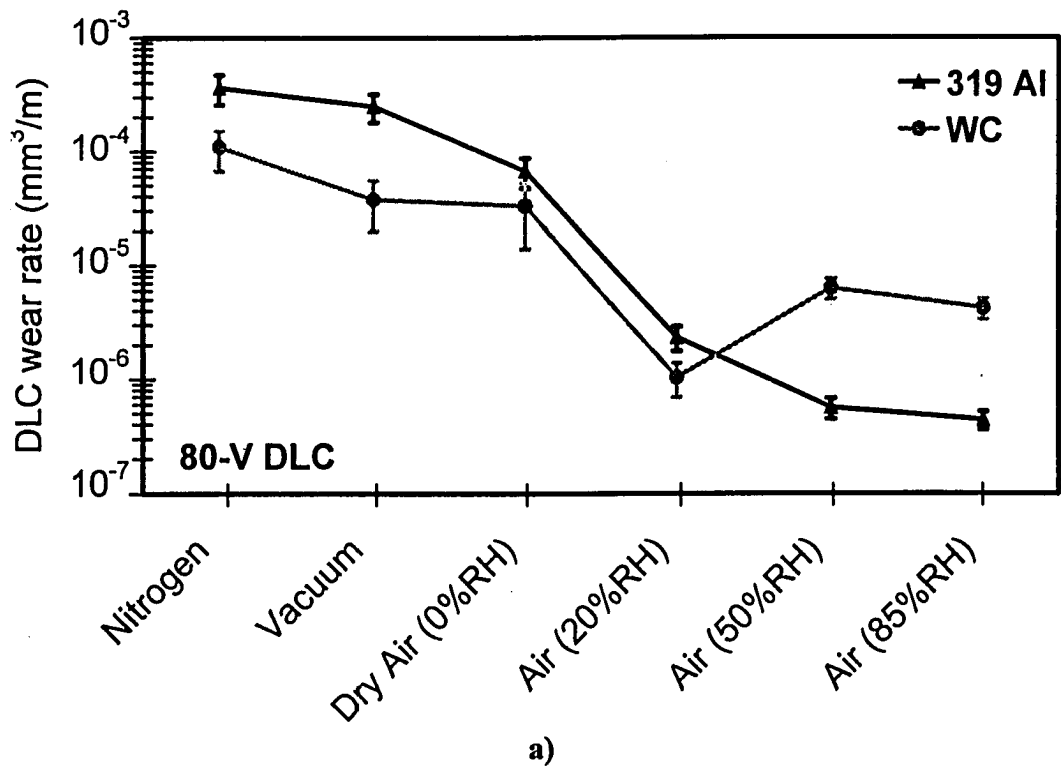


Figure 5.8. a) The wear rates, and b) the steady state COF values of the 80-V DLC coating against 319 Al and WC under various test environments. The applied load and sliding speed were 5 N and 0.12 m/s.

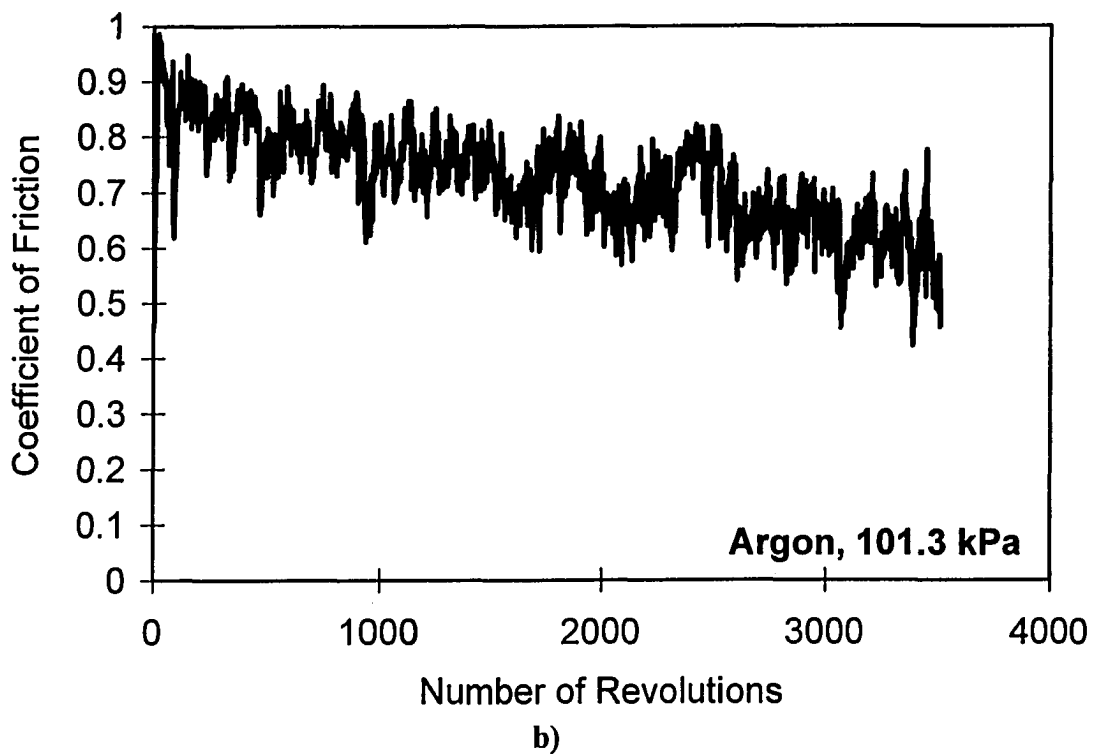
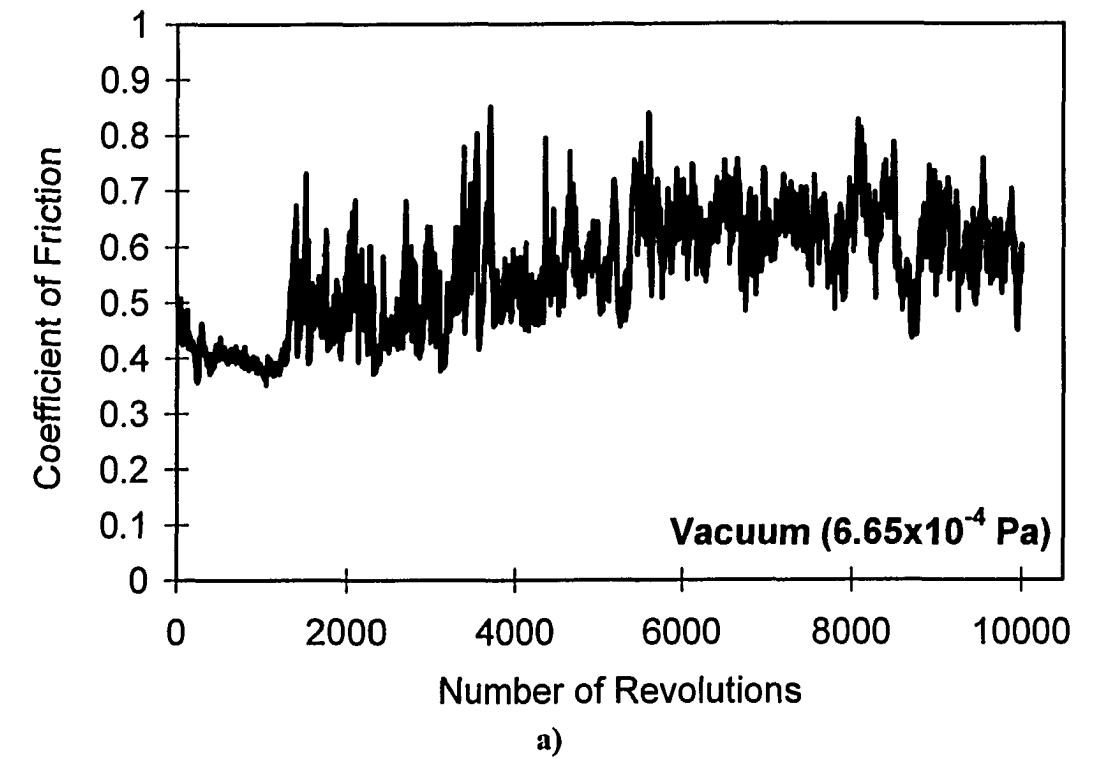
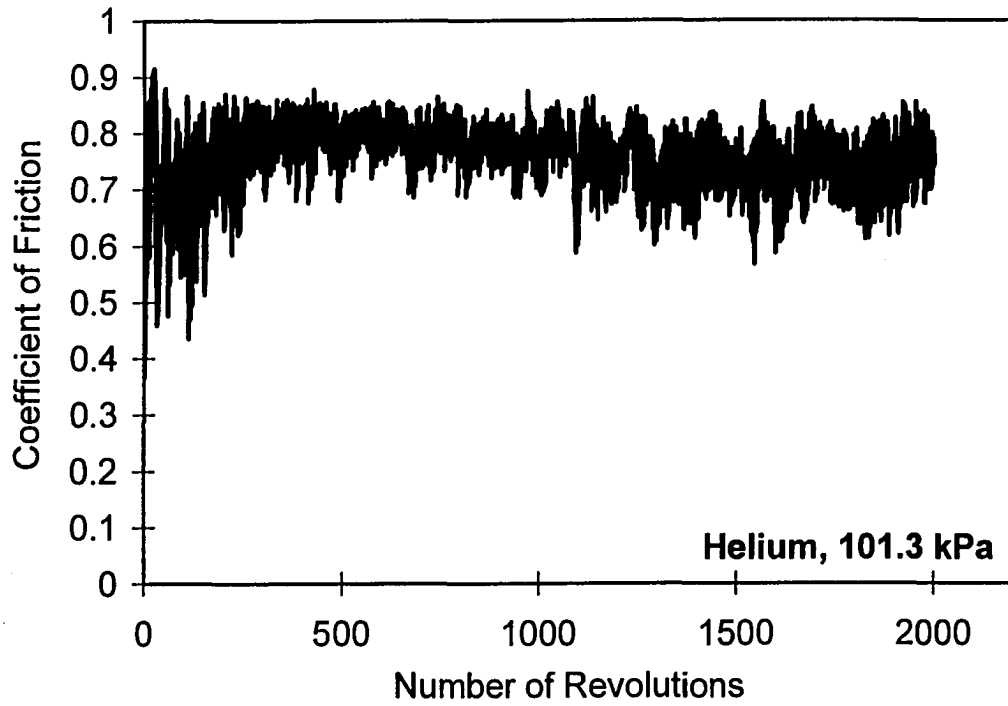
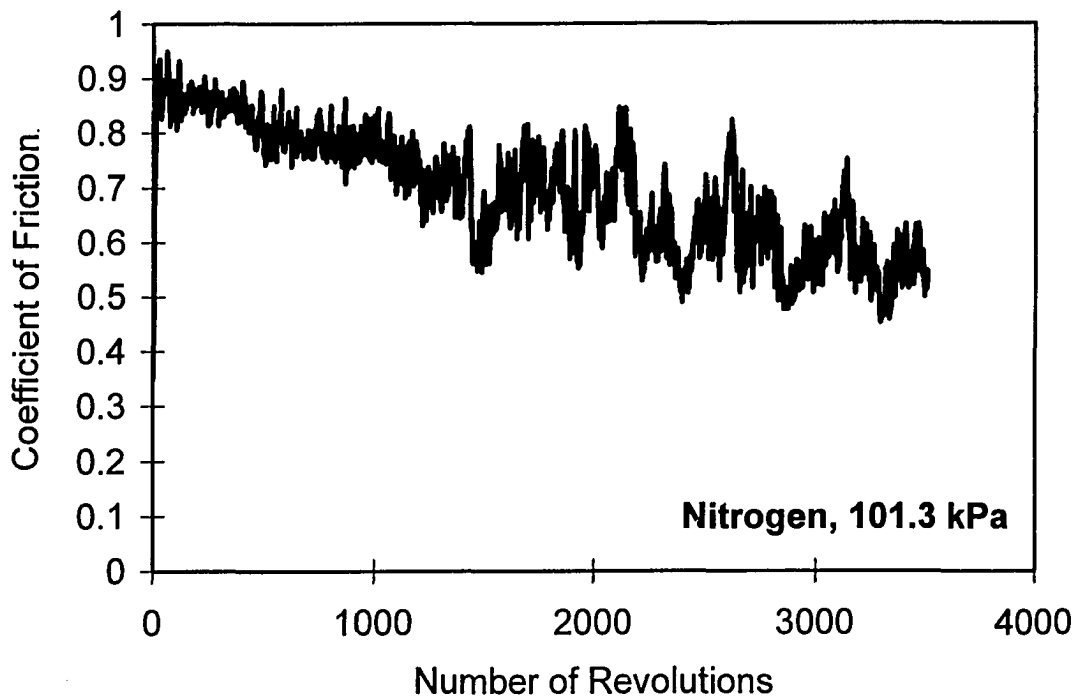


Figure 5.9. The COF curves for the Graphit-iC DLC coating tested against the 319 Al alloy in a) vacuum (6.65×10^{-4} Pa), b) argon.

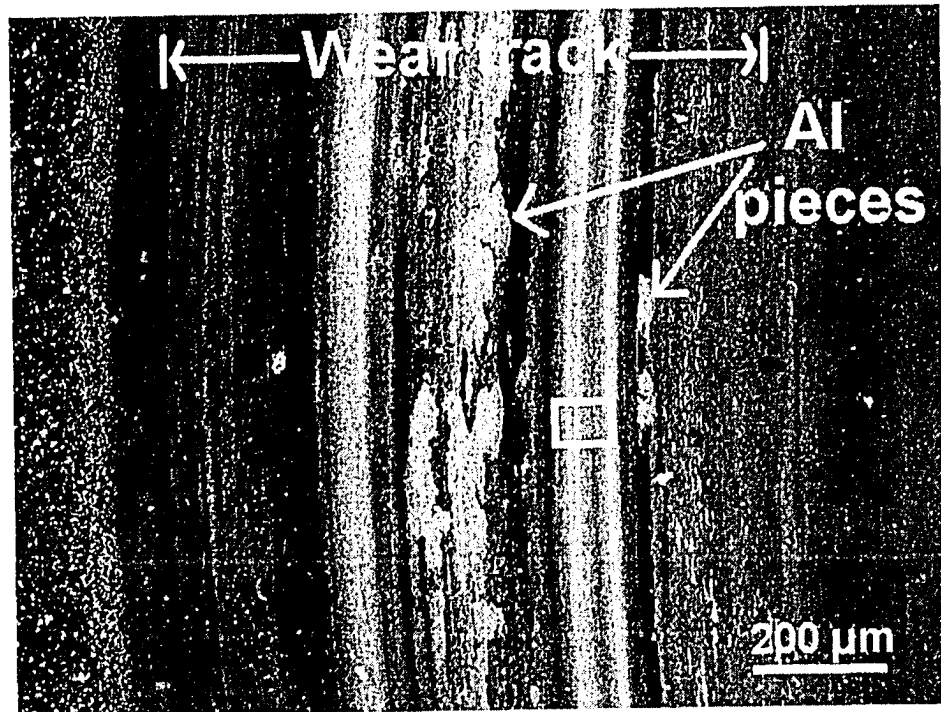


c)

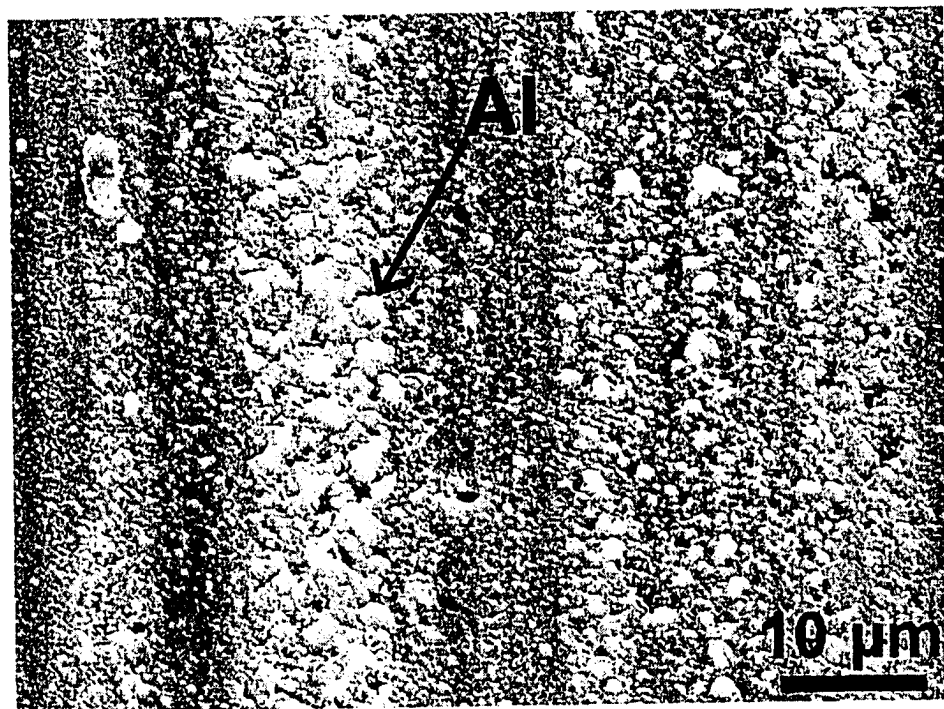


d)

Figure 5.9. The COF curves for the Graphit-iC DLC coating tested against the 319 Al alloy in c) helium, and d) nitrogen. The applied load was 5 N and the sliding speed was 0.12 m/s.

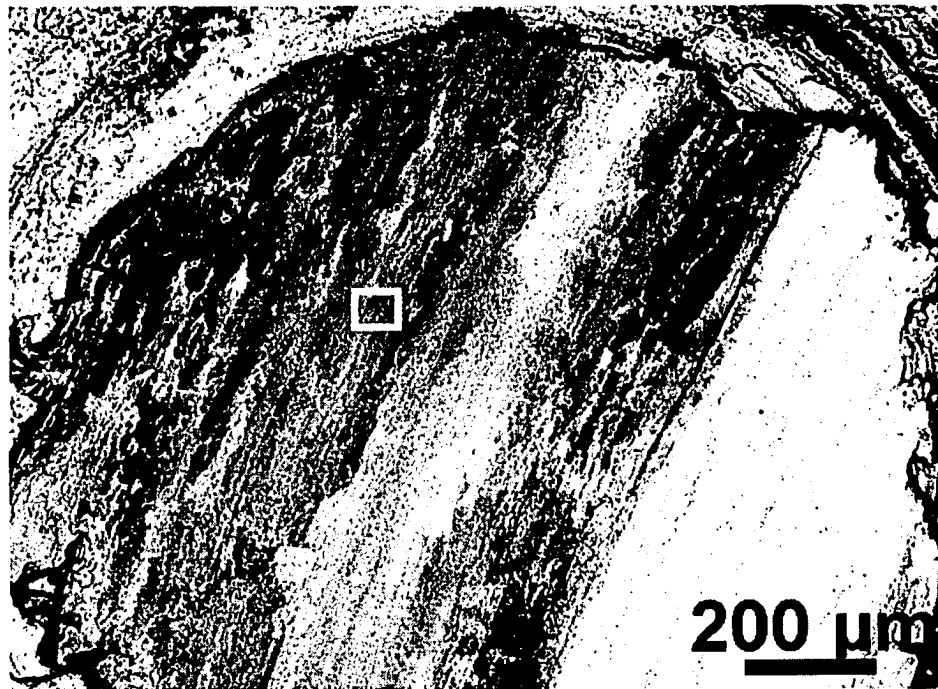


a)

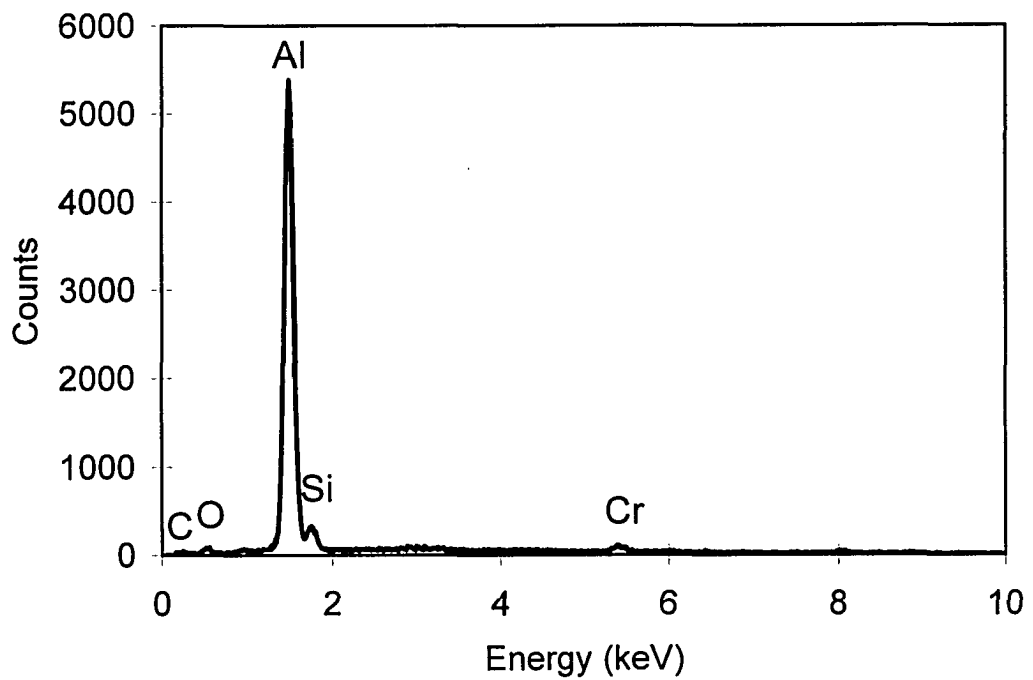


b)

Figure 5.10. a) SEI SEM image of a region of the wear track of the Graphit-iC DLC coating tested against 319 Al alloy in vacuum (6.65×10^{-4} Pa) for 1×10^4 revolutions, b) an enlarged view of the location indicated by a rectangle in b).



c)



d)

Figure 5.10. c) BEI SEM image of the contact surface of the corresponding 319 Al pin, and d) the EDS analysis of the location indicated in c). The applied load and the sliding velocity were 5 N and 0.12 m/s.

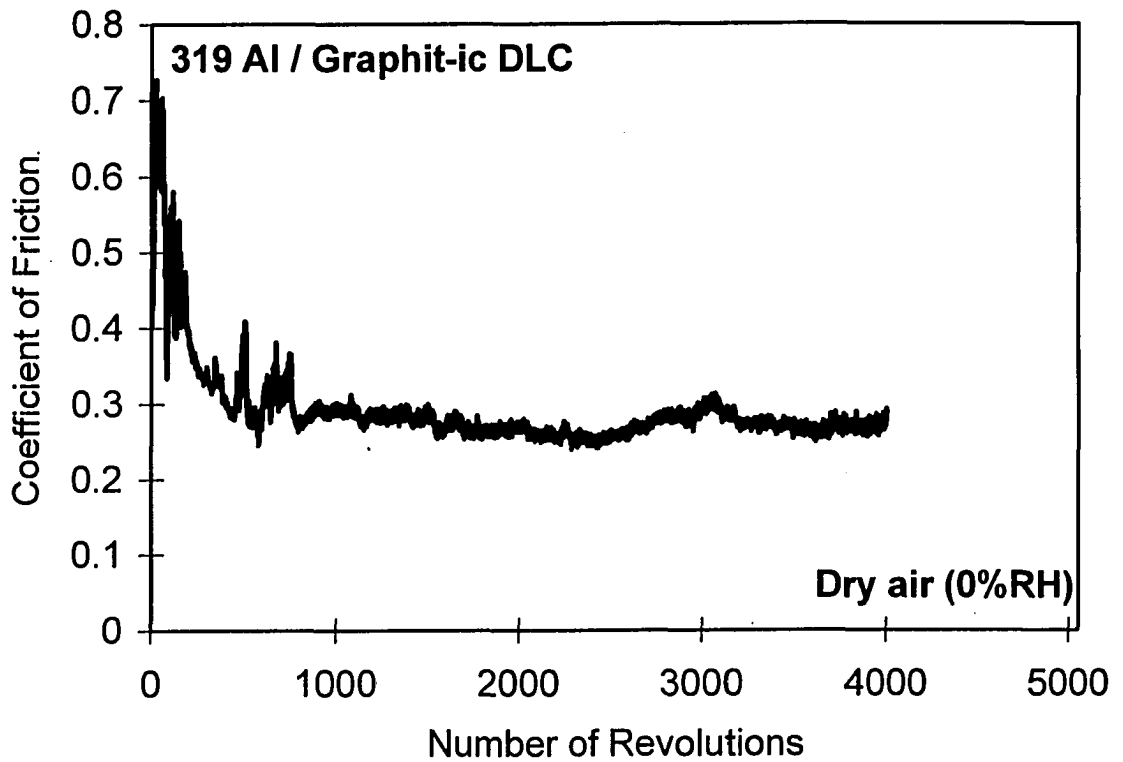


Figure 5.11. The variation of the COF between the 319 Al and Graphit-ic DLC during sliding in dry air. The applied load and sliding speed were 5 N and 0.12 m/s.

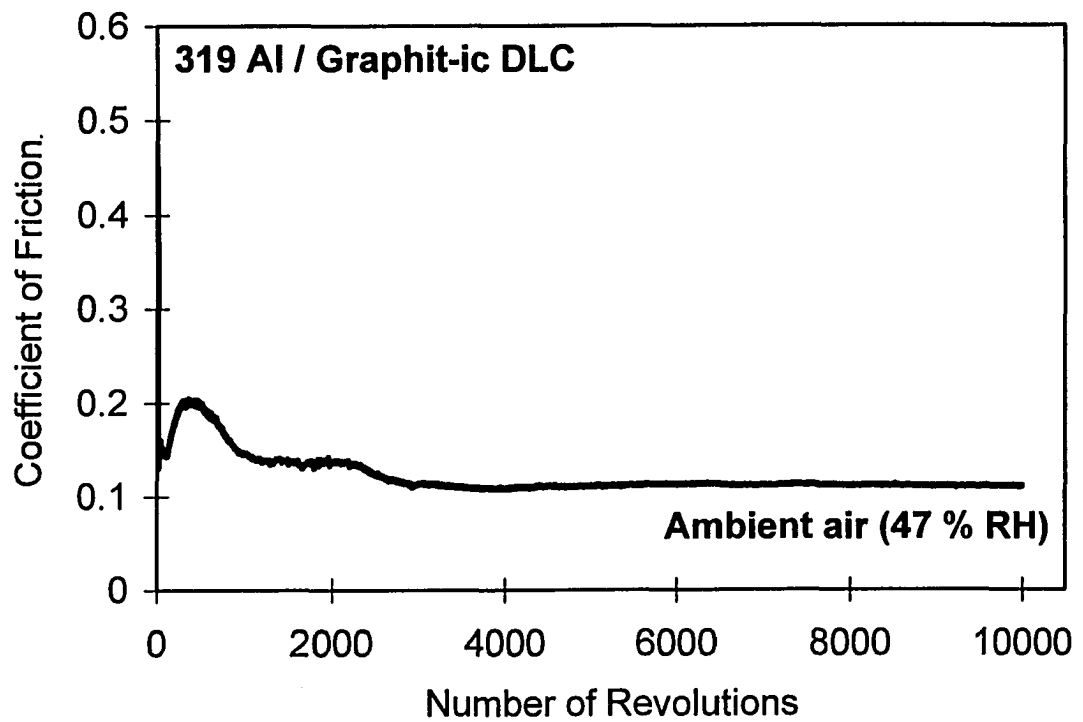


Figure 5.12. The COF curve for the Graphit-iC DLC coating tested against the 319 Al alloy at 0.12 m/s sliding speed and 5 N applied load in ambient air (47 % RH).

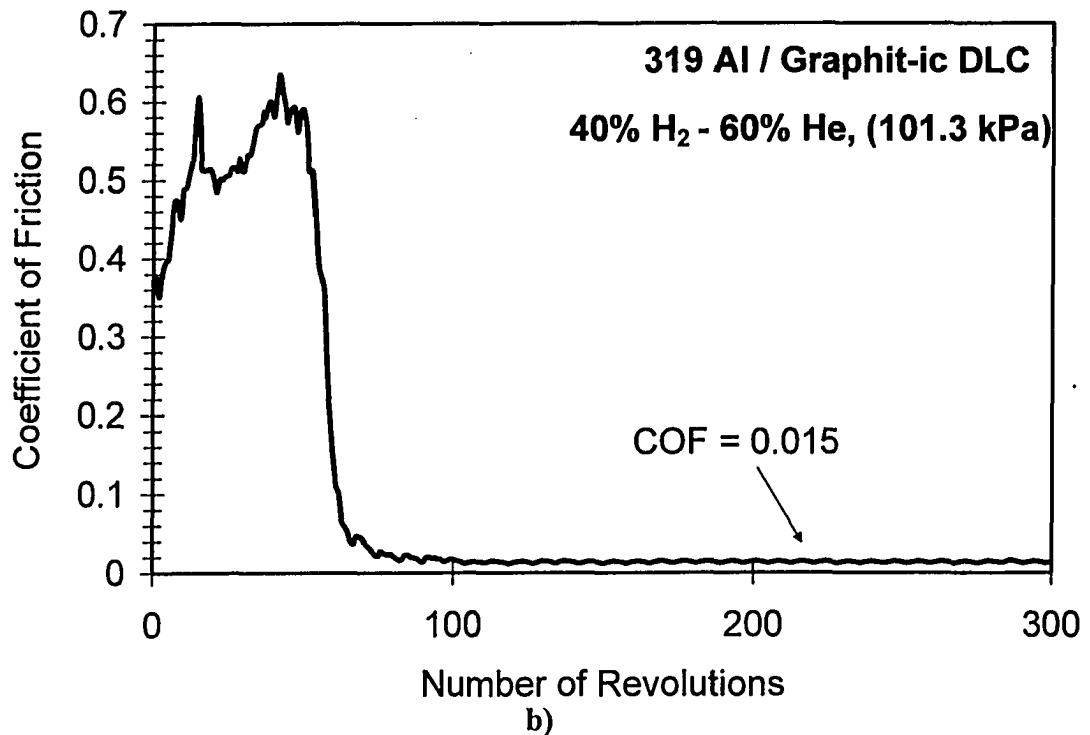
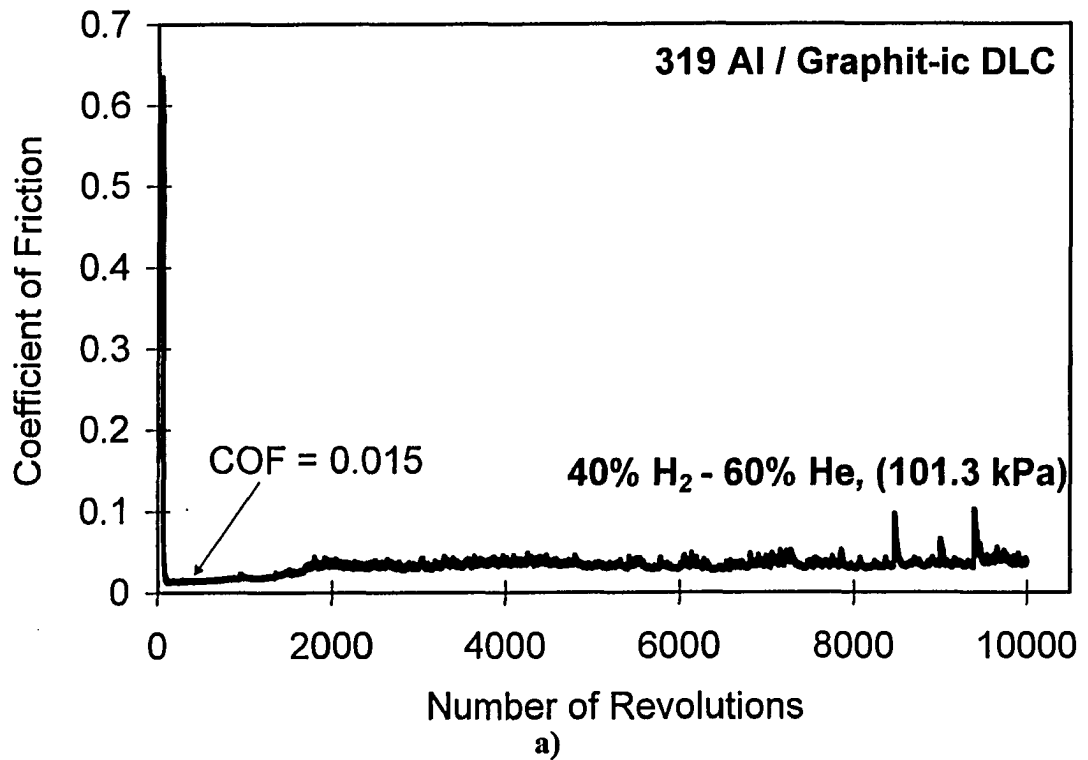


Figure 5.13. a) The COF curve for the Graphit-ic DLC coating tested against the 319 Al alloy at 0.12 m/s sliding speed and 5 N applied load in the 40% H₂-60% He atmosphere, b) expanded view of the first 300 revolutions.

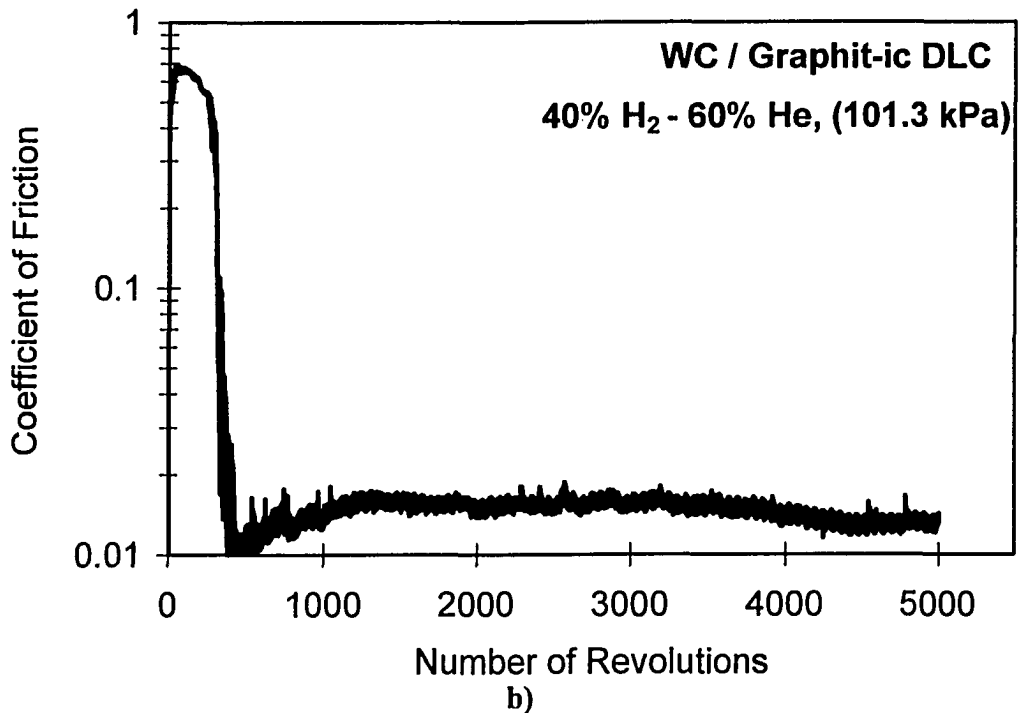
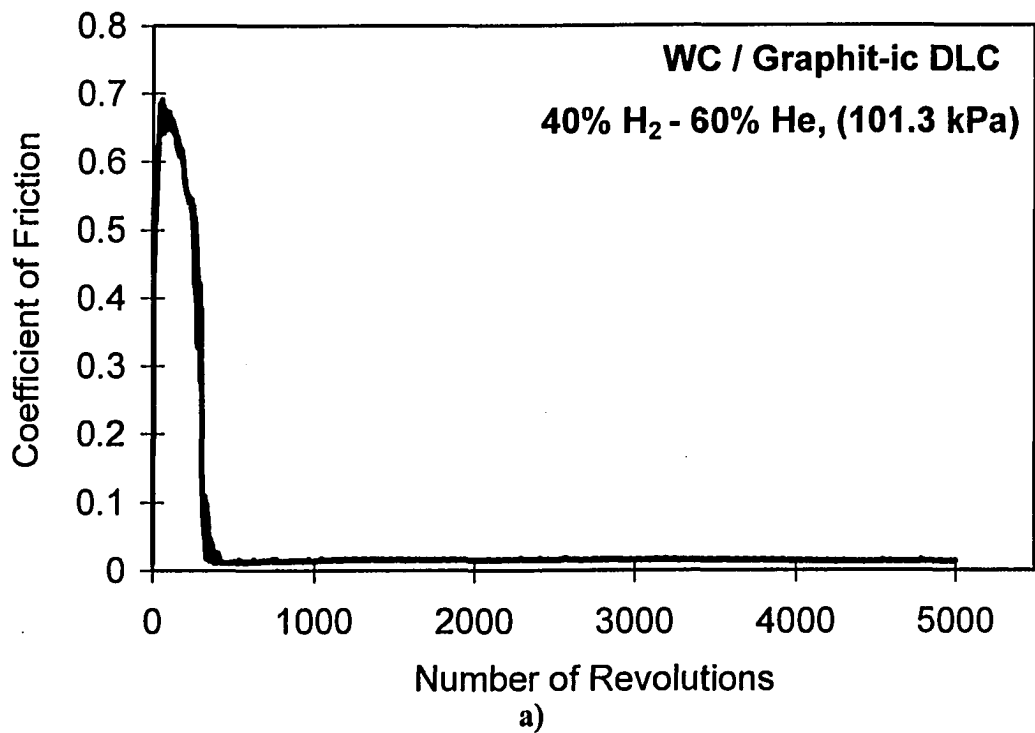


Figure 5.14. a) The COF curve for the non-hydrogenated DLC coating tested against WC at 0.12 m/s sliding speed and 5 N applied load in He-H₂ mixture, and b) semi-log scale plot of a).

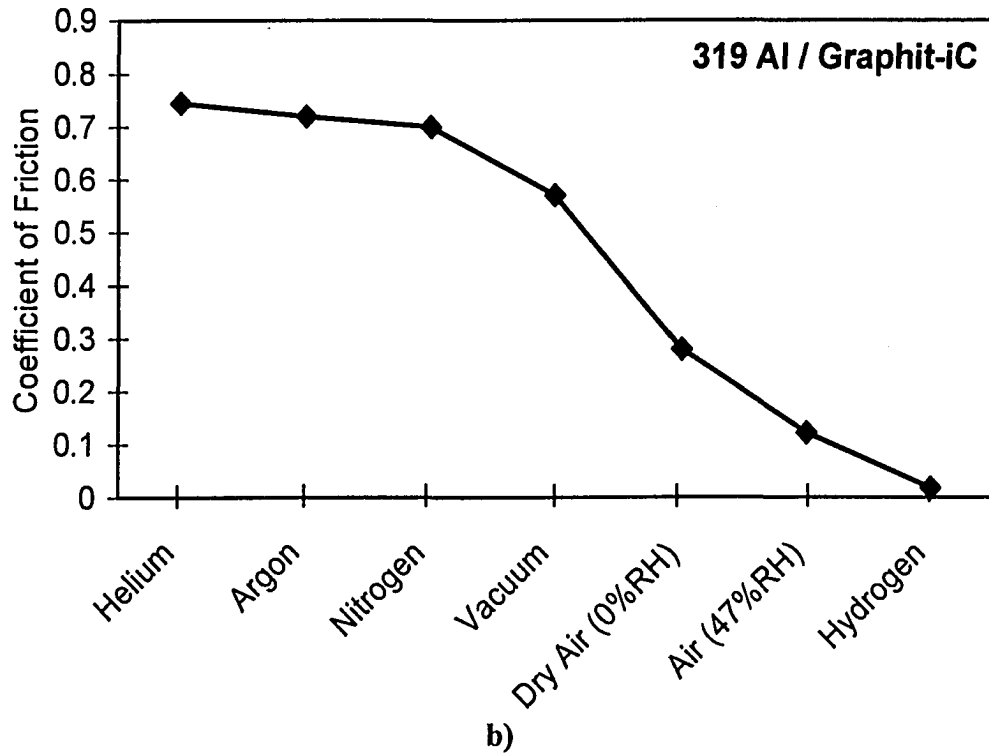
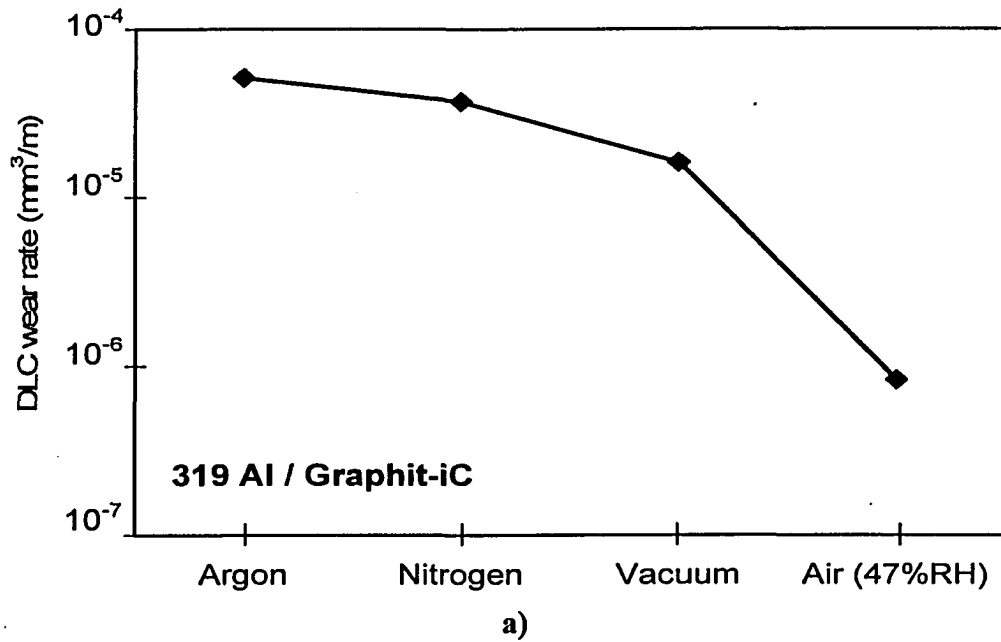


Figure 5.15. a) The measured wear rates, and b) the steady state COF values of the Graphit-iC DLC coating against 319 Al under various environments. The applied load and sliding speed were 5 N and 0.12 m/s.

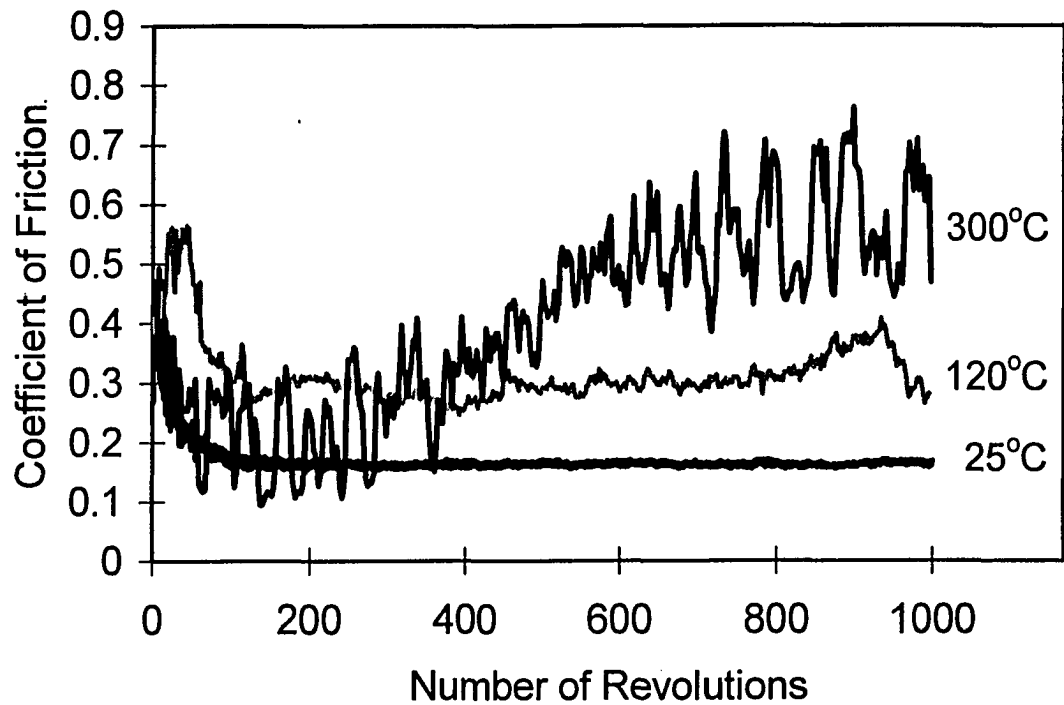


Figure 5.16. The COF curves between the 80-V DLC coated disc and the 319 Al pin at 25, 120 and 300°C. Tests were run for 60 m of sliding distance (1×10^3 revolutions) under an applied load of 5 N at 0.12 m/s sliding speed.

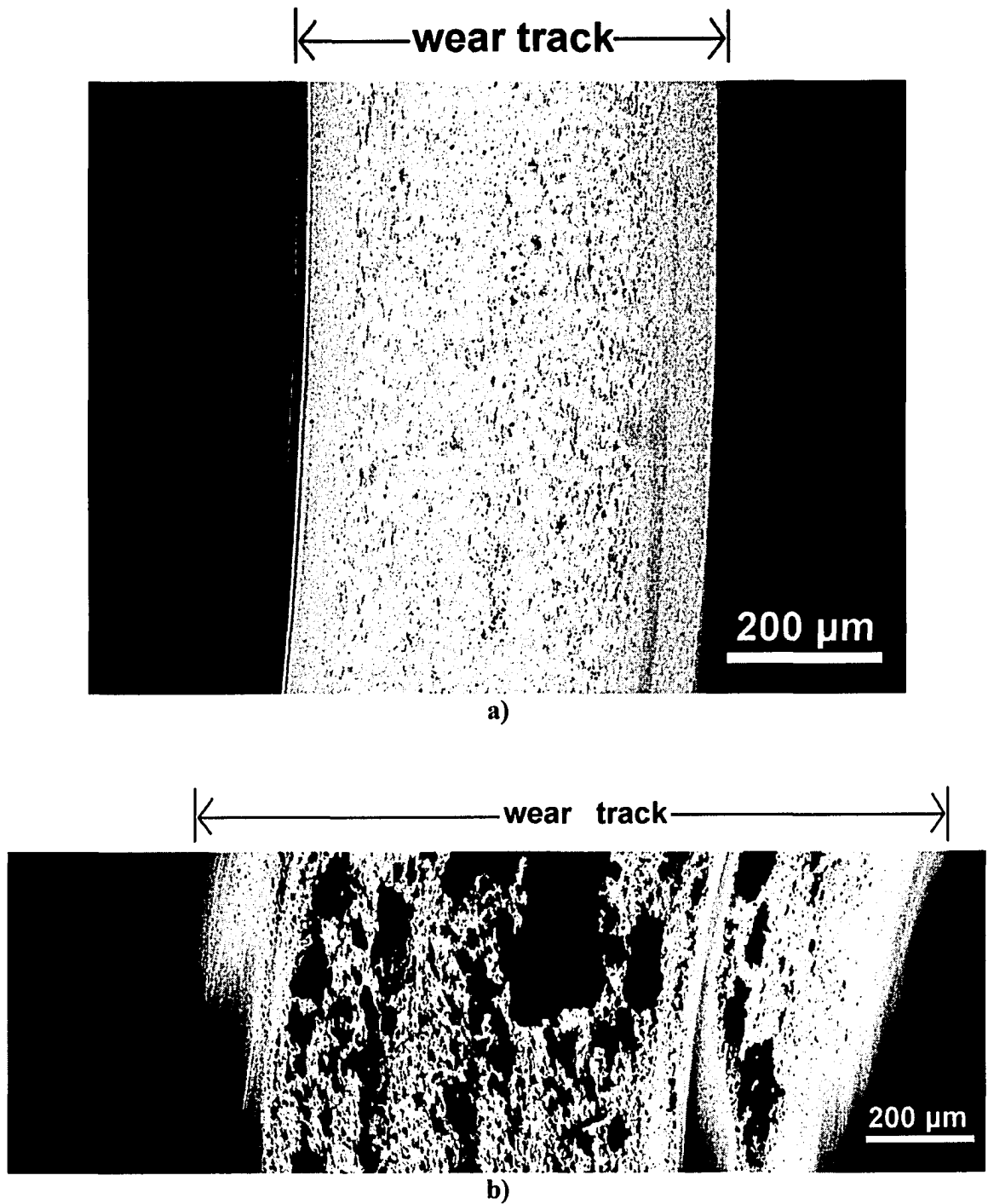


Figure 5.17. BEI SEM images of the regions of the wear tracks of the 80-V DLC coating tested against the 319 Al pin at 300°C for a) 1×10^3 revolutions and b) 1×10^4 revolutions. The applied load and sliding speed were 5 N and 0.12 m/s.

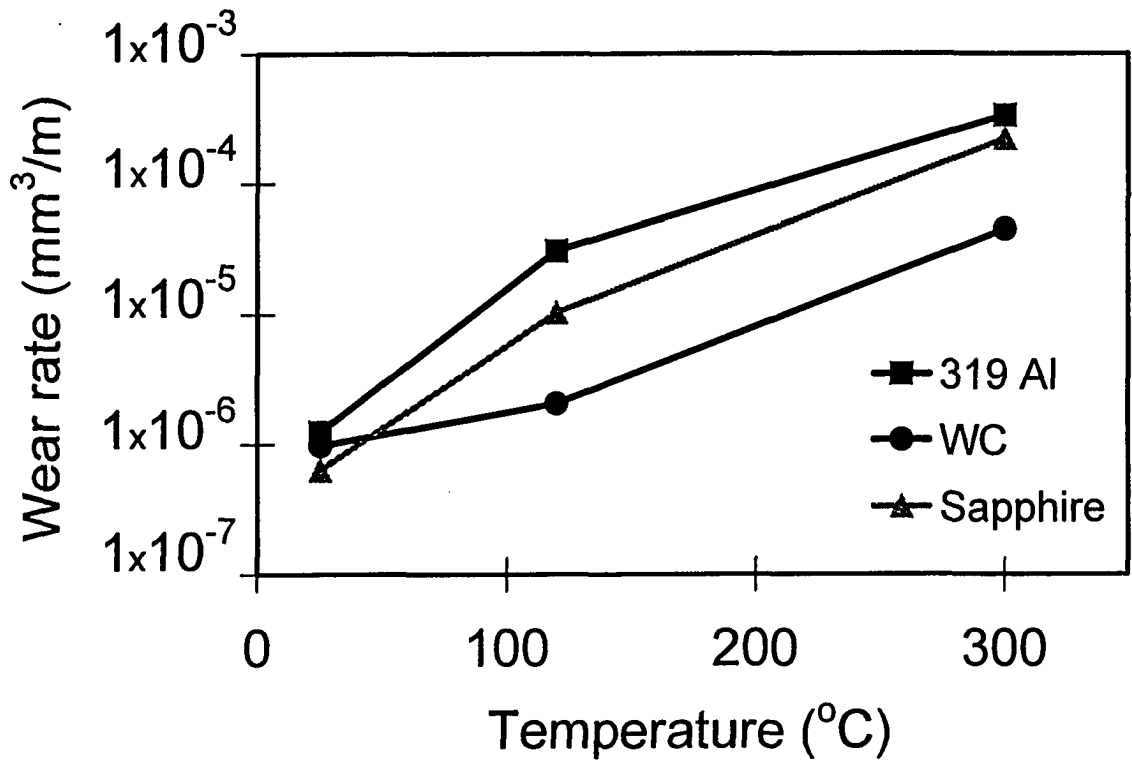


Figure 5.18. The variation of the wear rate of the 80-V DLC coating with temperature when tested against 319 Al, WC and sapphire at 25, 120 and 300°C. Tests were run for 1,500 m of sliding distance (2.5×10^4 revolutions) at 25°C and for 60 m of sliding distance (1×10^3 rev.) at 120 and 300°C using 5 N applied load.

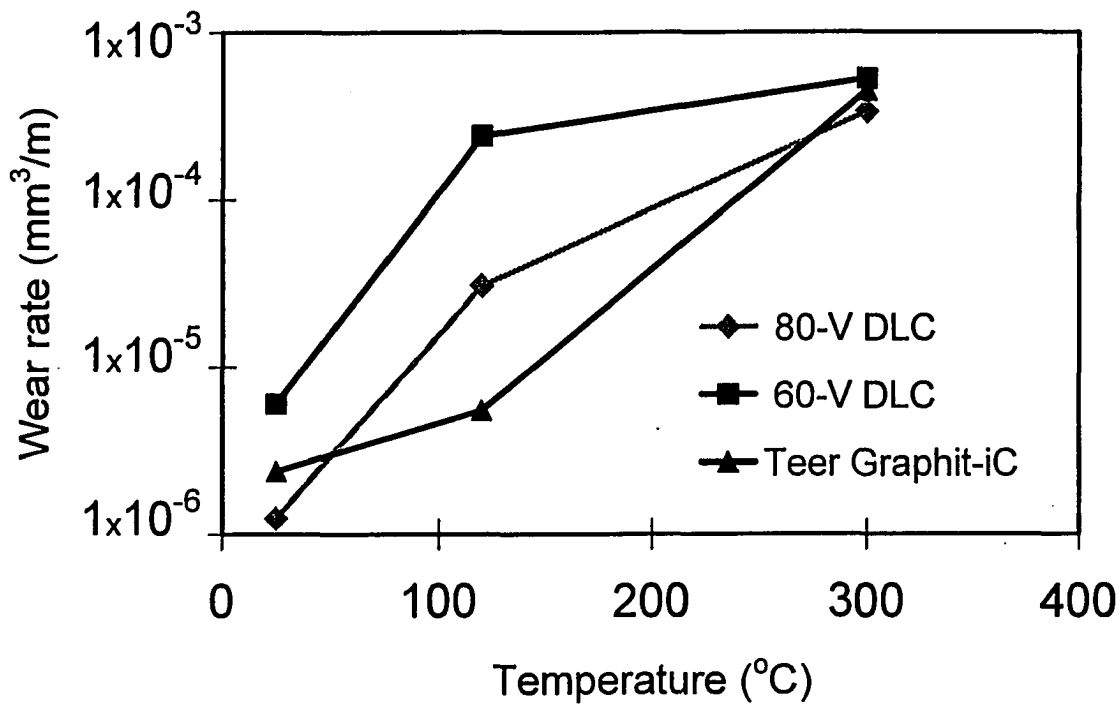


Figure 5.19. Comparison of the changes in the wear rates of the 60-V DLC, 80-V DLC and the Graphit-iC DLC coatings with temperature. Tests were run against 319 Al for 1,500 m of sliding distance (2.5×10^4 revolutions) at 25°C and for 60 m of sliding distance (1×10^3 revolutions) at 120 and 300°C under an applied load of 5 N.

|←wear track→|

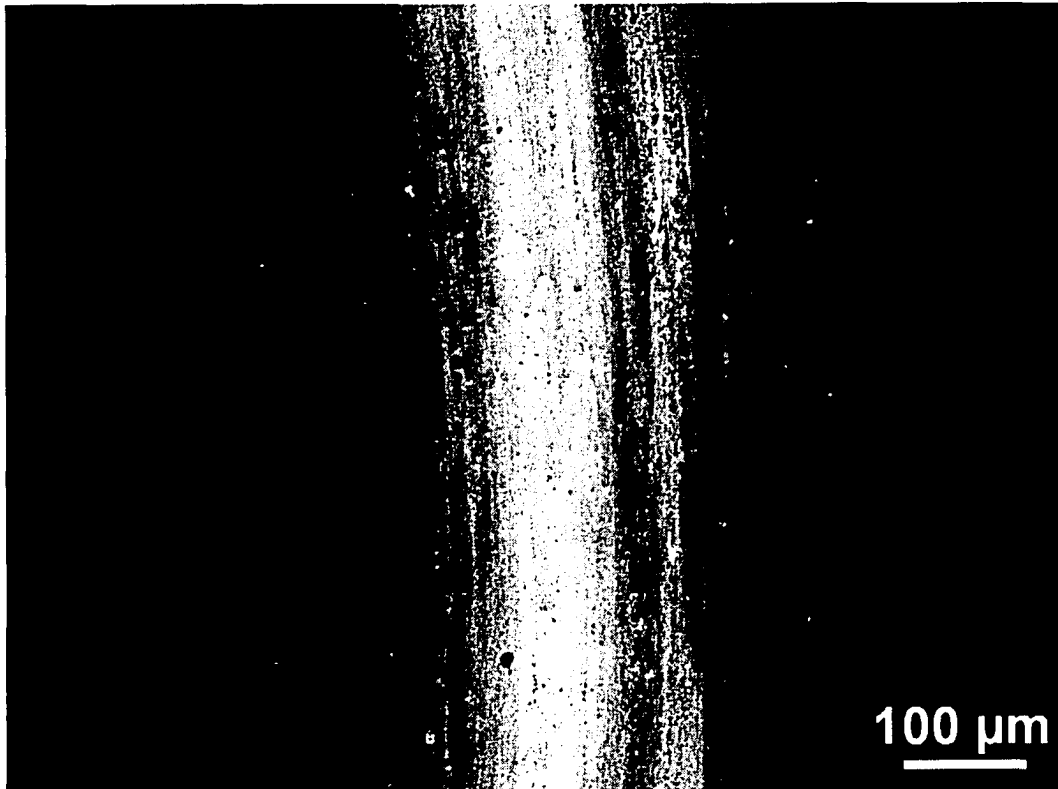


Figure 5.20. The BEI SEM image of a section of the wear track of the 60-V DLC coating tested against 319 Al pin at 120°C. Test was run for 60 m of sliding distance (1×10^3 revolutions) using 4.9 N applied load. In backscattered electron imaging mode, the image is created according to atomic mass difference where heavier elements appear brighter. Therefore the dark coloured area is the DLC coating and the lighter color areas are the M2 steel substrate.

←—wear track—→

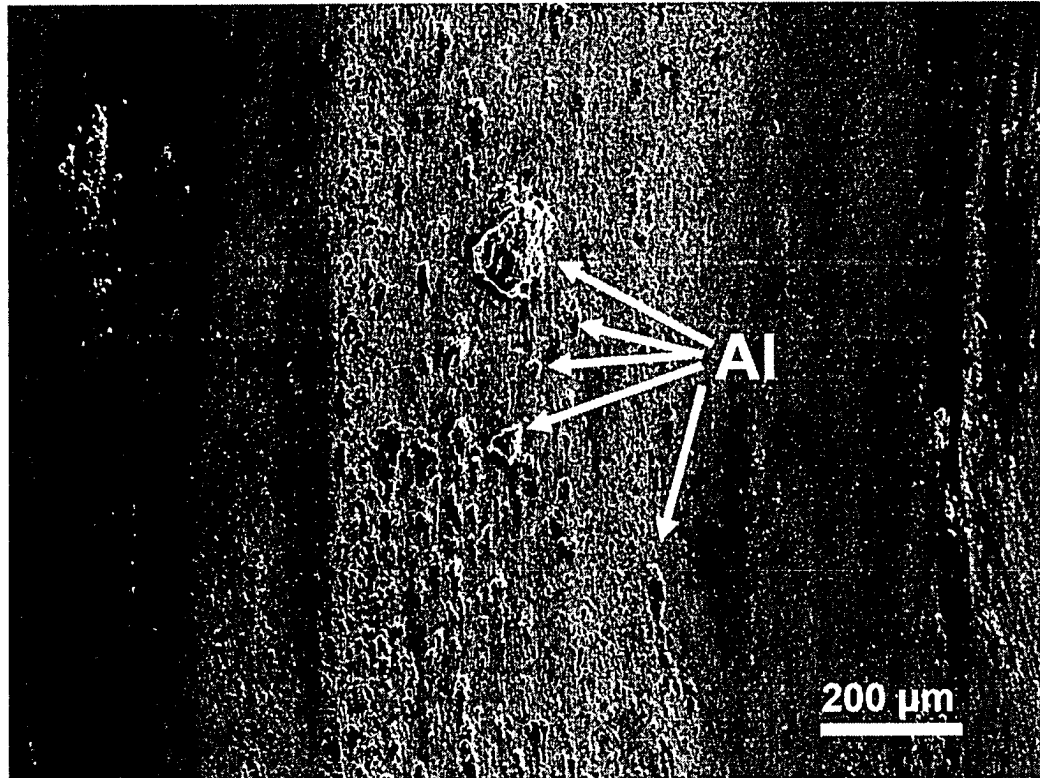


Figure 5.21. SEI SEM image of a section of the wear track of the Graphit-iC DLC coating tested against 319 Al alloy at 400°C showing a large amount of aluminum transfer. The test was run for 250 revolutions under applied load of 5 N at 0.12 m/s.

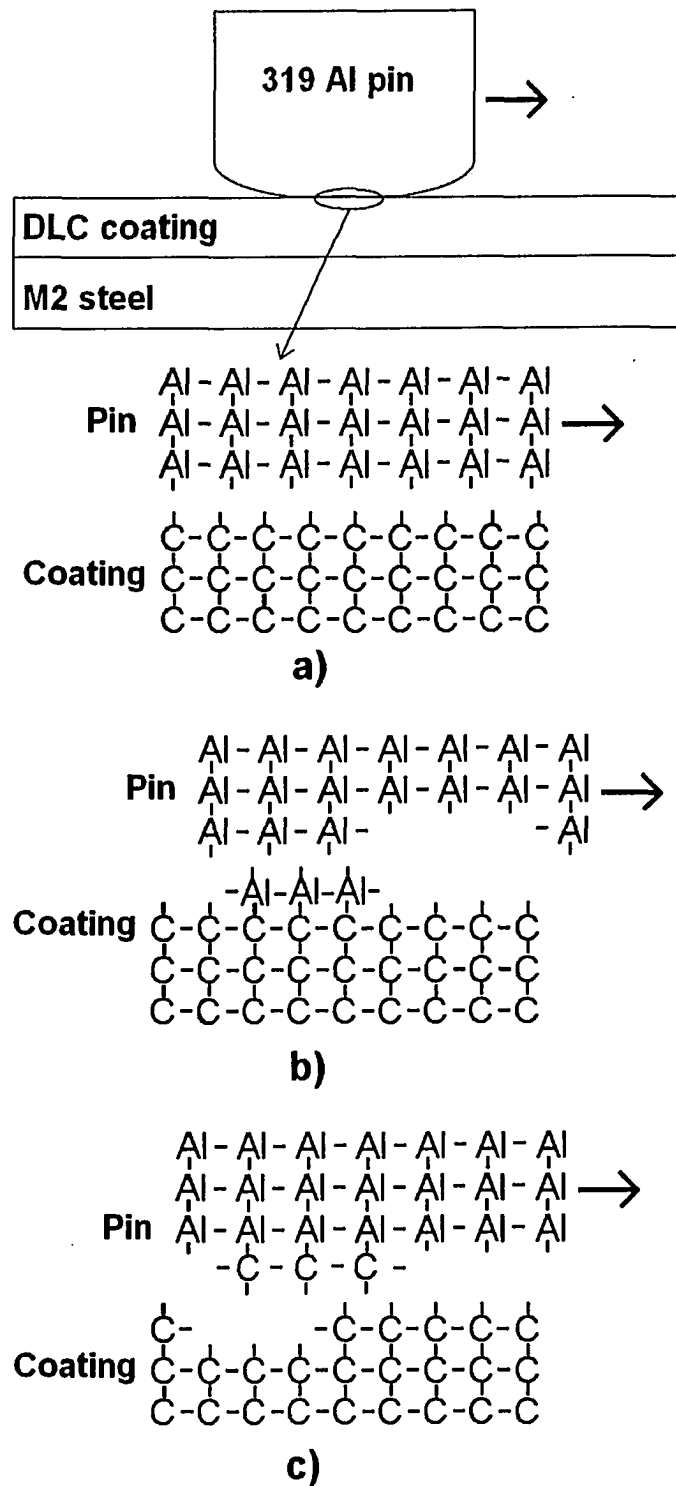


Figure 5.22. The adhesive wear mechanism that operates in vacuum and inert gas environments: a) The interaction of the surface atoms with unsatisfied bonds that results in, b) transfer of aluminum to the DLC surface, and/or c) transfer of carbon to the Al pin surface.

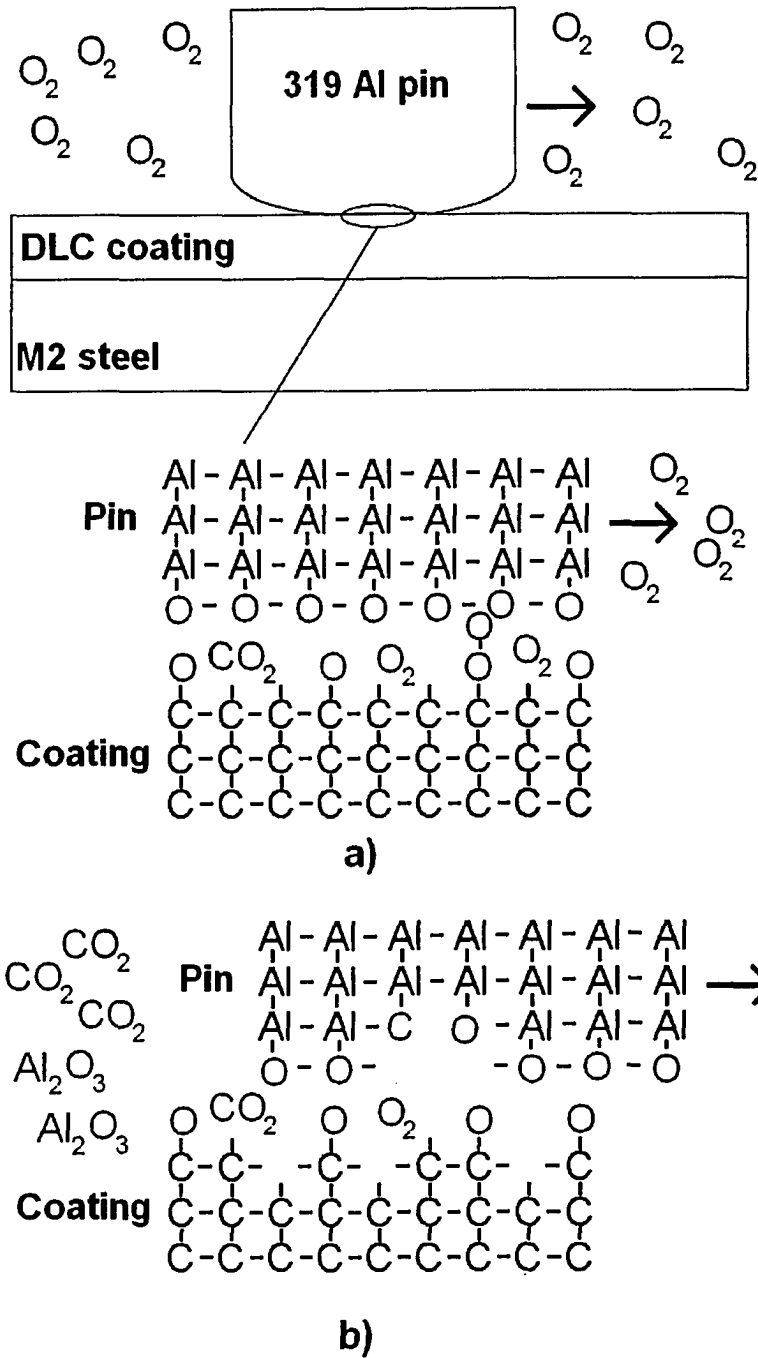


Figure 5.23. The oxidative and abrasive wear mechanisms of the non-hydrogenated DLC coating in dry air.

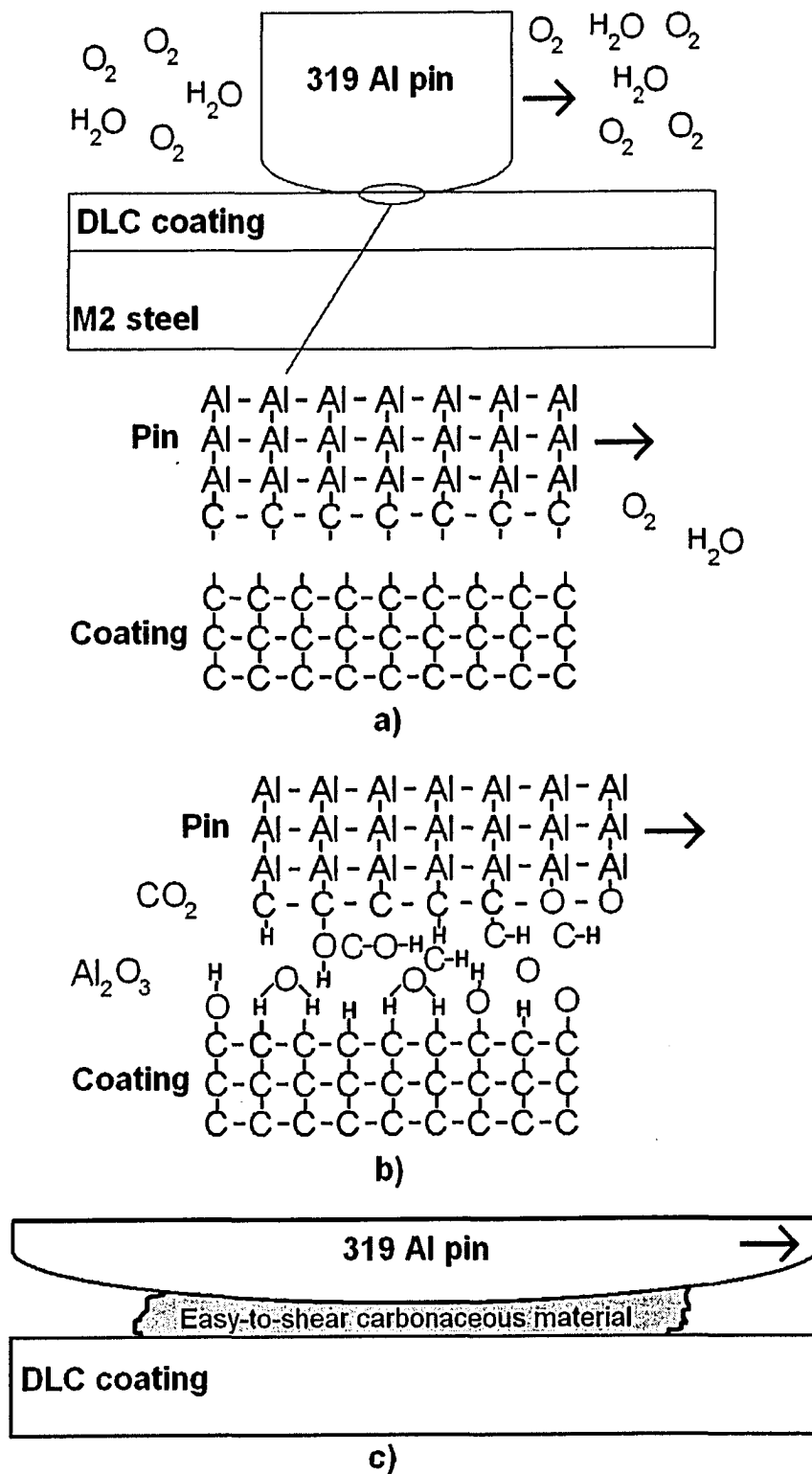


Figure 5.24. a) and b) The oxidative and abrasive wear mechanisms of the non-hydrogenated DLC coating in ambient air, c) easy-to-shear carbonaceous material at the sliding interface.

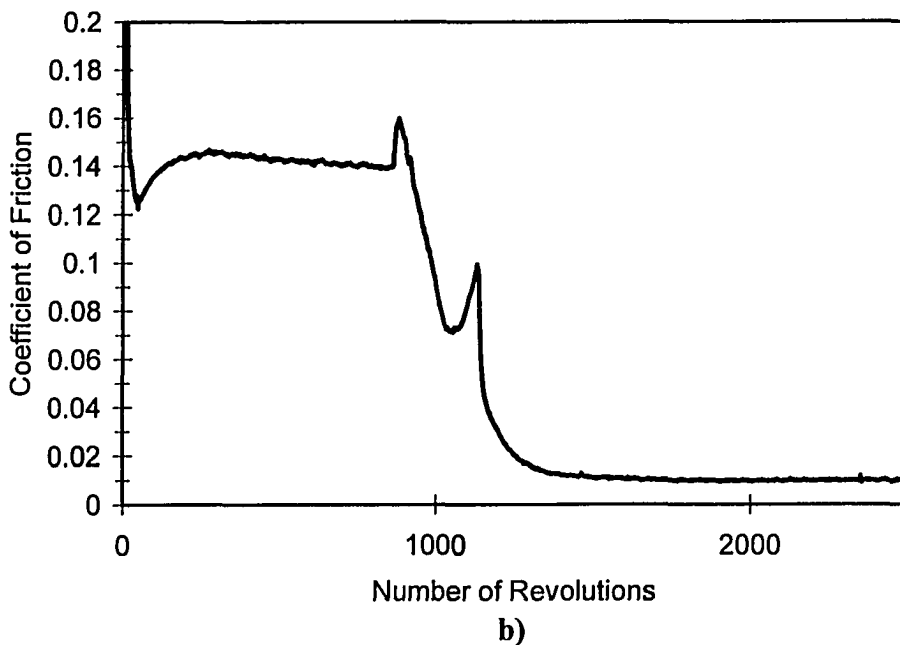
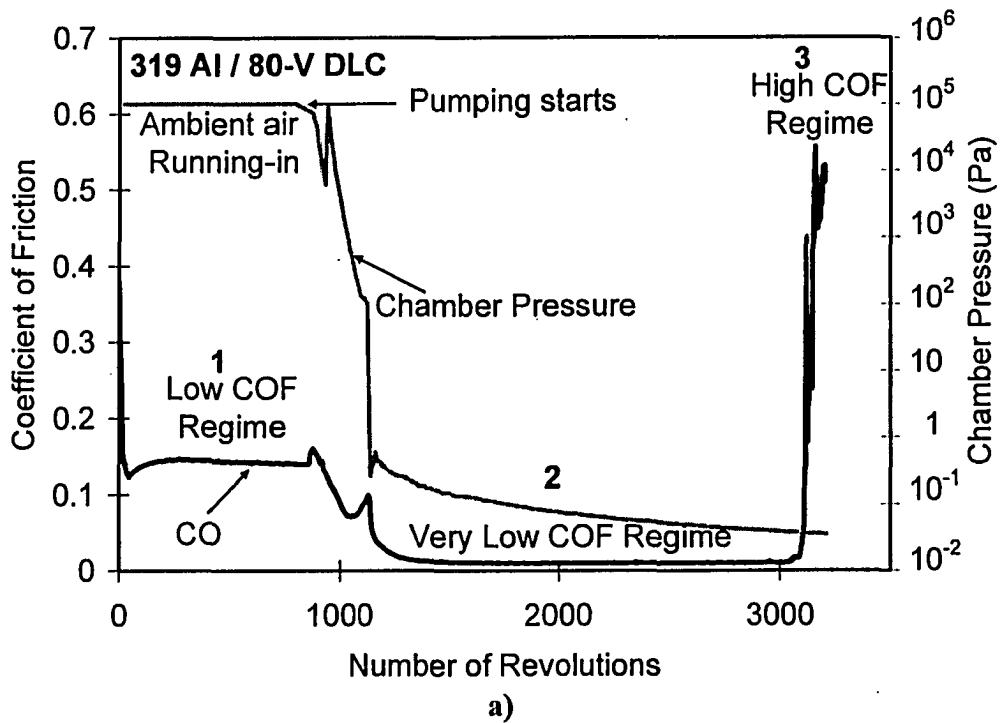


Figure 5.25. a) A typical COF curve for the ambient air to vacuum tests for 319 Al sliding against the 80-V DLC coating. The test started in ambient air (52% RH). After some sliding in ambient air (8.5×10^2 revolutions), the test chamber was pumped down to vacuum. The COF decreased with the pressure inside the chamber and reached its minimum value of 0.006 when the pressure was around 0.173 Pa. Further decrease in pressure did not change the COF value. Finally, the very low COF period ended and the COF abruptly jumped to high values (0.55). The applied load and the sliding speed were 5 N and 0.04 m/s, and **b)** expanded view of the initial portion of the COF curve.

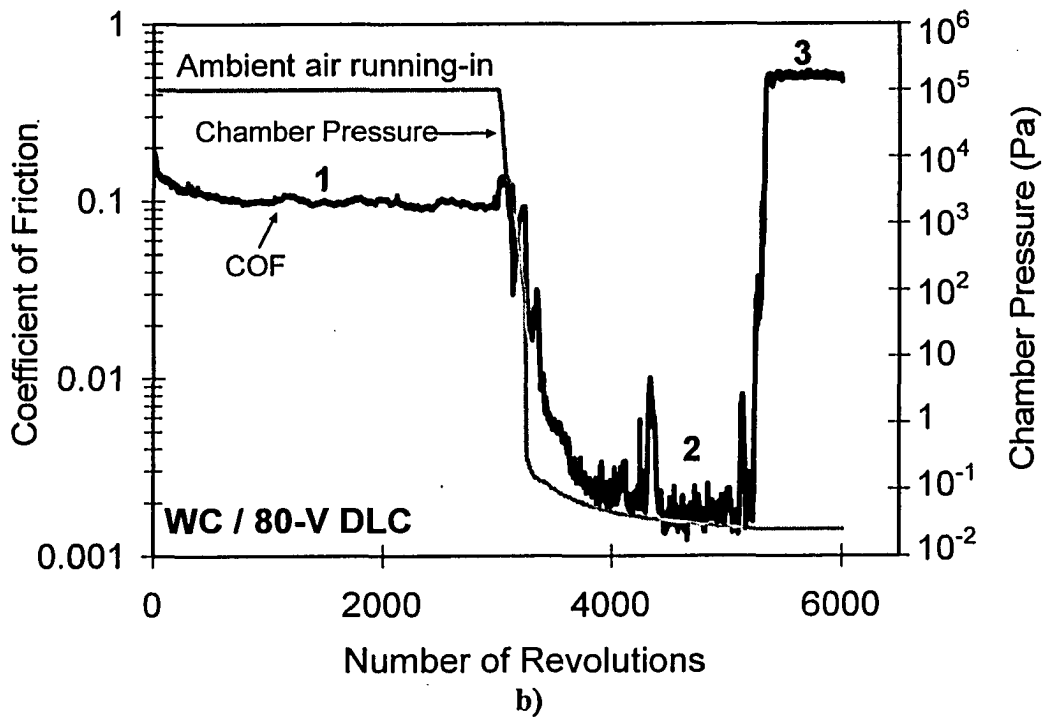
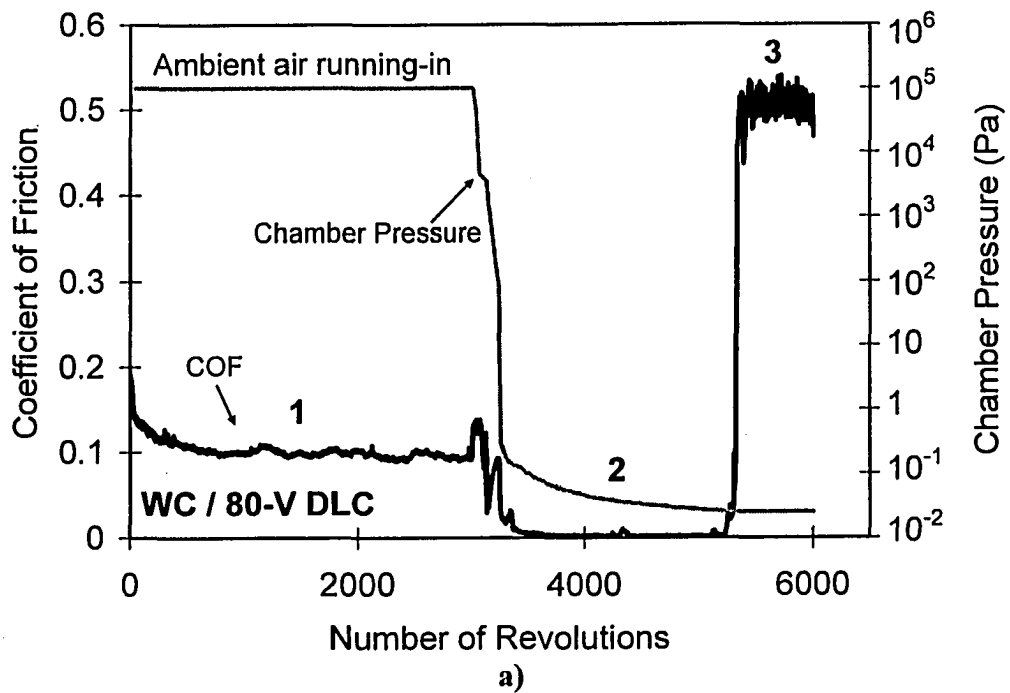
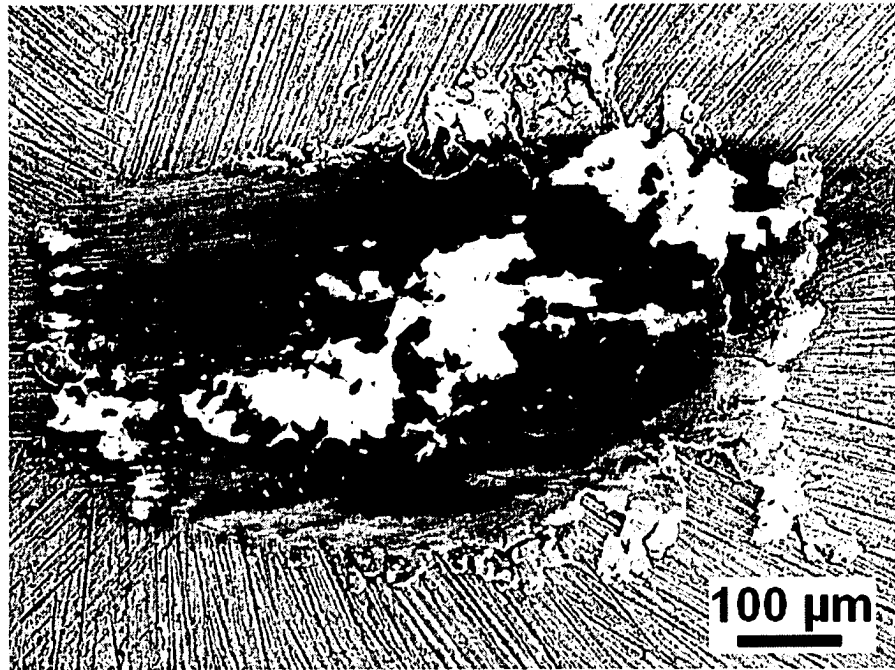
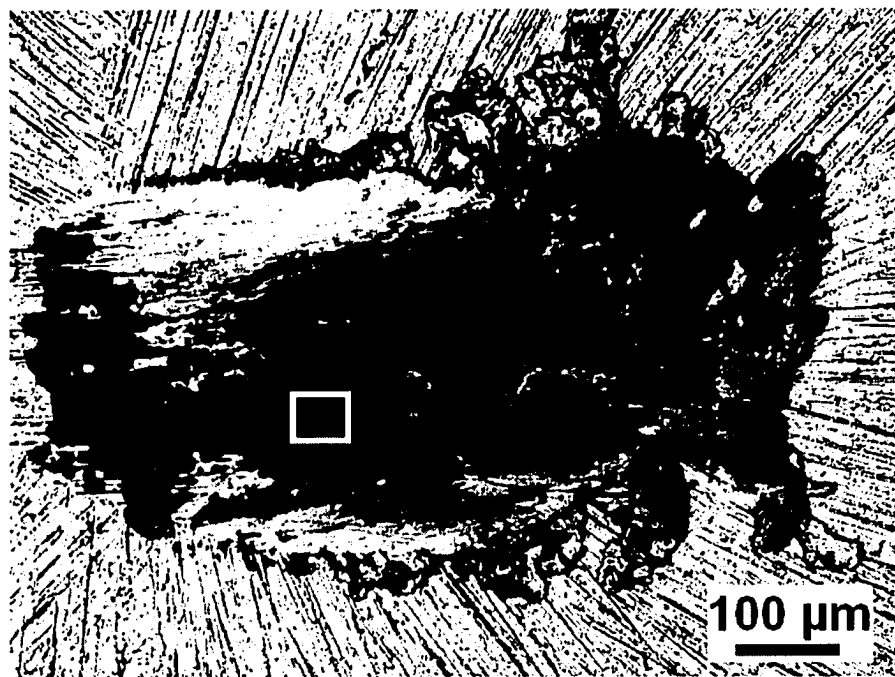


Figure 5.26. a) The COF curve for the ambient air to vacuum test when WC was tested against the 80-V DLC coating. The test started in ambient air (22% RH). After some sliding in ambient air (3.0×10^3 revolutions), the test chamber was pumped down to vacuum. The COF decreased as the pressure inside the chamber was lowered. The low COF period lasted for 2.2×10^3 revolutions and then the COF increased to high values (0.52). The applied load and the sliding speed were 5 N and 0.05 m/s, and **b)** a semi-log scale plot of the same curve.



a)



b)

Figure 5.27. a) SEI, and b) BEI SEM images of the contact surface of the 319 Al pin that was run against the non-hydrogenated DLC in H₂-He environment.

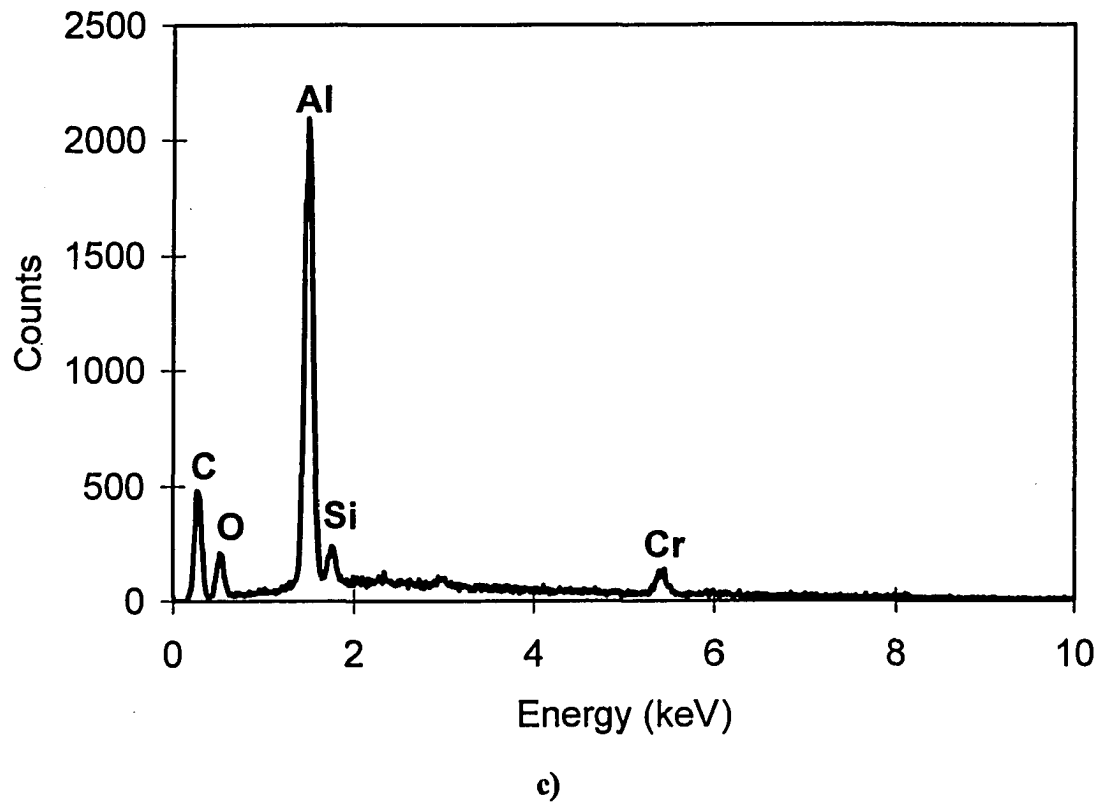


Figure 5.27. c) The EDS analysis of the location indicated in b).

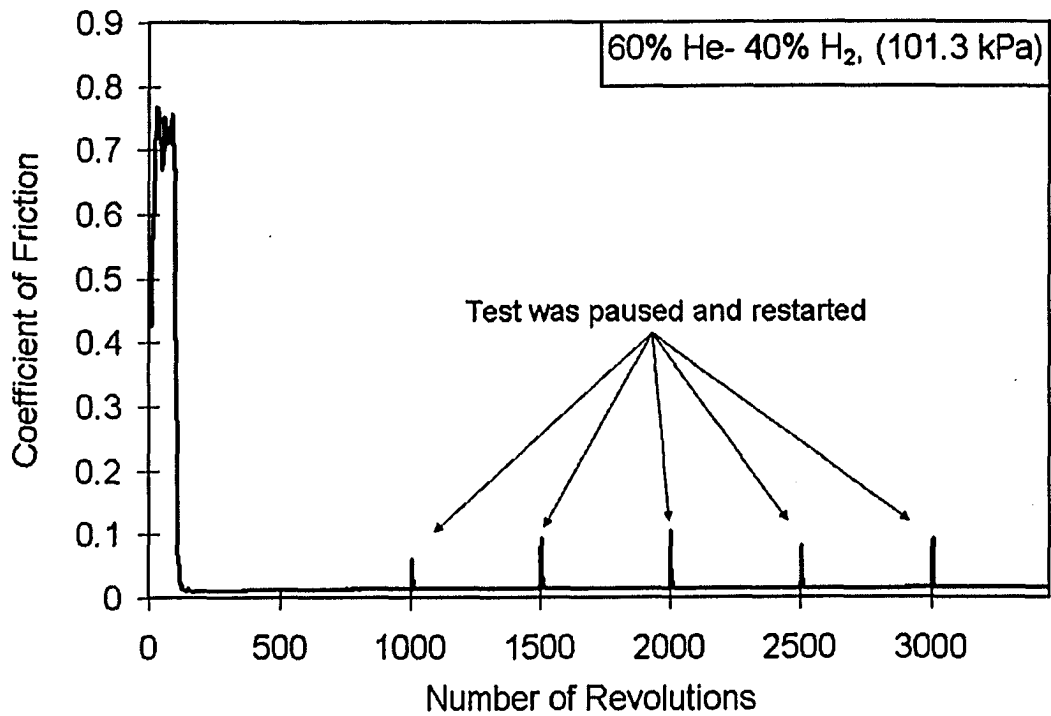


Figure 5.28. The COF between the 319 Al alloy pin and the Graphit-iC DLC coating in H₂-He environment at 0.12 m/s sliding speed and 5 N applied load. The test was paused for 30 seconds and then re-started at 1000, 1500, 2000, 2500 and 3000 revolutions (as indicated by the arrows). The high COF period was observed only at the beginning of the tests indicating that it was related with the formation the carbonaceous transfer layer.

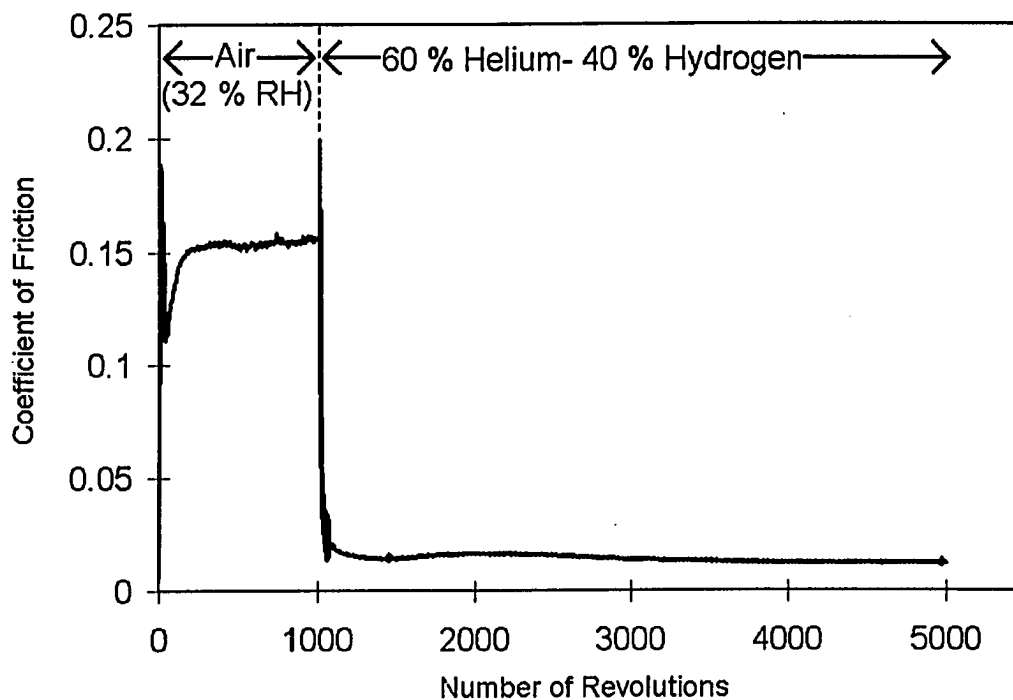


Figure 5.29. The COF between the Graphit-iC DLC coating and the 319 Al alloy pin at 0.12 m/s sliding speed under 5 N applied load. First, the tribopair was run in ambient air of 32% RH for 1×10^3 revolutions. Then, the test was stopped and the chamber was evacuated to 5.45×10^{-3} Pa. After flushing with nitrogen, the chamber was evacuated to 5.45×10^{-3} Pa again. Finally, the hydrogen (40% H₂-60% He mixture) was introduced and the test was resumed. Together with the test depicted in **Figure 5.25**, this test shows that the observed high COF at the beginning of the sliding in hydrogen was due to the transfer layer formation on the contact surface of the 319 Al alloy pin.

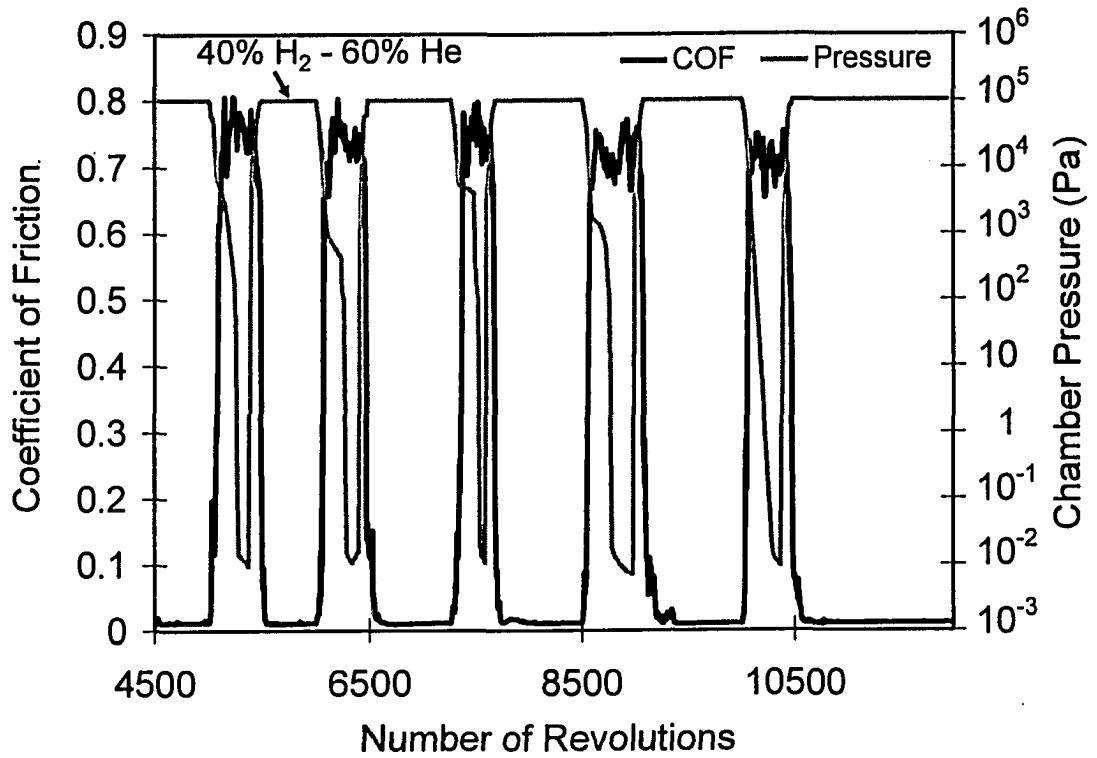


Figure 5.30. The effect of the pressure of the 40% H_2 -60% He mixture on the COF between the Graphit-iC DLC coating and the 319 Al alloy pin as a function of the number of revolutions. The sliding speed and the applied load were 0.12 m/s and 5 N.

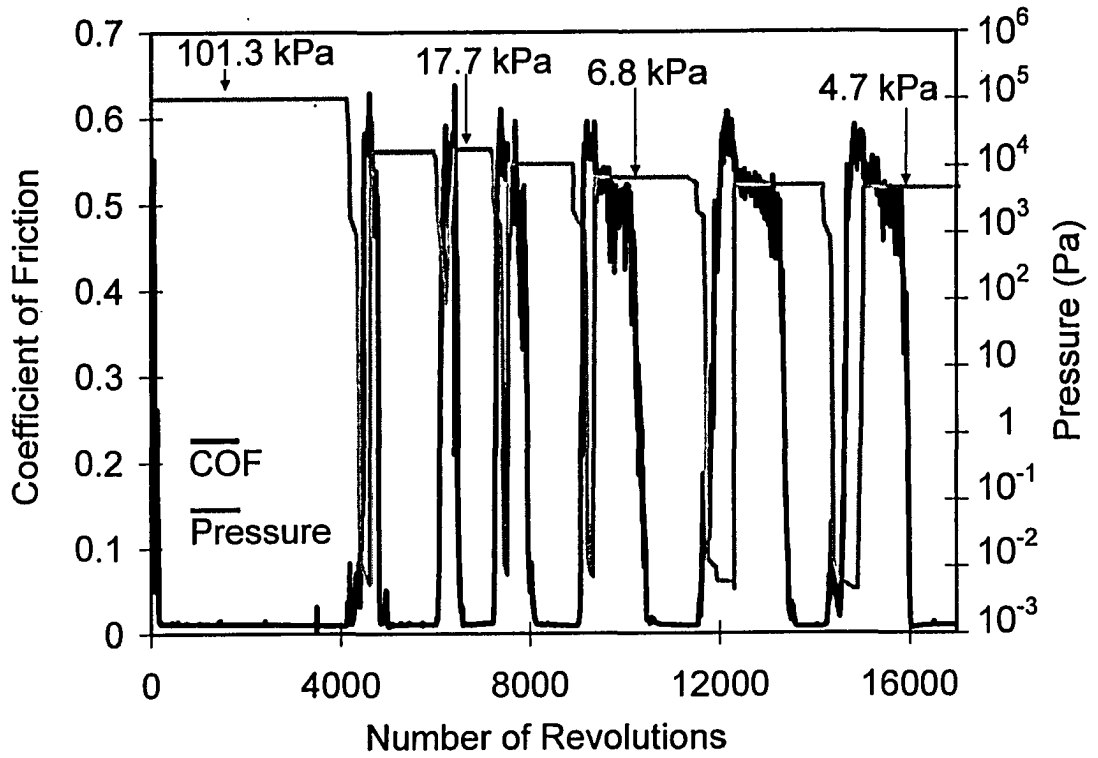


Figure 5.31. The COF between the Graphit-iC DLC coating and the 319 Al alloy pin as a function of the pressure of 40% H_2 -60%He. The sliding speed and the applied load were 0.12 m/s and 5 N.

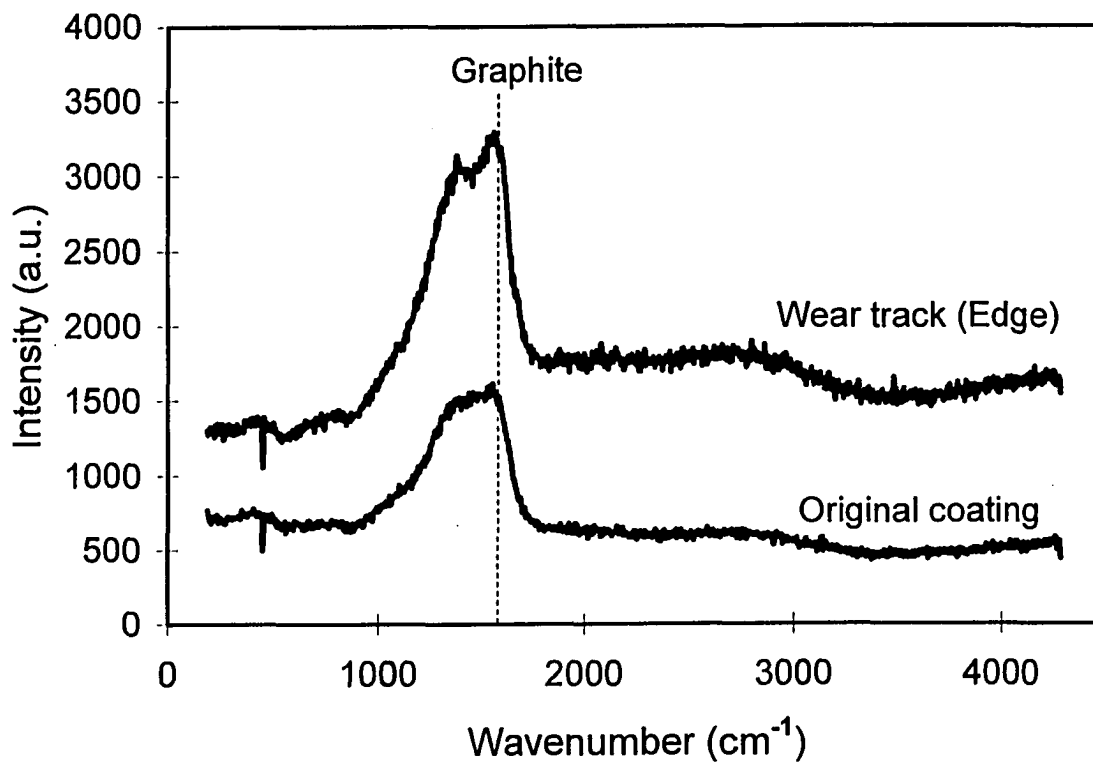


Figure 5.32. Micro-Raman spectra of the worn and unworn regions of the Graphit-IC DLC that was run against the 319 Al alloy pin in H₂-He mixture at 0.12 m/s and under an applied load of 5 N.

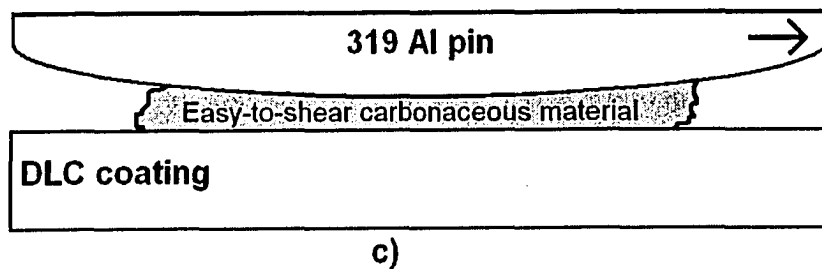
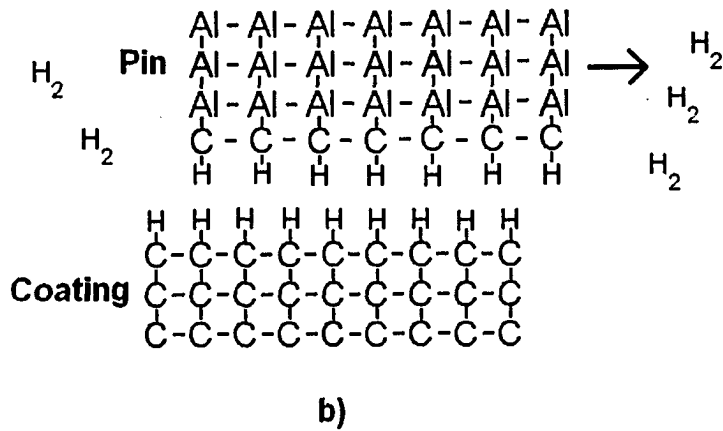
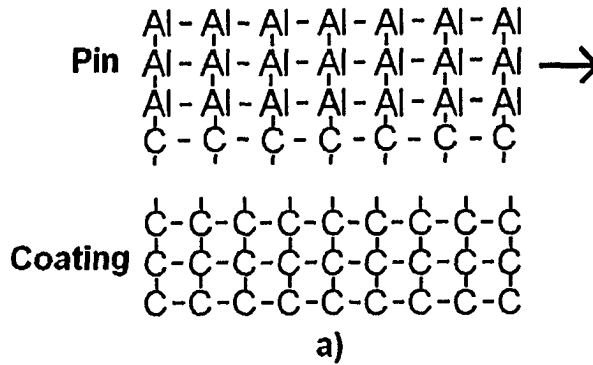
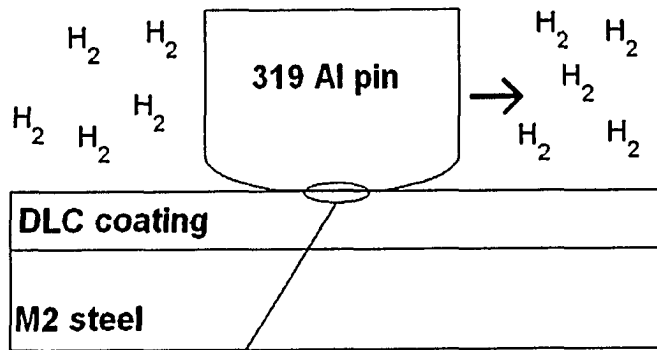


Figure 5.33. The friction mechanism of non-hydrogenated DLC coating in H₂-He environment.

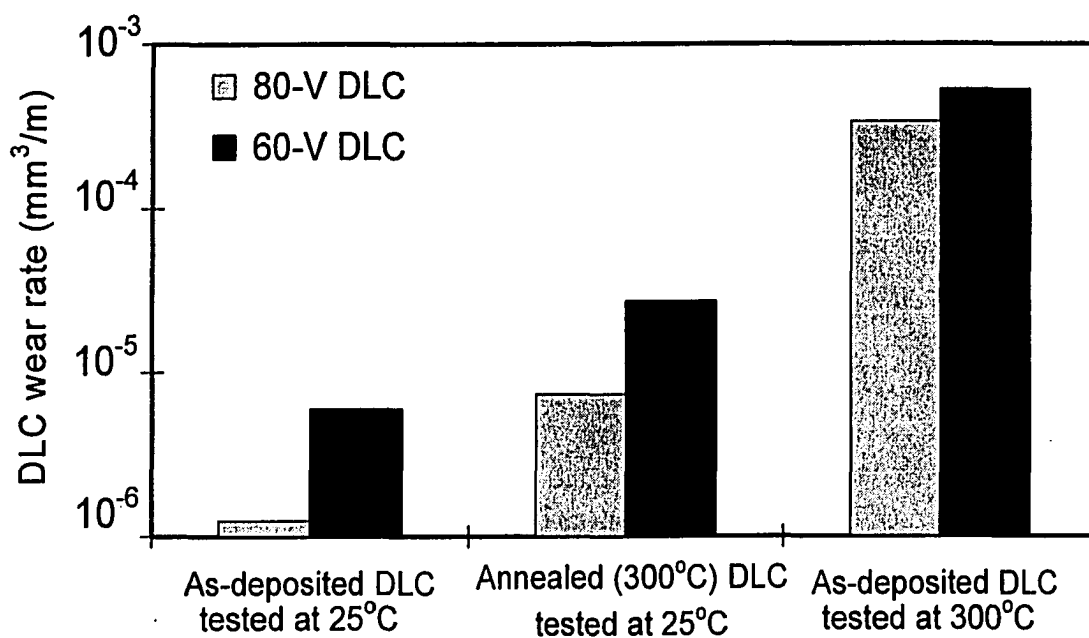
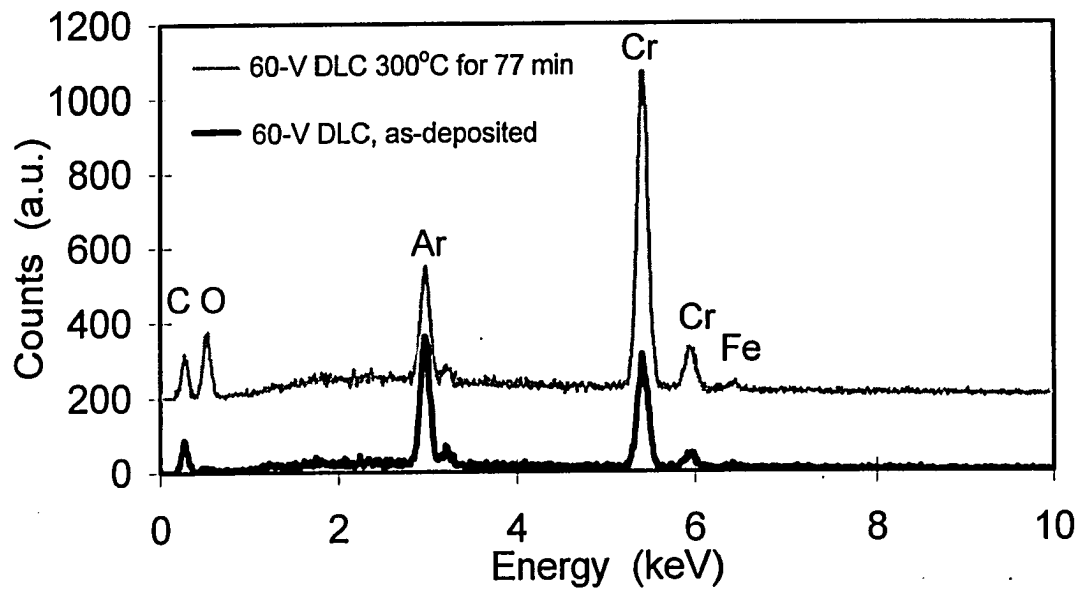
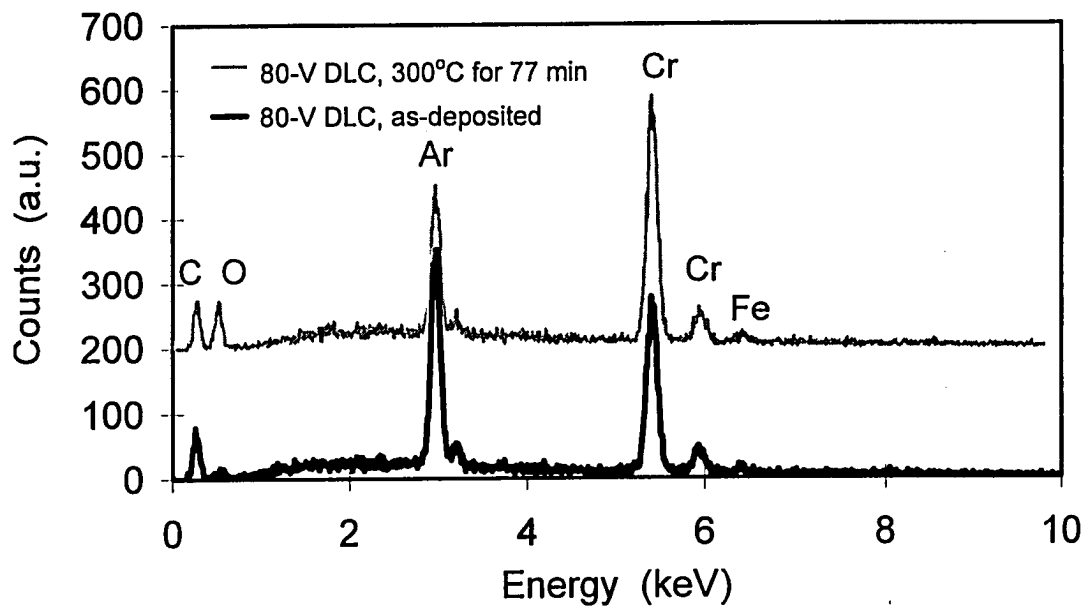


Figure 5.34. The wear rates of the 60-V DLC and 80-V DLC coatings before and after annealing at 300°C for 7.7 minutes. The tests that were done at 300°C are also included for comparison. All tests were run for 1×10^3 revolutions of sliding distance under an applied load of 5 N.

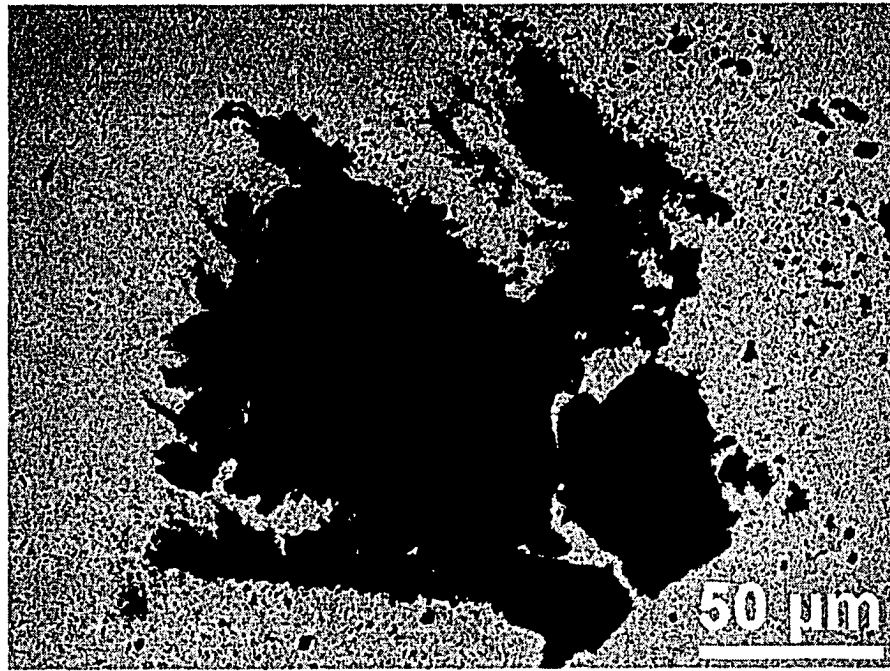


a)

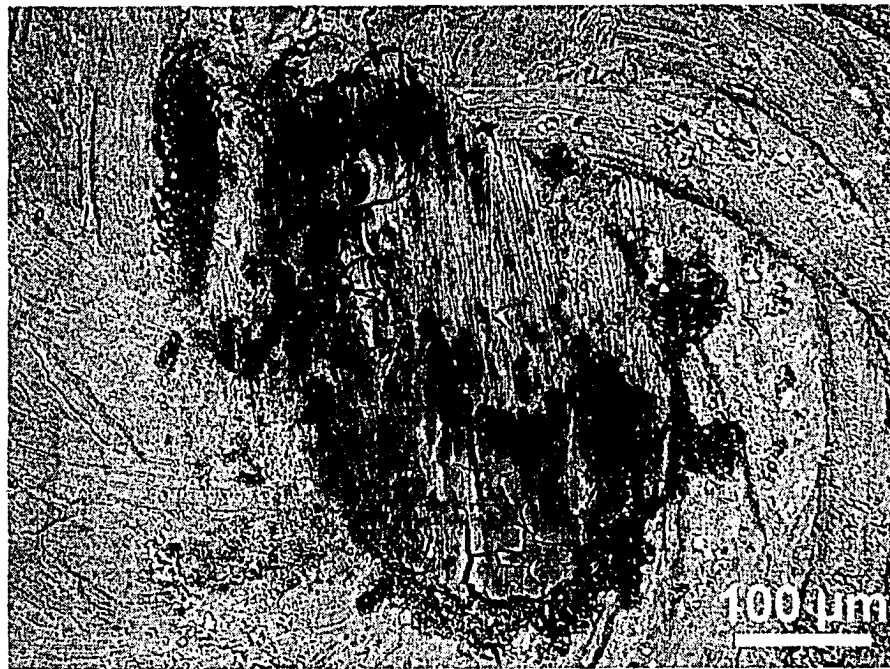


b)

Figure 5.35. The EDS analyses of the a) 60-V DLC and b) 80-V DLC coatings before and after annealing at 300°C in air for 77 minutes.

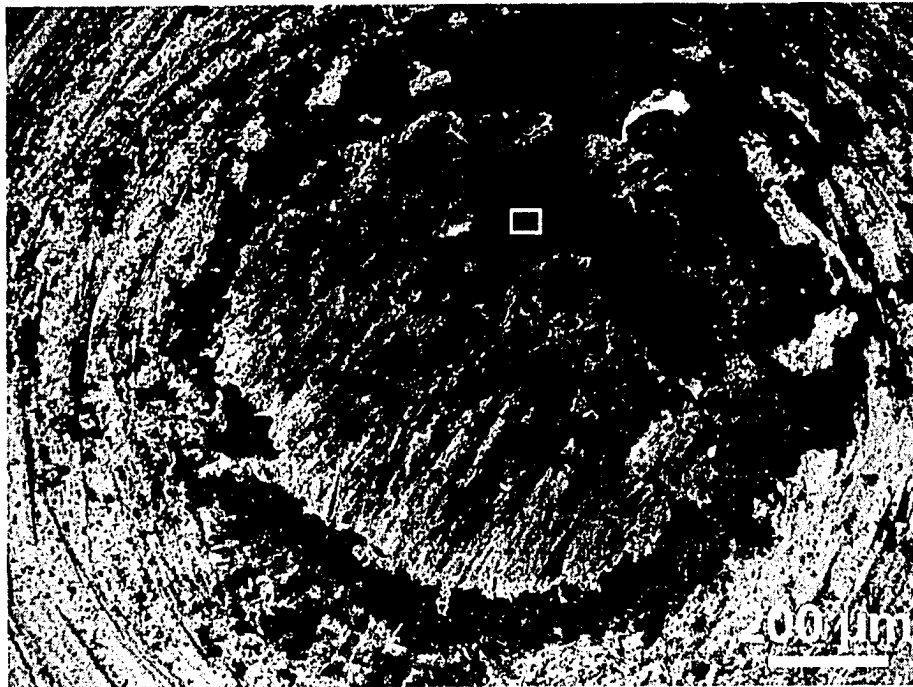


a)

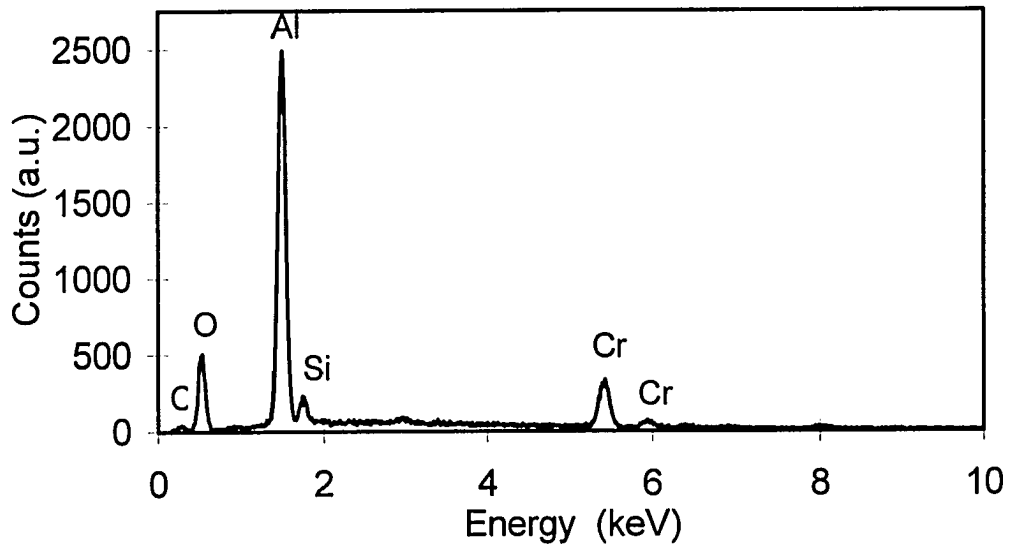


b)

Figure 5.36. SEM images of the contact surfaces of the counterface materials tested against the 60-V DLC coating for 1×10^3 revolutions under 5 N applied load at 0.12 m/s, **a)** WC ball at 25°C, and **b)** 319 Al pin at 25°C.



c)



d)

Figure 5.36. SEM images of the contact surfaces of the counterface materials tested against the 60-V DLC coating for 1×10^3 revolutions under 4.9 N applied load at 0.12 m/s, c) 319 Al pin at 120°C, d) the EDS analysis of the location indicated in c).

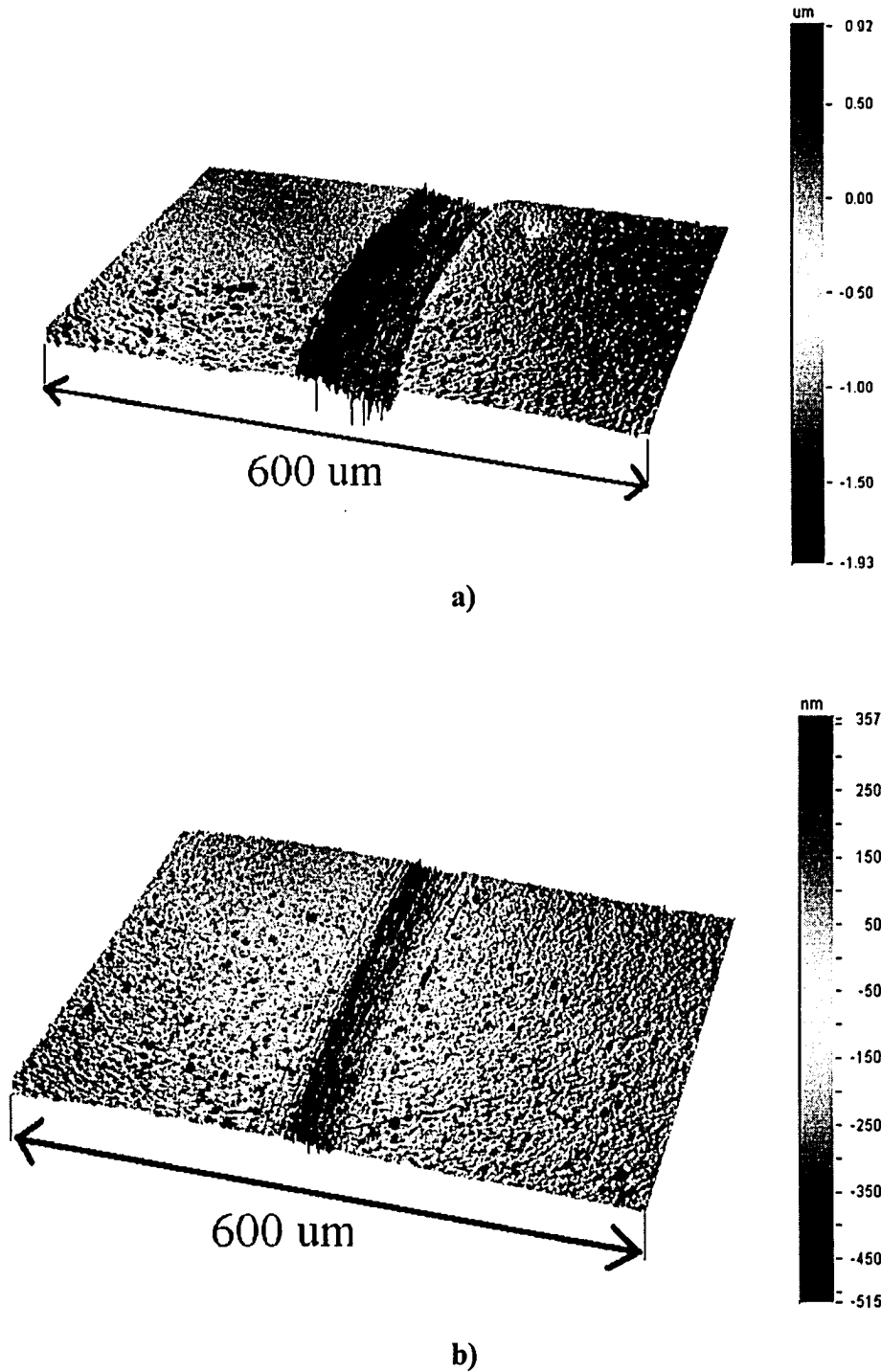


Figure 5.37. The surface profiles of the sections of the wear tracks of the 80-V DLC coating tested against a) 319 Al, b) WC and at 120°C for 1×10^3 revolutions of sliding distance under 5 N applied load.

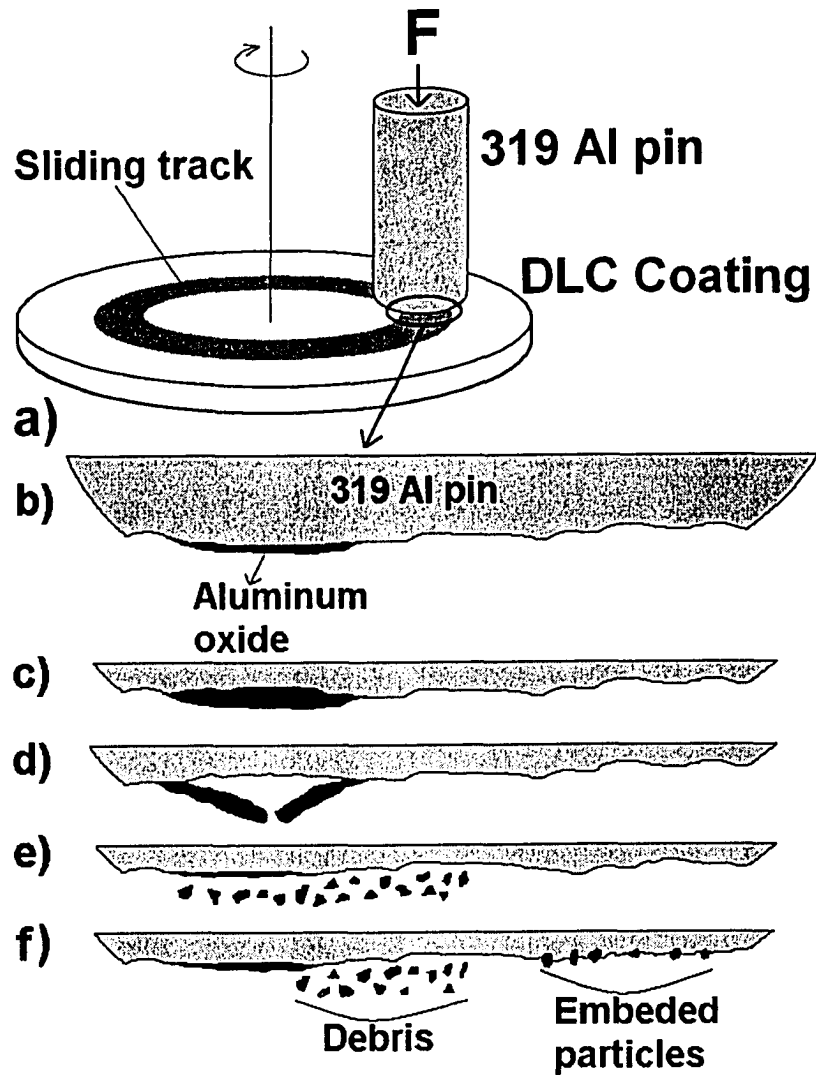


Figure 5.38. a) Schematic of the pin-on-disc test. Suggested mechanism of debris generation: First, the aluminum gets oxidized and the oxide thickness reaches a certain value (b & c). Then the oxide layer cracks, delaminates and fragments into loose debris (d & e). Some debris stay free at the sliding interface and some become embedded back on the 319 Al pin surface (f) causing abrasion of the DLC.

CHAPTER 6

ADHESION AND TRANSFER BEHAVIOUR OF PURE METALS (Al, Cu AND Ti) TO DLC, CrN, AND TiB₂ COATINGS

The work presented in this chapter was performed to contribute to understand the roles of the intrinsic (material properties) and extrinsic factors (environment and speed) on the adhesion and material transfer phenomena during dry sliding of metals and potential tool coatings. Rounded pins of 1100 Al, Cu and Ti were run against Graphit-iC DLC, TiB₂ ($R_a = 16$ nm) and CrN coated M2 tool steel discs in ambient air and argon. Three different sliding speeds of 0.02, 0.12 and 0.65 m/s were used. For the majority of the tests, sliding distances were kept short (300 rev. corresponding to 18 m of sliding) to focus on the initial stages of material transfer. After each test, the surfaces of the pins and discs were examined to characterize adhesion and transfer behaviour in different environments. Chapter 6 starts with the presentation of the results of the pin-on-disc tests with DLC coatings. This is followed by the presentation of the results of the tests with TiB₂ and CrN coatings. A detailed discussion and the interpretation of the results, together with the results of Chapters 4 and 5, will be given.

6.1. Adhesion and Transfer to Graphit-iC DLC

6.1.1. 1100 Al against Graphit-iC DLC in Argon

The tribological behaviour of the Graphit-iC DLC coating against 1100 Al was similar to the behaviour of Graphit-iC DLC coating against 319 Al presented in Section 5.3. In argon, the Graphitic-DLC coating experienced high wear rates (1.28×10^{-5} mm³/m) against 1100 Al at 180 m of sliding (3×10^3 rev.) at 0.12 m/s. There was some Al transfer to the Graphit-iC DLC coating surface at 0.12 and 0.65 m/s sliding speeds as shown in **Figure 6.1.a** and **b**. On the other hand, no adhesion of Al to the Graphit-iC DLC coating surface was observed at the lowest speed of 0.02 m/s. The 1100 Al pin experienced large surface deformation and material was displaced towards sliding direction as shown in **Figure 6.1.c** and **d**. The average COF values of the Graphit-iC DLC coatings against 1100 Al were 0.27 at 0.02 m/s, 0.63 at 0.12 m/s and 0.47 at 0.65

m/s (**Figure 6.2**). The latter two showed large fluctuations due to material transfer from the 1100 Al pin to the DLC coating surface.

6.1.2. 1100 Al against Graphit-iC DLC in Ambient Air

Compared to the tests performed in argon, the COF and the wear rate values of the Graphit-iC DLC coatings against 1100 Al were significantly reduced in ambient air (51% RH). At 0.12 m/s, the average COF and the wear rate of the Graphit-iC DLC coating against 1100 Al were 0.16 and 7.87×10^{-7} mm³/m. It should be noted that in all three sliding speeds, the tests started with high COF values of about 0.5 and then dropped to low values (0.13-0.16) in less than 50 revolutions (**Figure 6.3**). The COF curves recorded in ambient air had much less fluctuations compared to the ones recorded in argon (**Figure 6.2** vs. **Figure 6.3**). Also, the average COF values were relatively insensitive to sliding speed in ambient air; it was 0.14 at 0.65 m/s and 0.13 at 0.02 m/s. Accumulation of loose oxidized debris along the wear tracks of the DLC coating was observed (**Figure 6.4.a**). With increasing the sliding speed from 0.02 to 0.65 m/s, there was a slight decrease in the amount of debris generated. Similar to the case of 319 Al (**Section 5.1.4**), oxidized tribolayers containing C and Cr were observed on the contact surfaces of the 1100 Al pin as shown in **Figures 6.4.b-d** and verified by EDS (**Figure 6.4.e**).

6.1.3. Cu against Graphit-iC DLC in Argon

In argon, no material transfer was observed between the Cu pin and the Graphit-iC DLC coating in all three sliding speeds. The wear of the Graphit-iC DLC coatings against Cu was negligibly small ($<1 \times 10^{-9}$ mm³/m) in argon. **Figures 6.5.a** and **b** show optical and SEM images of the contact surfaces of the Cu pins tested against the DLC coating at 0.12 m/s sliding speed for 1×10^4 and 3×10^3 revolutions. These micrographs show no evidence of material transfer from the Graphit-iC DLC coating to the Cu pin. For a sliding period of 3×10^2 revolutions, the average COF of the Graphit-iC DLC coatings against the Cu pin in argon was 0.26 at 0.02 m/s, 0.42 at 0.12 m/s and 0.35 at 0.65 m/s with minor fluctuations due to the absence of material transfer between the

sliding surfaces (**Figure 6.6**). Extending test duration to 1×10^4 revolutions caused a small decrease in the average COF to 0.37.

6.1.4. Cu against Graphit-iC DLC in Ambient Air

In ambient air (58% RH), the Graphit-iC DLC coatings exhibited higher wear rate (7.99×10^{-7} mm³/m) against Cu compared to the minute amount of wear that occurred in argon. Loose debris was accumulated along the wear tracks of the Graphit-iC DLC coating as shown in **Figure 6.7.a**. **Figure 6.7.b** shows the SEM image of the Cu pin run against the Graphit-iC DLC coating in ambient air with 58% RH for 18 m of sliding. Oxidized tribolayers containing C and Cr were observed on the contact surfaces of the Cu pins (**Figures 6.7.c and d**). The COF curves were relatively smooth, especially at 0.02 and 0.12 m/s, with values between 0.36-0.46 (**Figure 6.8**).

It is interesting to note that, in contrast to the high wear of the Graphit-iC DLC against Al in argon, Cu only caused a negligible amount of wear under the same condition. On the other hand, both materials caused a similar amount of wear of the Graphit-iC DLC in ambient air while the COF against Cu (0.36-0.46) was considerably higher than against Al (0.13-0.16).

6.1.5. Ti against Graphit-iC DLC in Argon

At the sliding speeds of 0.12 and 0.65 m/s, significant adhesion and transfer of Ti to the Graphit-iC DLC coating surface causing the subsequent removal of the coating from the M2 substrate at several locations was observed as shown in **Figures 6.9.a-c**. Compared to 0.12 m/s, the adhered Ti pieces were larger at 0.65 m/s (**Figure 6.9.c**). On the other hand, there was no adhesion of Ti to the Graphit-iC DLC coating surface at 0.02 m/s (**Figures 6.10.a and b**). The average COF of the DLC coatings against Ti in argon was 0.29 at 0.02 m/s, 0.53 at 0.12 m/s and 0.59 at 0.65 m/s. Due to the large amount Ti transfer to the Graphit-iC DLC coating surface, the COF curves were highly fluctuating at 0.12 and 0.65 m/s (**Figure 6.11**).

6.1.6. Ti against Graphit-iC DLC in Ambient Air

In ambient air (59% RH) at a sliding speed of 0.12 m/s, the COF and the wear rate values of the Graphit-iC DLC coating against Ti were 0.09 and 7.34×10^{-7} mm³/m indicating a significant reduction compared to the tests in argon. As a typical characteristic of the pin-on-disc tests in ambient air, accumulation of loose debris along the wear tracks of the Graphit-iC DLC coating was observed (**Figure 6.12a**). Similar to the 1100 Al and Cu pins, the contact surfaces of the Ti pins were covered with oxidized tribolayers containing C and Cr, from the DLC coating (**Figure 6.12.b**). The average COF between the Graphit-iC DLC coating and Ti was 0.09 at 0.02 m/s and 0.11 at 0.65 m/s i.e. the COF was rather insensitive to sliding speed in the test range as seen in **Figure 6.13**.

6.2. Adhesion and Transfer to TiB₂ Coating

6.2.1. 1100 Al against TiB₂ in Argon

At 0.02 m/s sliding speed, some smearing of the Al to the TiB₂ coating surface was observed. The average COF was 0.32. The transferred pieces were small both in size (<10 μm) and quantity. At 0.12 m/s sliding speed, significant amount of smearing, transfer of material as in the form of very thin layers, occurred and Al fragments covered most of the sliding track (**Figures 6.14.a and b**). There were also large pieces of Al (50-100 μm) adhered to the TiB₂ coating surface. The average COF was high (0.76 ± 0.07) at 0.12 m/s. Similar to the tests at 0.12 m/s, significant amount of smearing occurred at 0.65 m/s sliding speed. After reaching a peak value of 0.89 around 50 rev., the COF dropped to 0.46 with larger fluctuations (**Figure 6.15**). The adhered pieces, however, were rather small in size compared to the ones adhered at 0.12 m/s.

When the test was extended to 180 m of sliding distance (3×10^3 revolutions) at 0.12 m/s sliding speed, some more Al transfer occurred in the form of chunks of 100-200 μm in size (**Figure 6.16.a**). The width of the wear track increased from 570 μm at 18 m of sliding to 700 μm at 180 m. The COF was initially high (about 0.78 at 250 revolutions) and dropped to a steady state value of 0.36 after 500 revolutions (**Figure 6.16.b**).

6.2.2. 1100 Al against TiB₂ in Ambient Air

No significant smearing, transfer in the form of very thin layers, was observed under any test speed in ambient air (43% RH). The adhered material was mostly in the form of chunks of 15-50 μm . The COF between 1100 Al and TiB₂ was high and largely fluctuating with average values of 0.64 at 0.02 m/s, 0.69 at 0.12 m/s and 0.72 at 0.65 m/s (**Figure 6.17**). Compared to the tests performed in argon, the most significant difference was in the formation of loose debris as shown in **Figure 6.18.a**. There was a large quantity of debris formed at 0.02 m/s and the amount of debris formed decreased with increasing the sliding speed. The EDS analyses of the both wear debris and the adhered pieces showed considerable amount of oxidation (**Figure 6.18.b**). When the sliding distance was increased from 18 to 180 m at 0.12 m/s sliding speed in ambient air, more debris was formed (**Figures 6.19.a and b**). Most of the loose debris stayed on the sliding track and some became agglomerated at various locations along the track.

6.2.3. Cu against TiB₂ in Argon

There was only a minute amount of Cu transfer to the TiB₂ coating surface at all test speeds. Very small pieces of Cu which probably adhered as a result of sliding contact with asperities on TiB₂ surfaces are shown in **Figures 6.20.a and b**. The contact area of the Cu pin was smooth and clean indicating the absence of material transfer (**Figure 6.20.c and d**). Longer sliding distance of 180 m at 0.12 m/s did not change this behaviour. At 0.12 m/s sliding speed, the COF curve was smooth throughout the test with a mean value of 0.48 ± 0.02 . The average COF was 0.56 at 0.65 m/s.

6.2.4. Cu against TiB₂ in Ambient Air

The amount of debris formed was the highest when Cu was run against the TiB₂ coating at a sliding speed of 0.12 m/s in ambient air (41% RH). Occasionally, there were Cu pieces adhered to the TiB₂ coating surface at sliding speeds of 0.12 and 0.65 m/s (**Figure 6.21.a**). The contact surfaces of the Cu pins were covered by oxidized tribolayers containing Ti and Cu (**Figure 6.21.b and c**). In all three test speeds, the COF was 0.17 initially and gradually increased to 0.80 at 300 rev. of sliding (**Figure 6.22**). Increasing the sliding distance to 3×10^3 rev. did not change the behaviour of the system; the COF

maintained its steady state value at 0.80, which was higher than the one observed in the argon test (0.48).

6.2.5. Ti against TiB₂ in Argon

In comparison to 1100 Al and Cu, the largest amount of adhesion and material transfer occurred from the Ti pin to the TiB₂ coating under the argon atmosphere. The amount and size of the adhered Ti increased with increasing sliding the speed. At 0.02 m/s, the adhered pieces were small in size (<15 μm) and smeared to the surface (**Figures 6.23.a and b**). However, the adhered pieces of Ti were much larger (30-120 μm) at 0.12 m/s and 0.65 m/s as shown in **Figures 6.24.a and b**. The average COF was 0.3 at 0.02 m/s and 0.7 at 0.12 m/s sliding speeds. At 0.65 m/s, the COF started at 0.60 and then increased to 1.2 around 5 m of sliding (90 revolutions) and gradually decreased to 0.6 (**Figure 6.25**). There was a part of the sliding track where the coating was detached from the substrate. With increasing sliding distance, more Ti adhered and covered larger portions of the TiB₂ coating surface. Meanwhile, the width of the sliding track increased from 466 μm at 18.00 m to 608 μm at 180.00 m. The COF had the average value of 0.54 with fluctuations of ± 0.15.

6.2.6. Ti against TiB₂ in Ambient Air

Compared to the tests performed under the argon atmosphere, the amount of Ti adhered to the TiB₂ coating surfaces was drastically reduced in ambient air (46% RH) at 0.02 m/s and 0.12 m/s sliding speeds. However, there was still considerable amount of Ti adhesion at 0.65 m/s in ambient air. A very small amount of debris was formed at this speed. A lot of debris formation was observed at 0.12 m/s and 0.02 m/s, the latter being more. At 0.02 m/s and 0.12 m/s sliding speeds, the COF started at low values (about 0.13) and then gradually increased to high values (0.55-0.75) at the end of the tests (**Figure 6.26**). When the sliding distance was extended to 180 m at 0.12 m/s, the average COF was 0.69 ± 0.20 after 18.00 m. There was no increase in the amount of Ti adhered to the TiB₂ surface with increasing sliding distance (**Figure 6.27.a**). However, a lot of debris formed during sliding (**Figure 6.27.b**). Some of the debris was in the form of small

rounded particles (with higher oxygen content) while the others were plate-like and more metallic (i.e. less oxidized).

6.3. Adhesion and Transfer to CrN

6.3.1. 1100 Al against CrN in Argon

At the sliding speed of 0.65 m/s, the transfer of aluminum to the CrN coating surface was essentially in the form of smears as shown in **Figure 6.28.a-d**. However, at a lower speed of 0.12 m/s, aluminum transferred to the CrN surface both in the form of smears and bulk pieces (**Figure 6.28.e and f**). There was no bulk transfer of Al at 0.02 m/s, but some smearing still occurred. At 0.65 m/s, the COF curve had fluctuations with the average value of 0.63. The average COF was 0.76 at 0.12 m/s and 0.26 at 0.02 m/s (**Figure 6.29**). As a general characteristic of the tests in argon, there was no loose debris generated during sliding.

6.3.2. 1100 Al against CrN in Ambient Air

Different than the other sliding pairs tested in this chapter, significant amount of Al transfer to the CrN coating surface occurred during sliding in ambient air of 42% RH (**Figures 6.30.a-f**). The amount of debris generated and Al transferred to the CrN coating surface increased as the sliding speed was decreased from 0.65 to 0.02 m/s as shown in **Figures 6.30.a, c and e**. The COF values were high and fluctuated (± 0.14) in all test speeds (**Figure 6.31**). In all test speeds, the COF quickly increased to values around 1.0 with the start of sliding. Then, it gradually decreased to 0.6 at 0.65 m/s, 0.5 at 0.12 m/s and 0.65 at 0.02 m/s.

6.3.3. Cu against CrN in Argon

The sliding tracks on the CrN coating were barely noticeable when tested against Cu in the argon atmosphere (**Figure 6.32.a**). No material transfer between the sliding surfaces was detected at 0.12 and 0.65 m/s sliding speeds (**Figure 6.32.b**). The COF curves were smooth (± 0.03 fluctuation) with the average values of 0.47 at 0.65 m/s and 0.43 at 0.12 m/s (**Figure 6.33**).

6.3.4. Cu against CrN in Ambient Air

When Cu was run against the CrN coating in ambient air (42% RH), a decreasing amount with debris formation with increasing sliding speed, was observed (**Figures 6.34.a-c**). There was very small adhesion of Cu to the CrN coating surface. The COF curves were smooth with average values of 0.40 at 0.65 m/s, 0.36 at 0.12 m/s and 0.35 at 0.02 m/s (**Figure 6.35**). In parallel with the amount of debris accumulated on the CrN coating surface, the relative amount of oxidized debris material accumulating around the contact surface of the Cu pin increased with decreasing sliding speed (**Figures 6.36.a-f**).

6.3.5. Ti against CrN in Argon

Significant amount of Ti adhered to the CrN coating surface in argon at 0.65 and 0.12 m/s (**Figures 6.37.a-b**). The COF curve had fluctuations with an average value of 0.81 at 0.65 m/s and 0.64 at 0.12 m/s (**Figure 6.38**). The CrN coating exhibited some wear against Ti. There was almost no Ti adhesion to the CrN coating surface at 0.02 m/s but it still was observed that the CrN coating suffered some surface damage (**Figures 6.37.e and f**). A smooth COF curve with a mean value of 0.30 was recorded at 0.02 m/s. The sizes and contents of the Ti pins also indicated that the direction of material transfer was from the Ti pins to the CrN coating at 0.65 and 0.12 m/s sliding speeds whereas it reversed at 0.02 m/s (**Figures 6.39.a -f**).

6.3.6. Ti against CrN in Ambient Air

In ambient air (51% RH), debris formation and adhesion of Ti to the CrN coating surface was observed at all speeds (**Figures 6.40.a-c**). Increasing test speed from 0.02 m/s to 0.65 m/s decreased the amount of debris generated. Sliding speed did not affect the average values of the COF appreciably; it was 0.54 at 0.65 m/s, 0.55 at 0.12 m/s and 0.54 at 0.02 m/s (**Figure 6.41**).

6.4. Remarks

Among the test results presented in this chapter, the following observations are worth highlighting:

1. Cu did not show any adhesion and transfer to CrN, Graphit-iC DLC or TiB₂ surfaces in argon.

2. In ambient air, Cu did not stay adhered to the CrN and Graphit-iC DLC coating surfaces. Although very small, some transfer of Cu to the TiB₂ surface was observed in ambient air.

3. Ti showed very large amount of transfer to all three coating surfaces in argon. Due to its high adhesion tendency, Ti caused some wear of the Graphit-iC DLC and CrN coatings during sliding contact in argon.

4. Compared to the tests in ambient air, COF was more depended on sliding speed in the argon atmosphere. The average COF increased with increasing the sliding speed in argon especially in the range of 0.02 m/s and 0.12 m/s. At sliding speed of 0.02 m/s in argon, the average COF was generally around 0.3 for all test pairs.

5. For all sliding combinations with the exception of the 1100 Al-CrN pair, changing the test atmosphere from argon to ambient air drastically reduced the amount of material remaining adhered on the coating surfaces and promoted oxidized loose debris formation. For the 1100 Al-CrN pair however, in addition to debris formation, a large amount of Al adhered to the CrN coating surface in ambient air than in argon.

6. Contact surfaces of the metal pins had a metallic appearance after the tests in argon indicating that the direction of material transfer was from them to the coating surfaces (i.e. absence of transfer layer formation on their surfaces). In ambient air however, oxidized material accumulated on the contact surfaces of the pins forming transfer layers for most test pairs.

7. In argon, all the material removed from the pins stayed adhered on the coating surface either in the form of pieces or smears. In ambient air, most of the material removed from the pins turned into loose debris during further sliding. The EDS analyses showed that the debris particles contained significant amount of oxygen. In both test environments, Al adhesion occurred in the form of pieces and/or smears whereas Ti always mostly adhered as pieces. Very thin smeared layers were only observed with Al.

8. Generally, the amount of debris formed decreased with increasing sliding speed.

9. In ambient air, Cu had higher average COF value (0.40) against the Graphit-iC DLC coating as compared to 1100 Al (0.14) and Ti (0.09). This suggested that the mechanism of friction between Cu and Graphit-iC DLC was not the same as the one between 1100 Al, Ti and Graphit-iC DLC.

6.5. General Discussion of the Adhesion and Material Transfer Phenomena during Sliding Wear

The section is devoted to the discussion of the factors that control and influence adhesion and material transfer between the surfaces in sliding contact. The results of the pin-on-disc tests presented in this and previous chapters will be used. The physical properties of the tested materials, the chemical affinities of the sliding pairs towards each other, their oxidation characteristics, and interactions with oxygen and water vapour will be the main elements of discussion.

6.5.1. Adhesion and Material Transfer in an Argon Atmosphere

It is suggested that in an inert atmosphere such as argon, in addition to the relative hardness values of the contact surfaces, material transfer behaviour between the sliding surfaces is controlled by the following two factors; i) the chemical affinity of the materials towards each other, and ii) their thermal characteristics. To support this statement, adhesion and transfer behaviour of Cu and Ti in argon will be discussed here.

6.5.1.1. Why Does Cu Not Adhere to the CrN, DLC or TiB₂ Coatings in Argon?

As shown in Sections 6.1.3, 6.2.3 and 6.3.3, only a negligible amount of transfer occurred from Cu to the CrN, DLC or TiB₂ coatings in argon at all sliding speeds. It is well known that the temperature rise ($T_b - T_o$) due to the frictional heating at the sliding interface (equation 6.1. below) is inversely proportional to the thermal conductivities of the sliding pair [142, 143].

$$T_b - T_o = \frac{\mu \cdot F \cdot v}{A_n} \left[\frac{1}{\frac{k_1}{l_{1b}} + \frac{k_2}{l_{2b}}} \right] \quad \text{Equation 6.1.}$$

In equation 6.1, A_n denotes the nominal contact area at the sliding interface between two solids in contact. μ , F and v represent the COF, normal force and the relative sliding speed between the sliding surfaces. k_1 and k_2 are the thermal conductivities of the materials in sliding contact, and l_{1b} and l_{2b} are the two lengths. A complete description is given in **Appendix A.1**.

Among all metals, Cu is the second highest metal thermal conductor with a thermal conductivity of 385 W/m.K after Ag. Therefore, local softening of the Cu pin due to the frictional heating that would initiate adhesion is not expected to occur since the heat generated at the sliding interface can dissipate quickly.

Cu does not have a high driving force for mixing or for compound forming with neither CrN nor TiB₂ or DLC. In the case of CrN, the solubility of Cu in Cr is almost nil as shown in **Figure 6.42** [144]. When DLC is concerned, Cu has a very small tendency towards C to form copper carbide. Cu has a limited solubility in Ti (maximum 2.1 wt. % at 790 °C) (**Figure 6.43**) [145]. It does not have a tendency to form a compound with boron either [146]. Therefore, there are not strong interactions between Cu and these coatings that could cause adhesion and material transfer during sliding contact in the argon atmosphere. Very small pieces of Cu, which adhered probably because of mechanical interlocking with TiB₂ asperities, were detected on the TiB₂ coating surface (**Figures 6.20.a and b**).

6.5.1.2. Why does Ti have high tendency to adhere to CrN, DLC and TiB₂ Coatings in Argon?

When the Ti pins were run against the CrN, DLC and TiB₂ coatings in argon, high amounts of Ti were transferred to these coatings as documented in **Sections 6.1.5, 6.2.5 and 6.3.5**. Naturally, Ti has high chemical affinity towards TiB₂ (**Figure 6.44**). In the case of DLC, Ti has a high driving force towards C to form TiC (Equation 6.2). The Gibbs free energy of formation of TiC is -180.0 kJ/mole at 300 K [129].



For the CrN coatings, the very high chemical affinity of Ti towards N to form TiN should be noted (Equation 6.3). The Gibbs free energy of formation for TiN is -243.8 kJ/mole at 300 K [129].



Ti also forms an intermetallic compound (TiCr_2) with Cr and they are completely miscible at elevated temperatures (**Figure 6.45**). Hence, it is not surprising that Ti had strong adhesional interactions with these coatings.

The thermal conductivity of Ti (21.9 W/m.K) is very low in comparison with Al (229 W/m.K) and Cu (385 W/m.K). Therefore among the metals tested, the flash temperature rise due to the frictional heating at the sliding interface and at the contacting asperities must have been the highest for Ti. It is thought that this frictional heating at the sliding interface promoted adhesion of Ti to the CrN, DLC and TiB_2 coating surfaces.

6.5.1.3. Effect of Sliding Speed on Adhesion and Material Transfer in Argon

In Chapter 6 (**Sections 6.1.5, 6.2.5 and 6.3.5**), it was reported that increasing the sliding speed of the Ti pin running against CrN, DLC and TiB_2 coatings from 0.02 m/s to 0.65 m/s increased the amount of Ti transferred to the surfaces of these coatings in argon. It is suggested that the increase in the amount of adhesion and material transfer with increasing the sliding speed in argon is due to the combined effects of the increased frictional heating at the sliding interface and the decrease in the interaction time of the remaining reactive gaseous species with the sliding surfaces. Although the number of adhesion spots/junctions decreased with the sliding speed, the amount of material adhered per junction increased. In the case of Cu however, the increase in the frictional heating was not high enough to cause a local softening that would initiate its adhesion to these coatings.

6.5.2. Frictional Heating of the Sliding Surfaces

In order to have an idea on the extent of temperature rise at the asperities due to the frictional heating during sliding, a computational approach coupled with experimental

measurements was taken. A K-type thermocouple connected to a personal computer via a data acquisition system was used to continuously measure and record the temperature of the pins at a location 2.5 mm far from the sliding interface (**Figure 6.46**). Al and Ti pins were run against the 80-V DLC and CrN coated and uncoated M2 tool steel discs in ambient air (43-57% RH) at sliding speeds of 0.12 and 0.65 m/s under an applied load of 5N. The measured increases of the actual bulk temperatures compared to the ambient temperature are shown in **Figure 6.47**. Against the 80-V DLC coating, the temperature increase due to sliding at 0.12 cm/s was only 0.6°C for Al and 0.4°C for Ti, the two lowest measured values. At the same sliding speed, the temperature increases of the Al and Ti pins sliding against uncoated M2 tool steel were higher; 4.0°C and 3.8°C respectively. When the sliding speed was increased from 0.12 m/s to 0.65 m/s, the bulk temperatures of the Al and Ti pins running against the 80-V DLC coating increased by 4.8°C and 3.4°C. On the other hand, the temperature increase at 0.65 m/s was much more pronounced when the pins were run against the M2 tool steel disc; 18.9°C for Al and 17.8°C for Ti. Sliding against the CrN coated disc at this speed also caused significant increases in the bulk temperatures of the pins; 19.0°C for Al and 16.2°C for Ti.

The computational procedure described in **Appendix A.1**, developed by Ashby and his colleagues [143, 159, 160], was used to calculate the bulk and flash temperatures of Al and Ti running against the 80-V DLC and CrN coated and uncoated M2 tool steel discs at the same conditions as the experiments described in the previous paragraph [147]. The material properties, the values of the other parameters and assumptions used for the calculations are given in **Table A.1.2 and A.1.3**.

The calculated increases in bulk temperature values were mostly in agreement with the experimentally measured ones as seen in **Figure 6.48** supporting the validity of the computation method. The calculated flash temperature values, the ones of more interest than bulk temperatures because of their “suspected role” in initiating adhesion, are given **Table 6.1**. At 0.65 m/s sliding speed, the flash temperature value of the contacting asperities between M2 steel and Al was calculated as 143.7°C. At the same sliding speed, the calculated flash temperature value for Al/80-V DLC pair was 93°C. At a lower speed of 0.12 m/s, the flash temperature values for Al/M2 steel and Al/80-V DLC pairs were calculated as 49°C and 38°C. The highest flash temperature value (879.9

Celsius) was for the Ti/CrN pair running at a sliding speed of 0.65 m/s. Therefore, these calculations showed that the role of frictional heating in initiating adhesion became larger with the sliding speed.

Table 6.1. The calculated flash temperature values.

Pin	Disc	Speed (m/s)	Flash T (°C)	Flash T (K)	Homologus T (T/T_m)
Ti	CrN	0.65	904.9	1178.1	0.61
Ti	M2 Steel	0.65	452.9	726.0	0.37
Al	CrN	0.65	252.1	525.2	0.56
Al	M2 Steel	0.65	143.7	416.9	0.45
Al	DLC	0.65	92.9	366.0	0.39
Ti	DLC	0.65	318.4	591.6	0.30
Ti	M2 Steel	0.12	106.4	379.6	0.20
Al	M2 Steel	0.12	48.7	321.9	0.34
Al	DLC	0.12	38.5	311.6	0.33
Ti	DLC	0.12	76.3	349.4	0.18
T _m (Al) = 933 K					
T _m (Ti) = 1941 K					

6.5.3. Adhesion and Material Transfer in Ambient Air

Compared to the tests in argon, one of the most obvious differences of the results of the pin-on-discs tests in ambient air was the formation of oxidized loose debris. In argon, almost all the material removed from pins stayed adhered on the coating surface either in the form of fragments or smears. In ambient air however, most of the material removed from the pins turned into loose debris. Actually, for all combinations except Al/CrN pair, changing the test atmosphere from argon to ambient air drastically reduced the amount material remaining adhered to the coating surfaces and promoted oxidized loose debris formation.

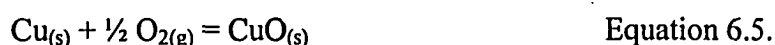
The mechanism of debris formation was previously discussed in **Section 4.5.1** when the results of dry sliding between 319 Al alloy and various coatings in argon and ambient air were analyzed. At this point, it is useful to have a closer look at the debris formation process in more detail.

6.5.3.1. Mechanism of Debris Generation during Sliding

Some theories on the mechanism of debris generation suggest the transfer of material to the counterface as the first step of the debris generation process [12, 23, 27]. For example, Kerridge and Lancaster [12] proposed that the debris generation process consists of two steps; i) the transfer of metal from the wearing surface to the opposing surface and ii) the formation of wear debris from the transferred layer on the opposing surface. After the initial transfer from pin to the coating surface, the transferred material was detached from the coating surface during the next visit(s) of the pin. This was followed by the fragmentation of the adhered material into loose debris and/or its temporary back-transfer to the pin surface.

Since there was a significant amount of debris formation in ambient air tests, it is proposed that the adhesion and material transfer in ambient air was far more than one would estimate by only considering the material remained adhered at the end of the tests. Therefore, a more accurate statement would be to claim that compared to an inert atmosphere, the presence of air and/or water vapour in the test environment was effective in reducing the amount of material that remains strongly adhered to the coating surface for all test pairs except Al/CrN.

Comparison of the EDS analyses of the adhered materials formed in argon and ambient air showed that the adhered material that was formed in ambient air was significantly oxidized. The occurrence of oxidation is not surprising due to the very high chemical affinity of especially Al and Ti for oxygen. The standard Gibbs free energies of formation for Al₂O₃ (Equation 5.2), TiO₂ (Equation 6.4) and CuO (Equation 6.5) at 300 K are -1,582.3, -888.8 and -129.7 kJ/mole, respectively [138].



Since the compositions of the adhered materials were different, the composition and structure of the interfaces between the coatings and the adhered materials must also be different in argon and in ambient air. Due to the fact that increasing the sliding distance increased the amount of material adhered in argon but not in ambient air, the bonding strength of the interface formed between the adhered materials and the coatings must be weaker in ambient air.

Among the pairs tested in Chapter 6, the Al/CrN pair is an exception. For the Al-CrN pair, in addition to debris formation, more Al adhered to the CrN coating surface in ambient air compared to that in argon (**Figure 6.28 vs. 6.30**). A similar observation was also documented in Chapter 4 when 319 Al was run against the nitrogen containing coatings (CrN, TiN, TiAlN and TiCN) (**Figure 4.7**). As shown in **Figure 4.4**, most of the sliding track of the CrN coating was covered by 319 Al after sliding in ambient air for 3×10^2 revolutions. Consequently, the bonding formed between the adhered aluminum and CrN coating in ambient must be stronger than the one formed in argon.

This example shows that the bonding strength of the interface forming in ambient air is the most important factor to determine whether the adhered material would stay on the counterface or transform into loose debris during further sliding.

6.5.3.2. Tribochemistry at Sliding Interfaces in Ambient Air

In ambient conditions, the surfaces of most solids are oxidized and covered by water vapour. Even if the adsorbed species (water vapour and oxygen) are removed by some means (frictional, thermal), it roughly takes about 7.6×10^{-6} milliseconds for water to be re-adsorbed forming a monolayer coverage on the surface in ambient conditions [see Appendix A.2 for the calculation]. In this work, the highest sliding speed of 0.65 m/s was created by running the discs at 575 rpm. Consequently, it takes 0.104 s to complete one revolution. Thus, in ambient air at all three test speeds, the disc surface was re-covered with adsorbed water layer(s) between the two visits of the pin to the same location. Therefore, the tribosystems in ambient air had four material constituents; pin material, disc material, oxygen and water vapour.

The Al/CrN example showed that when generalizing on the effects of oxygen and water vapour on adhesion and material transfer, the following factors should be taken into account. Depending on the characteristics of the pin and disc materials, the presence of oxygen and water vapour can affect each tribosystem in a different way. Oxygen and water vapour in the environment can affect the tribo-system by interacting with i) pin material, ii) coating material, or iii) both. All three metals tested here, Al, Cu and Ti, are well known for their oxides. In addition, they also form hydroxides ($\text{Al}(\text{OH})_3$, $\text{Cu}(\text{OH})_2$, $\text{Ti}(\text{OH})_3$) by interacting with H_2O [127, 148-150]. Therefore, it is certain that there will be interactions between these metals and O_2 and H_2O during sliding in ambient air.

There is some literature on the interactions of oxygen and water vapour with DLC, carbon, graphite and diamond. Adsorption of O_2 molecules to form C=O bonds, adsorption and dissociation of H_2O to form C-OOH and C-H bonds are shown by experiments, calculations and simulations [115]. However, the open literature is rather limited on the interactions of water vapour with CrN and TiB_2 coatings.

It is quite possible that the interfaces formed between the coatings and adhered materials contained oxygen and water vapour. For example, it is known that a thin layer (1-2 nm) of aluminum oxide (Al_2O_3) always forms on the surface of the aluminum in the presence of oxygen in the atmosphere [127, 151]. On the other hand, aluminum hydroxide ($\text{Al}(\text{OH})_3$ or gibbsite = $\text{Al}_2\text{O}_3 \cdot 3\text{H}_2\text{O}$) forms on top of this layer when water vapour is present [127, 148-150]. Therefore, it is plausible that a bond is formed between

the CrN coating and the aluminum hydroxide or aluminum oxide compounds on the surface of aluminum rather than between CrN and aluminum.

Another possibility can be based on the interaction of CrN with oxygen and water vapour. Surface chemistry of CrN could change as a result of these interactions that would promote adhesion of aluminum to its surface.

6.5.3.3. Effect of Sliding Speed on Adhesion and Material Transfer in Ambient Air

Pin-on-disc tests in ambient air showed that the amount of loose oxidized debris formed during sliding was inversely proportional to the sliding speed in most cases (Sections 4.2, 6.1.2, 6.2.2, 6.2.6, 6.3.2, 6.3.4, 6.3.6).

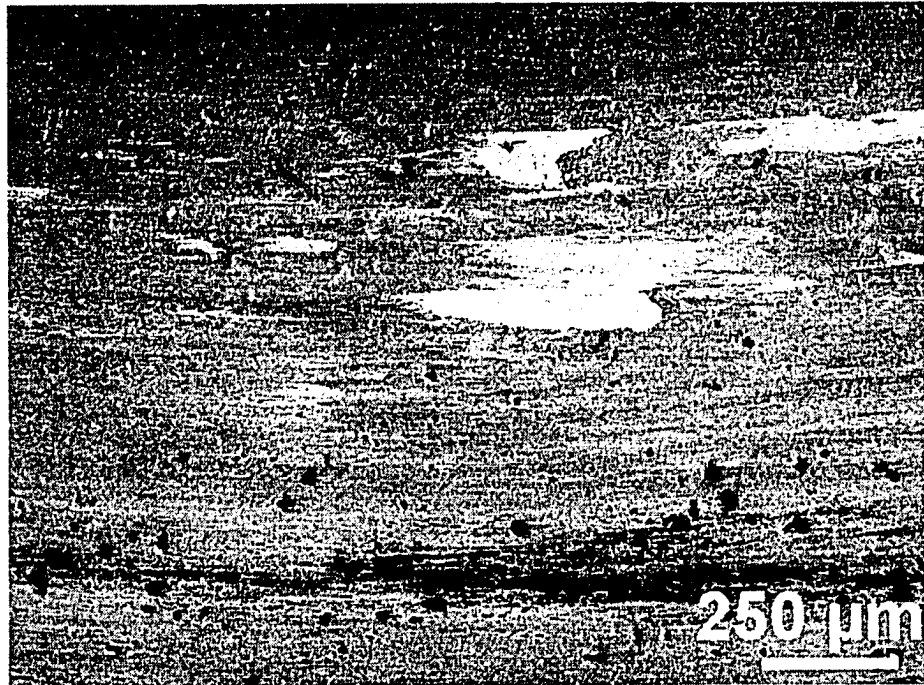
In a pin-on-disc configuration, increasing the sliding speed can affect the system in three ways: First, it increases the interfacial temperature due to frictional heating. Second, for a particular spot on the sliding track, the exposure time to the atmosphere between two contacting events decreases. Finally, increasing the sliding speed can change the deformation characteristics (i.e., adiabatic shear localization etc.) of the materials under investigation.

In the current pin-on-disc test configuration, different sliding speeds were achieved by varying both the number of revolutions of the disc per unit time and the diameter of sliding tracks. The sliding speeds of 0.02, 0.12 and 0.65 m/s were made possible by rotating discs at 25, 125 and 575 rpm respectively.

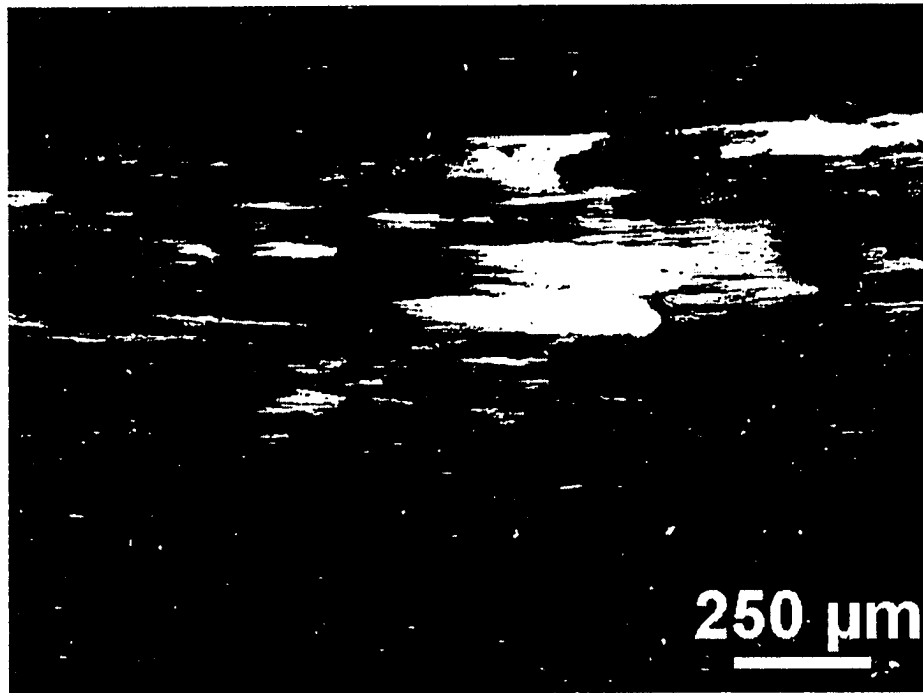
It is suggested that the observed decrease in the amount of debris formed with increasing sliding speed was related to the decrease in interaction time of the pin and the atmosphere with a certain location of the sliding track on the counterface in two different ways. The time needed for two consecutive visits of the pin to a certain location of the sliding track can give an idea about the time period allowed for tribochemical reactions. At 25 rpm, it takes 2.400 s to complete one revolution. It is 0.480 s at 125 rpm and 0.104 s at 575 rpm. Therefore, compared to 25 rpm, the time period allowed for chemical reactions is 80.0% less at 125 rpm, and 95.7% less at 575 rpm. Therefore, there was more time available for oxidation during the transfer of a material from the pin to the coating surface at lower sliding speeds. This could have created a weaker or stronger adhered material-coating interface compared to the one in argon. Also, lower sliding speeds

allowed longer time periods for the adsorption of the atmospheric species (water vapour) and the oxidation of adhered material until the next visit of the pin to the same location.

As mentioned in Section 6.5.3.1, transfer of pin material to a disc surface is considered as the first stage of debris formation mechanism. It is natural to think that the probability of junction formation between two sliding surfaces would increase as the time of contact increases. Similarly, with increasing sliding speed, the probability of material transfer from pin to the disc surface decreases due to the decrease in interaction time. Comparison of the SEM images of the sliding tracks tested at 0.12 and 0.65 m/s shows that the number of junctions/adhesion locations per unit area of sliding track was less at 0.65 m/s (e.g. **Figures 6.9.a** and **c**). Although they were less in number, the amount of material adhered per junction was much larger at 0.65 m/s. Since the transfer of pin material to the disc surface decreases with increasing sliding speed, the rate of the second part of debris generation process (i.e. removal of the adhered piece from the counterface and its fragmentation into debris) also automatically decreases.



a)



b)

Figure 6.1. a) SEI and b) BEI SEM images of a section of the wear track of the Graphitic DLC coating tested against 1100 Al in argon for 300 revolutions (18 m).



c)



d)

Figure 6.1. c) SEI and d) BEI SEM images of the corresponding 1100 Al pin. The applied load and the sliding speed were 5 N and 0.65 m/s.

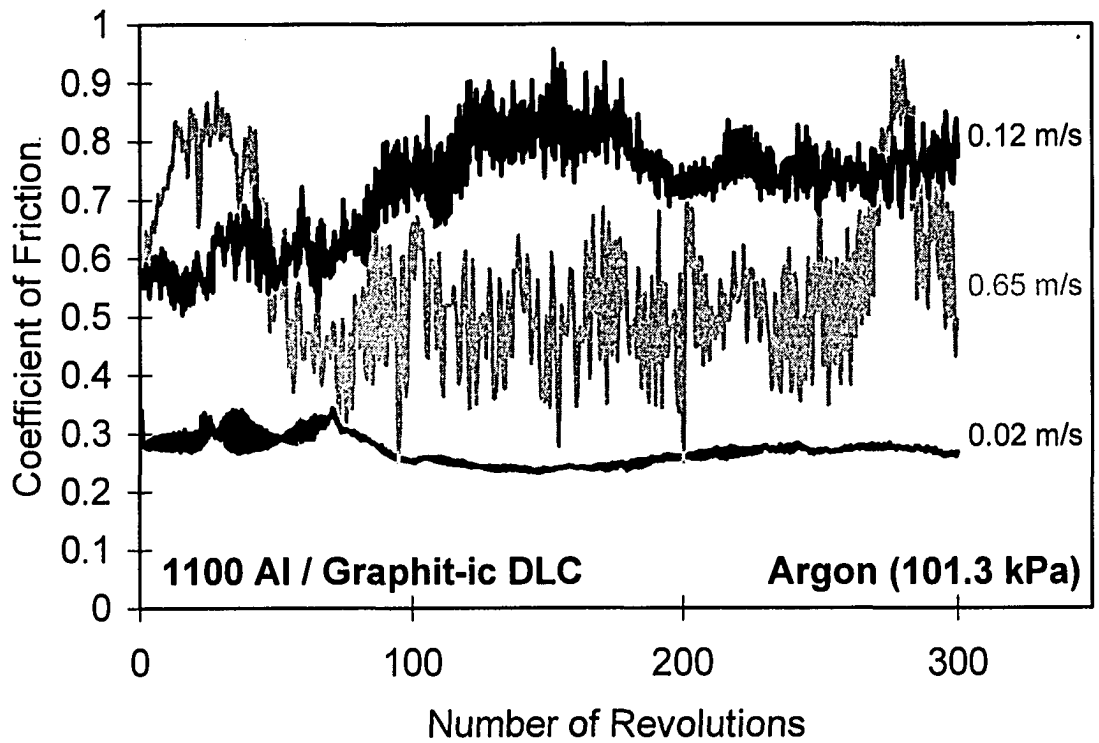


Figure 6.2. The variation of the COF between Al and the Graphit-ic DLC coatings in argon at 0.02, 0.12 and 0.65 m/s. The constant applied load was 5 N.

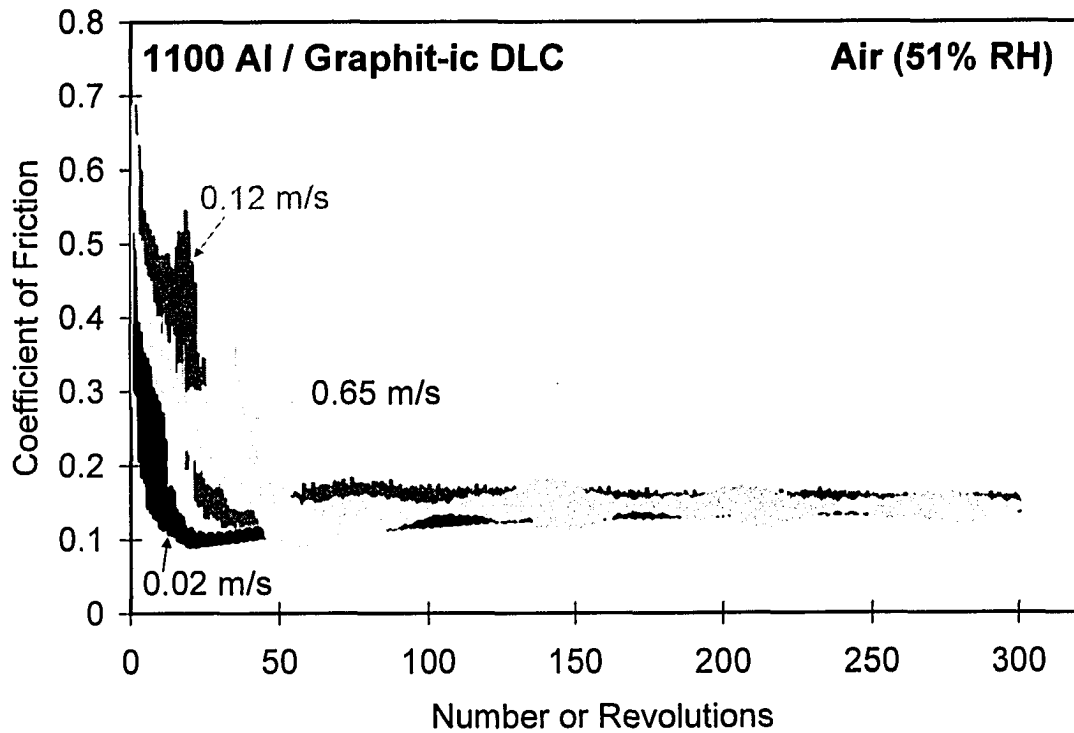
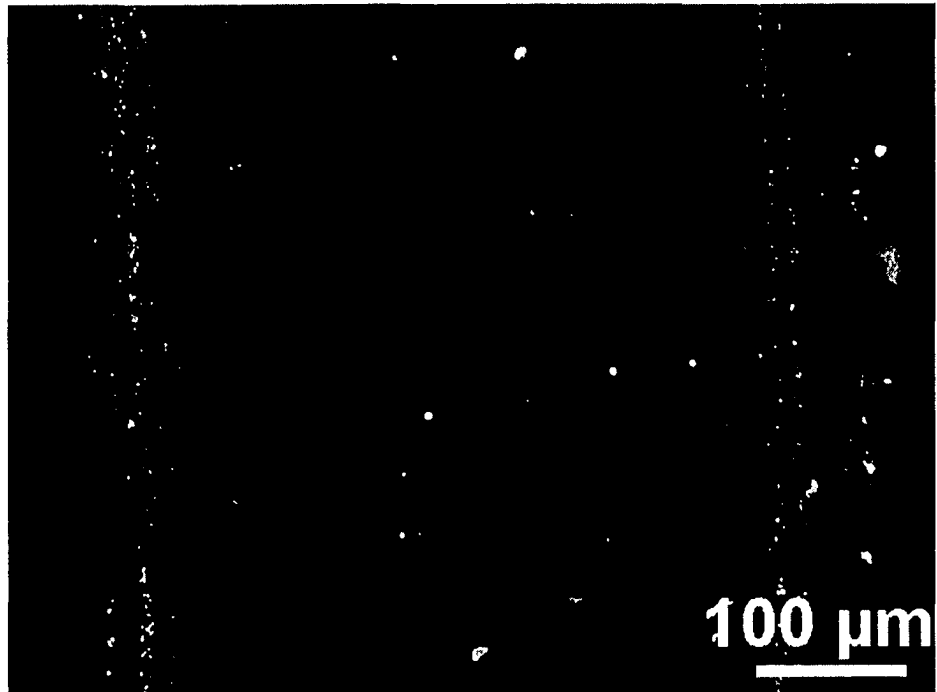
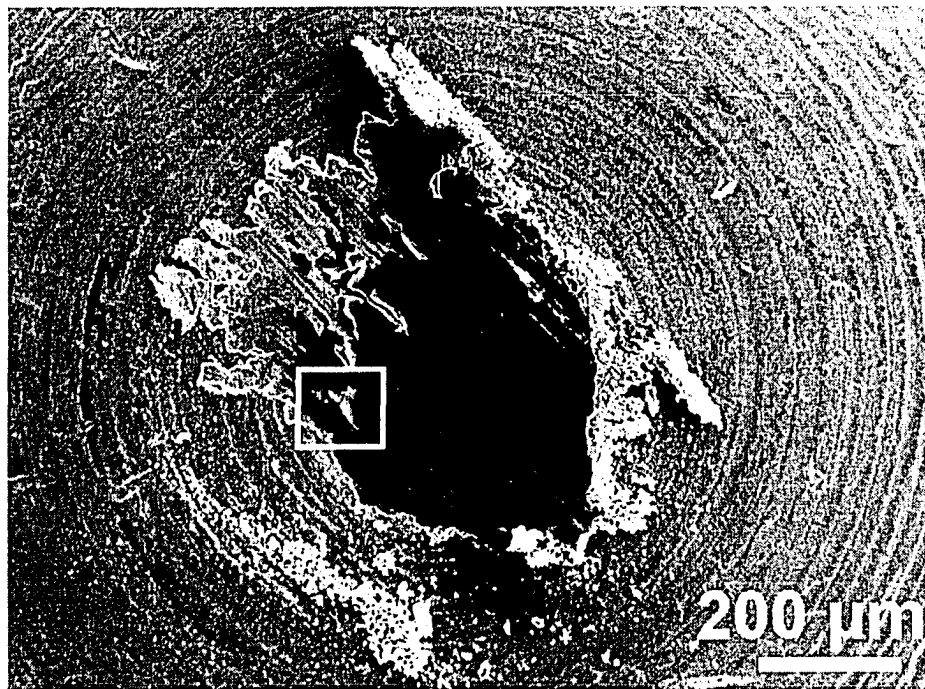


Figure 6.3. The variation of the COF between 1100 Al and the Graphit-ic DLC coatings in ambient air (51% RH) at the sliding speeds of 0.02, 0.12 and 0.65 m/s. The constant applied load was 5 N.

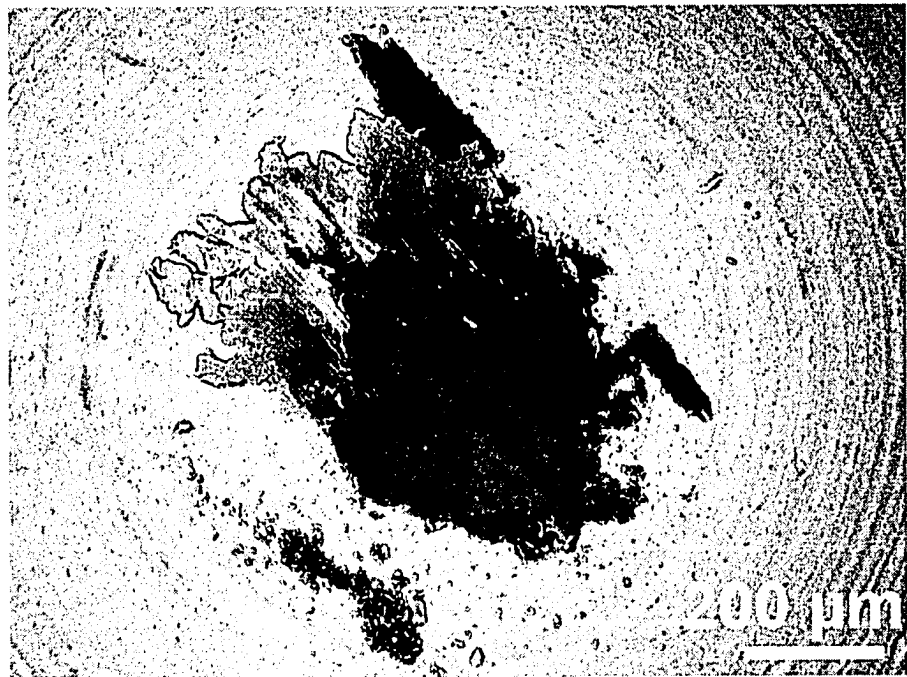


a)

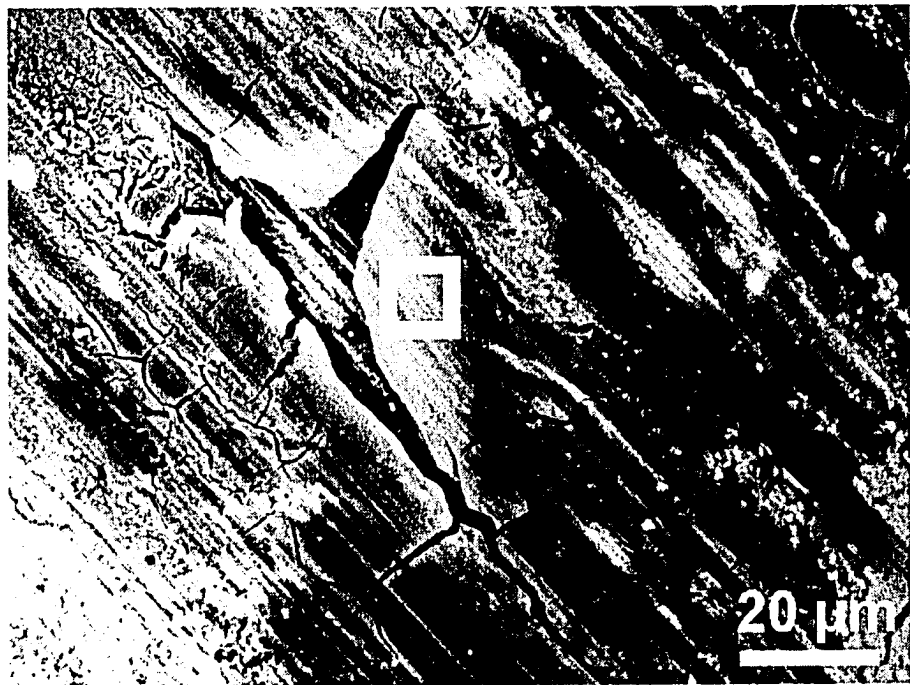


b)

Figure 6.4. SEI SEM images of **a)** a section of the wear track of the Graphit-iC DLC coating tested against Al in ambient air (51% RH) for 300 revolutions (18 m). **b)** the contact surface of the corresponding Al pin.



c)



d)

Figure 6.4. BEI SEM images of c) the contact surface of the corresponding Al pin, d) an enlarged view of the location indicated in b) showing the layer delamination.

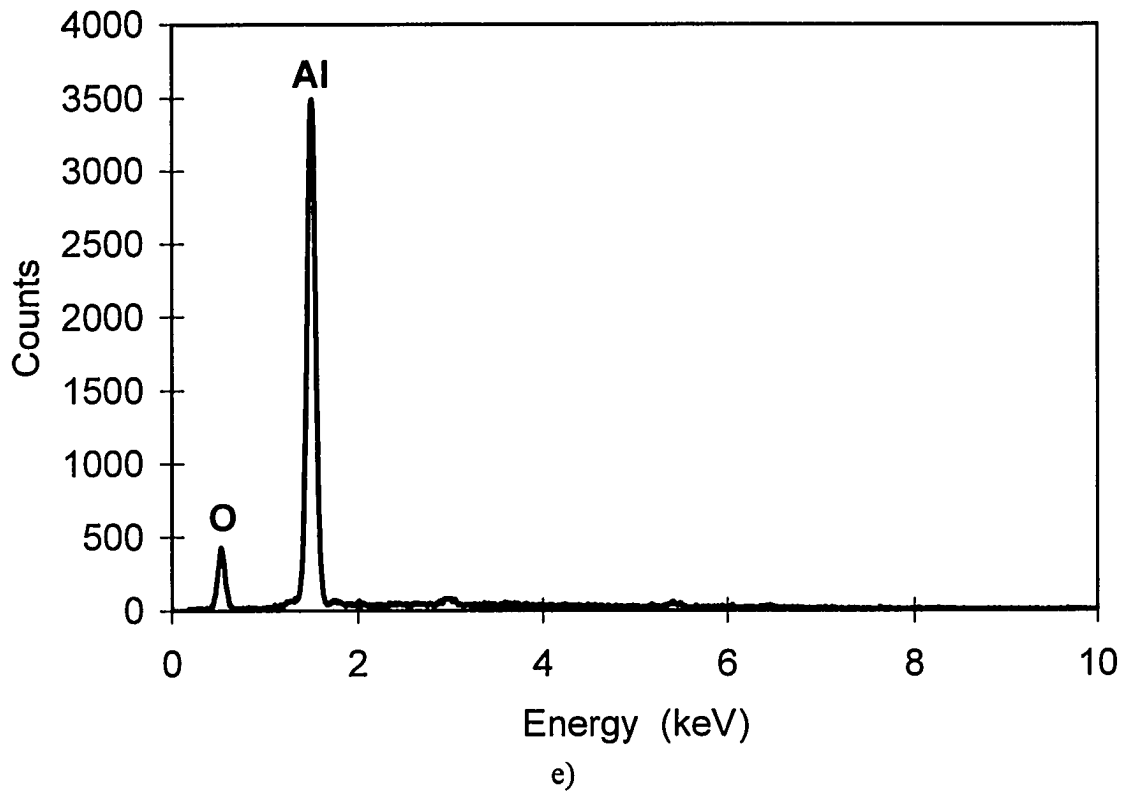
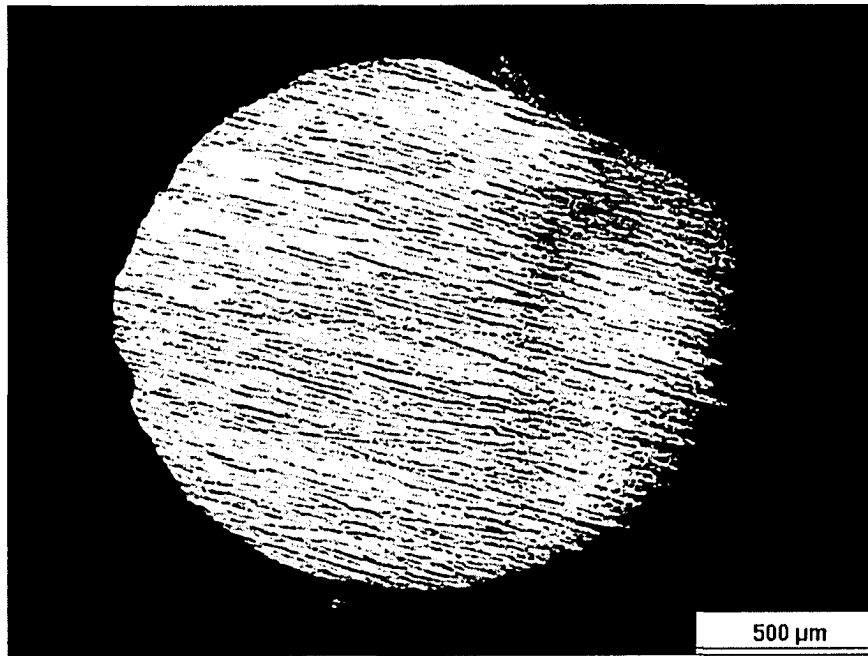
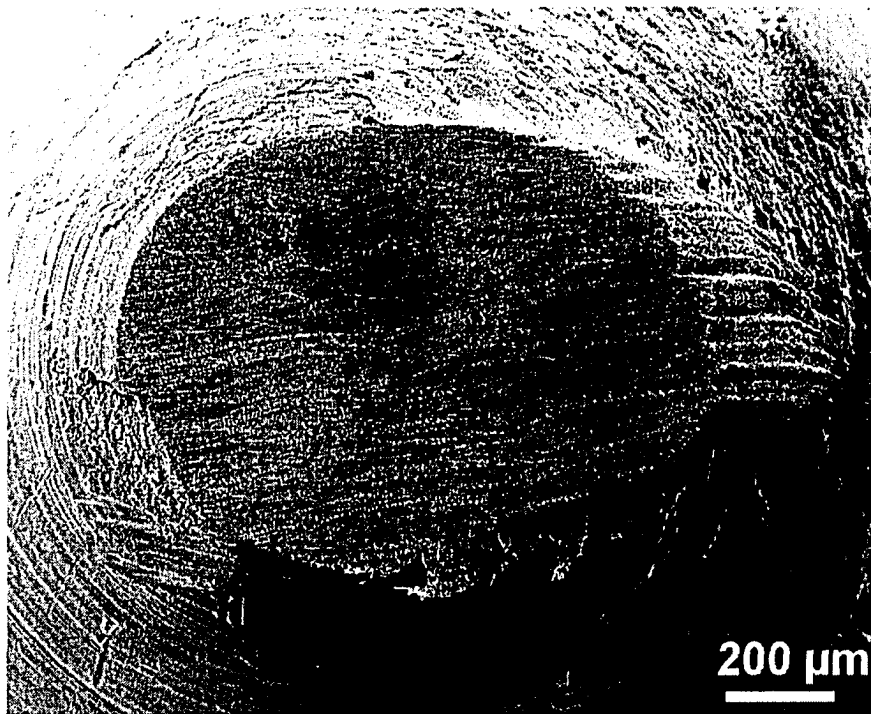


Figure 6.4.e) EDS analysis of the location indicated in d). The applied load and the sliding speed were 5 N and 0.12 m/s.



a)



b)

Figure 6.5 a) Optical image of the contact surface of the Cu pin tested against the Graphit-iC DLC coating in argon at a sliding speed of 0.12 m/s for 1×10^4 revolutions, b) SEI SEM image of the contact surface of the Cu pin tested against the Graphit-iC DLC coating in argon at a sliding speed of 0.12 m/s for 3×10^3 revolutions.

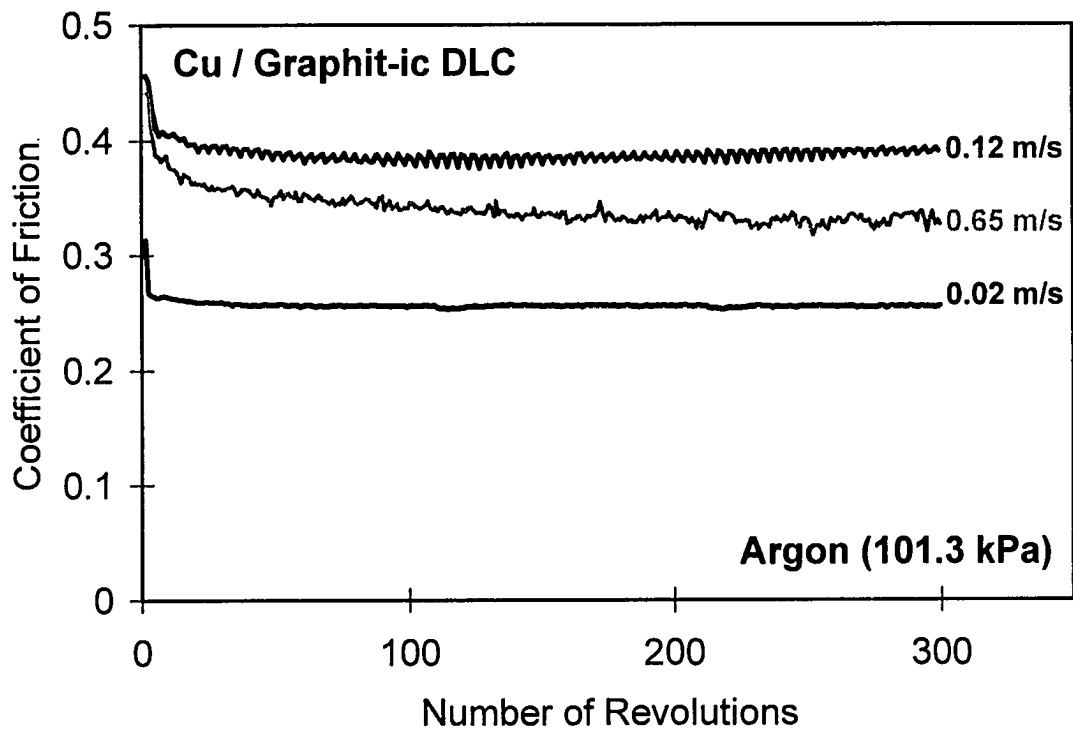
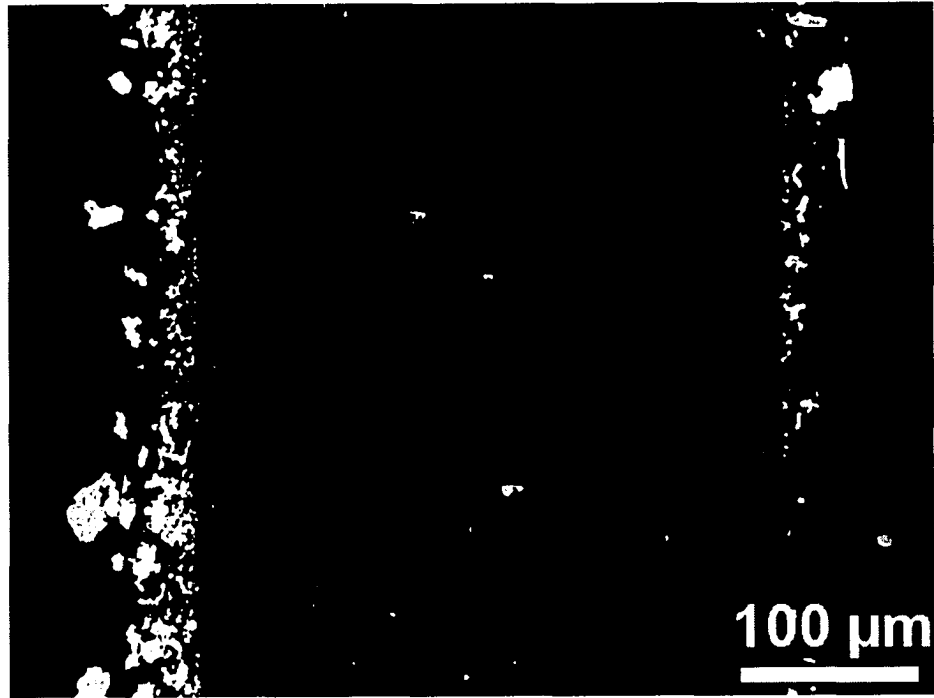
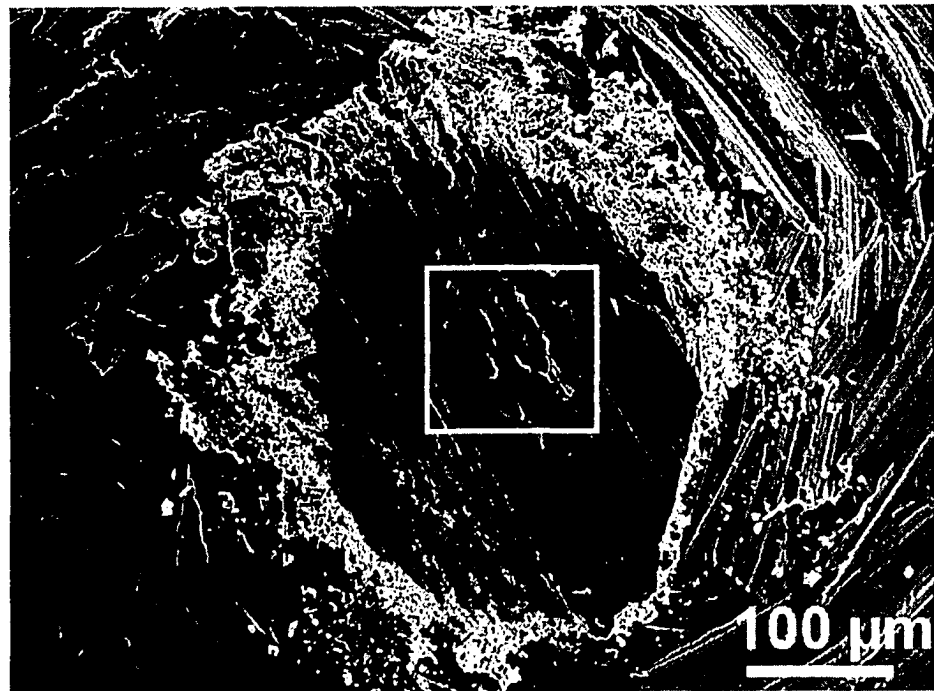


Figure 6.6. The variation of the COF between Cu and the Graphit-ic DLC coatings in argon at 0.02, 0.12 and 0.65 m/s.

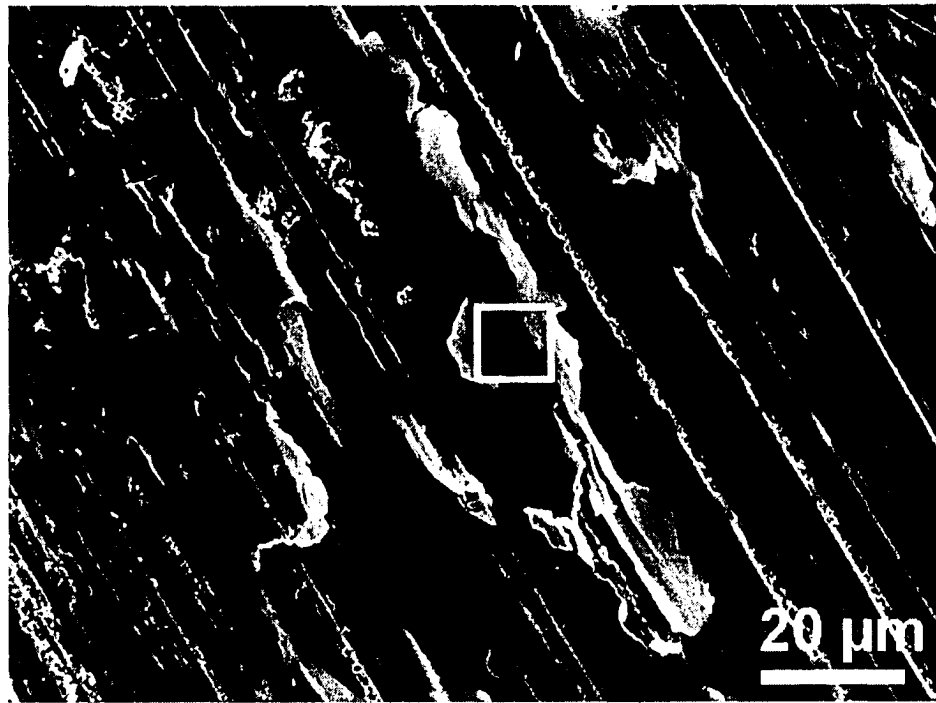


a)

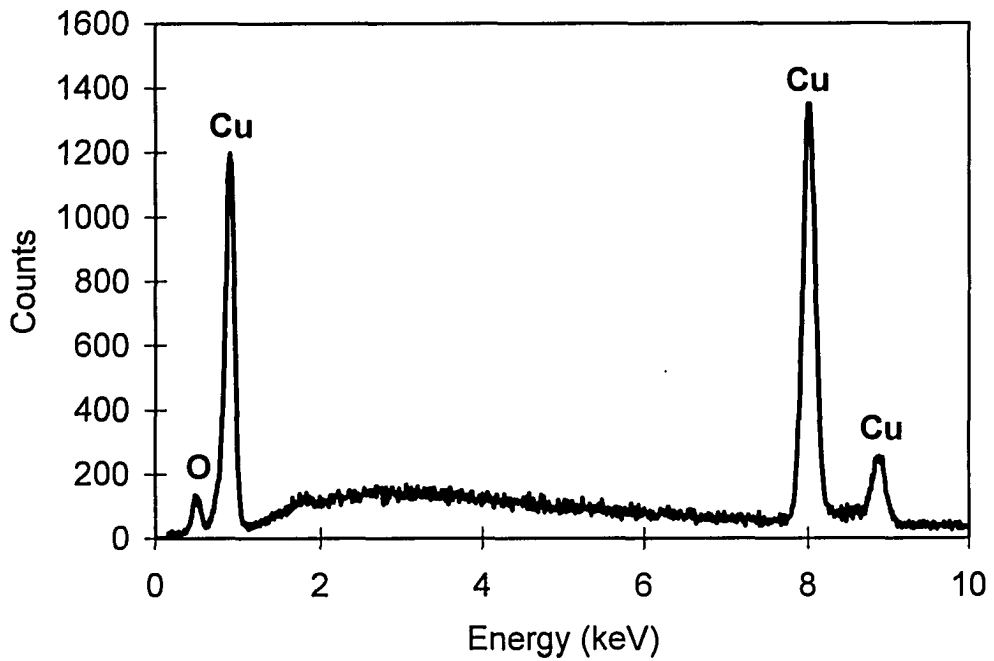


b)

Figure 6.7 a) SEI SEM image of a section of the wear track of the Graphit-iC DLC tested against Cu in ambient air (58% RH) for 3×10^2 revolutions (18 m), b) the contact surface of the corresponding Cu pin.



c)



d)

Figure 6.7.c) an enlarged view of the location indicated in b) showing the layer formation, and **d)** EDS analysis of the location indicated in c). The applied load and the sliding speed were 5 N and 0.12 m/s.

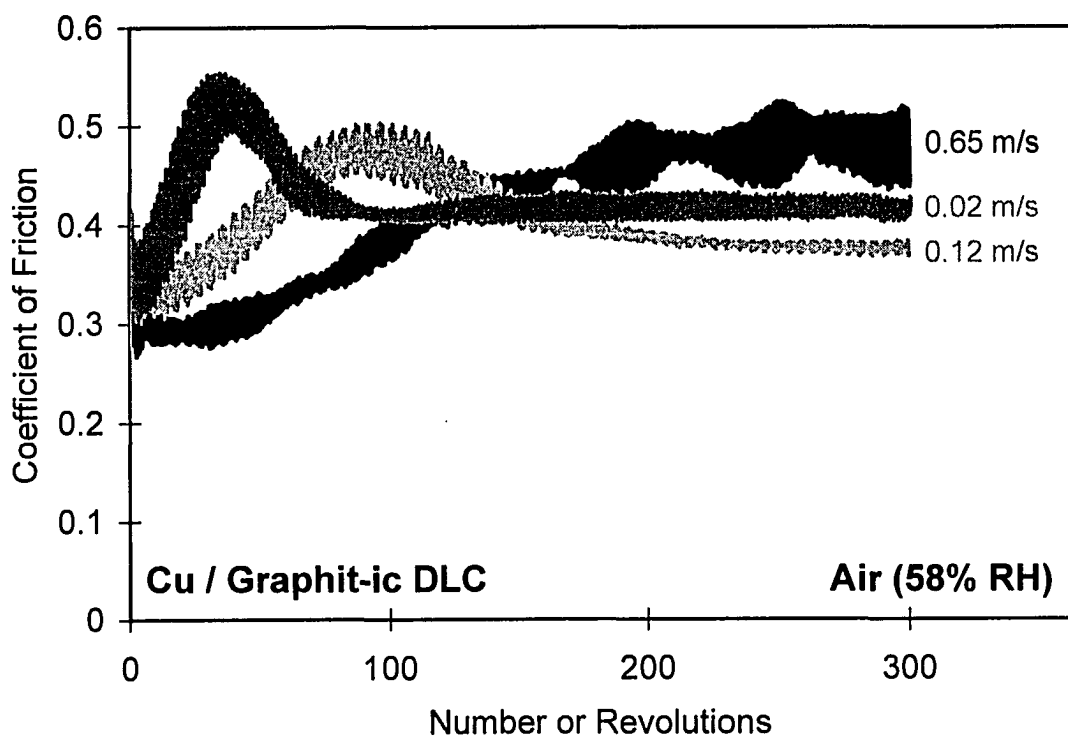
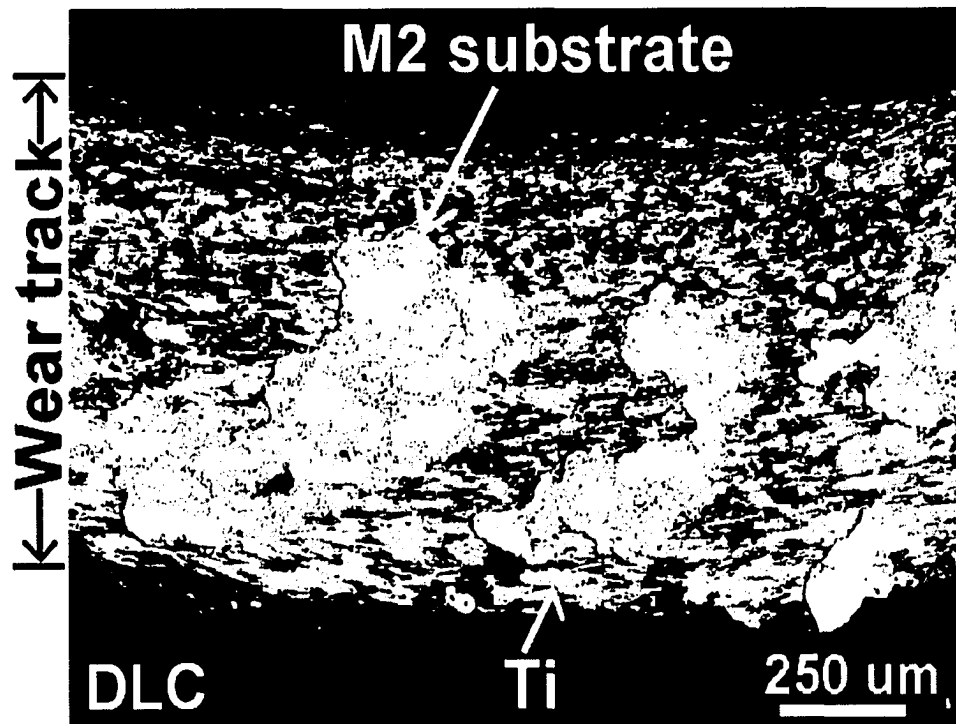
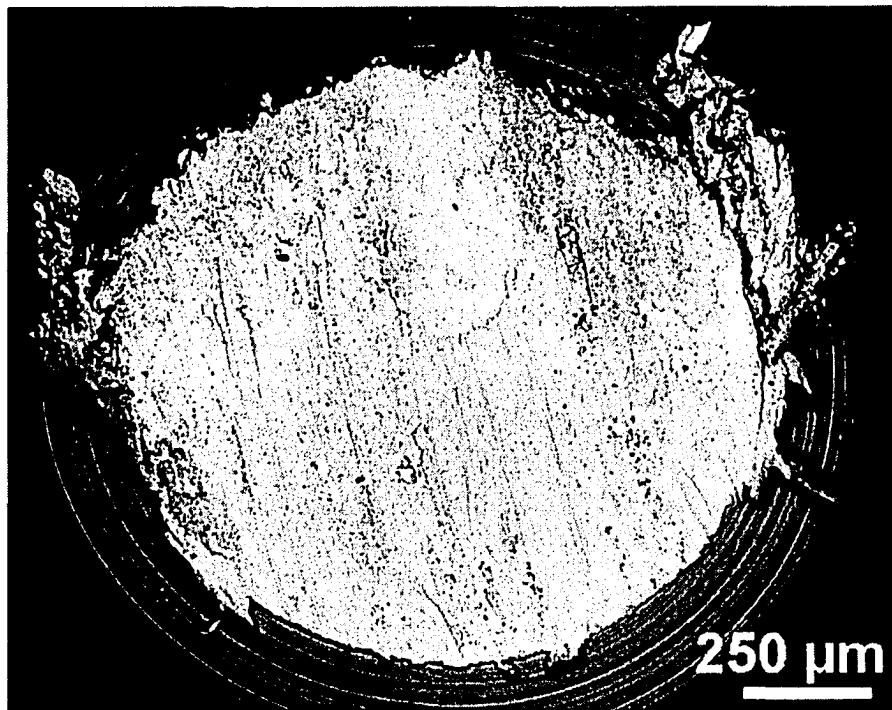


Figure 6.8. The variation of the COF between Cu and the Graphit-ic DLC coatings in ambient air at 0.02, 0.12 and 0.65 m/s. The applied load was 5 N.

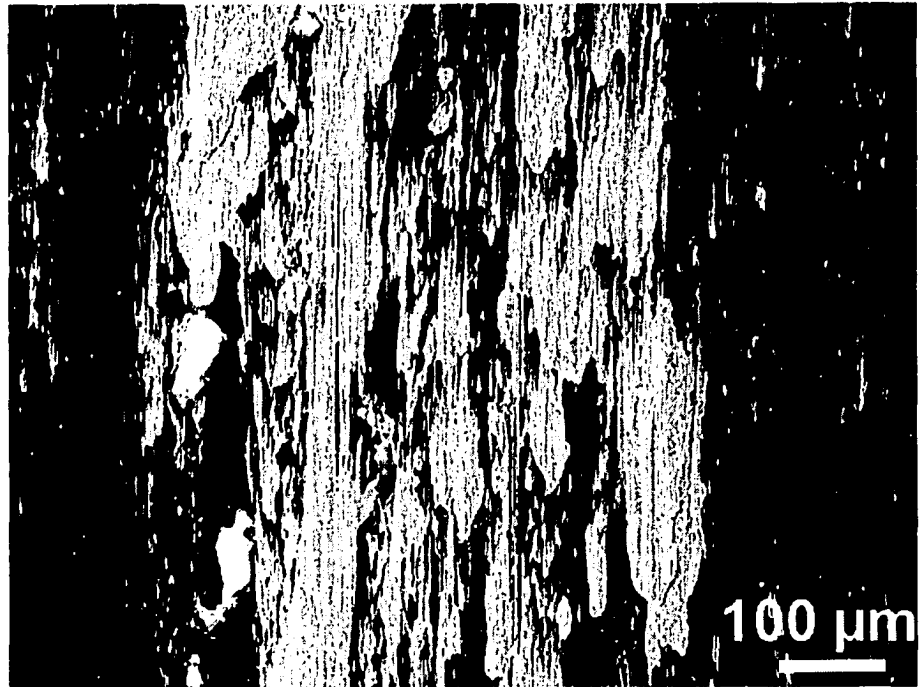


a)

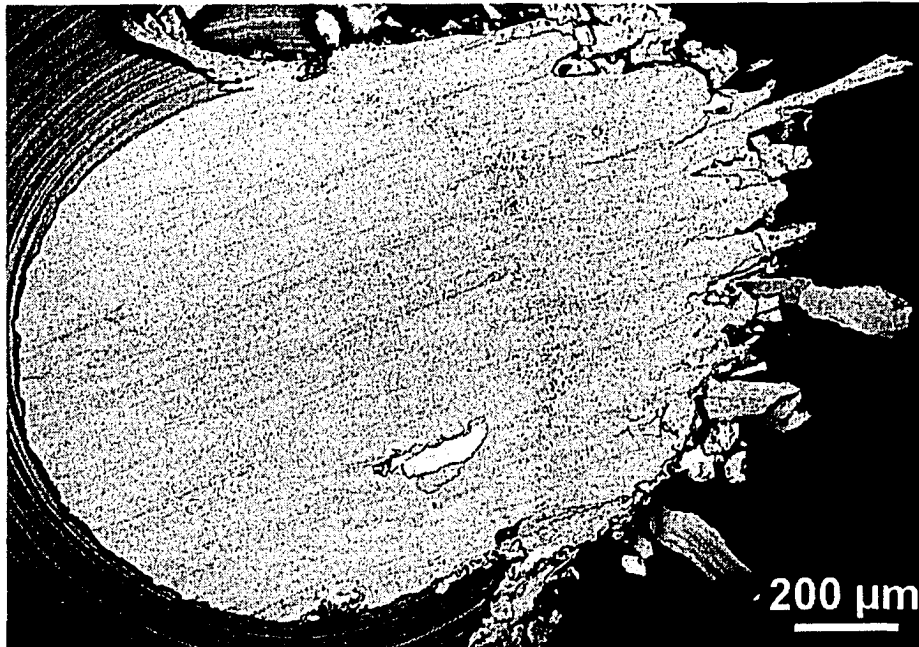


b)

Figure 6.9. SEM images of **a)** a section of the wear track of the Graphit-iC DLC coating tested against Ti in argon at 0.12 m/s for 3×10^2 rev., **b)** the corresponding Ti pin.

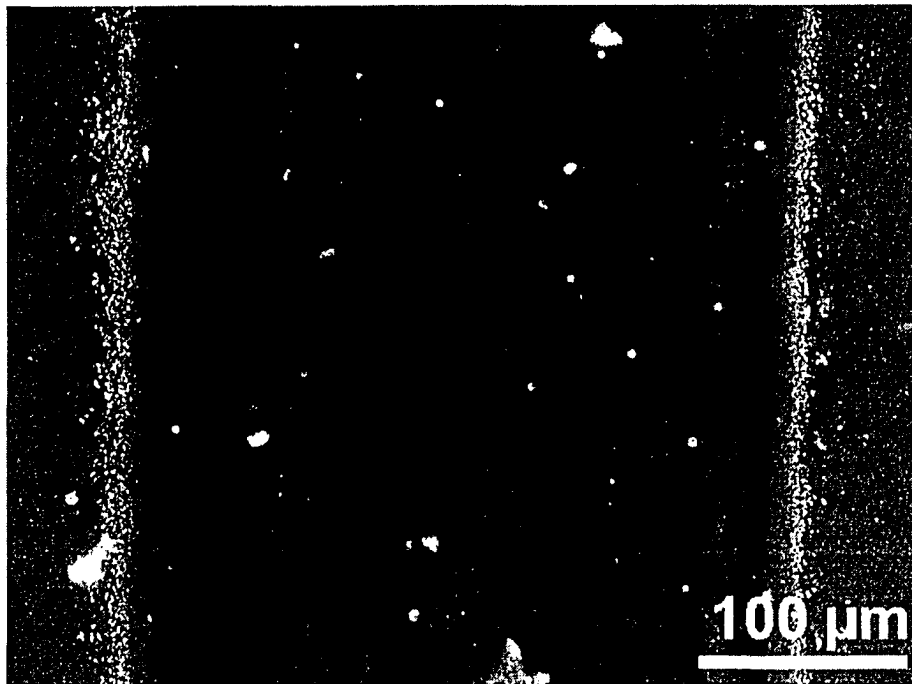


c)

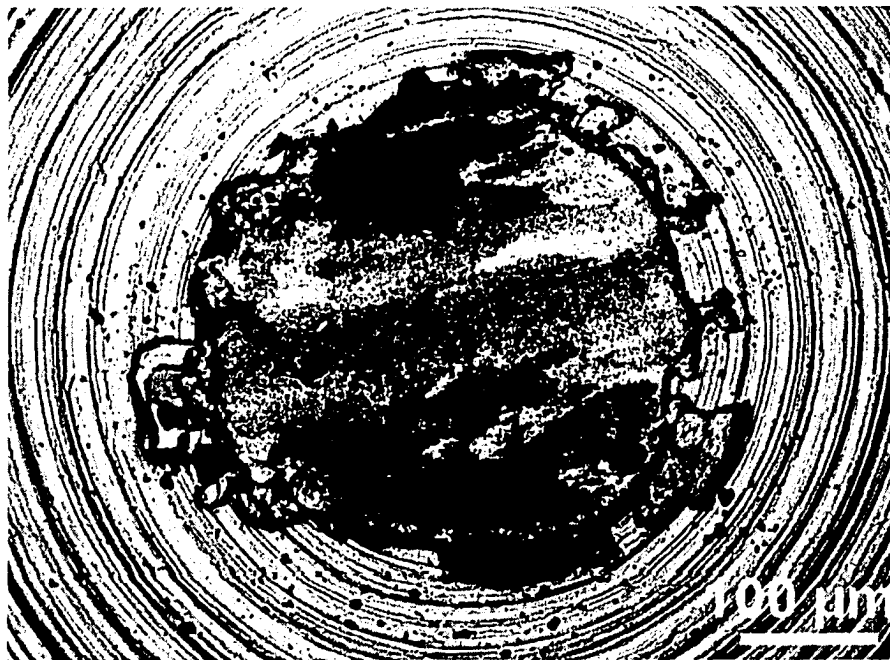


d)

Figure 6.9. SEM images of **c)** a section of the wear track of the Graphit-iC DLC coating tested against Ti in argon at 0.65 m/s for 3×10^2 rev., and **d)** the corresponding Ti pin. The applied load was 5 N in all tests.



a)



b)

Figure 6.10. SEM images of a) a section of the wear track of the Graphit-iC DLC coating tested against Ti in argon at 0.02 m/s for 3×10^2 rev., b) the corresponding Ti pin showing material transfer to its surface. The applied load was 5 N.

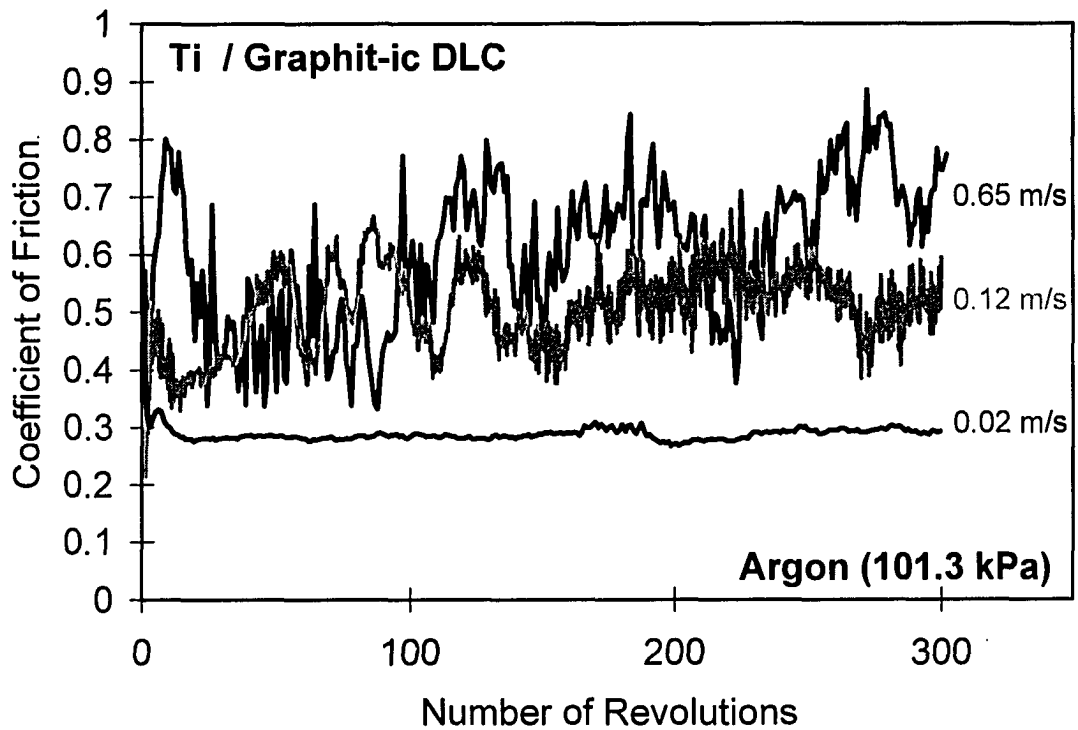
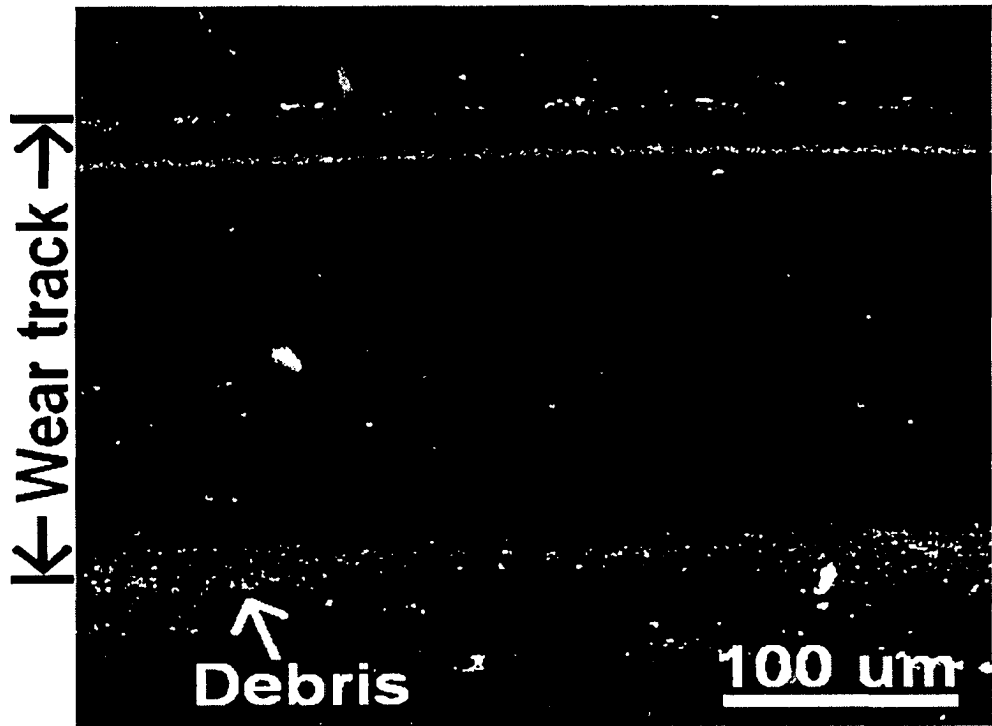
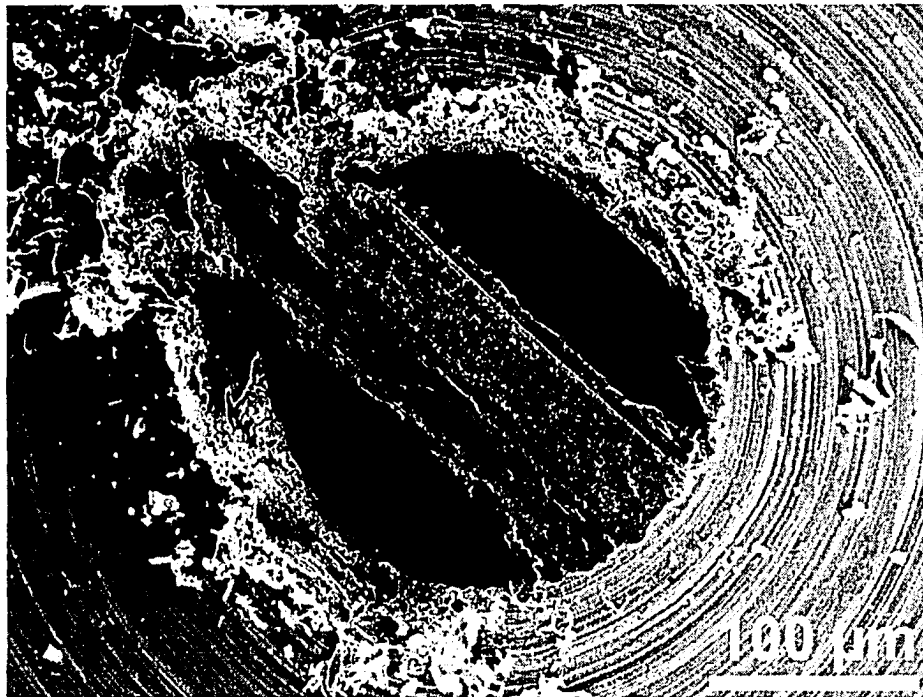


Figure 6.11. The variation of the COF between Ti and the Graphitic DLC coatings in argon at 0.02, 0.12 and 0.65 m/s. The applied load was 5 N.



a)



b)

Figure 6.12. SEM images of **a)** a section of the wear track of the Graphit-iC DLC tested against Ti in ambient air (59% RH) at 0.12 m/s for 3×10^3 rev., **b)** the corresponding Ti pin. The applied load was 5 N.

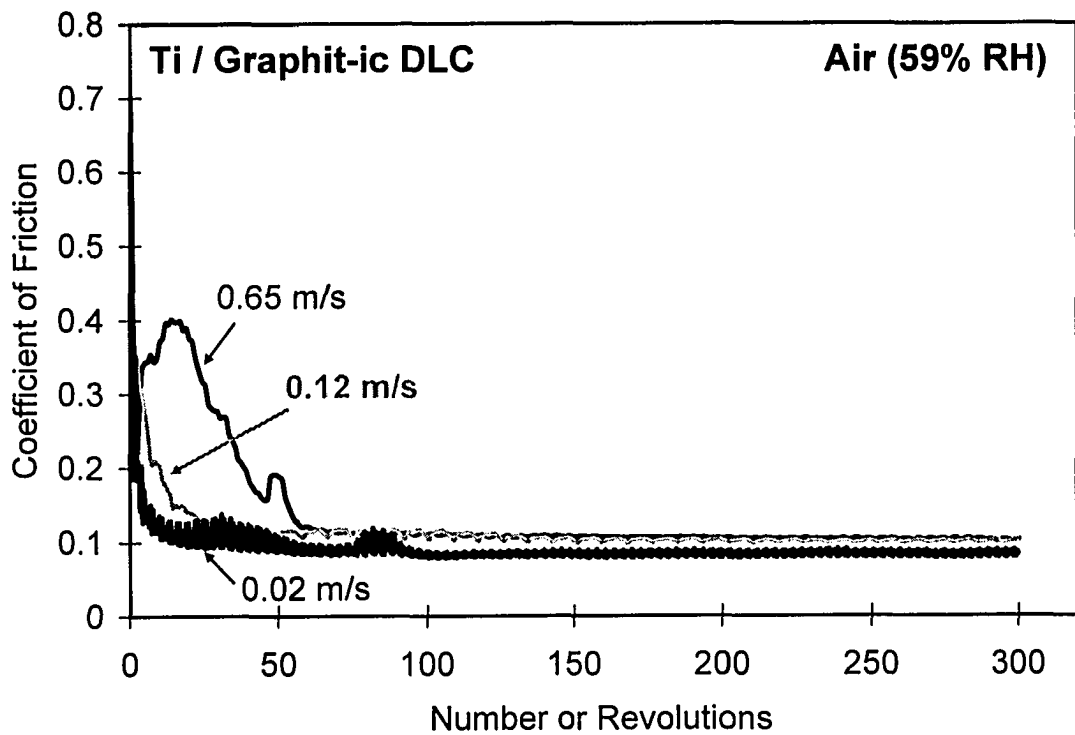
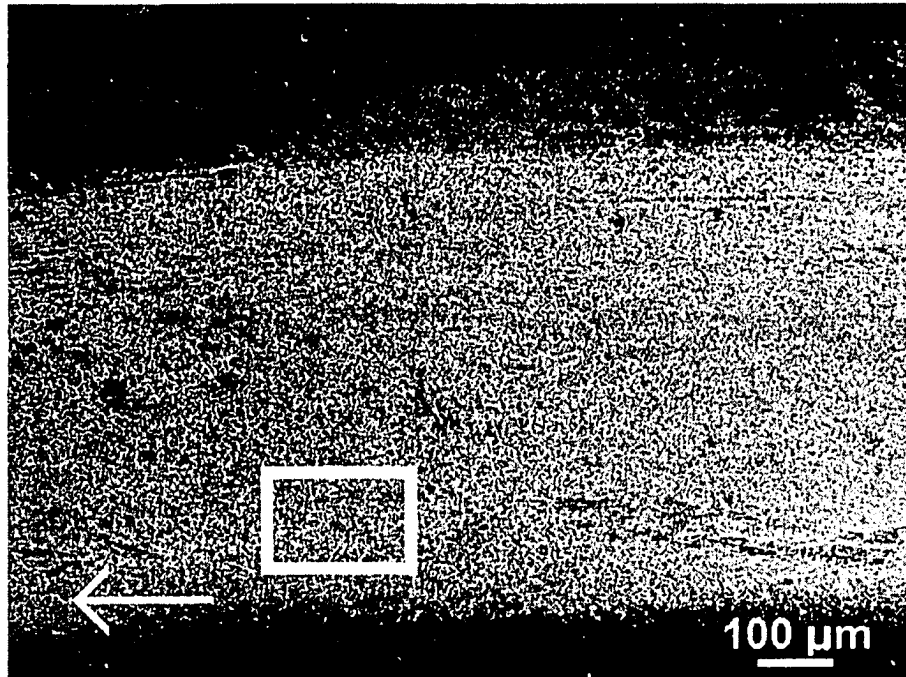
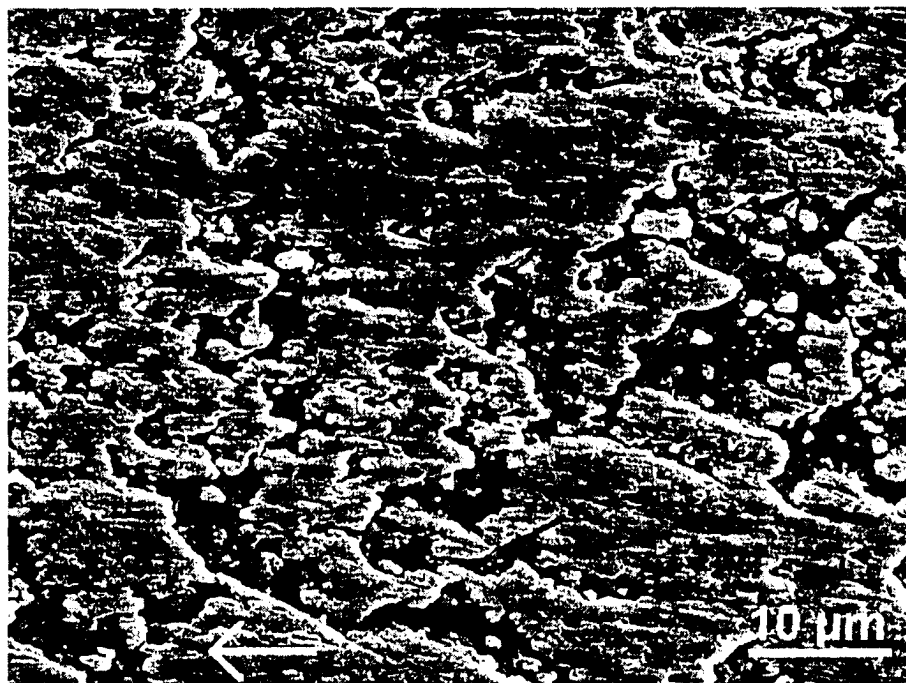


Figure 6.13. The variation of the COF between Ti and the Graphitic DLC coatings in ambient air (59% RH) at 0.02, 0.12 and 0.65 m/s.



a)



b)

Figure 6.14. SEM images of a) a section of the sliding track of TiB_2 coating tested against Al pin at 0.12 m/s sliding speed in the argon atmosphere. The sliding distance and the applied load were 18 m and 5 N, respectively, b) an enlarged view of a part of the sliding track showing the severely smeared Al. The direction of sliding is indicated with an arrow.

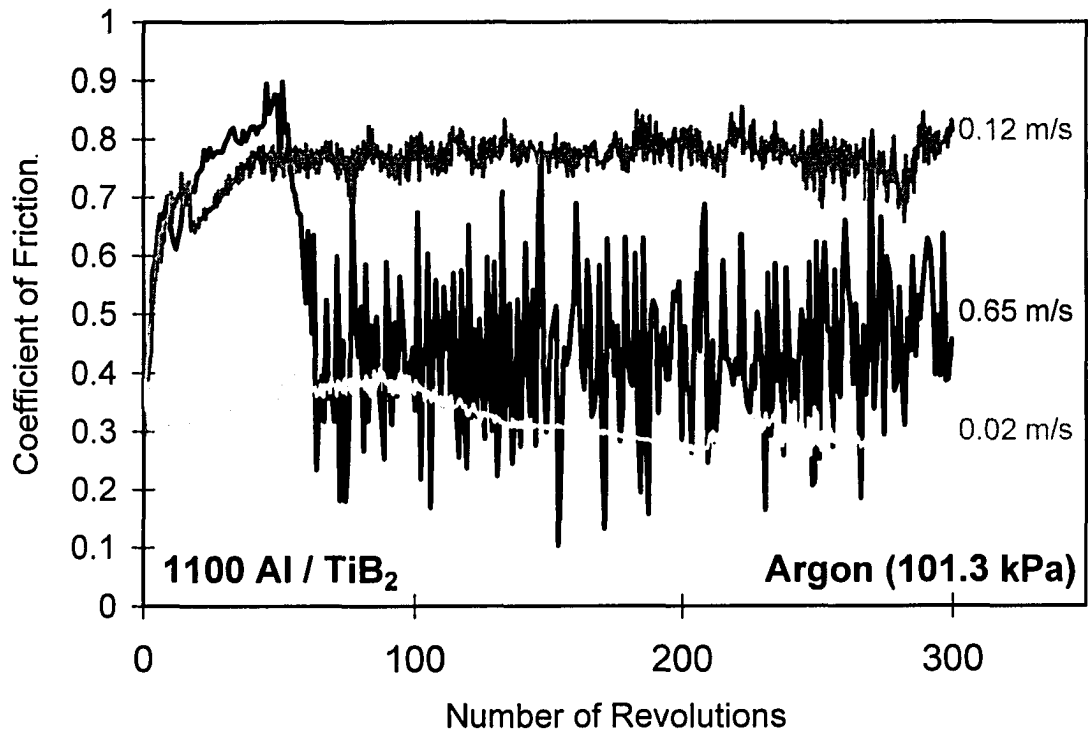
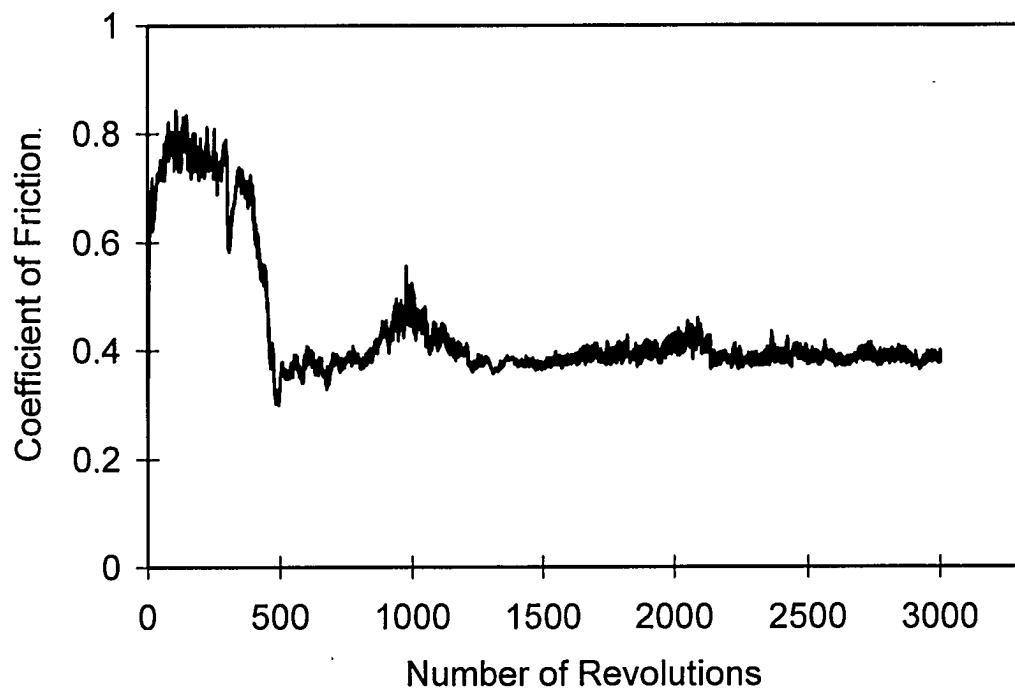


Figure 6.15. The variation of the COF between 1100 Al and the TiB₂ coating in argon 0.02, 0.12 and 0.65 m/s. The applied load was 5 N.



a)



b)

Figure 6.16. a) SEM image of a section of the sliding track of the TiB_2 coating tested against the 1100 Al pin at 0.12 m/s speed in the argon for 180 m under 5 N load, respectively. b) The corresponding COF curve.

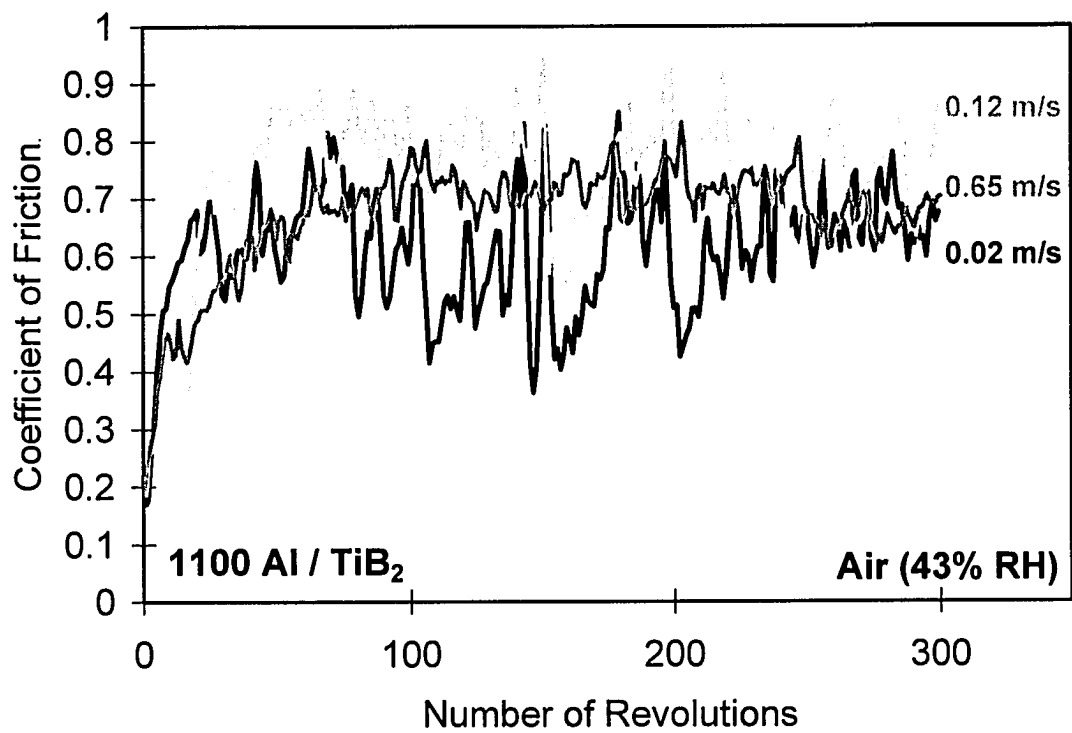
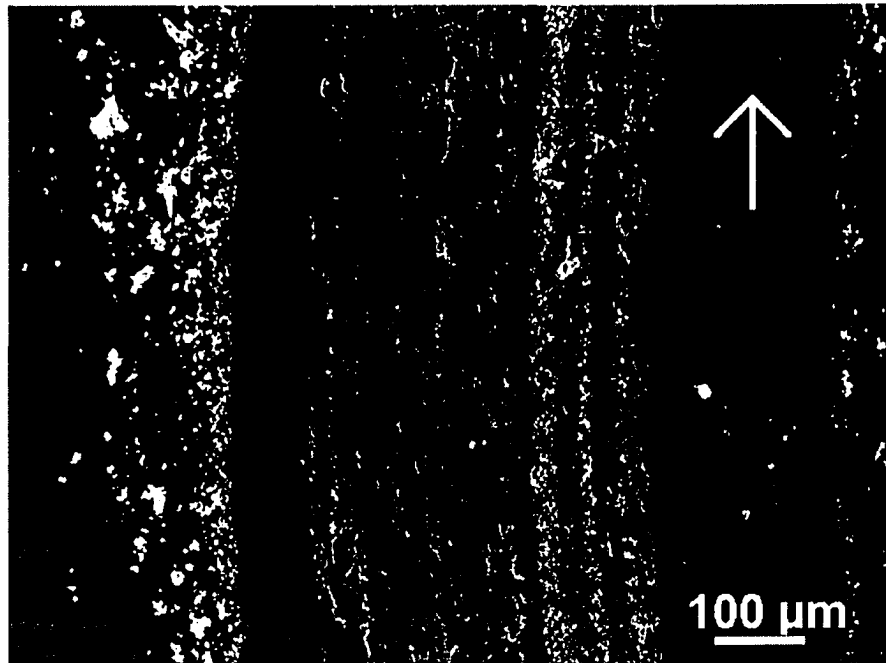
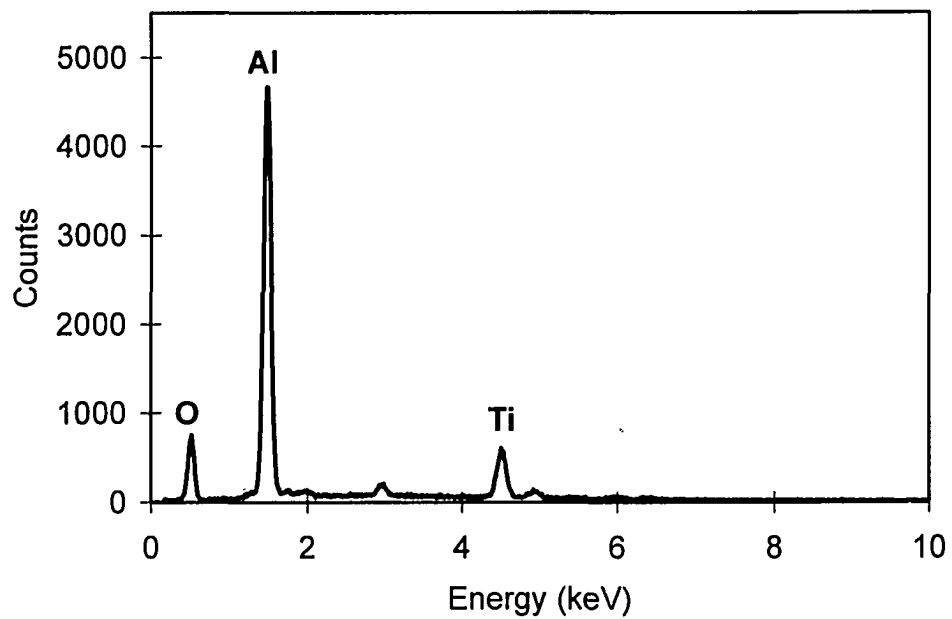


Figure 6.17. The variation of the COF between 1100 Al and the TiB₂ coating in ambient air (43% RH) at 0.02, 0.12 and 0.65 m/s. The applied load was 5N.

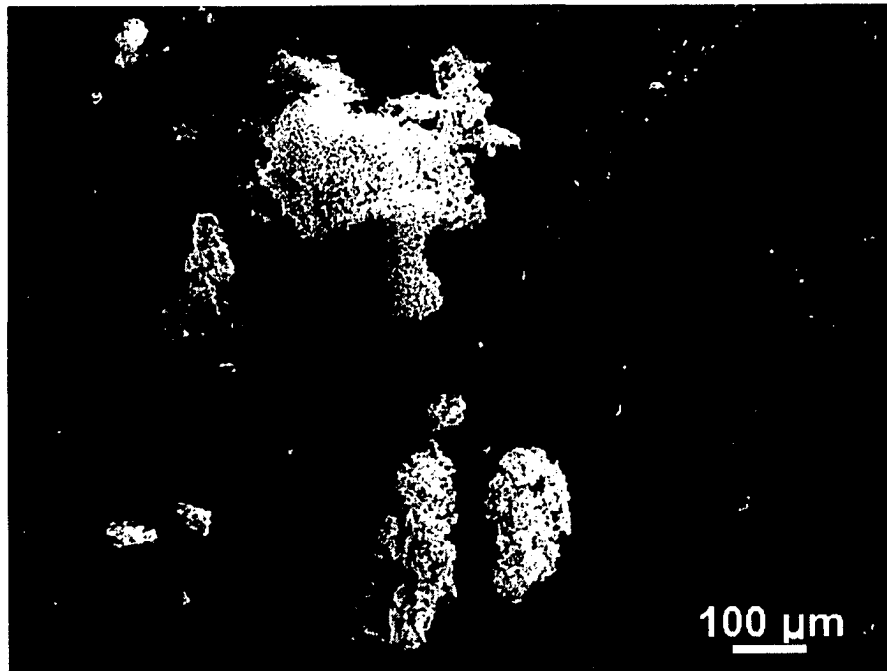


a)

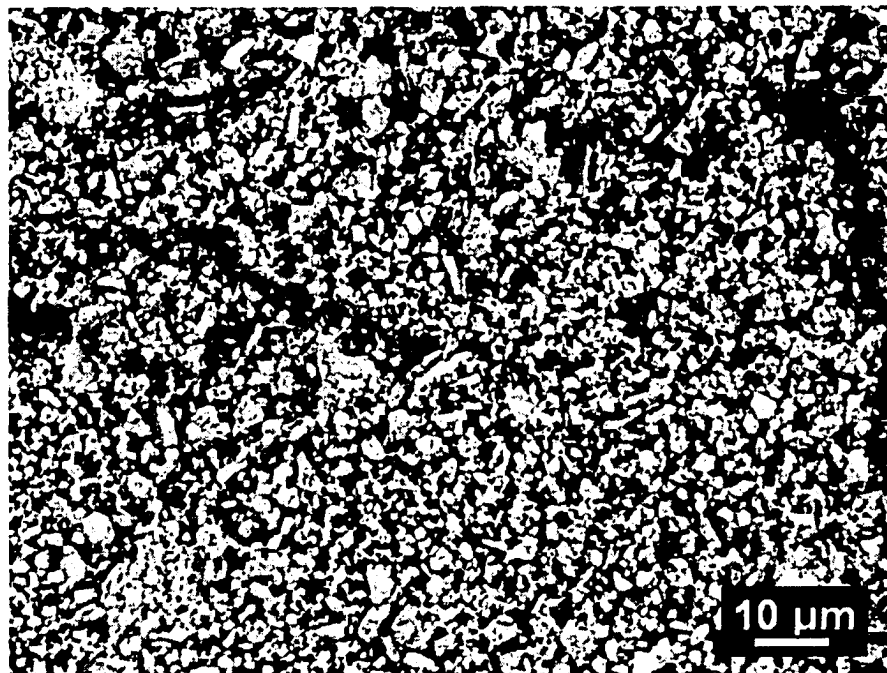


b)

Figure 6.18. a) SEM image of a section of the sliding track of the TiB_2 coating tested against Al pin at 0.02 m/s sliding speed in ambient air (43% RH) for 3×10^2 rev. of sliding. A significant amount of loose debris (white) was detected on and along the sliding track, b) the EDS analysis of the one of the debris particles showing the extent of oxidation. The applied load was 5 N.

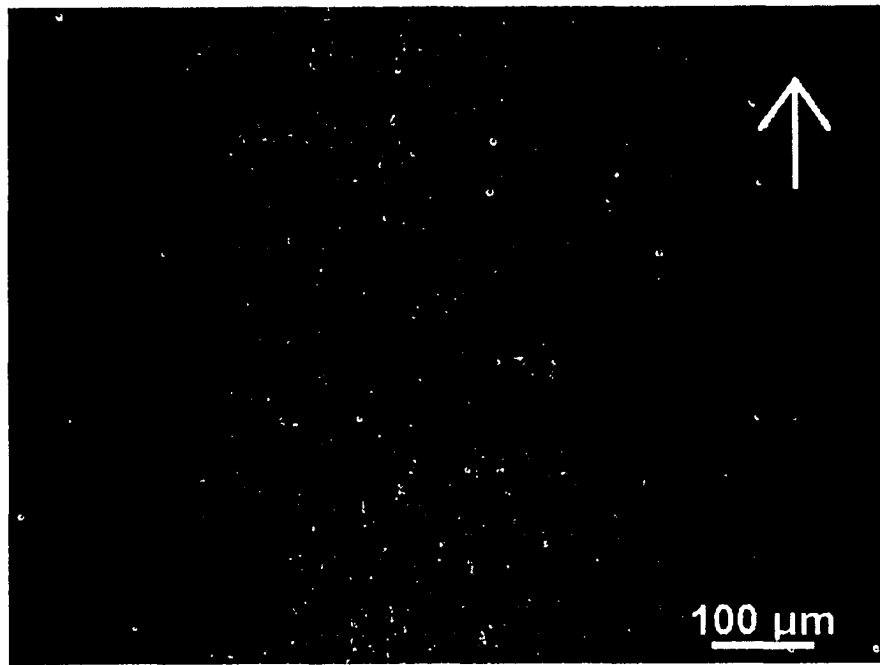


a)

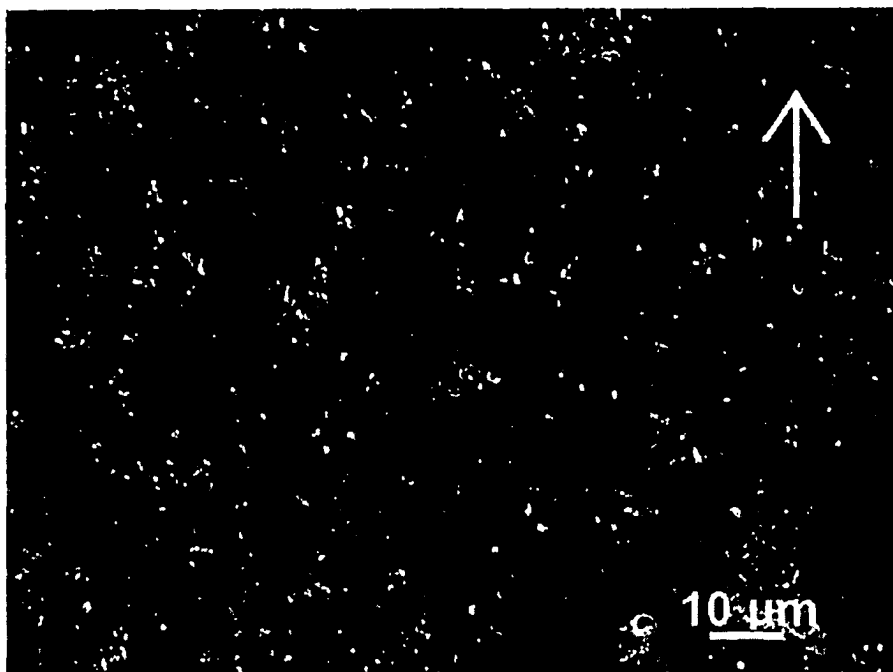


b)

Figure 6.19 a) The SEM image of the debris particles gathered along the sliding track when Al was tested against TiB_2 coating at 0.12 m/s sliding speed in ambient air (50.8 % RH) for 180 m of sliding distance, b) a closer view of the debris particles in BEI mode. The applied load was 5 N.

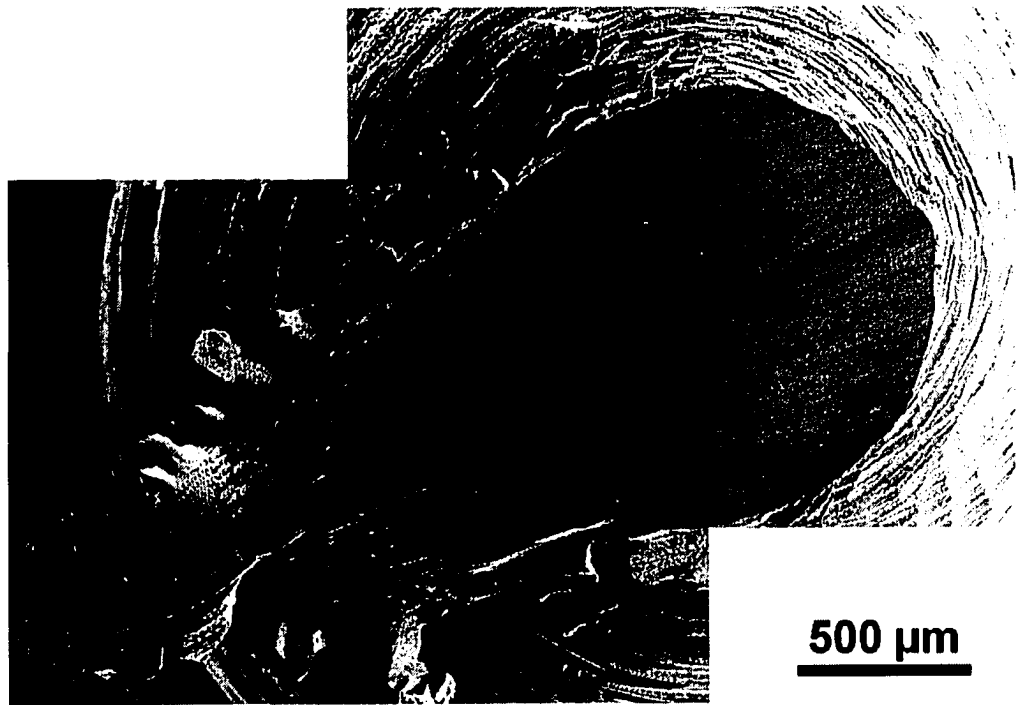


a)

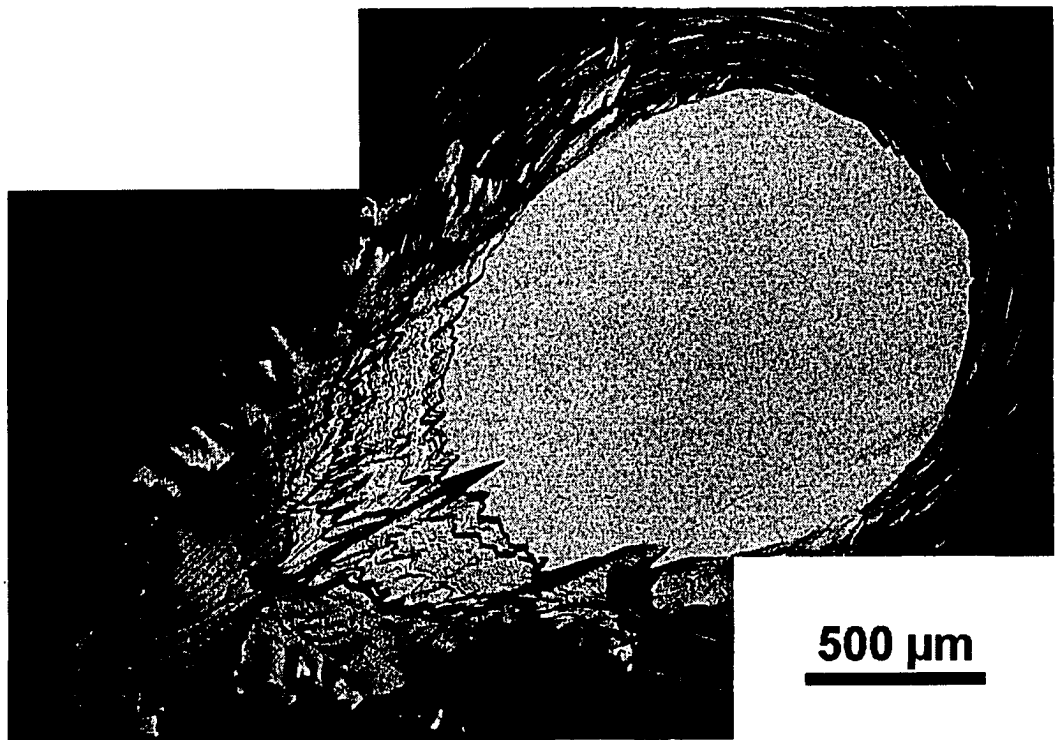


b)

Figure 6.20. a) SEM image of a section of the sliding track of the TiB_2 coating tested against Cu at 0.12 m/s sliding speed for 180 m of sliding distance in argon. The applied load was 5 N. b) an enlarged view of a part of a). The white particles are Cu adhered to the TiB_2 surface.

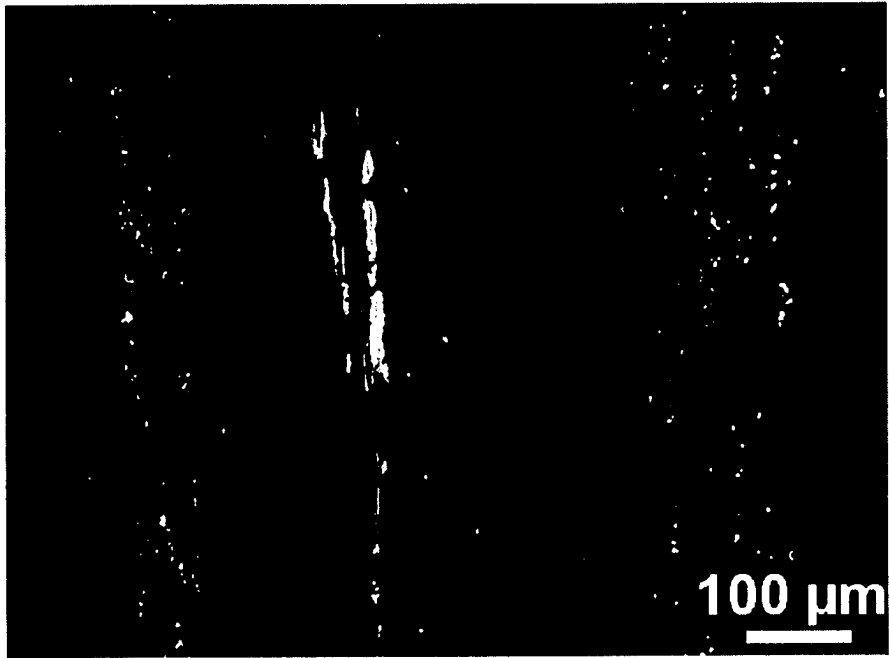


c)

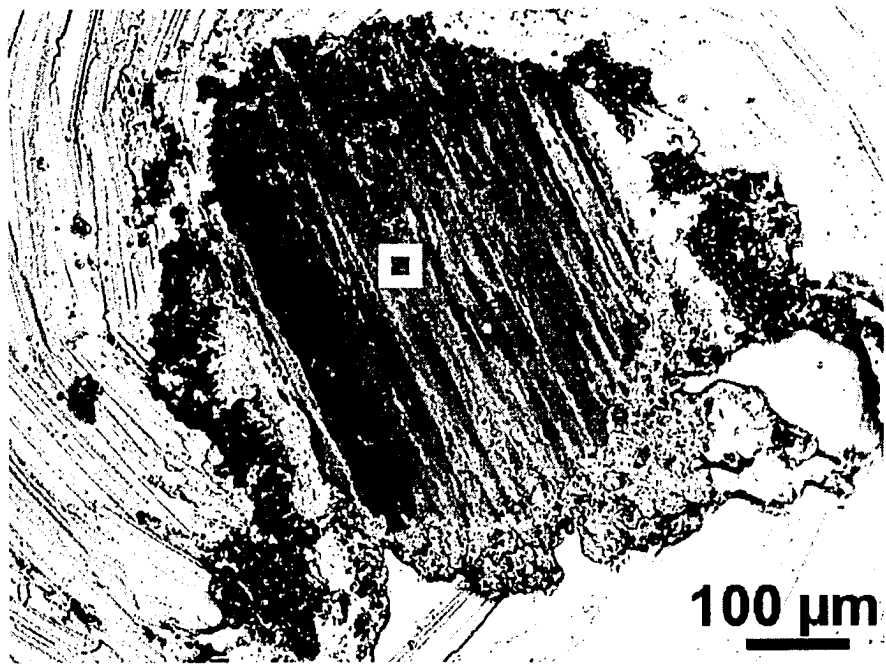


d)

Figure 6.20. SEM images of the corresponding Cu pin in c) SEI and d) BEI modes.



a)



b)

Figure 6.21. SEM images of a) a section of the wear track of the TiB_2 coating tested against Cu in ambient air at 0.65 m/s for 3×10^2 rev., b) the corresponding Cu pin showing material transfer to its surface. The applied load was 5 N.

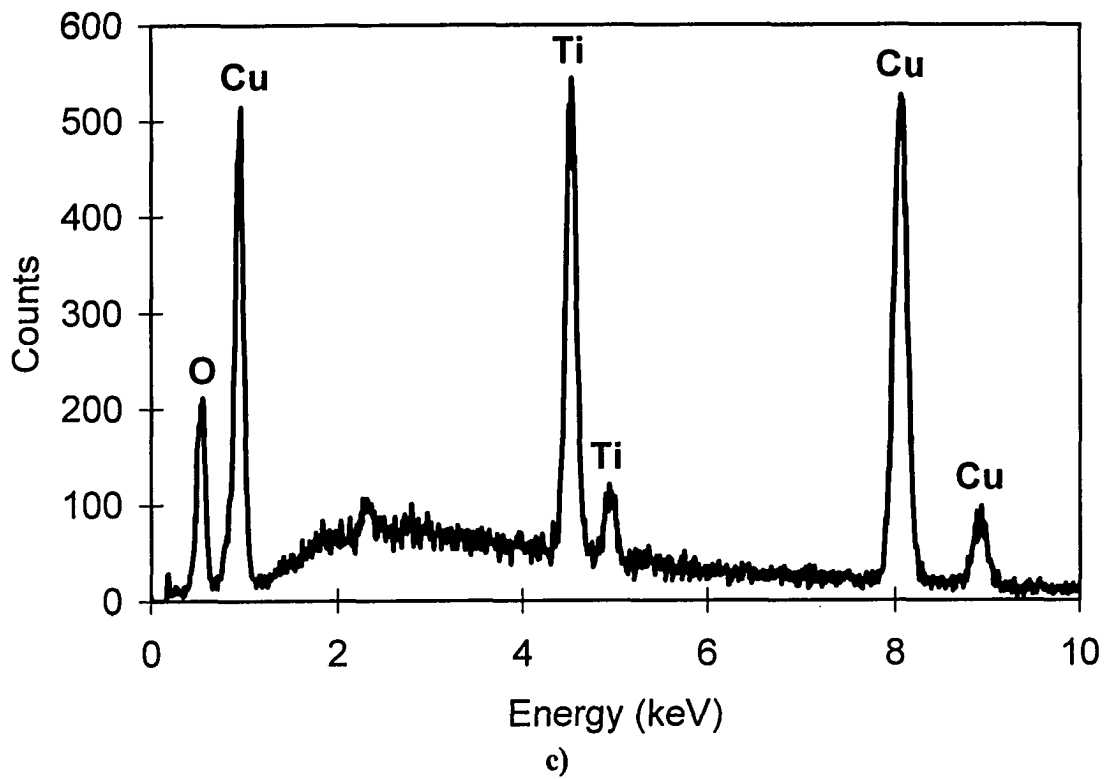


Figure 6.21. c) EDS analysis of the location indicated in b).

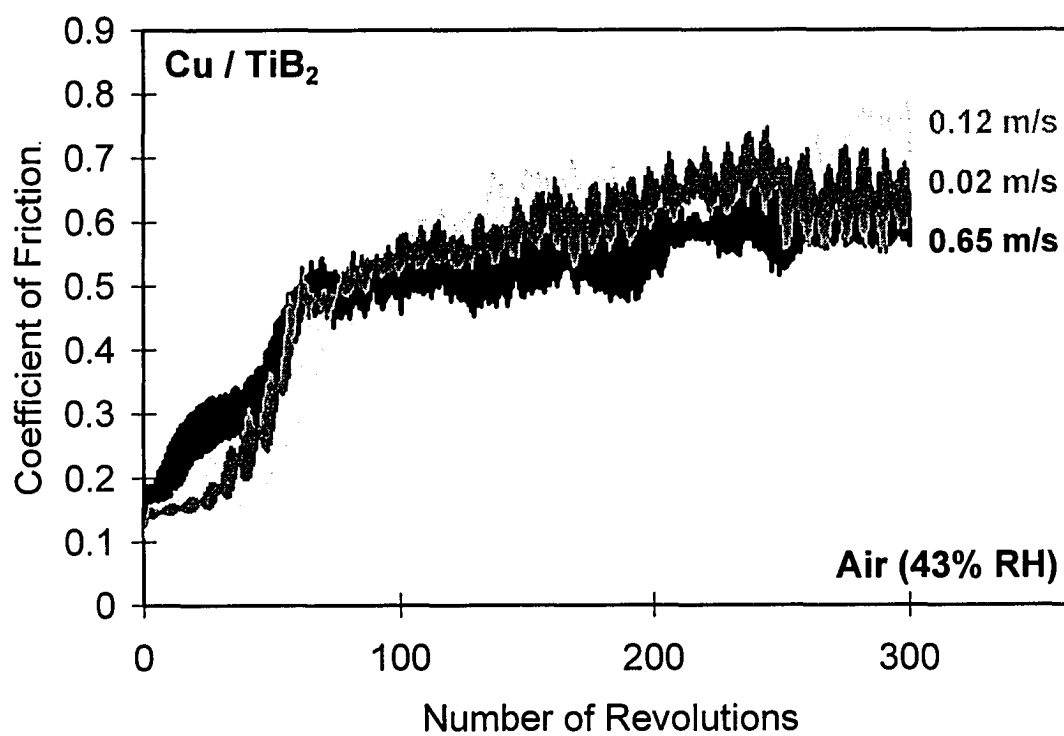
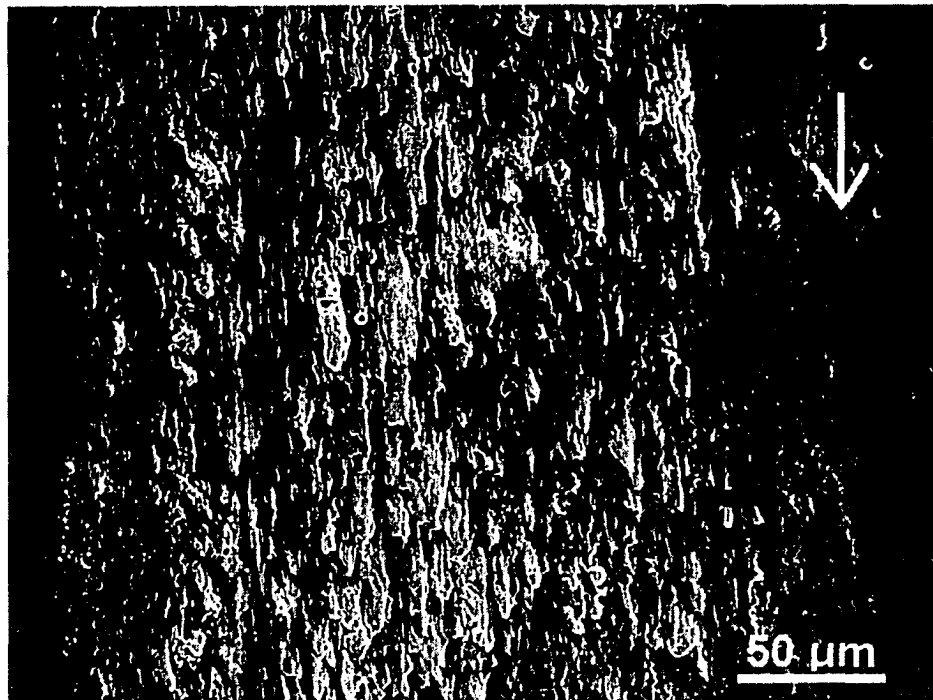
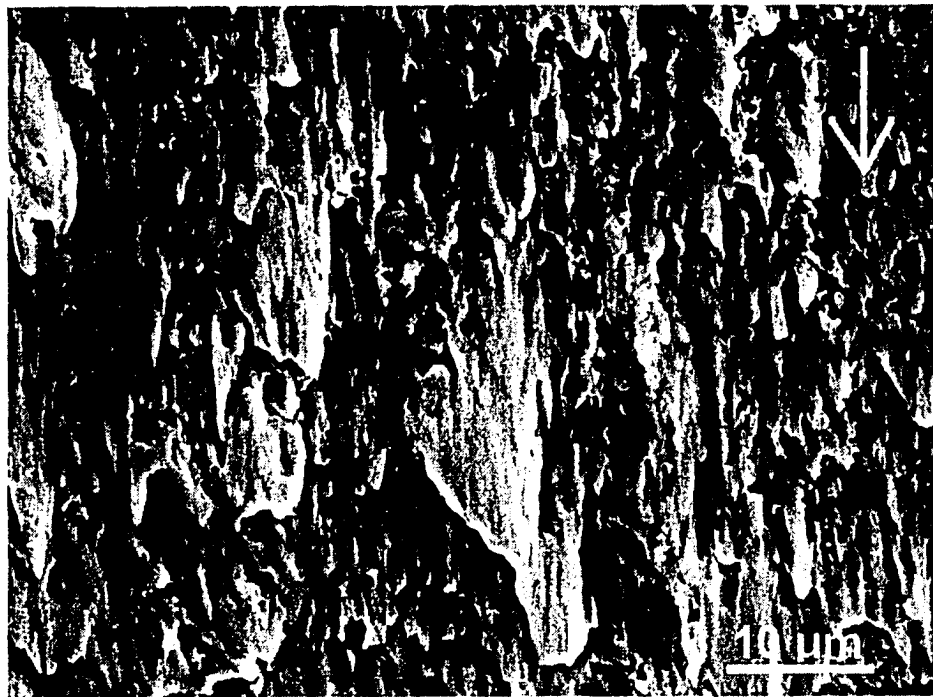


Figure 6.22. The variation of the COF between Cu and the TiB₂ coatings in ambient air at 0.02, 0.12 and 0.65 m/s.

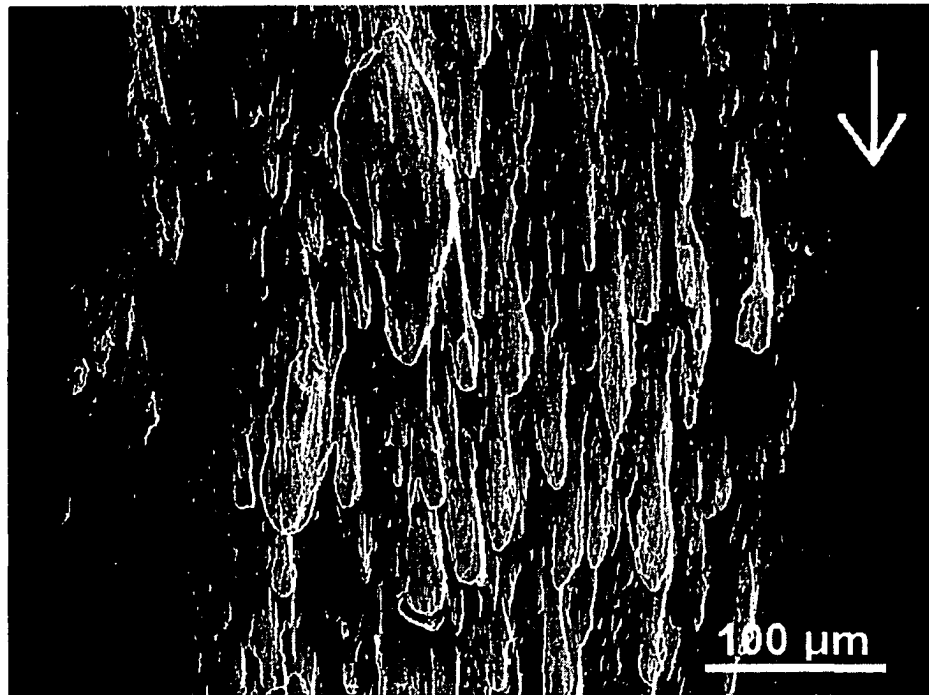


a)

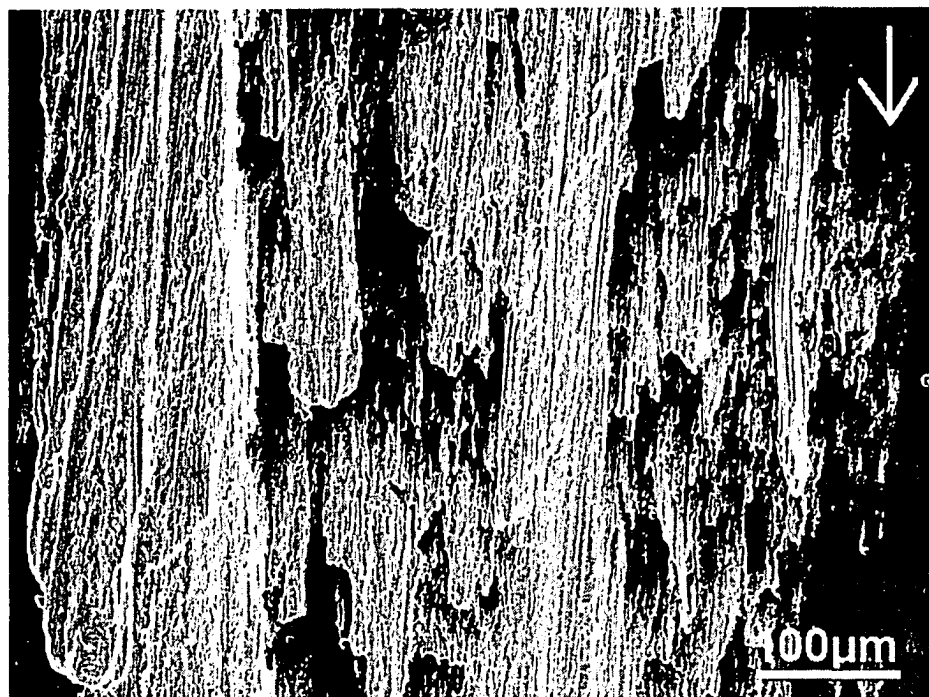


b)

Figure 6.23. a) SEM image of a section of the sliding track of the TiB₂ coating tested against Ti pin at 0.02 m/s sliding speed in argon for 3×10^2 rev. of sliding in argon., b) an enlarged view of a part of a). The applied load was 5 N.



a)



b)

Figure 6.24. SEM images of sections of the sliding tracks of the TiB_2 coating tested against Ti pin in argon a) at 0.12 m/s and b) at 0.65 m/s sliding speed for 3×10^2 rev. of sliding. The applied load was 5 N in all tests.

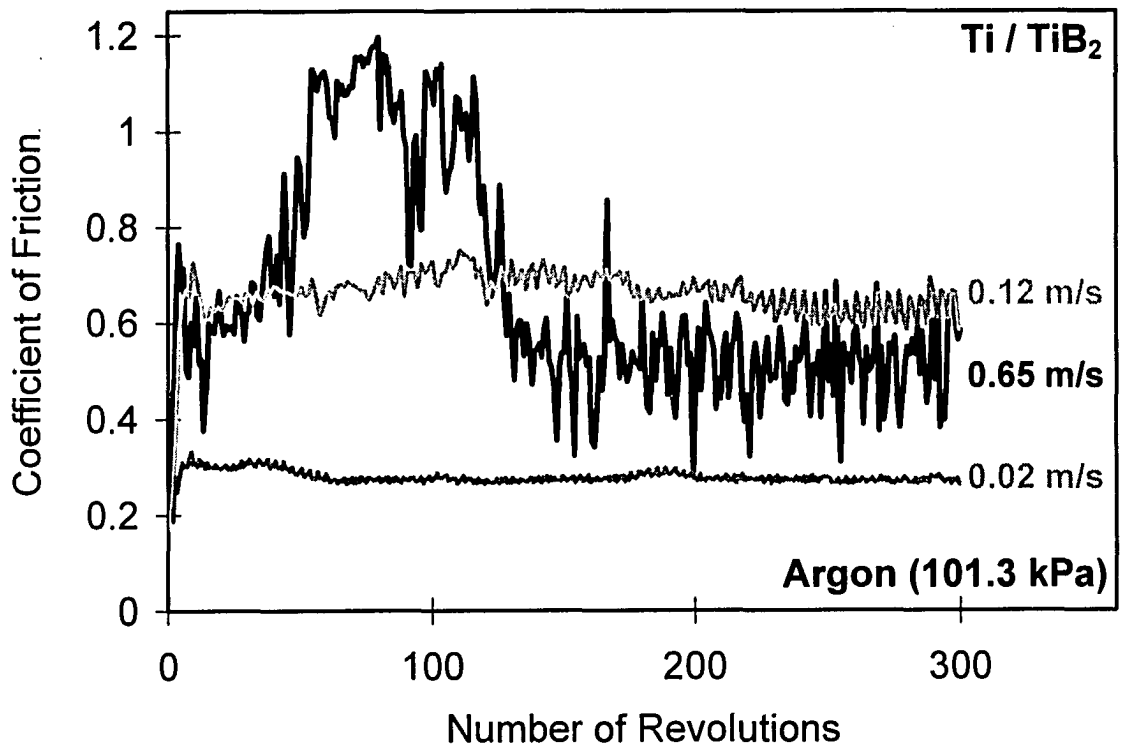


Figure 6.25. The variation of the COF between Ti and the TiB₂ coating in argon at 0.02, 0.12 and 0.65 m/s sliding speeds under a constant load of 5 N.

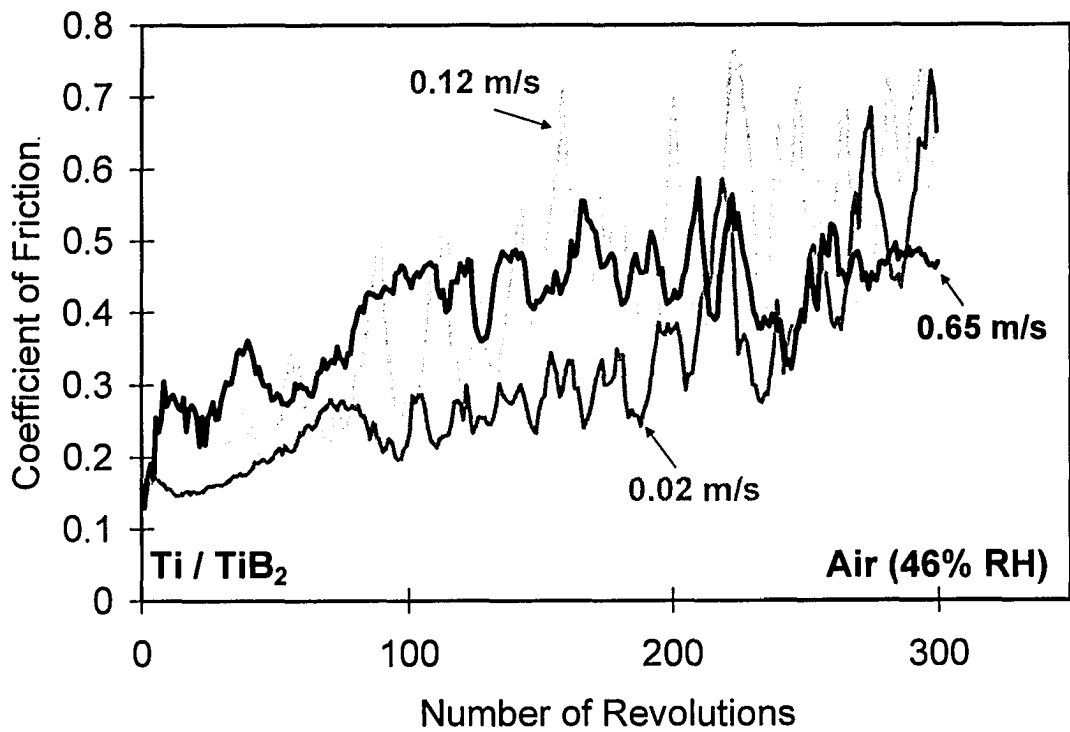
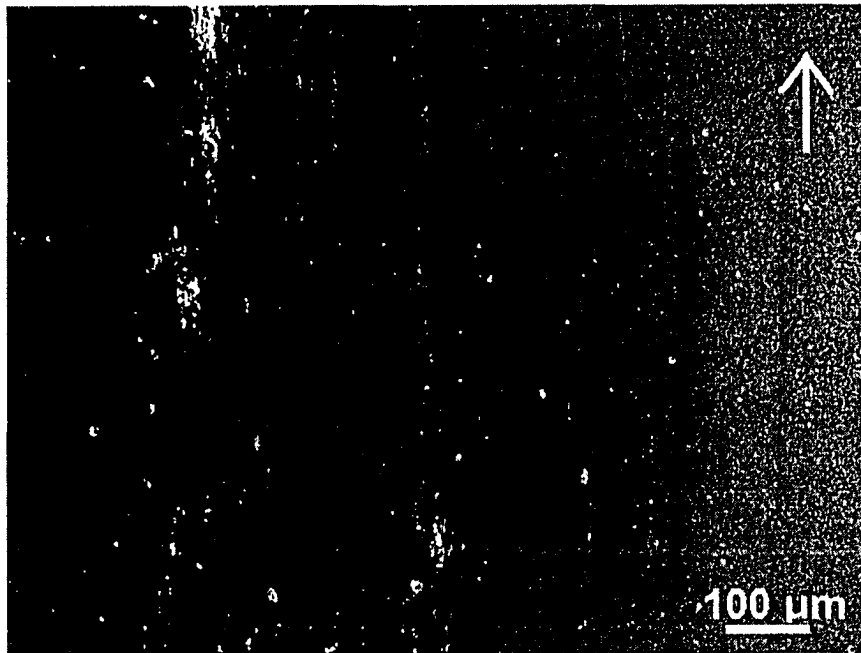
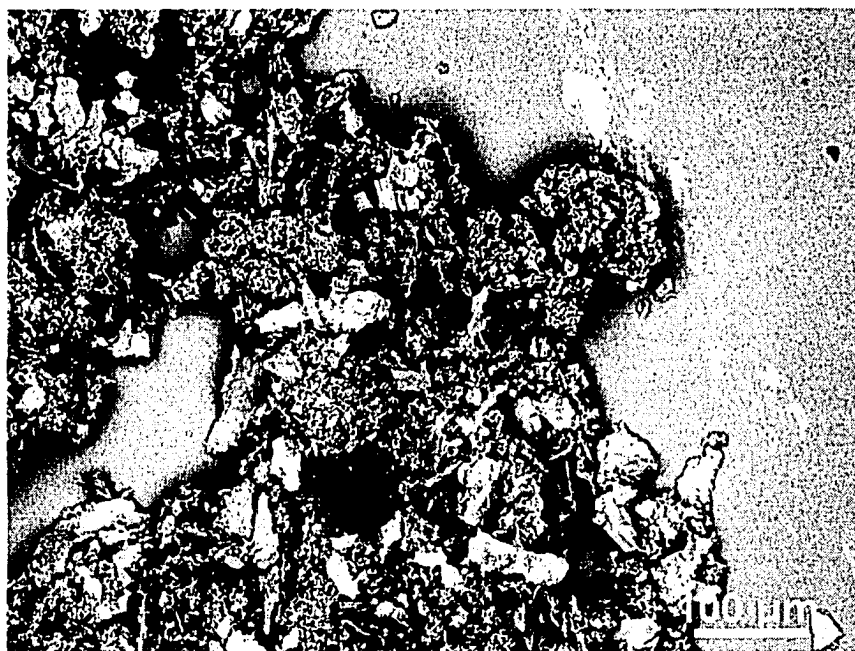


Figure 6.26. The variation of the COF between Ti and the TiB₂ coatings in ambient air (46% RH) at 0.02, 0.12 and 0.65 m/s.



a)



b)

Figure 6.27. SEM images of sections of the sliding tracks of the TiB_2 coating tested against Ti pin at 0.12 m/s sliding speed in ambient air (49.1% RH), **a)** for 3×10^3 rev. of sliding. The applied load was 5 N, **b)** the debris particles generated during the test described in a) showing the two different kinds of debris (rounded small and larger plate-like metallic) generated in ambient air.

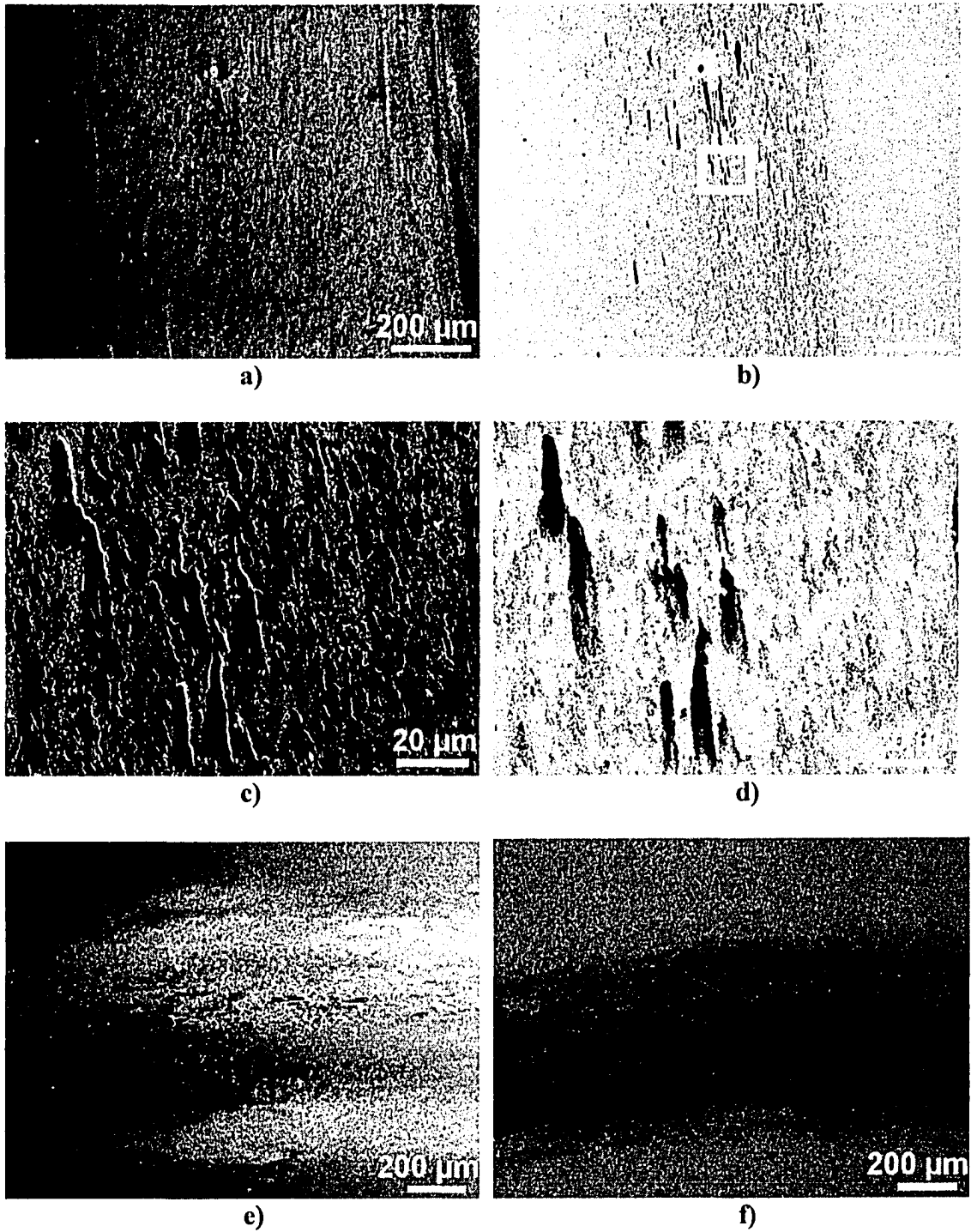


Figure 6.28. SEM images of sections of the sliding tracks of the CrN coating tested against 1100 Al in argon; **a)** and **b)** at 0.65 m/s, **c)** and **d)** enlarged section of **b)**, **e)** and **f)** at 0.12 m/s sliding speed for 300 rev. of sliding. The applied load was 5 N in all tests.

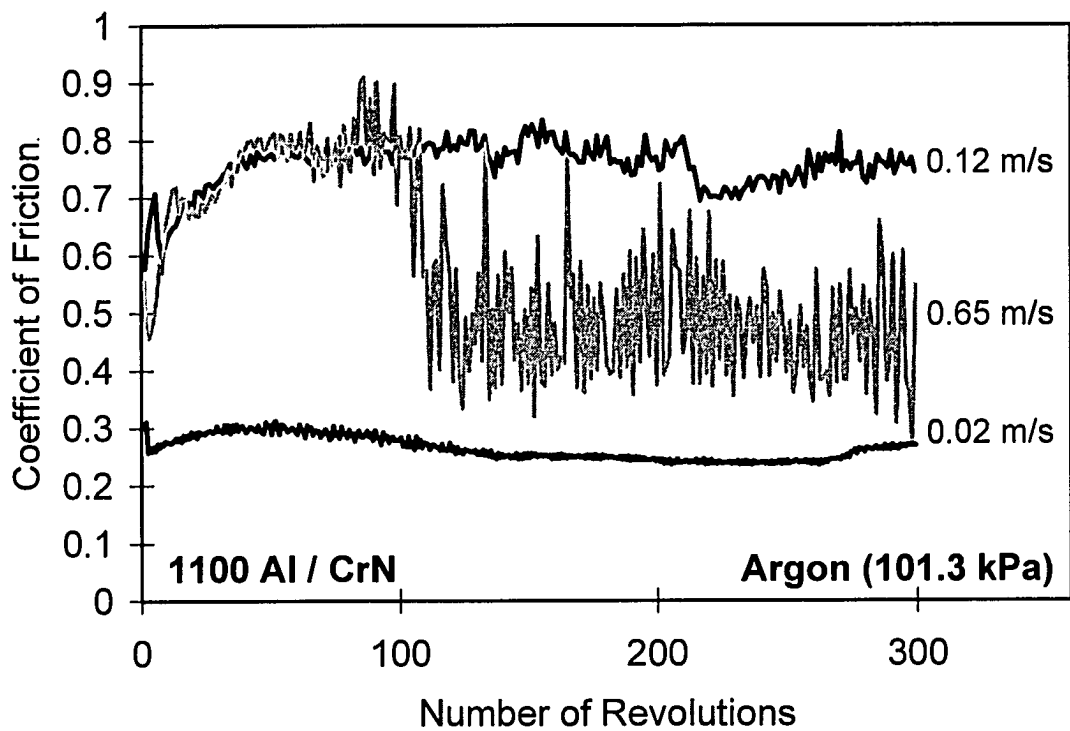


Figure 6.29. The variation of the COF between 1100 Al and the CrN coating in argon at the sliding speeds of 0.02, 0.12 and 0.65 m/s under a constant load of 5 N.

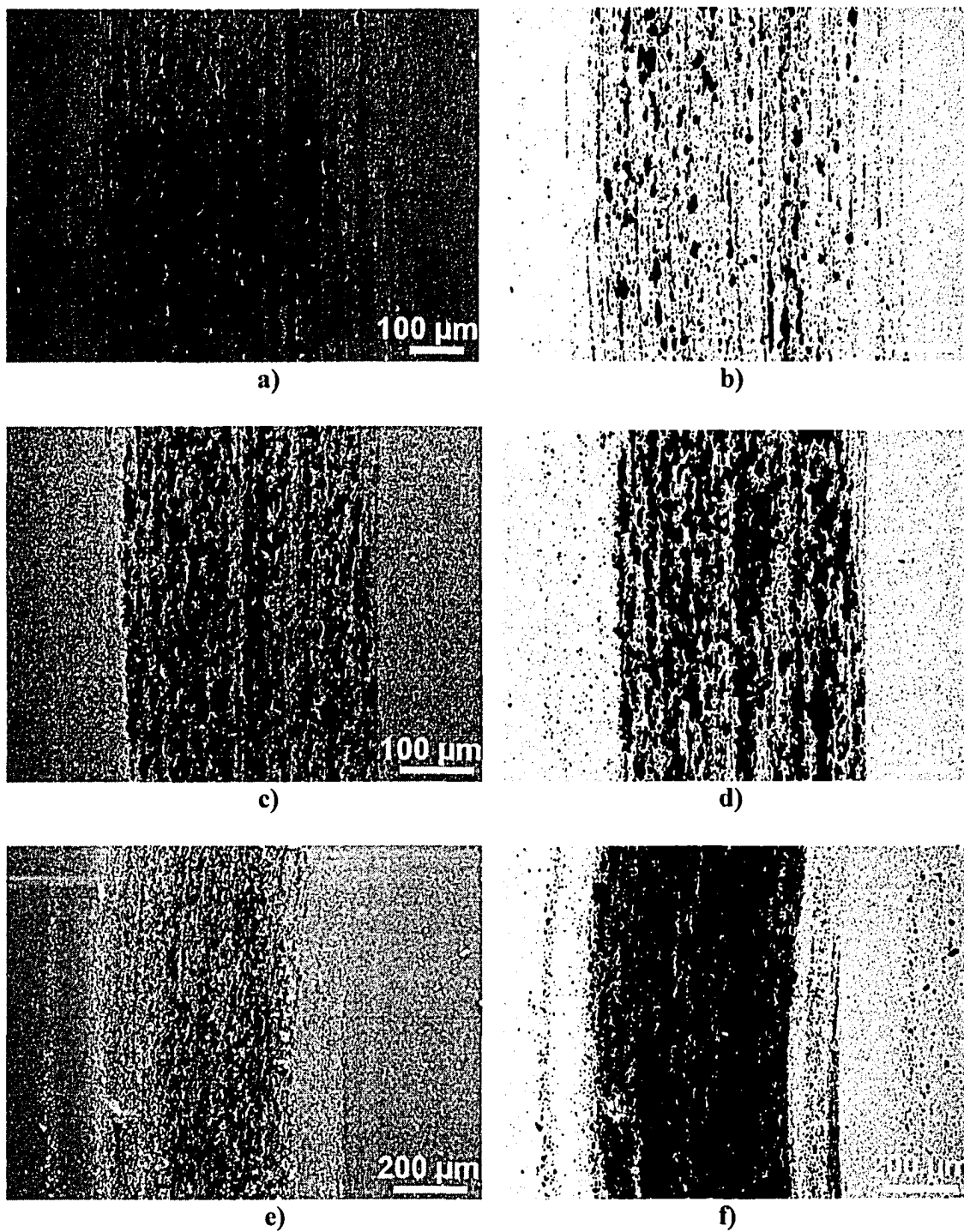


Figure 6.30. SEI and BEI SEM images of sections of the sliding tracks of the CrN coating tested against 1100 Al pin in ambient air (42% RH); **a)** and **b)** at 0.65 m/s, **c)** and **d)** at 0.12 m/s, **e)** and **f)** at 0.02 m/s sliding speed for 300 rev. of sliding. The applied load was 5 N in all tests.

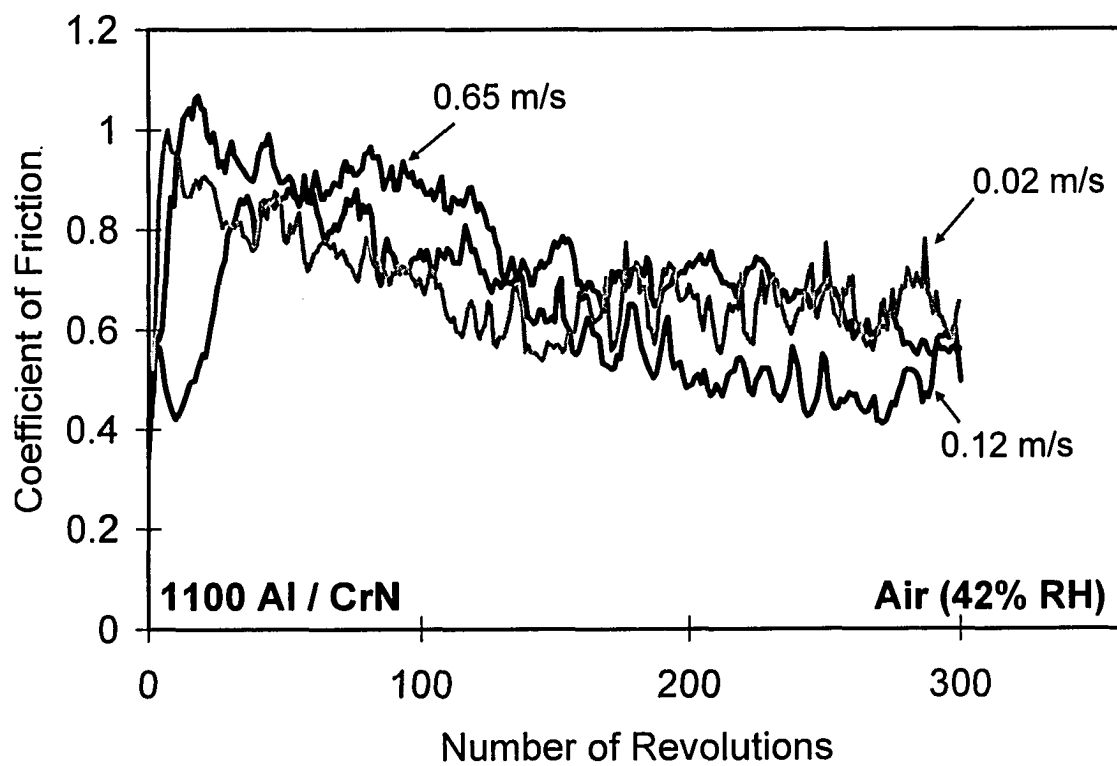
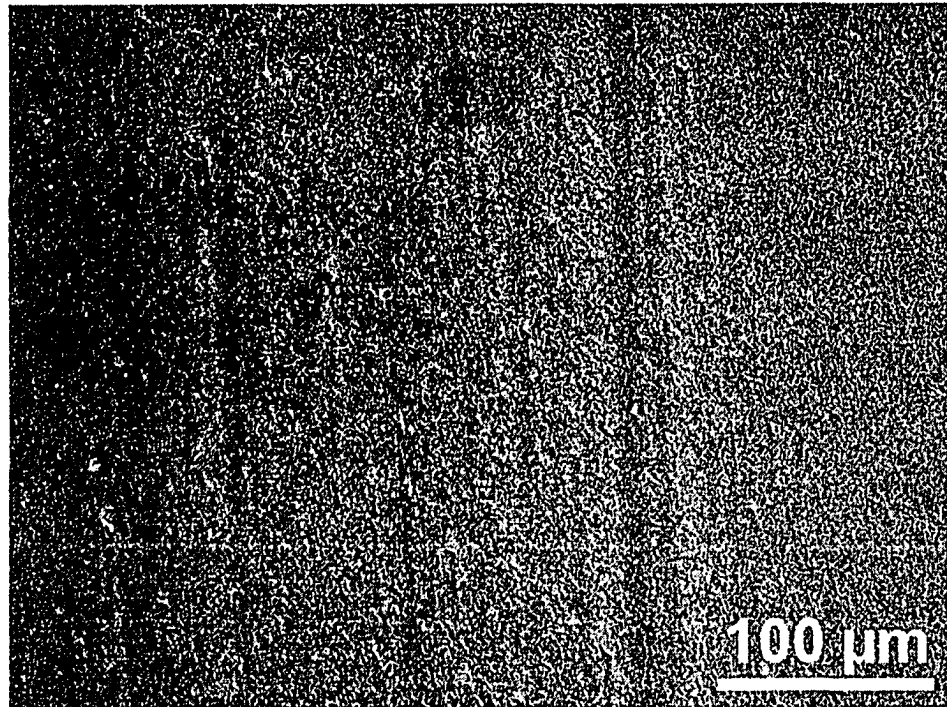


Figure 6.31. The variation of the COF between Al and the CrN coatings in ambient air (42% RH) at 0.02, 0.12 and 0.65 m/s sliding speeds under a constant load of 5 N.



a)



b)

Figure 6.32. SEM images of a) a section of the wear track of the CrN coating tested against Cu in argon at 0.65 m/s for 3×10^2 rev., b) the corresponding Cu pin showing the absence of material transfer to its surface. The applied load was 5 N.

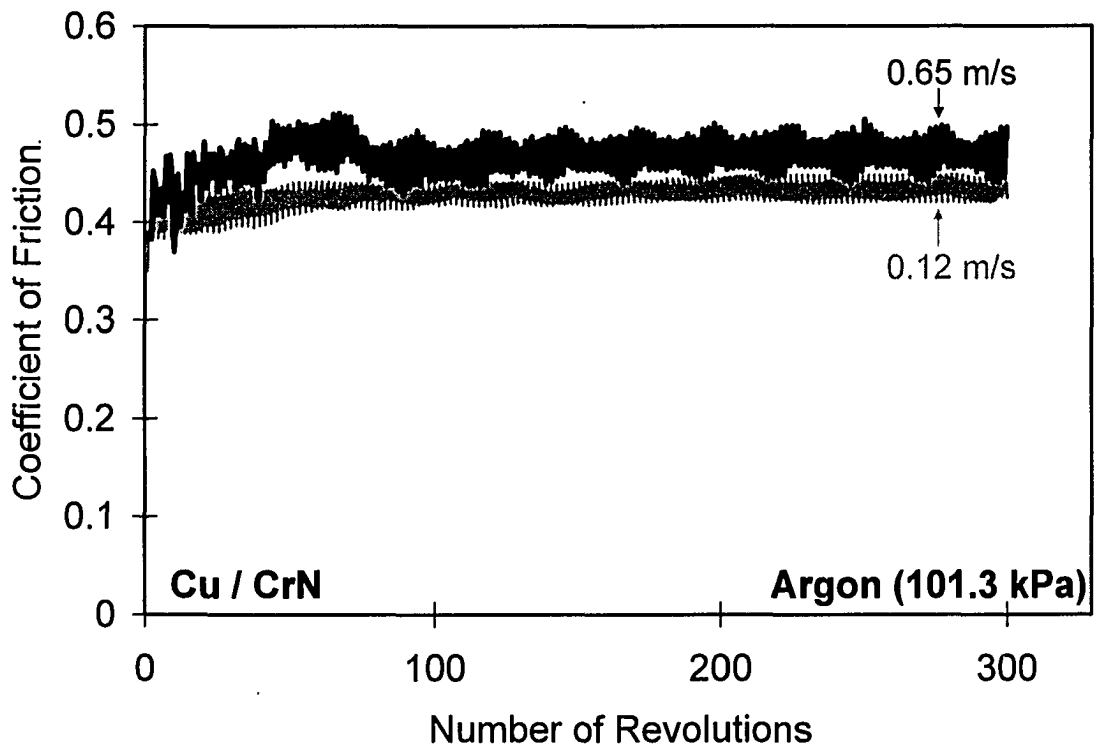
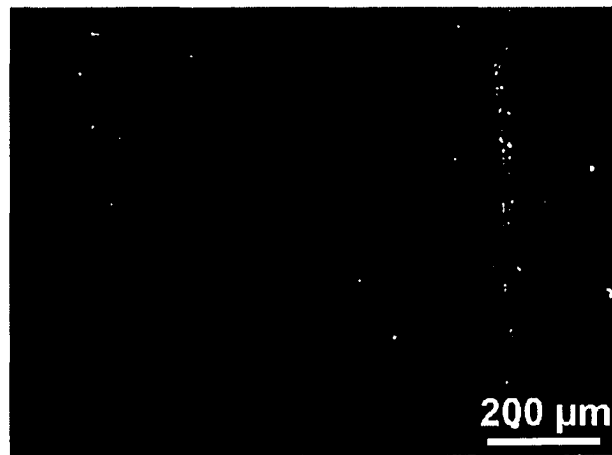
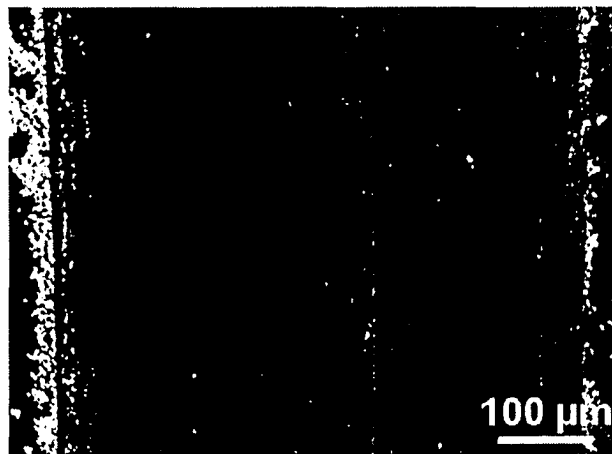


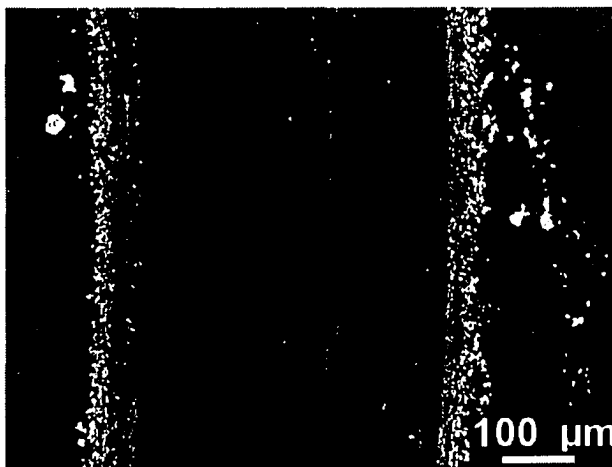
Figure 6.33. The variation of the COF between Cu and the CrN coatings in argon at the sliding speeds of 0.12 and 0.65 m/s under a constant load of 5 N.



a)



b)



c)

Figure 6.34. SEM images of sections of the sliding tracks of the CrN coating tested against Cu pin in ambient air (42% RH) **a)** at 0.65 m/s, **b)** at 0.12 m/s, and **c)** at 0.02 m/s sliding speed for 3×10^2 rev. of sliding. Debris formation in decreasing amount with increasing sliding speed was observed. The applied load was 5 N in all tests.

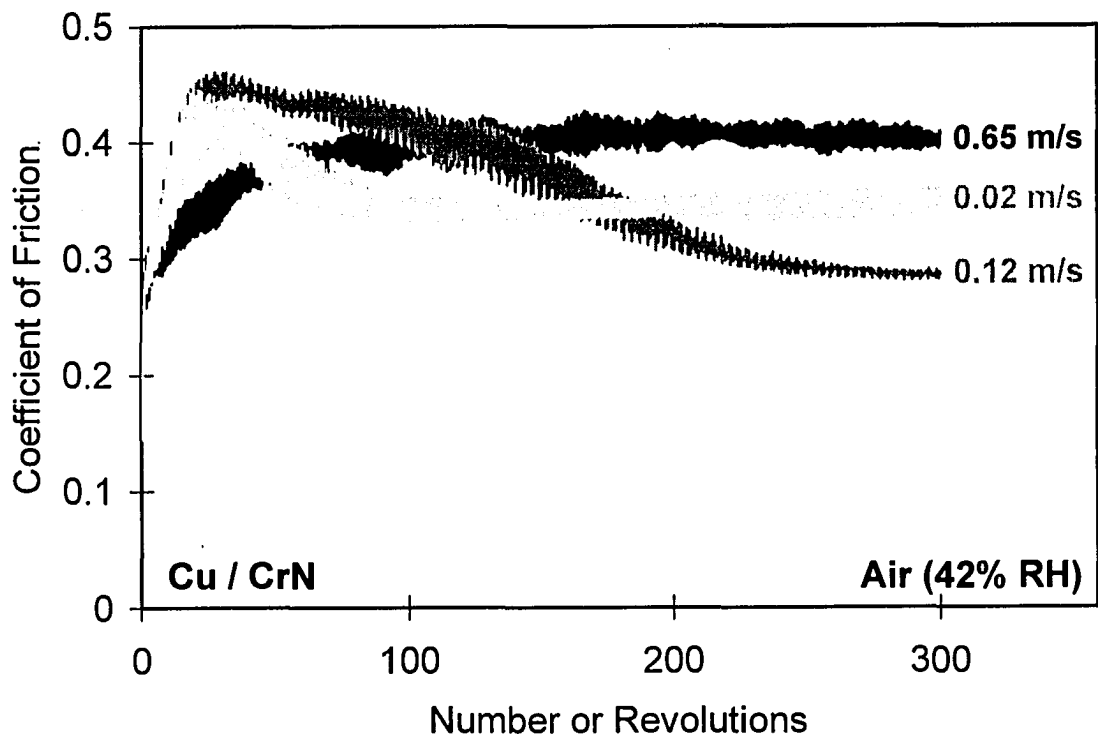


Figure 6.35. The variation of the COF between Cu and the CrN coatings in ambient air (42% RH) at the sliding speeds of 0.02, 0.12 and 0.65 m/s under a constant load of 5 N.

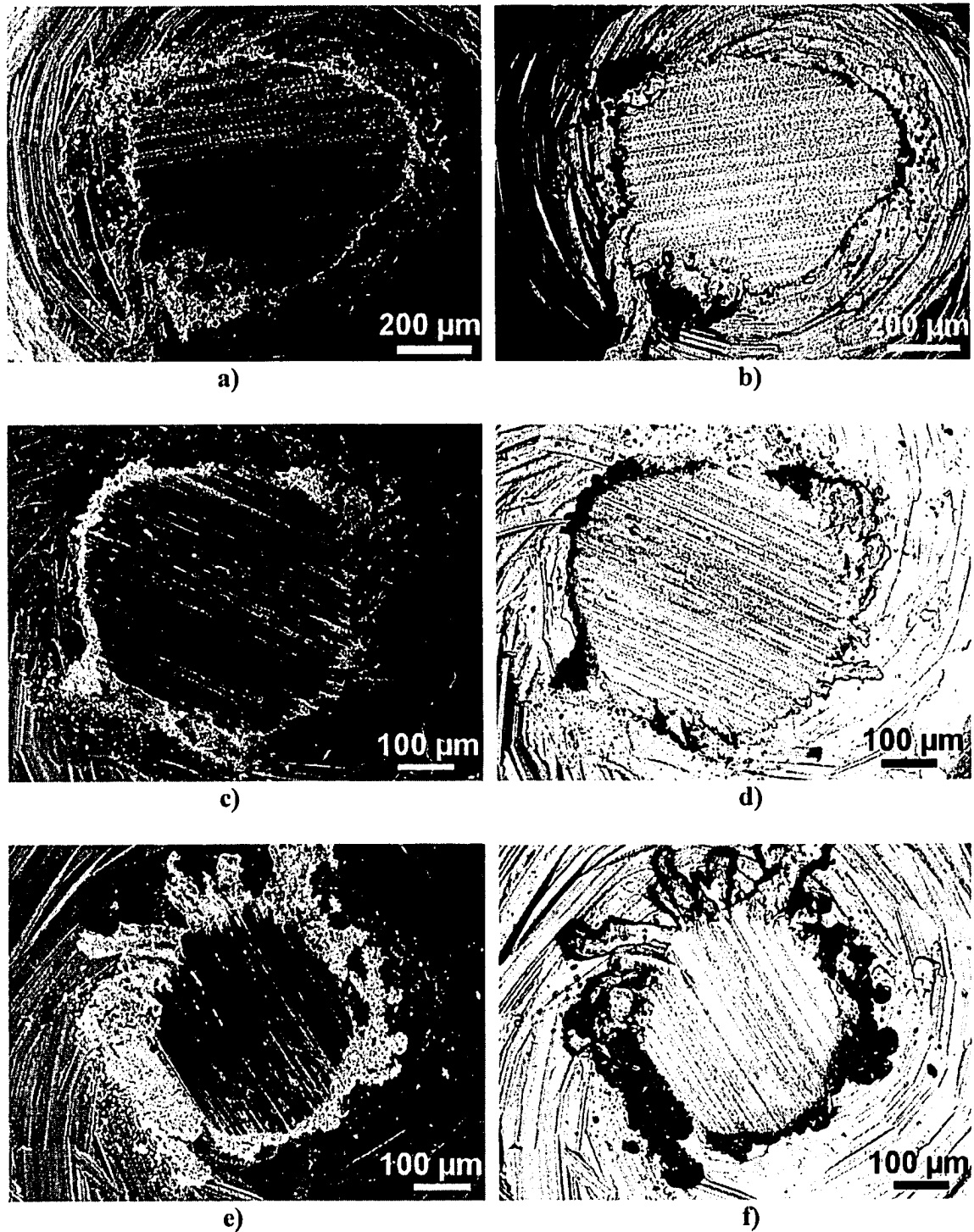


Figure 6.36. SEI and BEI SEM images of contact surfaces of the Cu pins tested against CrN coating in ambient air (42% RH); **a)** and **b)** at 0.65 m/s, **c)** and **d)** at 0.12 m/s, **e)** and **f)** at 0.02 m/s sliding speed for 3×10^2 rev. of sliding. The applied load was 5 N in all tests.

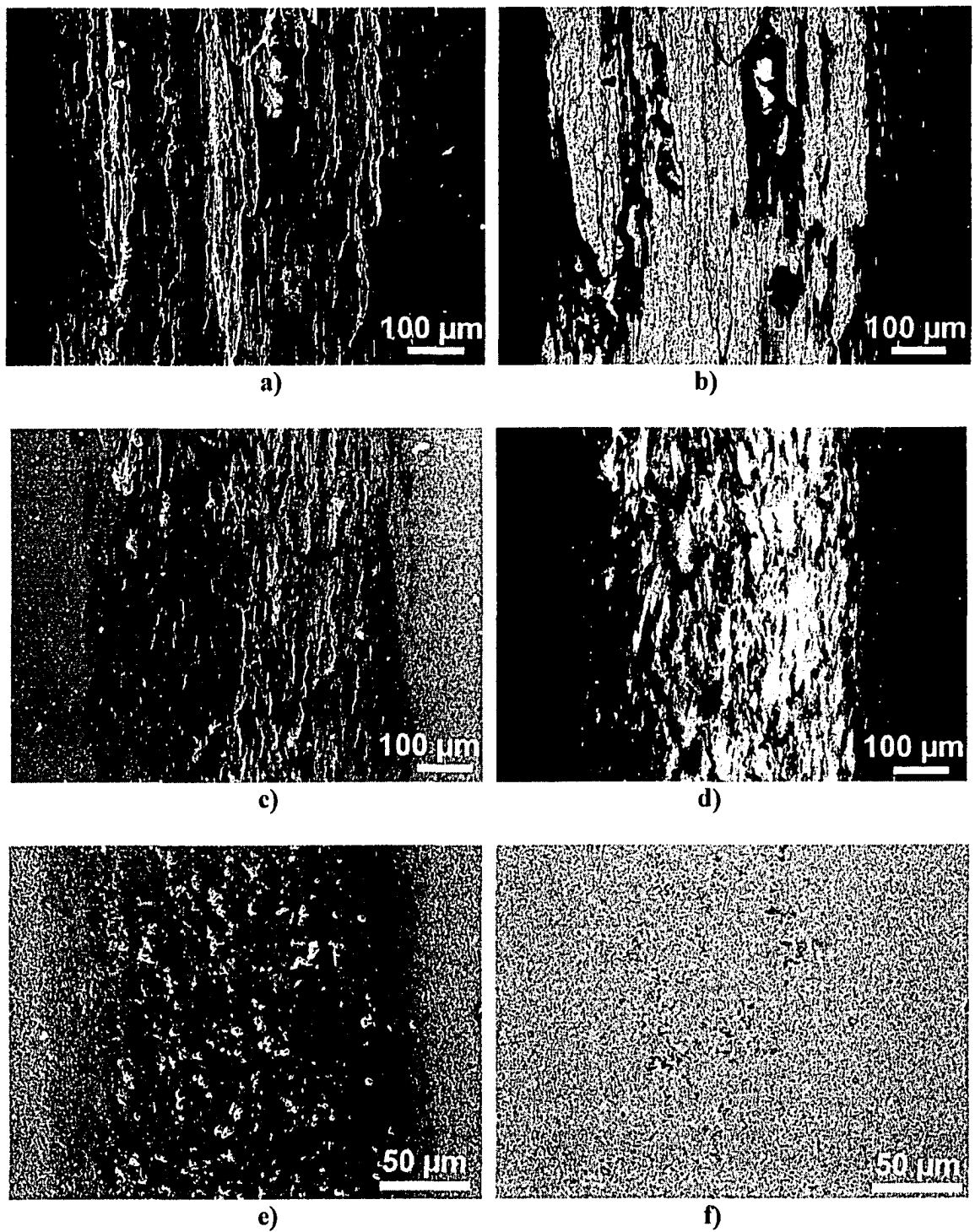


Figure 6.37. SEI and BEI SEM images of sections of the sliding tracks of the CrN coating tested against Ti in argon; **a)** and **b)** at 0.65 m/s, **c)** and **d)** at 0.12 m/s, **e)** and **f)** at 0.02 m/s sliding speed for 3×10^2 rev. of sliding. The applied load was 5 N in all tests.

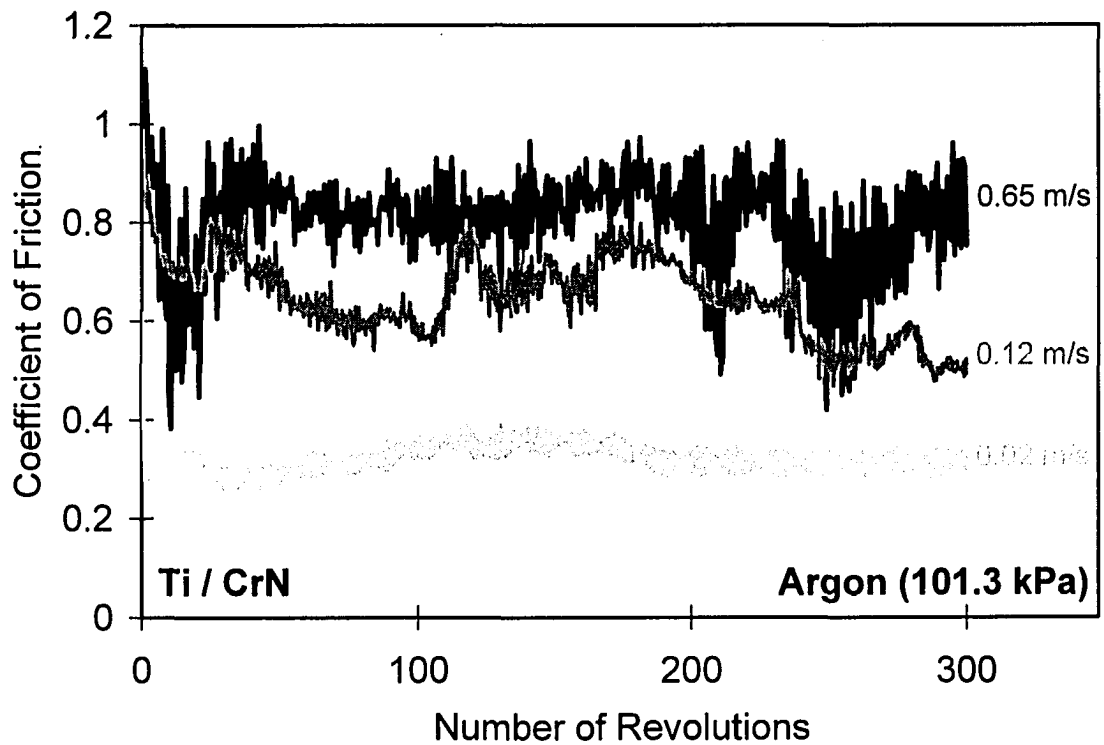
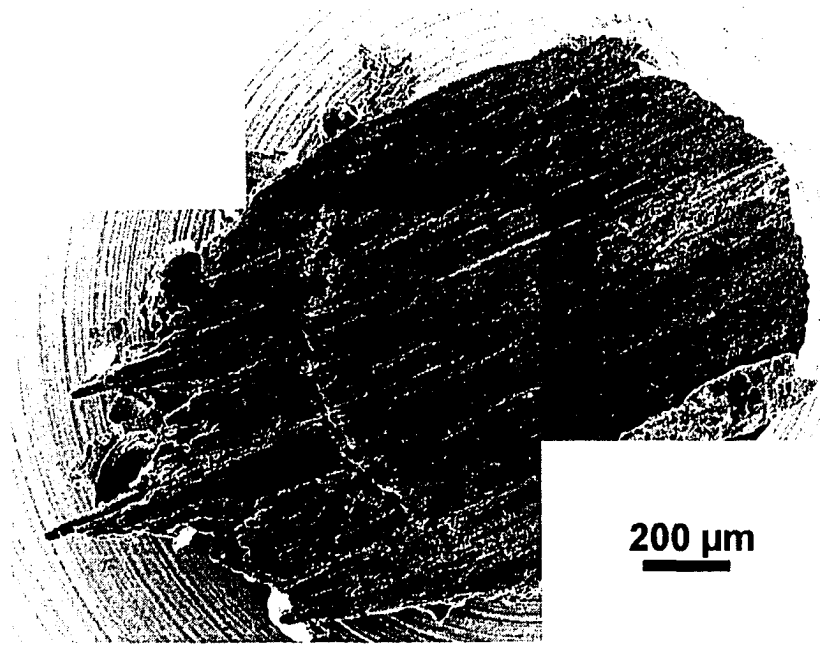
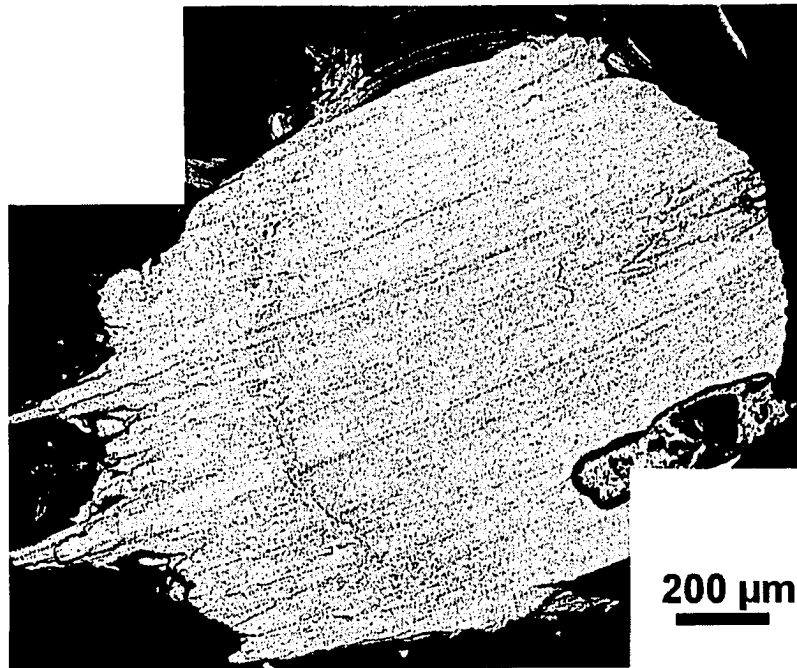


Figure 6.38. The variation of the COF between Ti and the CrN coatings in argon at the sliding speeds of 0.02, 0.12 and 0.65 m/s under a constant load of 5 N.



a)



b)

Figure 6.39. SEI and BEI SEM images of contact surfaces of the Ti pins tested against the CrN coating in argon; **a)** and **b)** at 0.65 m/s.

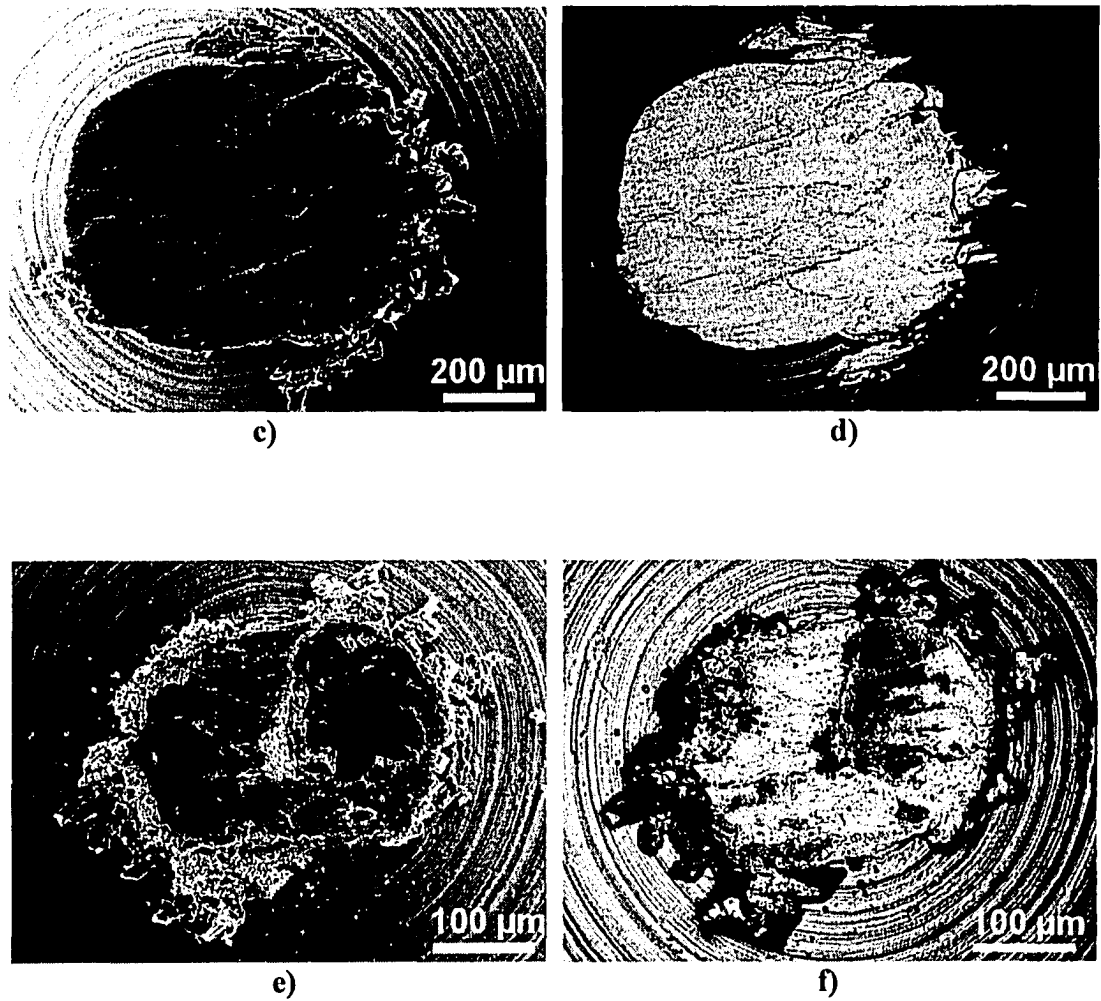
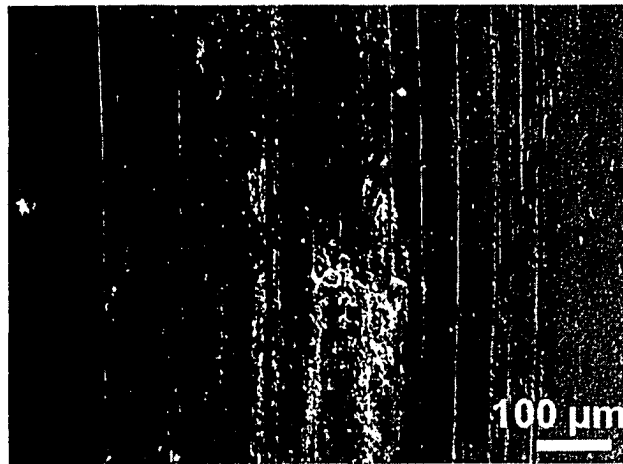
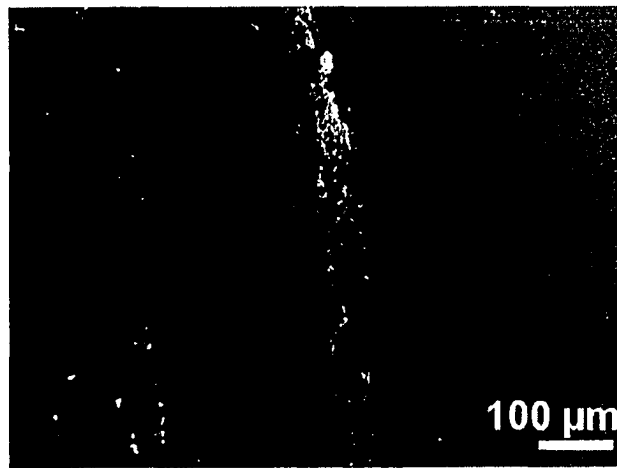


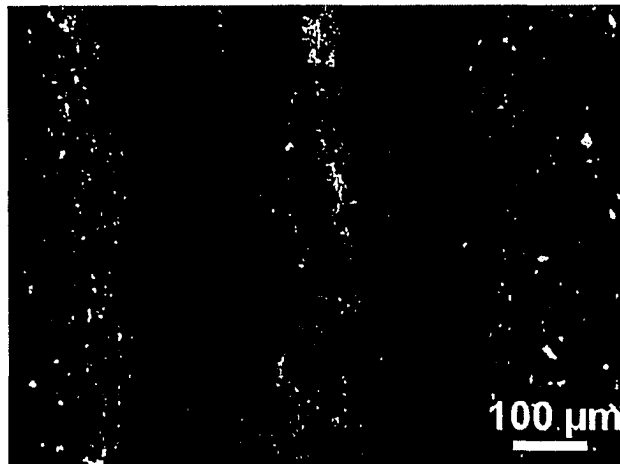
Figure 6.39. SEI and BEI SEM images of contact surfaces of the Ti pins tested against the CrN coating in argon; c) and d) at 0.12 m/s, e) and f) at 0.02 m/s sliding speed for 3×10^2 rev. of sliding. The applied load was 5 N in all tests.



a)



b)



c)

Figure 6.40. SEM images of sections of the sliding tracks of the CrN coating tested against Ti pin in ambient air (51% RH) **a)** at 0.65 m/s, **b)** 0.12 m/s and **c)** at 0.02 m/s sliding speed for 3×10^2 rev. of sliding. The applied load was 5 N in all tests.

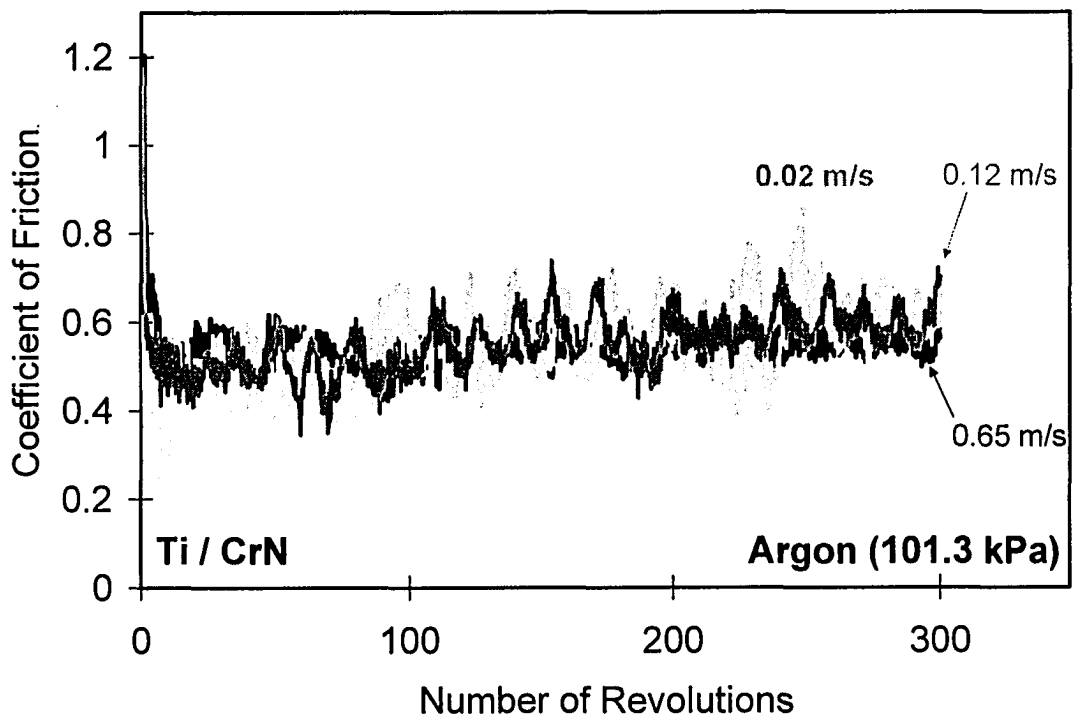


Figure 6.41. The variation of the COF between Ti and the CrN coatings in ambient air at 0.02, 0.12 and 0.65 m/s sliding speeds under a constant load of 5 N.

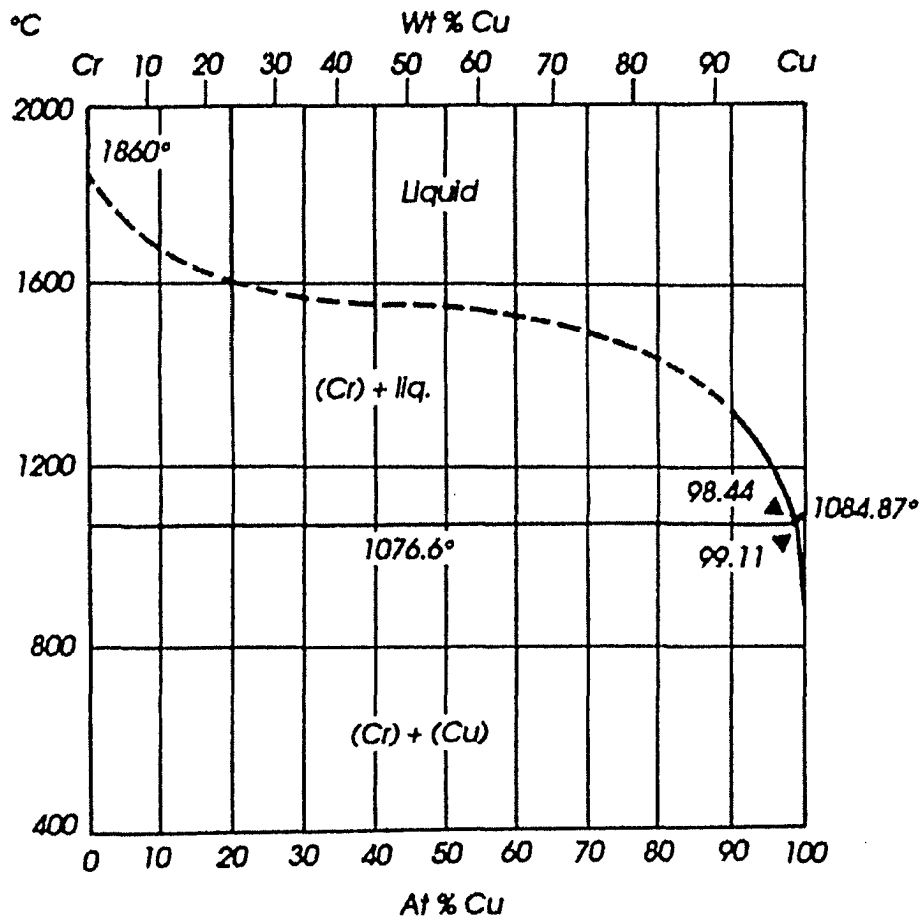


Figure 6.42. Cr-Cu phase diagram [144].

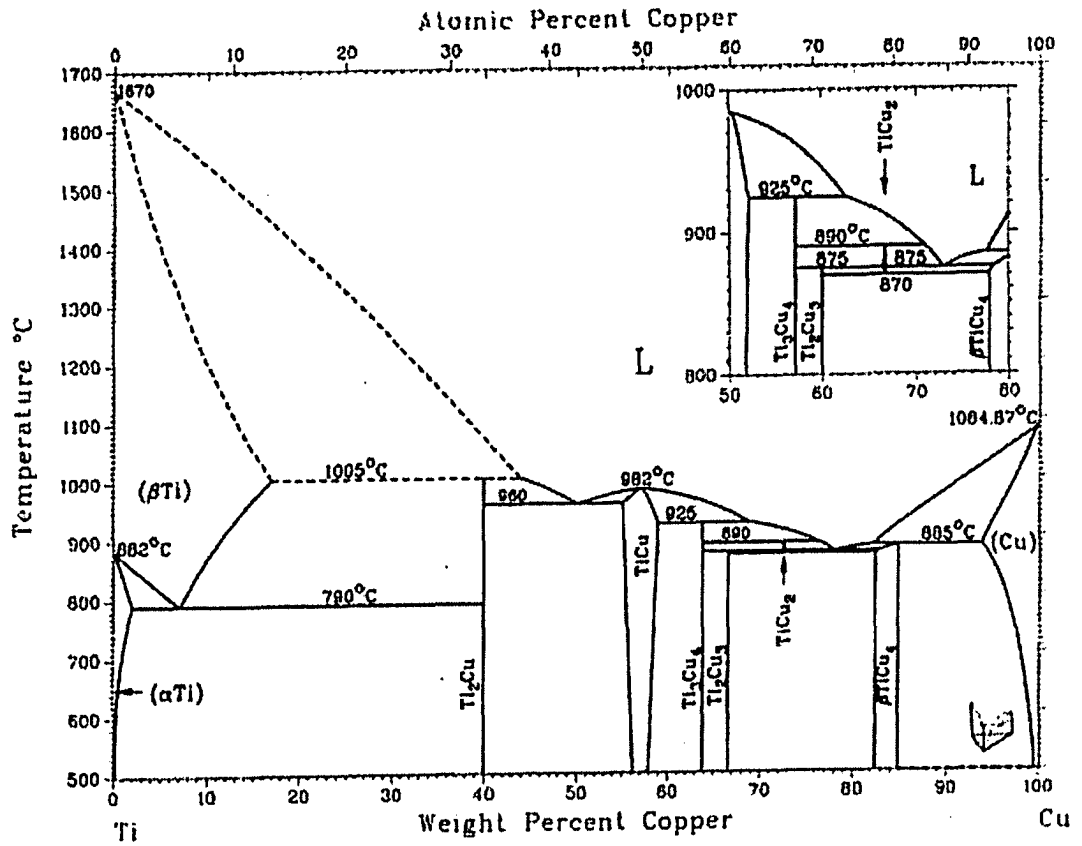


Figure 6.43. Ti-Cu phase diagram [145].

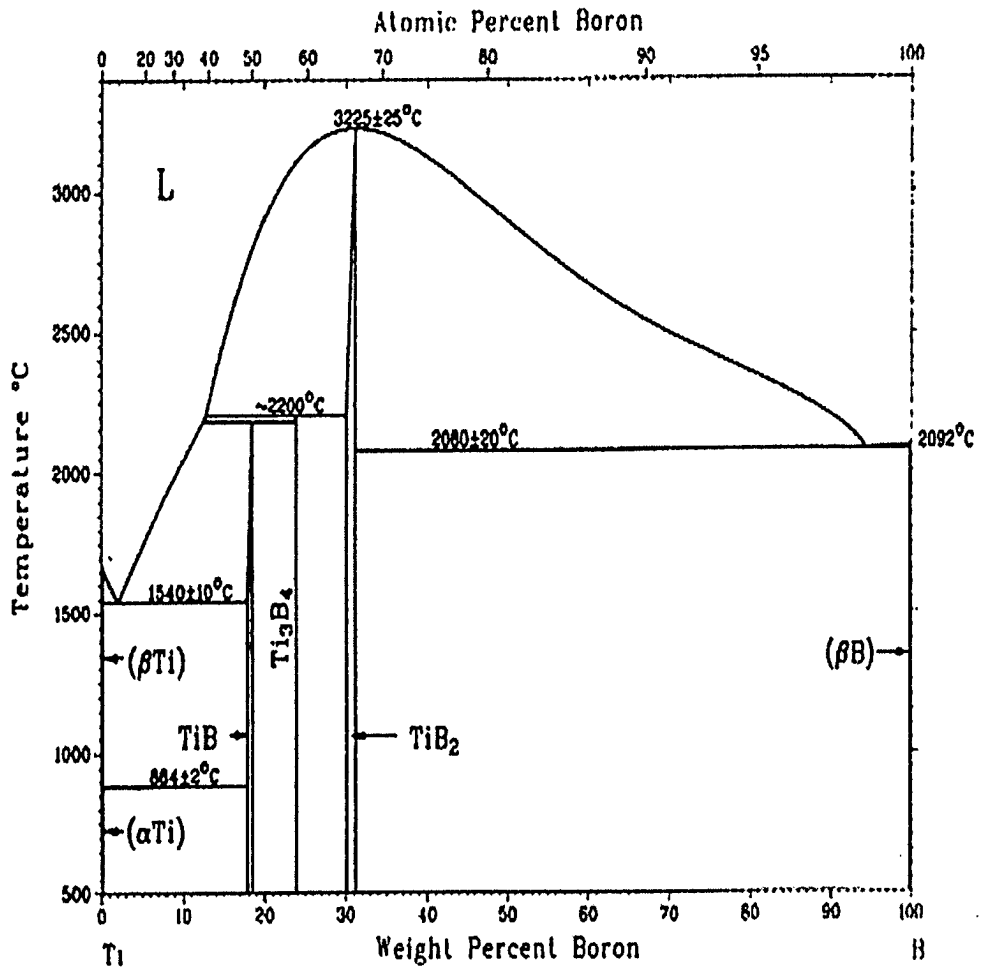


Figure 6.44. Ti-B phase diagram [145].

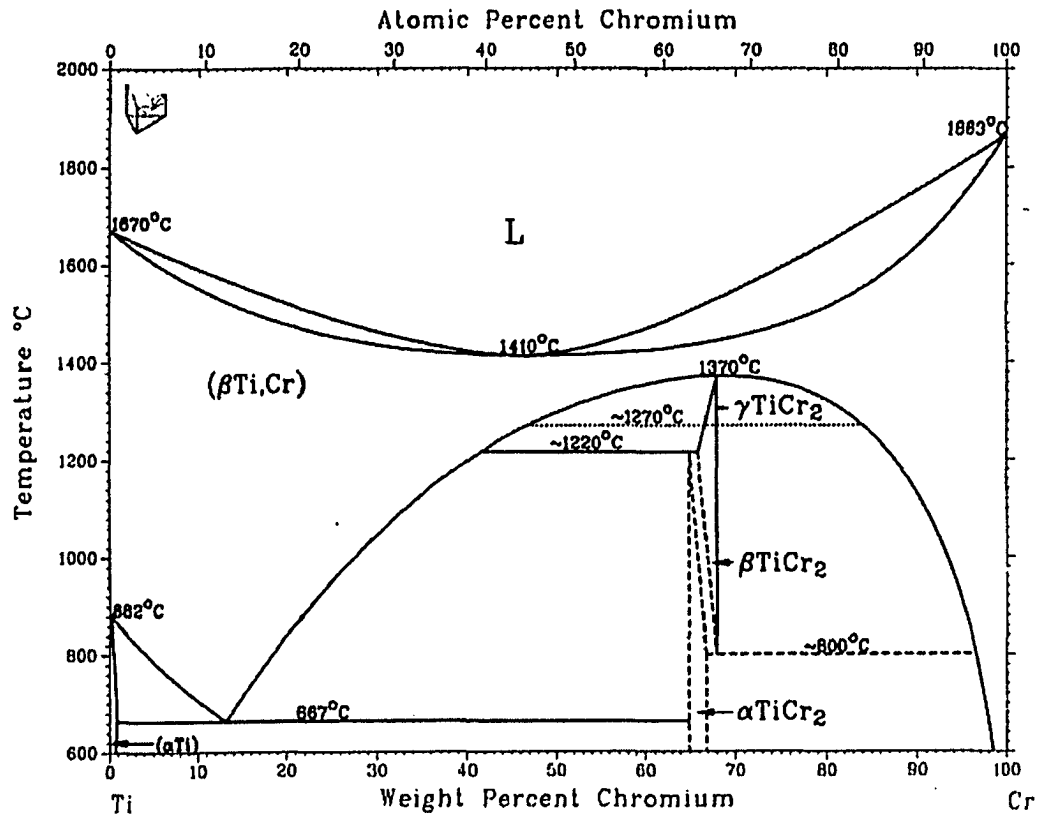


Figure 6.45. Ti-Cr phase diagram [145].

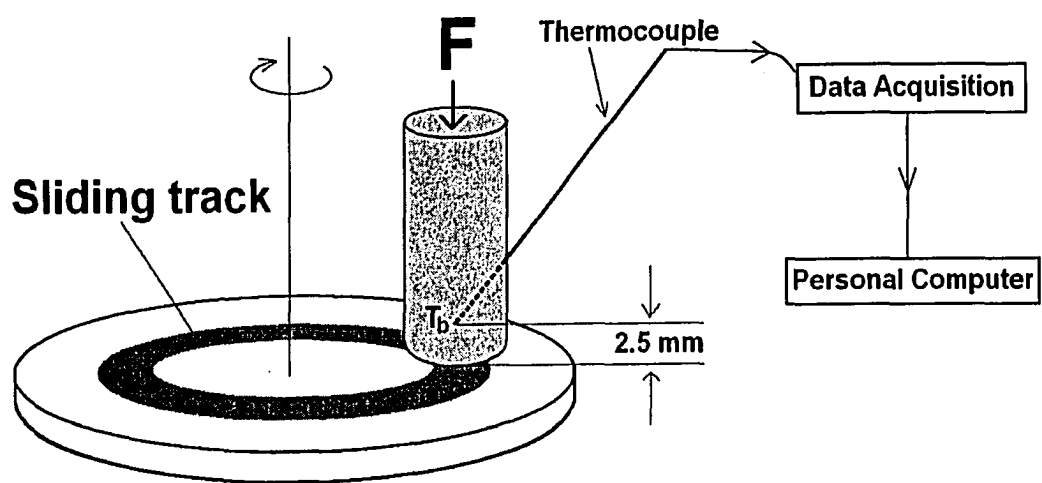


Figure 6.46. Experimental setup to measure the temperature increase of the pins.

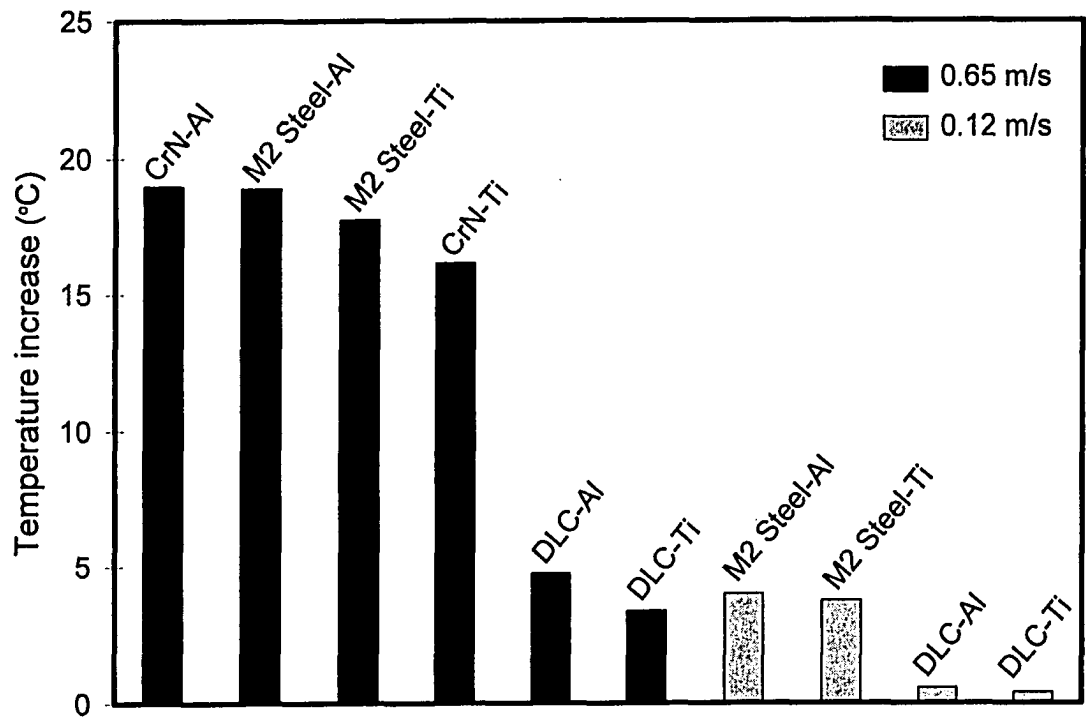


Figure 6.47. The measured increases in the bulk temperatures of the Al and Ti pins while running against the non-hydrogenated DLC, CrN and M2 steel in ambient air at 0.12 and 0.65 m/s sliding speeds under the applied load of 5 N. These values were obtained by subtracting the steady state temperatures during running from the ones measured before the tests were started.

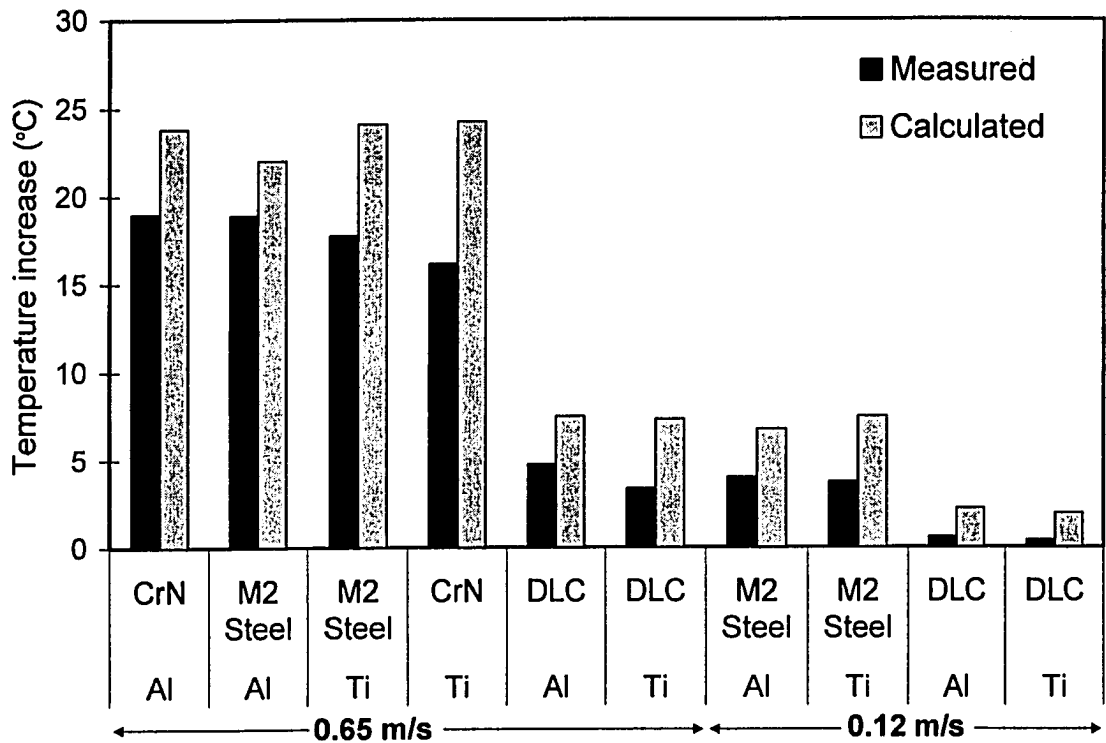


Figure 6.48. The calculated and measured increases in the bulk temperatures of the Al and Ti pins while running against the 80-V DLC, CrN and M2 steel at 0.12 and 0.65 m/s under the applied load of 5 N. The calculations are based on the method developed by Ashby and his co-workers [143, 159, 160]. The method is described in **Appendix A.1**.

CHAPTER 7

CONCLUSIONS

In order to fulfill the objectives stated in **Chapter 1**, the tribological behaviour during dry sliding contact between 319 Al, 1100 Al, Cu, Ti and surfaces coated with DLC and other industrial coatings (CrN, TiB₂, TiN, TiAlN and TiCN) have been investigated under various test conditions. The main conclusions can be summarized as follows:

7.1. Transfer of 319 Al to Various Coating Surfaces

1) Under the ambient testing conditions, no Al transfer occurred to the non-hydrogenated DLC coating surface after dry sliding contact. All other coatings had varying amounts of aluminum adhered to their surfaces. This observation confirms that among the coatings tested, DLC coatings are the most promising class of coatings for dry machining of Al alloys.

2) Except for the non-hydrogenated DLC coating, TiB₂ picked up the minimum amount of Al regardless of its surface roughness in ambient conditions. This was followed by TiCN, TiAlN, TiN and CrN coatings in the order of increasing amount of Al transferred on their surfaces.

3) Increasing the sliding speed from 0.12 to 0.60 m/s decreased the amount of aluminum transferred on all the coatings tested.

4) For all coatings except TiB₂, there was a sharp decrease in the amount of aluminum adhered to their surfaces when tested under the argon atmosphere. This suggested that the presence of oxygen and/or water vapour promoted aluminum adhesion to these coatings. The amount of aluminum transfer to the TiB₂ coating was a weak function of the inertness of the environment, which was attributed to the high chemical stability of TiB₂.

5) Surface roughness played a critical role in material transfer especially in the very early stages of sliding of rough TiB₂ (83 nm Ra). The amount of aluminum transferred increased until a certain sliding distance, followed by a decrease in the

amount of aluminum, finally approaching the value of the TiB₂ coatings with smoother surfaces (16 nm Ra).

7.2. Transfer of Al, Cu and Ti to CrN, DLC and TiB₂ Coatings

1) The lower yield strength, the higher chemical affinity towards the counterface, and lower thermal conductivity were found as the three main material properties that promoted the adhesion and transfer of a material to a counterface during dry sliding contact.

2) In both argon and ambient air, Al adhered as pieces and/or smears whereas Ti always adhered as pieces. Very thin smeared layers were only observed with Al.

3) In the argon atmosphere, almost all the material removed from the pin was transferred and remained adhered to the coating surfaces. In ambient air, however, significant amount of material removed from the pins was converted into oxidized loose wear debris during sliding. Since the transfer of material to the counterface was the first step of the debris generation mechanism, the total amount of transferred material in ambient air was much higher than the one remained adhered at the end of the tests.

4) The relative strength of the interface bonding formed in ambient air is suggested as the most important factor to determine whether transferred material would remain adhered to the counterface or transform into loose debris during successive sliding.

5) For all combinations except Al-CrN pair, changing the test atmosphere from argon to ambient air drastically reduced the material remaining adhered on the coating surfaces and promoted oxidized loose debris formation. For the Al-CrN pair however, in addition to debris formation, much more Al adhered to the CrN coating surface in ambient air than in argon. This observation suggested that contrary to other sliding pairs, the strength of the interfacial bonding formed between the adhered Al and the CrN coating surface in ambient air was stronger than the one forming in argon.

6) The amount of debris formed was found to be inversely proportional to the sliding speed. Increasing the sliding speed from 0.02 to 0.65 m/s decreased the amount of debris formed in ambient air for all three metals. It is suggested that the decrease in the amount of debris formed with increasing sliding speed was related to the decrease in

interaction time of the pin and the atmosphere with a certain location of the sliding track on the counterface.

7) The fluctuations in the COF curves were related to the removal, back and forth transfer of material, and debris generation processes. The debris generation mechanism involved the removal of the adhered material from the counterface and its fragmentation into loose small oxidized debris.

7.3. Tribological Behaviour of Non-hydrogenated DLC Coatings

1) The non-hydrogenated DLC coatings experienced high COF and wear rates in vacuum and inert gas environments against counterface materials that either had comparable hardness (WC) as the coating or had strong chemical affinity towards it (Al, Ti). In argon, Ti caused the highest wear rate of non-hydrogenated DLC coatings followed by 319 Al and WC. Although there was a considerable COF (0.40), Cu caused only a negligible amount of wear to the non-hydrogenated DLC coatings.

2) Low COF (≤ 0.16) and low wear rates ($\leq 2.31 \times 10^{-6} \text{ mm}^3/\text{m}$) of the non-hydrogenated DLC coatings associated with the formation of carbonaceous transfer layers on the counterface materials (Al, Ti and WC) were observed in air with $\text{RH} \geq 20\%$. This indicated that the presence of water vapour in the test environment was essential for the low COF and wear rates of the non-hydrogenated DLC coatings against counterface materials that are either comparably hard or have strong chemical affinity towards it. Increasing the relative humidity from 20 to 85% slightly decreased the COF and wear rates against 319 Al, but increased that against WC.

3) In ambient air, a carbonaceous transfer layer formed on counterface materials. Sliding in other environments (vacuum, argon, and nitrogen) did not cause the formation of this carbonaceous tribolayer. Formation of the carbonaceous transfer layer on the counterface material and the passivation of the non-hydrogenated DLC coating surface by adsorption and dissociation of the water molecules were suggested as two mechanisms responsible for the low COF and wear rate of the non-hydrogenated DLC coatings in air with humidity.

4) A very low COF (0.006) was observed under vacuum ($<0.173 \text{ Pa}$) after an initial running-in period in ambient air during which a tribolayer was formed on the

counterface materials of Al, Ti, and WC. Longer running-in sliding distances in ambient air prolonged the duration of the very low COF regime in vacuum. Higher sliding speeds reduced it. Together with the creation of an easy-to-shear transfer layer on the contact surface of the pins during the ambient air running in period, the adsorption of the remaining water vapour in the test chamber on to the non-hydrogenated DLC coating surface has been suggested as the cause of the subsequently observed very low COF regime in vacuum.

5) Adhesive and abrasive wear mechanisms were suggested as the two dominant wear mechanisms in vacuum and inert gas environments, i.e. when the materials in contact did not have other appropriate species, such as O₂ and H₂O in the test environment, to meet their bonding requirements. Chemical affinity of the counterface material towards the DLC coating promoted adhesive wear. Oxidational and abrasive wear mechanisms were the dominant wear mechanisms in dry and humid air. Catalytic effect of some metals and their oxides might have also accelerated the oxidational wear of the non-hydrogenated DLC coatings in dry and humid air.

6) The non-hydrogenated DLC coatings exhibited very low COF values (0.01-0.02) against aluminum under the molecular hydrogen atmosphere. The very low COF values were reached after an initial high COF (0.70 ±0.15) period. The initial high COF period corresponded to the formation of a carbonaceous transfer layer on the contact surface of the 319 Al pin. The presence of this carbonaceous transfer layer on the counterface was found to be essential to reach the very low COF state in the presence of hydrogen.

7) It was proposed that the very low COF state was maintained by the instantaneous passivation of available carbon bonds by the hydrogen molecules. The chemisorption of the hydrogen molecules, which consists of the breaking of the H-H bonds and the formation of C-H bonds, is suggested as the mechanism for the passivation. When C-H bonds break due to frictional and/or thermal means, hydrogen molecules are instantaneously chemisorbed forming C-H bonds. Changing the test environment from hydrogen to vacuum caused the COF to increase immediately, suggesting that the production of the C-H bonds was limited to the very top layers of both sliding surfaces.

8) The wear resistance of this particular type of DLC coatings is poor at elevated temperatures. The mechanisms that provide the high wear resistance of the coating in ambient temperature cease to operate at temperatures as low as 120°C.

9) Annealing at elevated temperatures in air causes the loss of the stability and the significant oxidation of the coating.

10) Different counterface materials caused differences in the wear behaviour of the DLC coatings. Although much softer than WC and sapphire, the 319 Al alloy caused more severe wear of the DLC coating both in terms of wear volume and depth of the wear track especially at elevated temperatures. A two- and three-body abrasive wear model is proposed to explain this observation.

11) It is possible to improve the tribological performance of the DLC coatings by optimizing the deposition parameters. For example, increasing the bias voltage and decreasing the flow rate was shown to improve the coating stability and wear resistance.

7.4. Practical Conclusions

1) The method developed here, although it does not exactly simulate the drilling conditions, was found to be very useful as a screening tool to eliminate the poor performing coatings for dry machining of aluminum alloys.

2) The implementation of non-hydrogenated DLC coated tools with water or water based lubricants under MQL conditions is suggested as an intermediate solution before the total elimination of metalworking fluids in machining operations.

7.5. Suggestions for Future Work

1) TEM investigation of the interface between the adhered aluminum and the coating surface. The aim of this investigation will be to find out the nature of the interface between the adhered material and the coating surface and whether aluminum experiences any recrystallization, etc. during transfer. Thus, by examining the nature of the interfaces, the microstructural basis of adhesion will be better characterized.

2) TEM investigation of the aluminum-coating interface after heating and cooling to various temperatures under static loaded condition. The aim of these experiments is to

assess the elevated temperature chemical stability of the coating against aluminum, which is one of the key requirements for a successful tool coating for dry machining.

3) Measurement of the adhesion strength of the interface experimentally.

4) Closer look to the first revolutions of sliding contact. For example, what is occurring after 1st, 2nd, 5th and 10th revolutions? In addition to the pin-on-disc tribometer, the scratch test equipment can also be used for this purpose.

5) Designing an experimental configuration that is more representative to study adhesion and material transfer during machining. As a repeated sliding test configuration, pin-on-disc tests are almost inevitably associated with the formation of tribolayers on one of the two sliding surfaces. However, tribolayers of the workpiece material does not form in machining operations and the cutting tool is always faced with the nascent material. Therefore, a test configuration where the tool always faces new workpiece material may give better insights. For example a crossed twin cylinders (one coated steel cylinder running against an Al rod) configuration may be used.

6) Detailed examination of the drills coated with diamond and different types of DLC coating after they fail during dry drilling of aluminum alloys. The aim will be to identify the failure mechanisms of the DLC coatings. Do they wear out uniformly or catastrophically? Do they fail because of poor adhesion to substrates when they become clogged?

7) More characterization of the transfer layers forming on the counterfaces that were run against non-hydrogenated DLC coatings. Are these really oxides or amorphous material with a lot of oxygen dissolved? Are the transfer layers forming on different counterfaces identical to each other in term of composition and degree of graphitization? Are there two layers on top of each other (First the mixed layer and then carbonaceous transfer layer on top of it)? What are the mechanical properties of the transfer layers?

8) Effect of doping with N, S, P, Cl on the tribological behaviour of DLC coatings against aluminum. There is substantial evidence that environmental dependency of the tribological behaviour of DLC coatings can be altered by appropriate doping elements [76-78]. It is of interest to investigate whether dopants could affect the friction and wear behaviour of DLC coatings against aluminum.

9) Investigation of the Si size, shape and content on the tribological behaviour of DLC coatings. It is known that the size of the Si particles in Al-Si alloys affect the wear rate of the cutting tools used for their machining [152]. Therefore, it is of interest to investigate if the wear rates of the DLC coatings are affected by the size of Si particles in Al-Si alloys.

APPENDICES

A.1. Frictional Heating of Sliding Surfaces

Temperature increase at the sliding interface due to the heat generated by friction is a well known observation that has a lot of importance in the tribological behaviour of especially dry sliding tribosystems. There have been many studies to measure, calculate, and model the surface and flash temperatures at the interface between the sliding surfaces [153-158]. In the following subsection, the methodology developed by Ashby and his co-workers will be described [143, 159, 160].

A.1.1. Ashby's Method of Calculating Surface and Flash Temperatures

The rate of heat generation (q) per unit nominal contact area (A_n) at the sliding interface between two solids in contact can be represented as

$$q = \frac{\mu.F.v}{A_n} \quad \text{Equation A.1.1}$$

Here, μ , F and v represent the COF, normal force and the relative sliding speed between the sliding surfaces, respectively. The generated heat is shared between the sliding surfaces according to their geometry and thermal properties. For the purposes of this study, the temperature calculations are done for a pin-on-disc configuration as shown in **Figure A.1.1**.

Two different temperatures are defined; the bulk temperature (T_b) and the flash temperature (T_f). The first one, the bulk temperature, is the surface temperature that would be reached if the frictional heat was passed uniformly across the nominal contact area A_n . It is given as:

$$T_b - T_o = \frac{\mu.F.v}{A_n} \left[\frac{1}{\frac{k_1}{l_{1b}} + \frac{k_2}{l_{2b}}} \right] \quad \text{Equation A.1.2}$$

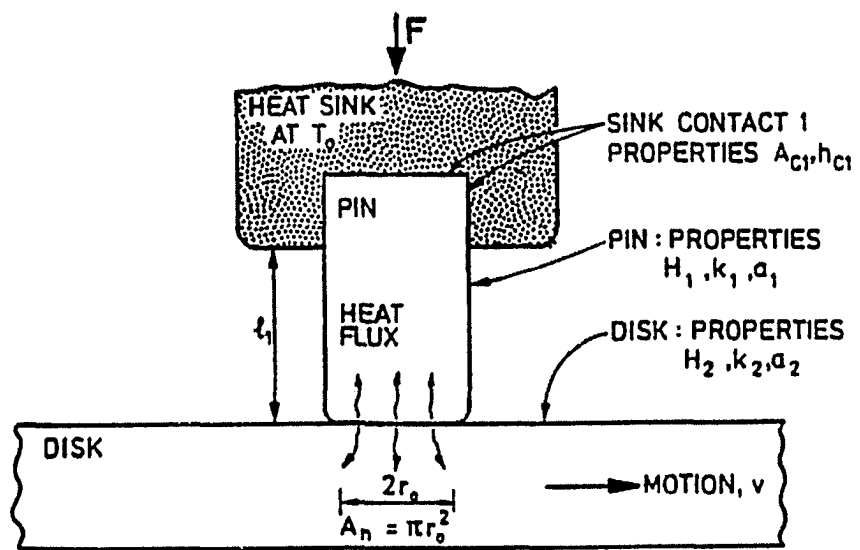


Figure A.1.1. A typical pin-on-disc configuration [160].

where T_o denotes the temperature of the remote sink to which the heat flows, k_1 and k_2 are the thermal conductivities of the materials in sliding contact, and l_{1b} and l_{2b} are the two lengths. The l_{1b} and l_{2b} are the equivalent linear heat diffusion distances from the sliding surface to the heat sink for the surfaces 1 and 2.

The second calculated temperature, the flash temperature, is the one experienced at the true contact area A_r , where the heat generated enters into the material. Due to the fact that A_r is much smaller than A_n in most cases, the T_f is usually much higher than T_b . In a similar way to T_b , T_f is expressed as,

$$T_f - T_b = \frac{\mu.F.v}{A_r} \left[\frac{1}{\frac{k_1}{l_{1f}} + \frac{k_2}{l_{2f}}} \right] \quad \text{Equation A1.3}$$

Here, l_{1f} and l_{2f} are the new equivalent heat diffusion distances and T_b' is the effective sink temperature that is given as,

$$T_b' = T_b - \frac{A_r}{A_n} (T_b - T_o), \text{ where} \quad \text{Equation A1.4}$$

$$\frac{A_r}{A_n} = \frac{F}{F_s} \quad \text{Equation A1.5}$$

F_s is defined as the seizure load at which A_r becomes equal to A_n and is calculated as,

$$F_s = \frac{H_o \cdot A_n}{\sqrt{1 + 12\mu^2}} \quad \text{Equation A1.6}$$

H_o is the hardness on the softer of the two surfaces. The open expressions and nomenclature for the equivalent heat diffusion distances l_{1b} , l_{2b} , l_{1f} and l_{2f} are given in **Tables A.1.1.a** and **b**. The material properties and the values of the other parameters

used to calculate the bulk and flash temperatures that were discussed in Section 6.5.2 are listed in Tables A.1.2 and A.1.3.

Table A.1.1. a) Nomenclature, and b) expressions and assumptions for the equivalent heat diffusion distances

A_{c1}, A_{c2}	Contact areas at heat sinks, (m^2)
a_1, a_2	Thermal diffusivities of surfaces 1 and 2, (m^2/s)
H_o	Hardness at 25°C
h_{c1}, h_{c2}	Heat transfer coefficients at heat sinks 1 and 2, (W/m^2K)
l_1, l_2	Linear distances from surface to heat sinks 1 and 2, (m)
n, n_1, n_2	A measure of the lifetime of a contacting asperity; it survives a sliding distance, $(\pi/2)n r_a$
r_a	Radius of a single isolated asperity junction, (m)
r_j	Radius of a contact-junction that can be made up of many unit asperities ($r_a < r_j < r_o$), (m)
r_o	Radius of nominal contact area ($r_o = (A_n/\pi)^{1/2}$), (m)

a)

Bulk	$l_{1b} = l_1 + \frac{A_n \cdot k_1}{A_{c1} \cdot h_{c1}}$ $l_{2b} = \frac{r_o}{\sqrt{\pi}} \tan^{-1} \left[\frac{2 \cdot \pi \cdot a_2}{r_o \cdot v} \right]^{1/2}$
Flash	$l_{1f} = \frac{r_j}{\sqrt{\pi}} \tan^{-1} \left[\frac{n \cdot 2 \cdot \pi \cdot a_1}{r_j \cdot v} \right]^{1/2} \quad (\approx \frac{\sqrt{\pi}}{2} r_j) \text{ for small } v$ $n = 100$ $l_{2f} = \frac{r_j}{\sqrt{\pi}} \tan^{-1} \left[\frac{n \cdot 2 \cdot \pi \cdot a_2}{r_j \cdot v} \right]^{1/2} \quad (\approx \frac{\sqrt{\pi}}{2} r_j) \text{ for small } v$ $r_j = r_o \left(\left[1 - \frac{F}{F_s} \right] \left[\frac{r_o}{r_a} \right]^2 + 1 \right)^{-1/2}$ $r_a = \frac{100}{H_o (\text{Pa})}, H_o = \text{Hardness of the softer body is taken}$

b)

Table A.1.2. The material properties used to calculate the bulk and flash temperatures that were discussed in Section 6.5.2.

	Al	Ti	CrN	DLC	M2
Density g/cm ³	2.7	4.5	6.1	2.3	7.9
Heat Capacity J/g-°C	0.904	0.528	0.665	0.711	0.450
Thermal Conductivity W/mK	229	22	16	15	48
Thermal Diffusivity m ² /s	9.38x10 ⁻⁵	9.269x10 ⁻⁶	3.94 x10 ⁻⁶	9.17 x10 ⁻⁶	5.00 x10 ⁻⁶
Hardness N/m ²	3.58x10 ⁸	2.22x10 ⁹	2.20x10 ¹⁰	1.13x10 ¹⁰	7.00x10 ⁹

Table A.1.3. The measured average COF and radius of nominal contact area values in ambient air.

Disc	Pin	Speed (m/s)	COF	r _o (m)
M2 Steel	Al	0.65	0.88	0.00044
M2 Steel	Al	0.12	0.82	0.00036
M2 Steel	Ti	0.65	0.82	0.00029
M2 Steel	Ti	0.12	0.78	0.00031
DLC	Al	0.65	0.19	0.00020
DLC	Al	0.12	0.18	0.00020
DLC	Ti	0.65	0.13	0.00018
DLC	Ti	0.12	0.12	0.00018
CrN	Al	0.65	0.53	0.00059
CrN	Ti	0.65	0.81	0.00047

A.2. Impingement Rate (Flux) of Gaseous Species [134]

Impingement rate is defined as the total number of molecular impingements on unit area of surface in one second. It is expressed as

$$J = \frac{pN_A}{\sqrt{2\pi MRT}} \quad \text{Equation A.2.1}$$

In the equation, p and N_A stand for pressure (Pa) and Avogadro's number. M is the molecular mass (kg) of the species under consideration. R and T are the ideal gas constant and temperature (K).

The impingement rate in ambient conditions is

$$J = \frac{1.013 \times 10^5 \cdot 6.02 \times 10^{23}}{\sqrt{2 \cdot \pi \cdot 0.028 \cdot 8.314 \cdot 298}} = 2.8 \times 10^{27} \frac{\text{impingements}}{\text{m}^2 \text{s}}$$

$$J = 2.8 \times 10^{23} \frac{\text{impingements}}{\text{cm}^2 \text{s}}$$

The number of molecules necessary to form a monolayer is found using the following way: Diameter of a nitrogen molecule is about 0.3 nm. Then on a 1 cm of length, $1/(0.3 \times 10^{-8}) = 3.3 \times 10^7$ molecules can be aligned. Therefore, on a 1 cm² area, $(3.3 \times 10^7)^2 = 1.1 \times 10^{15}$ molecules can be fitted. Assuming a sticking coefficient of 0.5, it takes $\frac{1.1 \times 10^{15}}{0.5 \cdot 2.9 \times 10^{23}} = 7.6 \times 10^{-9}$ sec to form a monolayer on the surface.

REFERENCES

1. US National Institute for Occupational Safety and Health Publication No 98-102, Occupational exposure to metalworking fluids: A criteria for a recommended standard, January (1998) 1, 2, 44, 143.
2. M. Lahres, P. M.-Hummel and O. Doerfel, Applicability of different hard coatings in dry milling aluminum alloys, *Surf. Coat. Tech.*, 91 (1997) 116-121.
3. M. Lahres and G. Jorgensen, Properties and dry cutting performance of diamond-coated tools, *Surf. Coat. Tech.*, 96 (1997) 198-204.
4. F. Klocke and T. Krieg, Nanocoatings on cutting tools for dry Machining, *annals of the CIRP*, 48,2 (1999) 515-529.
5. V. Derflinger, H. Brandle and H. Zimmerman, New hard/lubricant coating for dry machining, *Surf. Coat. Tech.* 113 (1999) 286-292.
6. J.F. Kelly and M.G. Cotterell, Minimal lubrication machining of aluminum alloys, *J of Mater. Proc. Tech.*, 120 (2002) 327-334.
7. D.M. Haan, S. A. Batzer, W.W. Olson, J.W. Sutherland, An experimental study of cutting fluid effects in drilling, *J. Mater. Proc. Technol.*, 71 (1997) 305-313.
8. P.S. Sreejith and B.K.A. Ngoi, Dry machining: Machining of the future, *J. of Mater. Proc. Tech.*, 101 (2000) 287-291.
9. J. McCabe and M. Ostraff, Performance experience with near-dry machining of aluminium, *Lubrication Eng.* 57 (12) (2001) 22-27.
10. D. Markov and D. Kelly, Mechanisms of adhesion-initiated catastrophic wear: pure sliding, *Wear* 239 (2000) 189-210
11. E. S. Machlin and W. R. Yankee, Friction of metals and oxides with special reference to titanium, *J. Appl. Phys.* v25 n5 (1954) 576-581.
12. M. Kerridge and J.K. Lancaster, The stages in a process of severe metallic wear, *Proc. R. Soc. London. Ser. A*, 236 (1956) 250-264.
13. M.E. Sikorksi, The adhesion of metals and factors that influence it, *Wear* 7 (1964) 144-162.
14. E. Rabinowicz, Influence of surface energy on friction and wear phenomena, *J. Appl. Phys.* v32 n8 (1961) 1440-1444.

15. E. Rabinowicz, The influence of compatibility on different tribological phenomena, *ASLE Trans.*, 14(3) (1971) 206-212.
16. A.K. Vijh, The influence of metal-metal bond energies on the adhesion, hardness, friction and wear of materials, *J. Mater. Sci* 10 (1975) 998-1004.
17. D.H. Buckley, Wear and interfacial transport of material, *J. Vac. Sci. Technol.*, 13(1) (1976) 88-95.
18. T. Kayaba and K. Kato, The adhesive transfer of the slip-tongue and the wedge", *ASLE Transactions*, 24 (1981), 164-174.
19. L.H. Chen and D.A. Rigney, Adhesive theories of transfer and wear during Sliding of Metals, *Wear* 136 (1990) 223-235.
20. T. Akagaki, and D.A. Rigney, "Sliding Friction and Wear of Metals in Vacuum," in *Proc. Intl. Conf on Wear of Matls.*, (1991), ASME, NY, 265-275.
21. P. Diss and M. Brendle, A general approach to discontinuous transfer films: Influence of sliding speed and stick-slip phenomena, *Wear* 203-204 (1997) 564-572.
22. K. Miyoshi, Considerations in vacuum tribology (Adhesion, friction, wear and solid lubrication in vacuum), *Tribol. Inter.*, 32 (1999) 605-616.
23. D.H. Hwang, I.H. Sung, D.E. Kim and S.J. Lee, Effects of material pair properties on the frictional behavior of metals, *Wear* 225-229 (1999) 600-614.
24. D.A. Rigney, Transfer, mixing and associated chemical and mechanical processes during the sliding of ductile materials, *Wear* 245 (2000) 1-9.
25. M. B. de Rooij and D. J. Schipper, Analysis of material transfer from a soft workpiece to a hard tool: Part I-Lump growth model, *J. Tribol. - T. ASME*, 123 (3) (2001) 469-473.
26. M. B. de Rooij and D. J. Schipper, Analysis of material transfer from a soft workpiece to a hard tool: Part II-Experimental verification of the proposed lump growth model, *J. Tribol. - T. ASME*, 123 (3) (2001) 474-478.
27. G. Straffelini, A simplified approach to the adhesive theory of friction, *Wear* 249 (2001) 79-85.
28. J. Hersberger, O.O. Ajayi, J.Zhang, H.Yoon, G.R. Fenske, Evidence of scuffing initiation by adiabatic shear instability, *Wear* 258 (2005) 1271-1478.

29. O.O. Ajayi, J.G. Hersberger, J. Zhang, H. Yoon, G.R. Fenske, Microstructural evolution during scuffing of hardened 4340 steel - implication for scuffing mechanism, *Tribol. Int.* 38 (2005) 277-282.
30. F.F. Ling and E.Saibel, Thermal aspects of galling of dry metallic surfaces in sliding contact, *Wear* 1 (1957/58) 80-91.
31. R. Ramboarina and J. Lepage, Influence of water vapour and oxygen co-adsorption on adhesion: self-adhesion of aluminum, *Tribol. Lett.* 5 (1998) 243-248
32. X.G. Wang and J.R. Smith, Copper/diamond adhesion and hydrogen termination, *Phys. Rev. Letters.*, v87 n18 (2001) 186103, 1-4.
33. X.G. Wang, J.R. Smith and A. Evans, Fundamental influence of C on adhesion of the Al₂O₃/Al interface, *Phys. Rev. Letters.*, v89 n28 (2002) 286102, 1-4.
34. W.G. Hartweck and H.J. Grabke, The influence of adsorbed foreign atoms on the adhesion of iron surfaces, *Acta Metall.* 29 (1981) 1237-1246.
35. M. Brendle and P.Stemple, Triboreactions of graphite with moisture- A new model of triboreactor for integrating friction and wear, *Wear* 254 (2003) 818-826.
36. J.A. Heimberg, K.J. Wahl, I.L. Singer and A. Erdemir, Superlow friction behaviour of diamond-like carbon coatings: Time and speed effects, *Appl. Phys. Lett.*, v 78 n 17 (2001) 2449-2451.
37. H. Mohrbacher, B.Blanpain, J.P. Celis and J.R. Roos, The influence of humidity on the fretting behavior of PVD TiN coatings, *Wear*, 180 (1995) 43-52.
38. I.L.Singer, S. Fayeulle and P.D.Ehni, Friction and wear behavior of TiN in air: The chemistry of transfer films and debris formation, *Wear*, 149 (1991) 375-394.
39. H. Chen, P.Q. Wu, C. Quaeys, K.W. Xu, L.M. Stals, J.W. He and J.P. Celis, Comparison of fretting wear of Cr-rich CrN and TiN coatings in air of different relative humidities, *Wear* (2002) 527-532.
40. G.M. Kocker, T.Gross and E.Santer, Influence of the testing parameters on the tribological behavior of self-mated PVD coatings, *Wear*, 179 (1994) 5-10.
41. K. Lepper, M. James, J. Chashechkina and D.A. Rigney, Sliding behavior of selected aluminum alloys, *Wear*, 203-204 (1997) 46-56.
42. S.V. Pepper, Effect of interfacial species on shear strength of metal-sapphire contacts, *J. Appl. Phys.*, 50(12) (1979) 8062-8065.

43. N.P. Gravier, E.C. Cutiongco and Y. Chung, Effect of testing environments on friction and bidirectional material transfer during dry sliding of 3004 aluminum against H13 steel, *Tribol. Trans.* 38 (1995) 1, 168-172.
44. S. Wilson and A.T. Alpas, Effect of temperature on the sliding wear performance of Al alloys and Al matrix Composites, *Wear*, 196 (1996) 270-278.
45. U. Persson, H. Chandrasekaran and A. Merstallinger, Adhesion between some tool and work materials in fretting and relation to metal cutting, *Wear*, 249 (2001) 293-301.
46. Y. Qi and L. G. Hector, Hydrogen effect on adhesion and adhesive transfer at aluminum/diamond interfaces, *Phys. Rev. B* 68 (20) (2003) 201403.
47. W.M. Rainforth, A.J. Leonard, C. Perrin, A. Bedolla-Jacuinde, Y. Wang, H. Jones, Q. Luo, High resolution observations of friction-induced oxide and its interaction with the worn surface, *Tribol. Int.* 35 (2002) 731-748.
48. J.E. Gardner, W.G. Sawyer and T. Blanchet, Geometric effects in high-temperature vapour - phase lubrication using hydrocarbon feed gases, *Lubrication Sci.*, 14-2, (2002) 131-145.
49. T.F.J. Quinn, Review of oxidational wear. Part1: The origins of oxidational wear, *Tribol. Int.*, v16 n5 (1983) 257-271.
50. T.F.J. Quinn, Review of oxidational wear. Part1: Recent developments and future trends in oxidational wear research, *Tribol. Int.*, v16 n6 (1983) 305-315.
51. P. L. Dickrell, W. G. Sawyer, A. Erdemir, Fractional coverage model for the adsorption and removal of gas species and application to superlow friction diamond-like carbon, *J. of Tribol.*, Vol. 126 (2004), 615-619.
52. F. M. Borodich and L. M. Keer, Modeling effects of gas adsorption and removal on friction during sliding along diamond-like carbon films, *Thin Solid Films*, 475 (2005) 108-117.
53. P. Hollman, A. Alahelisten, T. Bjork and S. Hogmark, CVD-diamond coatings in sliding contact with Al, Al-17%Si and steel, *Wear*, 179 (1994) 11-16.
54. M.Chen, X.G. Jian, F.H. Sun, B. Hu and X. S. Liu, Development of diamond-coated drills and their cutting performance, *J. Mater. Proc. Tech*, 129 (2002) 81-85.
55. J. D. Kim and Y. H. Kang, High speed machining of aluminum using diamond endmills, *Int. J. Mach. Tools Manufact.*, v37 n8 1155-1165.

56. S.Y. Luo, J.K. Kuo, T.J. Tsai and C.W. Dai, A study of the wear behaviour of diamond-like carbon films under the dry reciprocating sliding contact, *Wear*, 249 (2001) 800-807.
57. Y. Sakamoto and M. Takaya, Preparation of diamond-coated tools and their cutting performance, *J. of Mater. Proc. Tech.*, 127 (2002) 151-154.
58. Y. Kagiya, K. Tsuda, H. Fukui, H. Iyori and K. Yamagata, Development of DLC coating film (Auroracoat) and its application to tools, *SEI Tech. Rev.*, no 55 January (2003) 89-94.
59. M. Nouari, G. List, F. Girot, D. Coupard, Experimental analysis and optimisation of tool wear in dry machining of aluminium alloys, *Wear* 255 (2003) 1359–1368.
60. H.L. Coldwell, R.C. Dewes, D.K. Aspinwall, N.M. Renevier and D.G. Teer, The use of soft/lubricating coatings when drilling BS L 168 aluminum alloy, *Surf. Coat. Technol.* 177-178 (2004) 716-726.
61. M. Nouari, G. List, F. Girot, D. Ge'hin, Effect of machining parameters and coating on wear mechanisms in dry drilling of aluminium alloys, *Int. J. Mach. Tools & Manufact.* 45 (2005) 1436–1442.
62. H.A. Kishawy, M. Dumitrescu, E.-G. Ng, M.A. Elbestawi, Effect of coolant strategy on tool performance, chip morphology and surface quality during high-speed machining of A356 aluminum alloy, *Int. J. Mach. Tools & Manufact.* 45 (2005) 219–227.
63. D. U. Braga, A. E. Diniz, G.W.A. Miranda and N.L. Coppini, Using a minimum quantity of lubricant (MQL) and a diamond coated tool in the drilling of aluminum-silicon alloys, *J. Mater. Proc. Technol.* 122 (2002) 127–138.
64. M. Berger and S. Hogmark, Evaluation of TiB₂ coatings in sliding contact against aluminum, *Surf. Coat. Technol.*, 149 (2002) 14-20.
65. M. Berger and S. Hogmark, Tribological properties of selected PVD coatings when slid against ductile materials, *Wear*, 252 (2002) 557-565.
66. T. Bjork, M. Berger, R. Westergard, S. Hogmark and J. Bergstrom, New physical vapor deposition coatings applied to extrusion dies, *Surf. Coat. Technol.*, 146-147 (2001) 33-41.
67. E. Lugscheider, O. Knotek, C. Barimani, T. Leyendecker, O. Lemmer and R. Wenke, PVD hard coated reamers in lubricant-free cutting, *Surf. Coat. Tech.*, 112 (1999) 146-151.

68. J. Rechberger, P. Brunner and R. Dubach, High performance cutting tools with a solid lubricant physically vapor-deposited coating, *Surf. Coat. Tech.*, 62 (1993) 393-398.
69. M. Murakawa, S. Takeuchi, Evaluation of tribological properties of DLC films used in sheet forming of aluminum sheet, *Surf. Coat. Technol.* 163-164 (2003) 561-565.
70. J. Robertson, Diamond-like amorphous carbon, *Mater. Sci. Eng., R* 37 (2002) 129-281.
71. C. Donnet, J. Fontaine, A. Grill and T. Le Mogne, The role of hydrogen on the friction mechanism of diamond-like carbon films, *Tribol. Lett.* v9 no 3-4 (2000) 137-142.
72. H. Zaidi, J. Frene, A. Senouci, M Schmitt and D. Paulmier, Carbon surface modifications during sliding test and friction behaviour of carbon thin films against XC48 steel, *Surf. Coat. Technol*, 123 (2000) 185-191.
73. Erdemir, O.L. Eryilmaz, I.B. Nilufer and G.R. Fenske, Sythesis of superlow-friction carbon films from highly hydrogenated methane plasmas, *Surf. Coat. Technol.* 133-134 (2000) 448-454.
74. Erdemir, The role of hydrogen in tribological properties of diamond-like carbon films, *Surf. Coat. Technol.* 146-147 (2001) 292-297.
75. H. Ronkainen, S. Varjus, J. Koskinen and K.Holmberg, Differentiating the tribological performance of hydrogenated and hydrogen-free DLC coatings, *Wear* 249 (2001) 260-266.
76. M. Grischke, K. Bewilogua, K. Trojan and H. Dimigen, Application-oriented modifications of deposition processes for diamond-like-carbon-based coatings, *Surf. Coat. Technol.* 74-75 (1995) 739-745.
77. Donnet, Recent progress on the tribology of doped diamond-like and carbon alloy coatings: a review, *Surf. Coat. Technol.* 100-101 (1998) 180-186.
78. Y.L. Su and W.H. Kao, Optimum Me-DLC coatings and hard coatings for tribological performance, *J. Mater. Eng. Perform.*, 9-1 (2000) 38-50.
79. Y. Liu, A. Erdemir and E.I. Meletis, An investigation of the relationship between graphitisation and frictional behaviour of DLC coatings. *Surf. Coat. Technol* 86-87 (1996) 564-568.
80. E. Yoon, H. Kong and K. Lee, Tribological behaviour of sliding diamond-like carbon films under various environments, *Wear* 217 (1998) 262-270.

81. W. Zhang, A. Tanaka, K. Wazumi and Y. Koga, Effect of environment on friction and wear properties of diamond-like carbon film, *Thin Solid Films* 413 (2002) 104-109.
82. J. Andersson, R.A. Erck and A. Erdemir, Frictional behavior of diamondlike carbon films in vacuum and under varying water vapor pressure, *Surf. Coat. Technol.* 163-164 (2003) 535-540.
83. J. Andersson, R.A. Erck and A. Erdemir, Friction of diamond-like carbon films in different atmospheres, *Wear* 254 (2003) 1070-1075.
84. J. Jiang, S. Zhang and R.D. Arnell, The effect of relative humidity on wear of a diamond-like carbon coating, *Surf. Coat. Technol.* 167 (2003) 221-225.
85. C. Donnet, T. Le Mogne, L. Ponsonnet, M. Belin, A. Grill, V. Paetl and C. Jahnes, The respective role of oxygen and water vapor on the tribology, *Tribol. Lett.* 4 (1998) 259-265.
86. J. Jiang and R.D. Arnell, The effect of sliding speed on wear of diamond-like carbon coatings, *Wear* 218 (1998) 223-231
87. B.K. Tay, D. Sheeja, Y.S. Choong, S.P. Lau and X. Shi, Pin-on-disk characterization of amorphous carbon films prepared by filtered cathodic vacuum arc technique, *Diam. Relat. Mater.*, 9 (2000) 819-824.
88. L. Zhang, Tribo-chemical wear of amorphous carbon overcoats and TiC in Al₂O₃ – TiC Sliders, *J. Tribol-T. ASME*, 123 (2001) 324-329.
89. A.A. Voevodin, A.W. Phelps, J.S. Zabinski and M.S. Donley, Friction induced phase transformation of pulsed laser deposited diamond-like carbon, *Diam. Relat. Mater* 5 (1996) 1264-1269.
90. Y. Liu and E.I. Meletis, Evidence of graphitisation of diamond-like carbon films during sliding wear, *J Mater. Sci.* 32 (1997) 3491-3495.
91. J. Koskinen, D. Schneider, H. Ronkainen, T. Muukkonen, S. Varjus, P. Burck, K. Holmberg and H.J. Scheibe, Microstructural changes in DLC films due to tribological contact, *Surf. Coat. Technol.* 108-109 (1998) 385-390.
92. J.C. Sanchez-Lopez, A. Erdemir, C. Donnet and T.C. Rojas, Friction-induced structural transformations of diamondlike carbon coatings under various atmospheres, *Surf. Coat. Technol.* 163-164 (2003) 444-450.
93. B.K. Gupta, A. Malshe, B. Bhushan and V. Subramaniam, Friction and wear properties of chemomechanically polished diamond films, *J. Tribol. - T. ASME*, 116 (1994) 445-453.

94. D.Y. Wang, C.L. Chang and W.Y. Ho, Oxidation behavior of diamond-like carbon films, *Surf. Coat. Technol.* 120-121 (1999) 138-144.
95. H. Liu, A. Tanaka and K. Umeda, The tribological characteristics of diamond-like carbon films at elevated temperatures, *Thin Solid Films* 346 (1999) 162-168.
96. T. Krumpiegl, H. Meerkamm, W. Fruth, C. Schaufler, G. Erkens and H. Bohner, Amorphous carbon coatings and their tribological behaviour at high temperatures and in high vacuum, *Surf. Coat. Technol.* 120-121 (1999) 555-560.
97. Vannhulsel, B. Blanpain, J.P.Celis, J. Roos, E. Dekempeneer and J. Smeets, Study of the wear behaviour of diamond-like coatings at elevated temperatures, *Surf. Coat. Technol.* 98 (1998) 1047-1052.
98. J. Fontaine, C. Donnet, A.Grill and T.L. Mogne, Tribochemistry between hydrogen and diamond-like carbon films, *Surf. Coat. Technol* 146-147 (2001) 286-291.
99. F. Rabbani, Phenomenological evidence for the wear-induced graphitization model of amorphous hydrogenated carbon coatings, *Surf. Coat. Technol.* 184 (2004) 194-207.
100. Paulmier, H. Zaidi, T. Lee Huu and A.M. Durand, *Diamond Film. Technol.* v4, n3 (1994) 167-179.
101. Donnet and A.Grill, Friction control of diamond-like carbon coatings, *Surf. Coat. Technol.*, 94-95 (1997) 456-462.
102. B.Racine, M. Benlahsen, K. Zellama, M. Zarrabian, J.P. Villain, G. Turban and A. Grosman, Hydrogen stability in diamond-like carbon films during wear tests, *Appl. Phy. Lett*, v75 n2 (1999) 3479-3481.
103. Erdemir, Design criteria for superlubricity in carbon films and related microstructures, *Tribology Inter.* 37 (2004) 577-583.
104. K. Miyoshi, Studies of mechanochemical interactions in the tribological behaviour of materials, *Surf. Coat. Technol.* 44 (1990) 799-812.
105. D.S. Kim, T.E. Fischer and B. Gallois, The effects of oxygen and humidity on friction and wear of diamond-like carbon films, *Surf. Coat. Technol.* 49 (1991) 537-542.
106. Y. Liu, A. Erdemir and E.I. Meletis, Influence of environmental parameters on the frictional behavior of DLC coatings, *Surf. Coat. Technol.* 94-95 (1997) 463-468.

107. H. Fukui, M. Irie, Y. Utsumi, K. Oda and H. Ohara, An investigation of the wear track on DLC (a-C:H) film by time-of-flight secondary ion mass spectroscopy, *Surf. Coat. Technol.* 146-147 (2001) 378-383.
108. S.J. Park, J.K. Kim, K.R. Lee and D.H. Ko, Humidity dependence of the tribological behavior of diamond-like carbon films against steel ball, *Diam. Relat. Mater* 12 (2003) 1517-1523.
109. M.P. Delplancke-Ogletree and O.R. Monterio, Wear behaviour of diamond-like carbon/metal multilayers, *Surf. Coat. Technol* 108-109 (1998) 484-488
110. T.W. Scharf and I.L. Singer, Thickness of diamond-like carbon coatings quantified with Raman spectroscopy, *Thin Solid Films* 440 (1-2) (2003) 138-144.
111. T.W. Scharf and I.L. Singer, Monitoring transfer films and friction instabilities with in situ Raman tribometry, *Tribol. Lett.* 14 (1) (2003) 3-8.
112. R.H. Savage, Graphite lubrication, *J. Appl. Phys.* 19 1 (1948) 1-10.
113. F.P. Bowden, and J.E. Young, Friction of diamond, graphite and carbon and the influence of surface films, *Proc. R. Soc. London, Ser. A* Vol. 208, No. 1095 (1951) 444-455.
114. J.K. Lancaster and J.R. Pritchard, The influence of environment and pressure on the transition to dusting wear of graphite, *J. Phys. D: Appl. Phys.* 14 (1981) 747-762.
115. Y. Kokaku and M. Kito, Influence of exposure to an atmosphere of high relative humidity on tribological properties of diamondlike carbon films, *J. Vac. Sci. Technol. A* 7(3) (1989), 2311-2314.
116. Grill, V. Patel and B. Meyerson, Tribological behavior of diamond-like carbon - effects of preparation conditions and annealing, *Surf. Coat. Technol.* 49 (1991) 530-536.
117. Bremond, P. Fournier and F. Platon, Test temperature effect on the tribological behavior of DLC-coated 100C6-steel couples in dry friction, *Wear* 7-8, 254 (2003) 774-783.
118. W.C. Oliver and G.M. Pharr, An improved technique for determining hardness and elastic modulus using load and depth sensing indentation experiments, *J. Mater. Res.*, Vol 7 No 6 (1992) 1564-1583.
119. M.F. Doerner, W.D. Nix, A method for interpreting the data from depth-sensing indentation instruments, *J. Mater. Res.* 1 (1986) 601-609.

120. Y.T. Cheng and C.M. Cheng, Scaling, Dimensional analysis, and indentation measurements, *Mat. Sci. Eng. R*, v44 iss4-5 (2004) 91-149.
121. B. Schrader, *Infrared and Raman Spectroscopy*; Schrader, B. ed., VCH Publishers Inc.: New York, 1995; Chapter 4.
122. S. Yang, D. Camino, A.H.S Jones and D.G. Teer, Deposition and tribological behaviour of sputtered carbon hard coatings, *Surf. Coat. Technol.* 124 (2000) 110-116.
123. S.K. Field, M. Jarratt, D.G. Teer, Tribological properties of graphite-like and diamond-like carbon coatings, *Tribol. Int.* 37 (2004) 949-956.
124. L. Greenspan, Humidity fixed points of binary saturated aqueous solutions, *J. of Res. National Bureau of Standards- A. Physics and Chemistry*, Vol. 81A, No. 1, (1977) 89-96.
125. R. Mitra, W.A. Chiou, M.E. Fine and J.R. Weertman, Interfaces in as-extruded Al/TiC and Al/TiB₂ metal matrix composites, *J. Mater. Res.*, v 8, n 9 (1993) 2380-2392.
126. M. Kornmann and R. Funk, Boride coated titanium - A tough material resistant against corrosion by liquid aluminium, *Aluminum*, 53, 4 (1977) 249-252.
127. Nylund and I. Olefjord, Surface analysis of oxidized aluminum: 1. Hydration of Al₂O₃ and decomposition of Al(OH)₃ in a vacuum as studied by ESCA, *Surf. & Interface Analysis*, 21 (1994) 273-289.
128. Private communication with Jean Dasch, GM. R&D Center (2003).
129. J.A. Dean, ed., *Lange's Handbook of Chemistry* 15th ed., McGraw Hill, New York, (1999) 6.81-6.123.
130. B. Marchon, M.R. Khan, N. Heiman, P. Pereira and A. Lautie, Tribochemical wear of amorphous carbon thin films, *IEEE Trans. Mag.* v 26 n 1 (1990) 168-170.
131. B. Marchon, M.R. Khan, N. Heiman, P. Pereira and A. Lautie, Evidence for tribochemical wear of amorphous carbon thin films, *IEEE Trans. Mag.* v 26 n 5 (1990) 2670-2675.
132. A.G. Ramirez, M.A. Kelly, B.D. Strom, R.G. Walmsley, Carbon-coated sliders and their effect on carbon oxidation wear, *Tribol. Trans.* v39 n3 (1996) 710-714.
133. B.D. Strom, D.B. Bogy, R.G. Walmsley, J. Brandt and C.S. Bhatia, Tribochemical wear of carbon films in oxygen, *J. Appl. Phys.* 76 (8), (1994) 4651-4655.

134. R. Chambers, K. Fitch and B.S. Halliday, *Basic Vacuum Technology* 2nd ed., Institute of Physics Publishing, Bristol and Philadelphia:1998, 27-28, 35-36.
135. S.L. Kanashenko , A.E. Gorodetsky, V.N. Chernikov, A.V. Markin, A.P. Zakharov, B.L. Doyle, W.R. Wampler, Hydrogen adsorption on and solubility in graphites, *J. Nucl. Mater.* 233-237 (1996) 1207-1212.
136. S. Orimo, G. Majer, T. Fukunaga, A. Zuttel, L. Schlapbach, H. Fujii, Hydrogen in the mechanically prepared nanostructured graphite, *Appl. Phys. Lett.*, v75 n 20 (1999) 3093-3095.
137. Y. Ferro, F. Marinelli, A. Jelea, A. Allouche, Adsorption, diffusion, and recombination of hydrogen on pure and boron-doped graphite surfaces, *J. Chem. Phys.*,v120 n24 (2004) 11882-11888.
138. D. R. Lide, ed., *CRC Handbook of Chemistry and Physics* 85th ed., CRC Press, Boca Raton, (2004) 5-17, 26, 28.
139. M. Li and H.F. Dylla, Model for water outgassing from metal surfaces II, *J. Vac. Sci. Technol. A* 12(4), (1994) 1772-1777.
140. D.Camino, A.H.S. Jones, D. Merics and D.G. Teer, High performance sputtered carbon coatings for wear resistant applications, *Vacuum* 52 (1999) 125-131.
141. S. Yang, D. Camino, A.H.S Jones and D.G. Teer, Deposition and tribological behaviour of sputtered carbon hard coatings, *Surf. Coat. Technol.* 124 (2000) 110-116.
142. K.C. Ludema, *Friction, Wear, Lubrication A textbook in Tribology*, (Boca Raton, FL: CRC Press, 1996), 61-68.
143. M.F. Ashby, J. Abulawi and H.S. Kong, Temperature maps for frictional heating in dry sliding, *Tribol. Trans.* v34 (1991), 4, 577-587.
144. E.A. Brandes and G.B. Brook, eds, *Smithsells Metals Reference Book*, 7th ed., Butterworth-Heinemann, Oxford , (1999), 11.210.
145. J.L. Murray in, "Binary Alloy Phase Diagrams", ed. T.B. Massalski, (Metals Park, OH: ASM Int. Publ, 1986), 873, 971.
146. M. E. Jones, The structures of some compounds of boron, PhD Thesis, California Institute of Technology, (1953), 51-52.
147. Personal communication with Levent Inci, University of Windsor, (2005).

148. H. Polzl, F. Zinka, D. Gleispach, A. Winkler, Adsorption of H₂O on Al (111) and the interaction of atomic D with the ice layer, *Surf. Sci.* 440 (1999) 196-212.
149. W. Eberhardt, Oxidation of Al single crystal surfaces by exposure to O₂ and H₂O, *Surf. Sci.*, 75 91978) 709-720.
150. J.E. Crowell, J.G. Chen, D.M. Hercules and J.T. Yates, The adsorption and thermal decomposition of water on clean and oxygen-pretreated Al(111), *J. Chem. Phys.* 86 (10) (1987) 5804-5815.
151. J.C. Fuggle, L.M. Watson, D.J. Fabian and S. Affrossman, X-ray photoelectron studies of the reaction of clean metals (Mg, Al, Cr, Mn) with oxygen and water vapour, *Surf. Sci.* 49 (1975) 61-76.
152. T. Tanaka and T. Akasawa, Machinability of hypereutectic silicon-aluminum alloys, *J. Mater. Eng. Perf.*, v8, n4, 1999, 463-468.
153. R. Komanduri and Z.B. Hou, A review of the experimental techniques for the measurement of heat and temperatures generated in some manufacturing processes and Tribology, *Tribol. Int.* 34 (2001) 653-682.
154. F.P. Bowden and K.E.W. Ridler, Physical properties of surfaces. III. The surface temperature of sliding metals the temperature of lubricated surfaces, *Proc. R. Soc. London, Ser. A* Vol. 154, No. 883 (1936) 640-656.
155. P. Bowden and P. H. Thomas, The surface temperature of sliding solids, *Proc. Royal Soc. Lon. A*, v223, n1152 (1954) 29-40.
156. B. Gecim, Transient hot spot temperatures at a sliding ceramic contact including surface coating effects, *Wear*, 123 (1988) 59-76.
157. S. Wilson and A.T. Alpas, Thermal effects on mild wear transitions in dry sliding of an aluminum alloy, *Wear* 225-229 (1999) 440-449.
158. A.V. Chichinadze, P.N. Kurochka, N.V. Polyakov and V.I. Klyuchnikov, On estimation of the flash temperature on the friction microcontact, *Journal of Friction and Wear*, v 20 n 2 (1999) 14-19.
159. S.C. Lim and M.F. Ashby, Wear-mechanism maps, *Acta metall.*, v35 n1 (1987) 1-24.
160. H.S. Kong and M.F. Ashby, Friction-heating maps and their applications, *MRS Bulletin*, 10 (1991) 41-48.

VITA AUCTORIS

Erkan Konca was born in December 1975 in Ankara, Turkey. He graduated from Ankara Gazi High School in 1992. Then, he attended the School of English at the Hacettepe University, Ankara Turkey. From there, Erkan went on to the Middle East Technical University in the same city, where he obtained his B.Sc. and M.Sc. degrees in Metallurgical and Materials Engineering in 1998 and 2000. Erkan joined the Engineering Materials Ph.D. Program at the University of Windsor in September 2000 and hopes to graduate in September 2005. His next endeavour will be a post-doctoral fellowship at Brown University in Providence, RI, USA.

List of the Publications Originated from This Work

1. E. Konca, Y.T. Cheng, A. Weiner, J.M. Dasch and A.T. Alpas, Vacuum tribological behaviour of the non-hydrogenated diamond-like carbon coatings against aluminum: Effect of running-in in ambient air, Wear of Materials Conference 2005, San Diego, CA, USA, April 24-28, 2005 (Published in *Wear*, 259 (2005) 795–799)

2. E. Konca, Y.T. Cheng, A. Weiner, J.M. Dasch, A. Erdemir and A.T. Alpas, “Transfer of 319 Al Alloy to titanium diboride and titanium nitride based (TiN, TiCN, TiAlN) coatings: effects of sliding speed, temperature and environment”, *Surface Coatings & Technology* (In Press, Available online from Scienccdirect, 26 November 2004).

3. E. Konca, Y.T. Cheng, A. Weiner, J.M. Dasch and A.T. Alpas, Elevated temperature tribological behavior of non-hydrogenated diamond-like carbon coatings against 319 aluminum alloy, *Surface Coatings & Technology* (In Press, Available online from Scienccdirect, 27 April 2005).

4. E. Konca, Y.T. Cheng and A.T. Alpas, Material Transfer between Al, Cu, Ti and TiB₂ Coatings: Effects of Atmosphere and Speed, 2005 TMS Annual Meeting & Exhibition, February 13-17, 2005, San Francisco, CA, USA (published in *Surface Engineering in Materials Science – III Symposium Proceedings*, pp345-354).

5. E. Konca, Y.T. Cheng, A. Weiner, J.M. Dasch and A.T. Alpas, Effect of test atmosphere on the tribological behaviour of the non-hydrogenated diamond-like carbon

coatings against 319 aluminum alloy and tungsten carbide, The International Conference on Metallurgical Coatings and Thin Films 2005, May 2-6, 2005 San Diego, CA, USA (Surface Coatings & Technology, In Press, Available online from Sciencedirect, 13 September 2005)